Università di Genova – Department of Mechanical, Energy, Management and Transport Engineering (DIME)

Industrial PhD in collaboration with BeDimensional S.p.A.

Ph.D. Course in Mechanical, Energy and Management Engineering

Curriculum in Mechanics, Measurements and Materials (MMM)

XXXVII cycle

Barrier properties and industrial applications of industrially produced 2D hexagonal boron nitride

Luca Gabatel

Supervisor:

Prof. Fabrizio Barberis

Industrial co-supervisors:

Dr. Francesco Bonaccorso

Dr. Luca Berdondini

A.A. 2024/2025

Abstract

The transition to greener energy systems, longer-lasting infrastructure and safer biomedical devices is increasingly constrained by the lack of lightweight, defect-free barriers that can protect structures and materials from water, ions and gases without relying on scarce metals or fluorinated polymers. Two-dimensional crystals have shown promising results, yet commercial adoption has stalled because most production processes are still available only at gram-scale and materials cannot be standardized, certified or used in industrial applications. Addressing this bottleneck requires research programs that operate simultaneously on the factory floor and in the application lab, by developing large-volume exfoliation processes, formulating industry-ready coatings and validating the resulting films under sector-specific qualification tests.

This industrial PhD project, jointly supervised by the DIME Dept – IMEG/MMM program with DICCA Dept Material Science Labs at Polytechnic School at University of Genova – and BeDimensional S.p.A., explores how ton-scale few-layer hexagonal boron nitride (*h*-BN) obtained through the company's wet-jet-milling patented process can be transformed into polymer-based barrier coatings for disparate technological sectors. After optimizing production and conducting a full structural, chemical and morphological characterization of the reference flakes, the research moves to application-driven studies.

First, *h*-BN is incorporated into poly-isobutylene varnishes and evaluated on carbon steel substrates under accelerated electrochemical tests designed in house for marine anticorrosion following ASTM standards. The same composite is then laminated – through a collaboration with the University of Roma "Tor Vergata" – onto perovskite solar cells and modules, which are aged according to ISOS standards while additional Pb-leaching and thermal-cycle tests probe industrial readiness. Finally, ultrathin poly-vinyl-butyral/*h*-BN films are assessed as hermetic layers for cortical microelectrodes: nano-indentation experiments at the University of "Roma Tre" examine mechanical stability, whereas cytocompatibility assays carried out at the Istituto Italiano di Tecnologia - IIT with the support of Corticale srl, examine cellular and neuronal response. By interlacing large-scale nanosheet manufacturing, thin-film engineering, environmental and electro-mechanical testing and preliminary bio-assessment, the thesis demonstrates how coordinated efforts among BeDimensional S.p.A., three universities, a research center, and an industrial partners can accelerate the translation of 2D-material science into application-ready barrier technologies for infrastructure, energy and bioelectronics.

Acknowledgements

I would like to express my deepest gratitude to my supervisor, Prof. Barberis, for their invaluable guidance, encouragement, and support throughout the course of this research. Their insights, patience, and expertise, have been instrumental in shaping both this thesis and my development as a researcher.

I am also grateful to my industrial co-supervisors, Dott. Bonaccorso and Dott. Berdondini, for their constructive feedback and for continually challenging me to improve my work.

Special thanks go to my colleagues and friends in BeDimensional. The collaborative spirit, discussions, and camaraderie made this journey not only intellectually rewarding but also personally enjoyable.

I would like to acknowledge BeDimensional S.p.A. and the University of Genova for their financial and institutional support, without which this work would not have been possible.

I would like to also thank whoever collaborated with me for this research work, including the researchers from Corticale and the IIT-NetS3 laboratory for the support with biocompatibility tests, those from the CHOSE – Centre for Hybrid and Organic Solar Energy of the University of Roma "Tor Vergata" for the assembly and testing of perovskite solar cells, Prof. Sebastiani and the researchers from the STM – Materials Science and Technology group of the University of "Roma Tre" for the nanoindentation tests, and, last but not least, Prof. Finocchio from the Surface Chemistry and Industrial Catalysis laboratory of the University of Genova for her support with FT-IR measurements.

I am indebted to my family for their unwavering love, patience, and encouragement. Their belief in me has been a constant source of strength throughout this process.

Finally, I wish to thank all those who, in ways big or small, contributed to this thesis and supported me during this challenging but rewarding journey.

List of abbreviations

E_{corr}	Corrosion potential
Q_C	Coating capacitance
Q_{dl}	Double-layer constant-phase element
R_C	Coating resistance
R_S	Solution resistance
R_t	Electron-transfer resistance
i_{corr}	Corrosion current density
δ_D	Dispersion Hansen parameter
δ_H	Hydrogen bonding Hansen parameter
δ_{Hild}	Hildebrand parameter
δ_P	Polar Hansen parameter
η_p	Corrosion inhibition efficiency
0D	Zero-dimensional
1D	One-dimensional
2D	Two-dimensional
3D	Three-dimensional
a-BN	Amorphous boron nitride
AcAc	Acetylacetone
ACN	Acetonitrile
AFM	Atomic force microscopy
APS	Active-pixel-sensor
ATR	Attenuated total reflectance
AVT	Average visible transmittance
BBB	Blood-brain barrier
BCP	Bathocuproine
BN	Boron nitride
BP	Black phosphorus
CA	Contact angle
CAPEX	Capital expenditure
CB	Chlorobenzene

c-BN	Cubic boron nitride
CDT	Chemodynamic therapy
CHO	Chinese hamster ovary
CMOS	Complementary Metal-Oxide-Semiconductor
CNT	Carbon nanotube
COF	Covalent organic framework
CR	Corrosion rate
c-Si	Crystalline silicon
CT	Computed tomography
c-TiO_2	Compact titanium dioxide
CTL	Charge-transport layer
CVD	Chemical vapor deposition
DCB	Dichlorobenzene
DIV	Day in-vitro
DMEM	Dulbecco's modified Eagles medium
DMF	Dimethyl formamide
DMSO	Dimethyle sulfoxide
DPPH	2,2-diphenyl-1-picrylhydrazyl
DUV	Deep ultraviolet
E'	Storage modulus
E''	Loss modulus
E_F	Fermi level
EIS	Electrochemical impedance spectroscopy
ETL	Electron-transport layer
EtOH	Ethanol
EVA	Ethylene vinyl acetate
FA	Formamidinium
FAI	Formamidinium iodide
FBS	Fetal Bovine Serum
FLG	Few-layer graphene
FTIR	Fourier-transformed infrared spectroscopy
FTO	Fluorine-doped tin oxide

GBM	Graphene-based material
GO	Graphene oxide
h-BN	Hexagonal boron nitride
h-BNNS	Hexagonal boron nitride nanosheet
HEC	Hydroxyethyl cellulose
HTL	Hole-transport layer
ICP-OES	Inductively coupled plasma optical emission spectroscopy
IEC	International Electrotechnical Commission
IPA	Isopropanol
ITO	Indium tin oxide
LA	Longitudinal acoustic
LAPS	Light-addressable sensors
LcoE	Levelized cost of energy
LCP	Liquid crystal polymer
LiTFSI	Lithium bis(trifluoromethane)sulfonimide
LO	Longitudinal optical
LPE	Liquid phase exfoliation
MA	Methylammonium
MABr	Methylammonium bromide
MACl	Methylammonium chloride
MBE	Molecular beam epitaxy
MC	Mechanical cleavage
MDCK	Madin-Darby Canine Kidney
MEA	Microelectrode array
MMC	Metal matrix composites
MOF	Metal organic framework
MR	Magnetic resonance
m-TiO_2	Mesoporous titanium dioxide
NA	Numerical aperture
NATM	Nanometer-thick atomic-level membranes
NGS	Normal Goat Serum
NIR	Near infrared

NMP	N-methyl-2-pyrrolidone
OCV	Open circuit voltage
OPEX	Operational expenditure
OTR	Oxygen transmission rate
PA	Photoacoustic
PBS	Phosphate buffered solution
PCBM	[6,6]-phenyl-C_{61}-butyric acid methyl ester
PCE	Power conversion efficiency
PDT	Photodynamic transducer
PEACl	Phenylethylammonium chloride
PEAI	Phenylethylammonium iodide
PEDOT	Poly(3,4-ethylenedioxythiophene)
PEG	Poly(ethylene glycol)
PEI	Poly(ethyleneimine)
PET	Positron-emission tomography
PFA	Paraformaldehyde
PIB	Poly(isobutylene)
PLLA	Poly(L-lactic acid)
POE	Polyolefins
Ppy	Polypyrrole
PSC	Perovskite solar cell
PSM	Perovskite solar module
PSS	Polystyrene sulfonate
PTAA	Poly[bis(4-phenyl)(2,4,6-trimethylphenyl)amine]
PTT	Photothermal transducer
PU	Polyurethane
PV	Photovoltaic
PVA	Poly(vinyl alcohol)
PVB	Poly(vinyl butyral)
RGO	Reduced graphene oxide
RMS	Root mean square
ROS	Reactive oxygen species

R_p	Polarization resistance
RT	Radiotherapy
RT	Room temperature
SBS	Sedimentation-based separation
SC	Solar cell
SDT	Sonodynamic therapy
SL-*h*-BN	Single-layer hexagonal boron nitride
spiro-OMeTAD	2,2′,7,7′-tetrakis[N,N-di(4-methoxyphenyl)amino]-9,9′-spirobifluorene
SRB	Sulforhodamine B
STM	Scanning tunnelling microscopy
TA	Transversal acoustic
tBP	Tert-butyl pyridine
TEC	Thermal expansion coefficient
TEM	Transmission electron microscopy
TGA	Thermogravimetric analysis
TIP	Titanium(IV) isopropoxide
TMD	Transition metal dichalcogenide
TO	Transversal optical
TPU	Thermoplastic polyurethane
TUBB3	Anti-Tubulin β 3
UHV	Ultra-high vacuum
UV	Ultraviolet
w-BN	Wurtzite boron nitride
WEP	Waterborne epoxy
WJM	Wet-jet milling
WVTR	Water vapor transmission rate
XPS	X-ray photoelectron spectroscopy
XRD	X-ray diffraction
Z	Impedance
ZA	Out-of-plane acoustic
γ	Interfacial tension

Table of Figures

*The internal panel shows the magnification of the figure in the 100-200 s time interval. (b) Infrared thermal images of glass/PIB/glass (left) and glass/PIB:*h-*BN/glass (right) systems acquired after 60 s of cooling.*[191]

Figure 4.6 (a) Sketch of the structure of the mesoscopic n-i-p PSCs based on $Cs_{0.08}FA_{0.80}MA_{0.12}Pb(I_{0.88}Br_{0.12})_3$ *perovskites and PTAA HTLs. (b) Schematic of the cell layout (active area = 1* cm^2*), in which the non-compact layers of the device are fully covered by the encapsulant. Two flat metallic ribbons are connected to the cell terminals to bring the electrical contacts externally. (c) Photograph of a representative mesoscopic PSC encapsulated with PIB:*h-*BN. (d) J-V curves (reverse voltage scan) measured for a representative mesoscopic PSC before and after encapsulation with PIB:*h-*BN (before and after 240 h-ISOS-D1). (e), (f) PV parameters of the mesoscopic PSCs without encapsulation and with PIB and PIB:*h-*BN encapsulants, acquired over >1000 h of ISOS-D-2 and ISOS-L-1 tests.*[191]

Figure 4.7 (a) Sketch of the structure of the large-area (1 cm^2*) mesoscopic n-i-p PSCs based on* $Cs_{0.08}FA_{0.80}MA_{0.12}Pb(I_{0.88}Br_{0.12})_3$ *perovskites and spiro-OMeTAD HTLs. (b) J-V curves measured for the as-fabricated mesoscopic n-i-p PSCs based on spiro-OMeTAD HTLs before and after encapsulation with PIB:*h-*BN (before and after 240 h-ISOS-D-1). (c) PV parameters of the investigated mesoscopic n-i-p PSCs based on spiro-OMeTAD HTLs acquired over >1000 h of ISOS-D-2 test.*[191]

Figure 4.8 (a) Sketch of the structure of the low temperature-processed large-area (1 cm^2*) planar n-i-p PSCs based on Cs0.08 FA0.80MA0.12Pb(I0.88 Br0.12)3 perovskites. (b) J-V curves measured for the as-fabricated planar n-i-p PSCs before and after encapsulation with PIB:*h-*BN (before and after 240 h-ISOS-D-1). (c) PV parameters of the investigated planar n-i-p PSCs acquired over >2000 h of ISOS-D-2 test.*[191]

Figure 4.9 (a) Sketch of the structure of the large-area (1 cm^2*) inverted p-i-n PSCs based on PTAA HTLs and PCBM ETLs. (b) J-V curves measured for the as-fabricated inverted p-i-n PSCs before and after encapsulation with PIB:*h-*BN (before and after 240 h-ISOS-D-1). (c) PV parameters of the investigated inverted p-i-n PSCs acquired over >1000 h of ISOS-D-2 test.*[191]

Figure 4.10 (a) Schematic of the mesoscopic n-i-p PSM layout (cell active area = 2 cm^2*; total active area = 10* cm^2*), in which the non-compact layers are entirely covered by the encapsulant. (b) Photograph of a representative mesoscopic n-i-p PSM as fabricated (front and read sides: top and bottom picture, respectively) and (c) after encapsulation (rear side) with PIB:*h-*BN. (d) J-V curves (reverse voltage scan) measured for the as-fabricated mesoscopic n-i-p PSMs before and after encapsulation with PIB (top panel) and PIB:*h-*BN (bottom panel) (before and after 240 h-ISOS-D1). (e), (f) PV parameters of the PSMs without encapsulation and with PIB and PIB:*h-*BN encapsulants acquired over >1000 h of the ISOS-D-2 and ISOS-L-1 tests.*[191]

*Figure 4.11 (a) Temperature profile of the thermal shock test performed on the mesoscopic n-i-p PSMs encapsulated with PIB and PIB:*h-*BN. (b) Temperature profile and environmental exposure conditions of the humidity freeze test performed on the mesoscopic n-i-p PSMs encapsulated with PIB and PIB:*h-*BN. (c) PV parameters of the mesoscopic n-i-p PSMs encapsulated with PIB and PIB:*h-*BN acquired over >200 cycles of the thermal shock test. (d) PV parameters of the mesoscopic n-i-p PSMs encapsulated with PIB and PIB:*h-*BN acquired over >10 cycles of the customized humidity freeze test.*[191]

Figure 4.12 (a) Comparison between the temperature profiles of the IEC 61215 thermal cycling and our thermal shock test. (b) Enlargement of the temperature profiles shown in panel a), evidencing the first cycle of our thermal shock test. (c) Comparison between the temperature and RH profiles of the IEC 61215 and our humidity freeze tests. (d) Enlargement of the temperature profiles and other environmental conditions (water immersion or ambient air exposure) shown in panel (a), evidencing the first cycle of our humidity freeze test, including a water immersion step.[191]

*Figure 4.13 (a),(b) Photograph of the unencapsulated PSM (rear side) and a PSM encapsulated with PIB:*h-*BN (rear and front side) after 24 h of immersion in water. (c) Areal Pb leakage from the investigated PSMs*

Table of Contents

Introduction and Thesis Outline

Two-dimensional (2D) materials stepped onto the scientific stage in 2004 with the mechanical isolation of few-layers graphene, and the discovery rapidly drew attention to this entire class of layered crystals, characterized by strong in-plane bonding, weak interlayer forces and quantum-confined electronic structures, which, when successfully exfoliated, unlock properties unavailable in bulk solids. Within this broad family, hexagonal boron nitride (*h*-BN) stands out for its distinctive combination of electrical insulation, optical transparency, thermal conductivity, and chemical inertness.

Hexagonal boron nitride features the same honeycomb geometry of graphene, yielding an electrically insulating sheet just 0.33 nm thick in its single-layer form, but the alternation of boron and nitrogen atoms opens a ≈ 6 eV band gap, which makes the material a strong electrical insulator. Its basal planes are almost completely impermeable to gases and ions, endowing *h*-BN with barrier properties that rival state-of-the-art inorganic oxides while retaining superior mechanical flexibility and specific surface area. The material also shows an in-plane thermal conductivity comparable to that of copper, while its outstanding chemical and thermal stability extend the range of possible applications. Biocompatibility and slow biodegradation further motivate biomedical exploration, although systematic studies of its behavior in presence of neural cells are rather scarce.

Laboratory exfoliation techniques have now matured into industrial processes, opening new possibilities for the industrialization of 2D crystals. A global vanguard is represented by BeDimensional S.p.A., a 2016 spin-off of the Istituto Italiano di Tecnologia, that has upscaled a laboratory-scale wet-jet milling technique into an industrial plant in Genoa, which was certified by late 2024 to produce more than three tons of few-layer *h*-BN per year, with a roadmap – supported by a € 20 million European Investment Bank loan – to exceed an annual productivity of thirty tons before 2030.

Industry is already embedding *h*-BN in several value chains, exploiting its peculiar properties, even in its bulk form. Micronized powders are used as electrically insulating yet thermally conductive fillers for power-electronic interface pads, thermoplastics and epoxy encapsulants. Their lamellar structure is exploited to lower the coefficient of friction in high-temperature lubricants and cutting fluids, while their chemical inertness allows its use in cosmetic formulations and food-contact plastics. Recent demonstrations show that incorporating only 1-3 vol% *h*-BN nanosheets in epoxy primers can extend salt-spray lifetimes beyond 2000 hours by lengthening the diffusion path for water

and chloride ions, offering a viable route to zinc-reduced, chromium-free anticorrosion barrier coatings.

Encapsulation – isolating a sensitive device or interface from its environment – sits at the heart of many of these applications. Ideally, an encapsulant must couple an ultralow water-vapor transmission rate (WVTR < 10^{-6} g m^{-2} day^{-1} for advanced optoelectronics) to transparency, chemical stability, and mechanical resistance. Some conventional solutions are thermoset epoxies, UV-curable acrylates, parylene C and multilayer stacks that alternate inorganic oxides with flexible polymers, but their performance, however excellent, is increasingly strained by the demands of flexible electronics and implantable bio-systems that can withstand even more aggressive conditions.

The challenge is particularly severe for perovskite solar cells (PSCs), whose certified power-conversion efficiency already exceeds 26%, but whose instability toward moisture, oxygen, heat and UV radiation limits outdoor lifetimes. The qualification under IEC 61215 and ISOS standards demands survival of the cells under high humidity, high temperature, thermal cycling and UV exposure. Glass/glass modules can meet these requirements by combining thick surface and edge sealants, yet flexible PSCs require thin-film barriers with sub-10^{-5} g m^{-2} day^{-1} WVTR. Printable nanocomposites that disperse *h*-BN nanosheets within UV-curable matrices have recently achieved WVTRs below 10^{-4} g m^{-2} day^{-1} in single-pass slot-die coating at tens of meters per minute, pointing toward a viable route for roll-to-roll encapsulation at gigawatt scale. Still, research demands industrially viable and low-temperature processable encapsulation systems, chemically compatible with perovskites and able to withstand standard accelerated ageing tests.

Biology represents the next frontier for the application of 2D materials. The atomic thinness, chemical inertness, and electrical insulation of *h*-BN favor its application as barrier filler in chronical devices. Nevertheless, the neurotechnology landscape remains almost untouched, with no reported results on the compatibility and use of *h*-BN in neural sensors. Chronic neural implants must combine minimum leakage currents, low WVTR, a Young's modulus compatible with tissues and sub-10 μm thickness, without compromising adherence to heterogeneous device layers and the mechanical robustness necessary to guarantee a safe removal of the device after use. Of course, their biocompatibility and the immune response to their presence are of outmost importance. Among the commonly used materials, parylene C, silicon nitride and inorganic laminates suffer from stress-induced cracking or hydrolytic degradation, while a finely tuned nanocomposite encapsulant could, in principle, overcome these limitations and provide the first truly multifunctional encapsulant for bioelectronics.

This thesis therefore pursues two intertwined objectives:

- First, to develop scalable, metal-free *h*-BN-based barriers for corrosion-protective metal coatings and for perovskite photovoltaics, exploiting and investigating the *h*-BN produced by BeDimensional S.p.A.
- Second, to evaluate the suitability of the same coating architectures for chronic neural interfaces, thereby addressing the knowledge gap surrounding *h*-BN in neurotechnology.

By integrating industrial production, advanced thin-film engineering, accelerated ageing and *in vitro* cytotoxicity testing, the work aims to bridge fundamental materials science with the stringent performance metrics demanded by both energy devices and implantable bioelectronics, charting a pathway toward sustainable barrier technologies for the next generation of industrial and biomedical applications.

The thesis is organized into five chapters. Chapter 1 surveys the broader field of 2D materials, outlining their physicochemical properties, predominant application sectors and current production routes, and closes with a detailed appraisal of *h*-BN. Chapter 2 describes the continuous wet-jet-milling process implemented by BeDimensional S.p.A. for the large-scale manufacture of few-layer graphene and *h*-BN, and presents the structural, chemical and morphological characterization of the *h*-BN grade exploited throughout the study. Chapter 3 evaluates *h*-BN as a barrier additive in poly-isobutylene-based anticorrosion coatings for carbon steel, with performance quantified by electrochemical tests carried out in agreement with relevant international standards. Chapter 4 transfers an analogous *h*-BN formulation to perovskite solar cells and minimodules, applying it as a blanket encapsulant and assessing stability via standardized accelerated ageing protocols. Chapter 5 offers a preliminary assessment of *h*-BN-loaded composite encapsulants for chronic neural interfaces, focusing on barrier performance in saline environment, mechanical properties and *in vitro* biocompatibility. Despite not achieving satisfactory results for the application of *h*-BN-based encapsulants in neurotechnology, this part of the study provides insights on the possible performance of the same, while showing preliminary results regarding their biocompatibility in the neural environment, subject suffering from a vast absence of experimental data. The conclusion and outlook section then summarizes the major findings and discusses future research directions stemming from this work.

The work has been carried out in collaboration with the University of Roma "Tor Vergata" for the testing and assembly of PSCs and PSMs, the Istituto Italiano di Tecnologia for biocompatibility tests, the University of "Roma Tre" for nanoindentation tests and with the supervision of Corticale srl regarding the work on neural sensors.

Chapter 1 2D materials: properties and synthesis

Over the past two decades, two-dimensional (2D) materials have gained attention as a central focus of scientific and technological investigations, due to their peculiar structure and unique combination of properties. These materials are characterized by a high aspect ratio,[1] which stems from their ultrathin, planar nature, and by remarkable physical[2] and chemical characteristics.[3,4] Such properties have sparked interest across multiple disciplines, ranging from materials science and physics to chemistry and engineering. Among their most notable characteristics are a high surface area,[5] exceptional optical transparency,[6] and the ability to fine-tune their (opto)electronic properties by varying the material thickness.[5,7] These qualities make 2D materials fundamentally different from their bulk counterparts, providing unique possibilities for a wide range of applications.

In nature, a virtually limitless array of layered materials exists, many of which can be exfoliated into atomically thin layers to create 2D crystals with diverse characteristics.[8] This broad rage of properties enable their use in diverse applications, including, among the others, energy storage and conversion, sensors, flexible electronics, and catalysis. The origins of modern research into 2D materials can be traced back to a milestone study in 2004 by Novoselov, Geim, *et al.*, who successfully isolated graphene in its few-layer form through mechanical exfoliation – a process often referred to as the "scotch tape technique".[2] Single-layer graphene will be then firstly reported by the same group in 2005.[9] This breakthrough not only demonstrated the feasibility of producing atomically thin materials but also paved the way to the exploration of the remarkable properties of graphene, including its unparalleled tensile strength, exceptional electrical conductivity, and high optical transparency.

At the atomic level, graphene is composed of carbon atoms arranged in a 2D honeycomb lattice. Each carbon atom forms σ-bonds with its three nearest neighbors, while contributing with a single electron to a delocalized molecular orbital over the entire 2D plane. This electronic structure endows graphene with unique characteristics, such as its exceptional electron mobility and the ability to sustain ballistic transport over micrometric distances,[10,11] properties that have made graphene a foundational material in the field of 2D materials, inspiring the discovery of numerous other 2D crystals, each exhibiting distinctive properties that often complement those of graphene.[12–15]

Typically, 2D materials consist of layered structures in which the individual layers are bonded through strong in-plane covalent bonds.[16] These layers are stacked together and held by weak van der Waals interactions,[16] which facilitate their separation into single layers or few-layered forms using chemical

or physical exfoliation methods.[17,18] This layered architecture is the root cause to the unique properties of 2D materials, enabling applications in diverse areas ranging from photonics,[19] to spintronics,[20] and nanoelectronics.[21] Although recent advancements have expanded the scope of 2D materials to include non-layered varieties,[22] their practical exploitation remains in its infancy, lagging behind the widespread adoption of layered 2D materials.

Given the richness and diversity of this class of materials, this chapter aims to provide a comprehensive overview of two of the most studied and industrially available 2D crystals, *i.e.* graphene and hexagonal boron nitride (*h*-BN). Additionally, the various production techniques[23] – ranging from micromechanical exfoliation[9] and chemical vapor deposition (CVD)[24] to liquid-phase exfoliation (LPE)[25] – that enable the synthesis of these materials will be explored and analyzed. The chapter will also highlight the potential applications of these materials, demonstrating how their unique characteristics can be harnessed for innovative solutions in technology and industry.

Section 1.1 Graphene

Graphene is a 2D layered material composed entirely of carbon atoms in an sp^2-hybridized configuration, arranged to form a hexagonal honeycomb structure only one atom thick.[26] Because of this atomic-scale thickness, graphene effectively represents the thinnest material known, and yet it displays extraordinary mechanical and electronic properties. Furthermore, this 2D allotrope of carbon is recognized as the fundamental unit for a variety of other carbon materials, including the zero-dimensional (0D) fullerene, the one-dimensional (1D) carbon nanotubes (CNTs), and the three-dimensional (3D) bulk graphite. The fullerene arises from wrapping a graphene sheet into a spherical structure,[27] whereas CNTs emerge by rolling a graphene layer into a cylindrical shape.[28,29] When numerous graphene sheets are stacked together, they constitute graphite, regarded as the only thermodynamically stable allotropic form of carbon (Figure 1.1). Within each single layer, the carbon atoms bond covalently in-plane, and the sheets themselves are held together along the c-axis by weak van der Waals forces.[30]

The exceptional attributes of graphene originate in its highly organized crystal structure. In particular, carbon 2s, $2p_x$, and $2p_y$ orbitals combine to form sp^2 orbitals, yielding robust σ bonds approximately 0.142 nm in length.[31] Meanwhile, the remaining $2p_z$ orbital projects perpendicularly from the graphene plane and overlaps with adjacent atoms $2p_z$ orbitals, creating the comparatively weaker π bonds that give graphene its unique semi-metallic electronic character.[32] A defining feature of the band structure of graphene is found at the *K* points of the Brillouin zone – commonly referred to as Dirac points – where the occupied π orbital and the unoccupied π* orbital meet (Figure 1.2a).[33] Near

the Fermi level (E_F), electrons exhibit a linear energy–momentum dispersion relationship and act as massless Dirac fermions (Figure 1.2b), conferring upon graphene the status of a zero-gap semiconductor.[31,34,35]

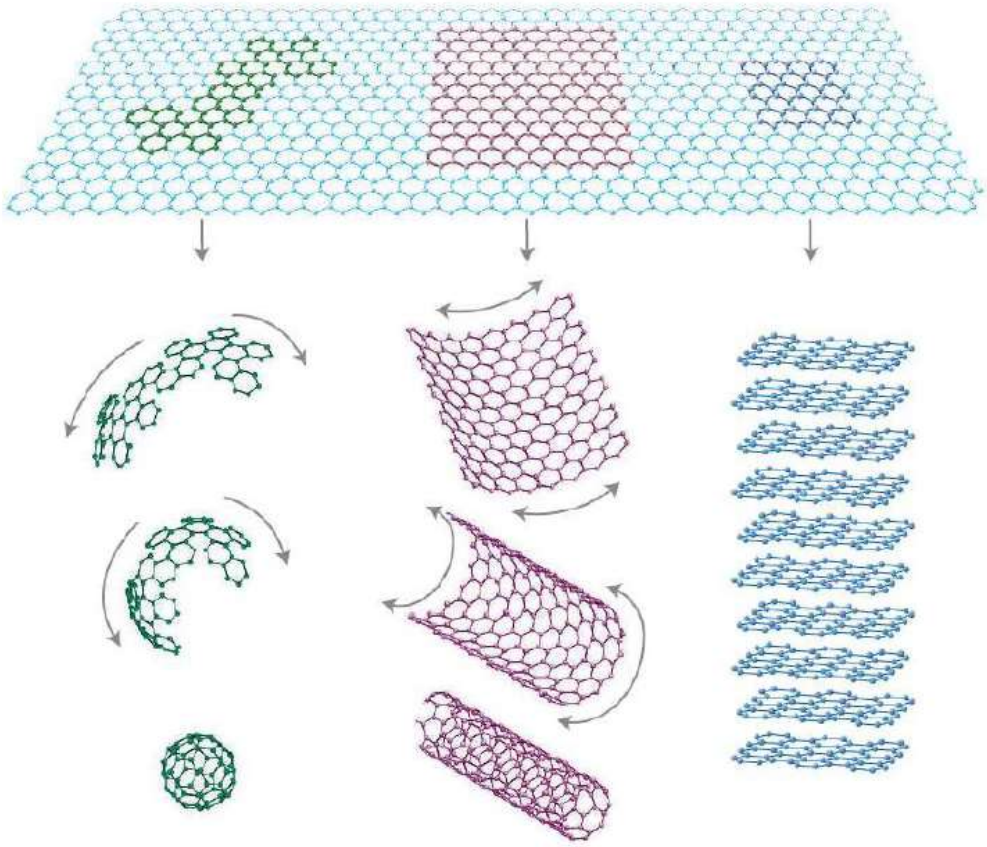

Figure 1.1 Allotropes of carbon formed by using graphene as building block. From left to right: fullerene (0D), carbon nanotube (1D), graphite (3D).[1]

One significant consequence of this electronic arrangement is remarkably high intrinsic electron mobility of graphene, which can reach approximately 250000 $cm^2\ V^{-1}\ s^{-1}$ at room temperature (RT).[32,36,37] This extraordinary charge-carrier mobility, combined with ballistic transport features at relatively long distances, underscores graphene potential for advanced electronic devices.[38–42] However, due to its semi-metallic band structure and the subsequent inability to provide a true off-state, unadulterated graphene is not suitable for applications in digital devices in the typical field-effect design, unless properly modified though bandgap engineering.[34,43–46] Additionally, graphene presents exceptional thermal conductivity, with measured values ranging from about 4800 to 6000 $W\ m^{-1}\ K^{-1}$,[47] a property attributable to the strong in-plane sp^2 bonding network and to its phonon structure. In pristine samples, heat conduction is dominated by acoustic phonons, particularly the longitudinal (LA), transverse (TA), and out-of-plane (ZA) modes. These modes have high group velocities and long mean free paths, enabling efficient heat conduction.[48] By contrast, the optical

phonons (longitudinal optical, LO, and transverse optical, TO) occur at higher energies and, despite being strongly influenced by electron-phonon interactions at specific points in the Brillouin zone, such as *Γ* and *K*, carry less heat overall due to their lower group velocities.[49] Furthermore, the strict 2D nature of graphene further leads to a specific surface area as high as 2630 m^2 g^{-1},[50] making it an attractive candidate for applications in which a high surface-to-volume ratio is crucial – such as in sensors,[17,34,51,52] catalysis,[53] and energy storage.[54–56]

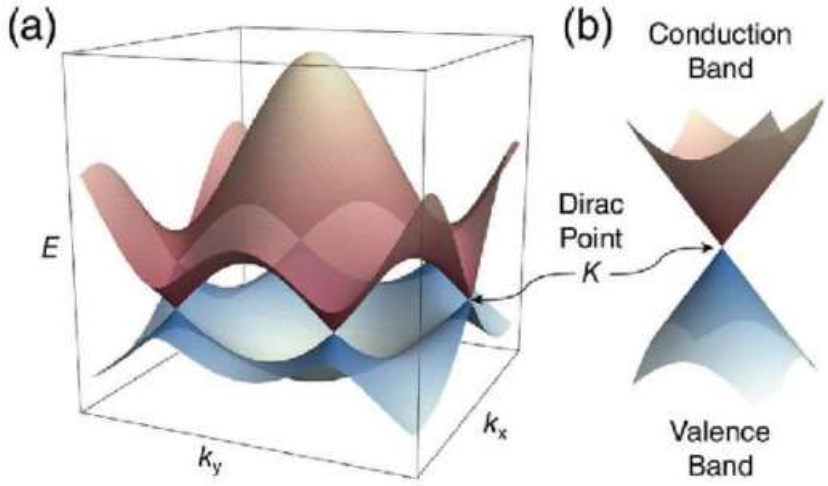

Figure 1.2 (a) Electronic band structure of graphene. (b) Linear dispersion relation showing the vertically mirrored Dirac cones intersecting at the E_F.[35]

The mechanical properties of graphene are equally impressive. Thanks to the strength of its in-plane σ bonds, it exhibits a Young's modulus of nearly 1060 GPa and a tensile strength of approximately 42 N m^{-1}, both of which surpass comparable measures for steel by a considerable margin.[57,58] In addition to its mechanical robustness, graphene is exceptionally thin and therefore absorbs only around 2.3% of visible light,[59] despite showing the highest known value of optical conductivity.[35]

Beyond its fundamental scientific interest, the unique properties of graphene have prompted active exploration across a variety of technological domains. Owing to its broadband optical absorption and ultrafast carrier dynamics, it is being widely investigated for photonic and optoelectronic applications,[60] while its high thermal conductivity makes it a promising material for thermal management solutions in microelectronics and other heat-intensive systems.[61] Moreover, the large specific surface area, chemical stability, and biocompatibility of graphene enable effective biosensing technologies.[52] Its robust mechanical strength and light weight are also advantageous for fabricating advanced composite materials that deliver superior durability and performance with respect to conventional materials.[62]

In the energy sector, graphene demonstrates potential as a catalyst support in various energy conversion processes,[63] as well as a high-performance electrode material in supercapacitors, thanks to its large specific surface area and excellent electrical conductivity,[64,65] or additive in anodes for rechargeable battery, where it is able to improve the durability of active materials such as silicon[66–70] or sulfur.[71–74]

Collectively, these extraordinary properties and wide-ranging applications continue to fuel intensive research on graphene, ensuring its status as one of the most transformative materials in contemporary science and technology.

Section 1.2 Hexagonal Boron Nitride

Boron nitride (BN) is a compound composed of an equal number of boron and nitrogen atoms, thus isoelectronic to similarly structured carbon lattices.[75] This balanced stoichiometry is reflected in its electron count and contributes to its wide array of physical and chemical properties.[76] Boron nitride exists in several crystalline forms, including the hexagonal (*h*-BN),[77] cubic (*c*-BN),[78] wurtzite (*w*-BN),[79] and amorphous (*a*-BN)[80] phases, among which *h*-BN has gathered the greatest scientific interest, mainly owing to its distinctive layered structure.[81] In *h*-BN, atoms of boron and nitrogen are covalently bonded within each plane, while neighboring sheets are held together by relatively weak van der Waals forces, as in other layered crystals, such as graphite.[76] This arrangement confers to *h*-BN a remarkable combination of thermal,[82–84] mechanical,[77] and chemical[83] characteristics that collectively make it a highly promising material in various research and industrial applications.[85,86]

The crystal structure of *h*-BN follows a AAA stacking pattern, wherein the nitrogen atoms in each layer are situated directly above the boron atoms in the layer beneath.[81], in contrast with what is found in graphite, which shows a ABA Bernal stacking configuration.[75] Within an *h*-BN layer, the bonding is predominantly covalent, though a degree of ionic character emerges due to the electronegativity disparity between boron (χ=2.04) and nitrogen (χ=3.04).[87] This partial ionicity not only increases the overall stability of the lattice, but also creates a large band gap, which gives rise to its insulating behavior and differentiates it from graphite, a material with semi-metallic properties.[88] The crystalline structure of *h*-BN is described by a lattice constant of a=0.25 nm and an interlayer distance of c=0.33 nm,[89] similar to those of graphite and underscoring its strong in-plane bonding and exceptional mechanical, thermal, and barrier properties.[89] A sketch of the crystallographic parameters and habit of *h*-BN is shown in Figure 1.3.

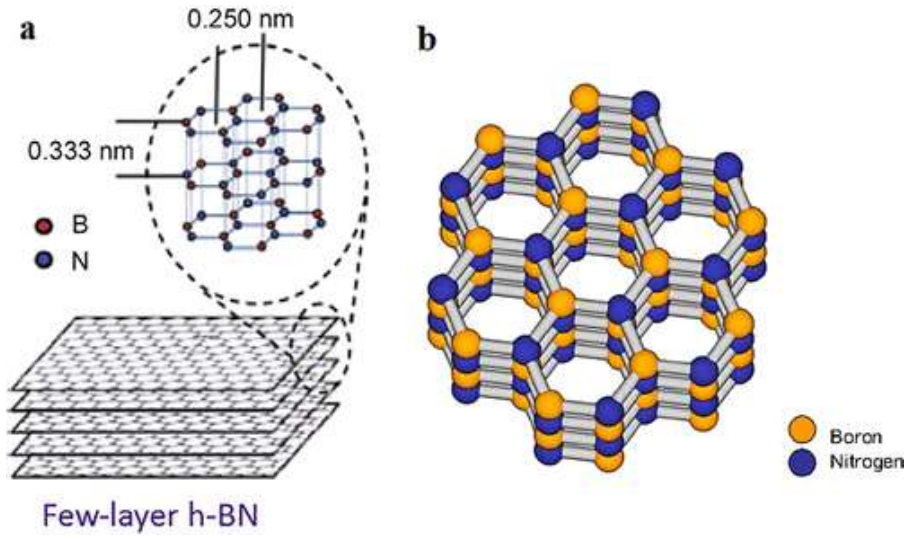

Figure 1.3 (a) The structure of h-*BN nanosheets.*[90] *(b) The lattice of* h-*BN with an AAA stacking in which the boron and nitrogen atoms are stacked on each other alternately.*[89]

One of the most notable attributes of *h*-BN is its outstanding thermal conductivity, which derives from the efficient propagation of phonons in the 2D plane.[91] Theoretical calculations suggest that monolayer *h*-BN can achieve thermal conductivity values exceeding 600 $W\,m^{-1}\,K^{-1}$ at ambient temperature – higher than its bulk counterpart, which has an in-plane thermal conductivity of roughly 400 $W\,m^{-1}\,K^{-1}$.[91,92] This enhanced thermal performance in monolayer *h*-BN is due to a diminished phonon-phonon scattering and more effective phonon transport pathways as the thickness is reduced, owing to symmetry-based selection rules arising in 2D lattices.[48,91,93,94] However, similarly to graphene, when multiple layers of *h*-BN are stacked, out-of-plane lattice vibrations and interlayer coupling become more significant, consequently lowering the overall thermal conductivity compared to the monolayer.[76,91,92] Experimental investigations of freestanding CVD-grown *h*-BN films indicate that they typically exhibit thermal conductivity values around $100\pm10\,W\,m^{-1}\,K^{-1}$,[95] which are substantially lower than those of exfoliated *h*-BN, in which values can reach up to 360 $W\,m^{-1}\,K^{-1}$.[84] These discrepancies are usually linked to microstructural flaws such as grain boundaries, wrinkles, or impurities introduced by the synthesis process. In contrast, *h*-BN films fabricated via dry-transfer methods, without using polymer-based contaminants, have revealed thermal conductivities as high as 484 $W\,m^{-1}\,K^{-1}$.[96] These findings underscore the critical importance of preserving intrinsic material quality through the exfoliation process to harness the full thermal capabilities of *h*-BN.[84,95,96]

Beyond its thermal properties, *h*-BN shows impressive mechanical strength, thanks to its strongly covalent in-plane bonds, achieving a Young's modulus that approaches 1000 GPa, with elastic constants in the range of 220 to 510 $N\,m^{-1}$.[97,98] The bending modulus of *h*-BN nanosheets has been shown to rise as the layer thickness decreases, approaching near-theoretical maxima for ultra-thin

films (below 50 nm).[99] This outstanding rigidity, coupled with notable flexibility at the nanoscale, makes *h*-BN a prime candidate for applications that demand consistent mechanical performance in challenging environments.[99–101]

Owing to its atomically smooth surfaces, chemical inertness, and impermeable lattice, *h*-BN acts as a great barrier and serves as an excellent protective coating against oxidation,[102,103] chemical etching,[104] and other forms of corrosion.[105–107] Monolayer *h*-BN exhibits oxidation resistance up to approximately 850 °C,[108] while few-layer *h*-BN can endure temperatures up to around 1100 °C in oxygen-rich atmospheres.[109] This enhanced oxidation resistance with respect to other 2D materials such as graphene is attributed to the high activation energy (around 15 eV) required to simultaneously remove boron and nitrogen atoms. These characteristics make *h*-BN a highly promising material for applications that require a robust barrier showing chemical and thermal stability over a wide range of operating conditions.[108–110] The barrier properties of 2D *h*-BN will be further discussed in Section 1.5.

Regarding the electronic and optical properties of *h*-BN, it functions as an electrical insulator because of its wide band gap, which has been measured and calculated to be around 6 eV and to show a direct nature for monolayer *h*-BN.[111–114] Similarly to 2D transition metal dichalcogenides,[115] the material transitions to an indirect band gap (similar value of around 6 eV)[116,117] passing from monolayer to bilayer[113] and maintains this characteristic up to bulk thicknesses.[111] This band structure imparts the material a high electrical resistivity and a significant dielectric breakdown strength of about 0.7 V nm^{-1},[118] and results in ultraviolet (UV) photoluminescence, rendering *h*-BN transparent to visible wavelengths[119,120] while exhibiting strong emissions in the deep ultraviolet (DUV) regime.[116,121,122] The properties of h-BN can be thus exploited in a variety of optoelectronic and photonic applications, where its electrical insulation capabilities, UV transparency, and robust mechanical attributes can be leveraged for diverse devices and systems.[116,117,123]

Section 1.3 Synthesis methods

The integration of 2D materials into nanotechnology and other industrial sectors is inextricably linked to their production methodologies. In fact, the synthesis technique used can lead to significant variations in terms of product quality (*i.e.*, morphological and chemical properties), production rate (*i.e.*, the amount of material produced within a specific period of time), and overall yield (*i.e.*, the percentage of good-quality material produced with respect to all the processed material). Over the years, an array of methods has been devised to produce 2D materials, and these can generally be classified into two main categories: bottom-up and top-down approaches.[23] This classification

highlights the different starting points of the synthesis process, which significantly influences the material properties and achievable output.

Bottom-up methods take advantage of physical and chemical mechanisms to assemble complex nanostructures from fundamental atomic or molecular constituents.[124] By precisely controlling reaction conditions such as temperature, pressure, and precursor concentration, it becomes possible to promote the formation of nanosheets that exhibit high crystallinity (*i.e.*, crystal size larger than 1 cm)[125,126] and low defect density (*i.e.*, no cracks, wrinkles, vacancies, substitutions or contaminations). Two of the most widely adopted techniques in this category are CVD and molecular beam epitaxy (MBE) (Figure 1.4a,b).

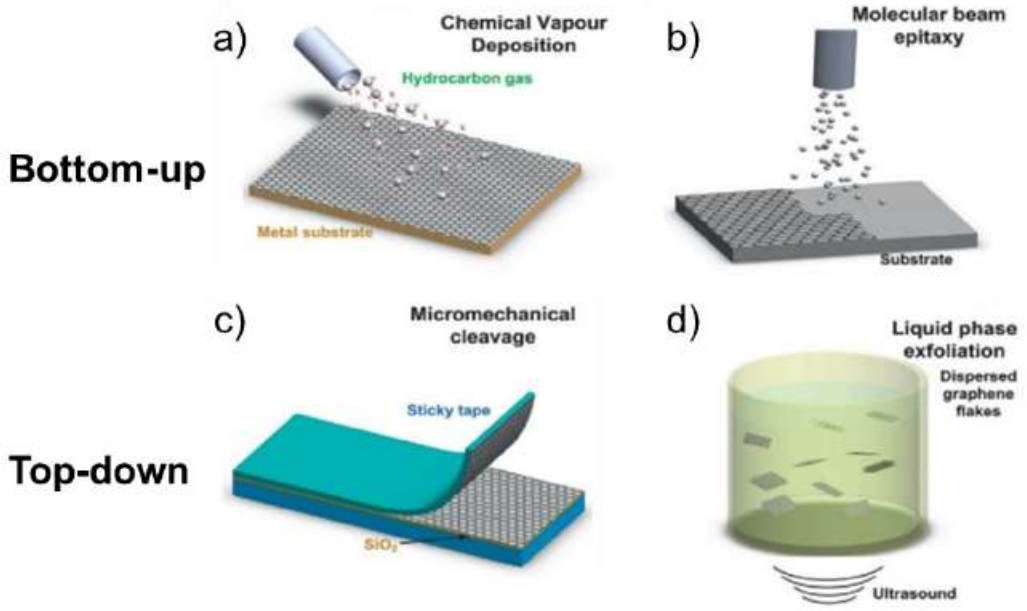

Figure 1.4 Schematic sketches of 2D materials production methods. Bottom-up approaches: (a) CVD; (b) MBE. Top-down exfoliation approaches: (c) MC; (d) LPE.[23]

Differently, top-down strategies revolve around the size reduction or exfoliation of bulk layered materials into thinner forms.[127] A defining principle here is the overcoming of van der Waals forces that keep the layers stacked, allowing single- or few-layer nanosheets to be separated from their bulk crystals.[127] One of the most recognizable techniques within this realm is micromechanical cleavage (MC) (Figure 1.4c).[23,124] In MC, adhesive tapes or related methods are used to peel off successively thinner layers from the bulk sample until only a few monolayers remain. Although MC can yield high-quality 2D sheets, it is usually limited in scalability, making it best suited for laboratory-scale investigations.

By contrast, other top-down techniques – such as various chemical, electrochemical or shear-based exfoliation methods – can process larger amounts of bulk precursor material, but often introduce more

defects or impurities, thereby influencing the final material performance. Nevertheless, these approaches offer a higher production rate compared to MC, thereby facilitating more extensive studies that require larger sample volumes.

Within the family of exfoliation methods, LPE stands out as a particularly promising strategy for achieving industrial-scale production of 2D crystals (Figure 1.4d).[23,25]

Section 1.3.1 Chemical vapor deposition

Chemical vapor deposition is a bottom-up strategy extensively used for the synthesis of high-quality 2D materials, owing to its ability to produce films with excellent structural integrity, controlled thickness, and minimal defect density.[24,128] In this process, the precursor materials – whether solid, liquid, or gaseous – are delivered into a specially designed deposition chamber (tested system range from furnaces,[24] to cold-wall single-wafer reactors,[129,130] and plasma reactors[131]), where they subsequently undergo chemical reactions or decomposition at temperatures as high as 1000 °C, ultimately giving rise to the desired 2D layers.[23] The initial precursors are generally vaporized or sublimated, then transported via inert carrier gases (*e.g.*, argon, nitrogen) into the heated reactor zone, ensuring a steady supply of reactive species.[30]

Once inside the deposition chamber, a substrate (which can be metallic, such as Ni,[132] Co,[133] Cu,[134] Ir,[135] Ru,[136] or an insulator, such as Si_3N_4,[137] ZrO_2,[138] MgO,[139] or SiC[140]) is maintained at high temperature, typically in the 600–1000 °C range, under low-pressure conditions (on the order of 10^{-7} mPa).[23] This high-temperature, low-pressure environment ensures that the precursors efficiently decompose or react on the substrate surface, which usually acts also as catalyst, leading to the formation of atomically thin layers. More specifically, the decomposition products coming from the precursors are usually dissolved into the substrate thanks to the high temperature. When the reaction chamber is cooled down, the solubility of these species is reduced, leading to the precipitation of the desired compound on the surface of the substrate. In this process, the crystal structure of the substrate and its binding energy with the species involved are crucial for the success of the synthesis.

A prototypical application of CVD is the production of single-layer graphene using Cu (111) as a substrate.[24] Common carbon sources (*i.e.*, precursors) include gaseous hydrocarbons (*e.g.*, methane, ethylene, acetylene), liquid organic compounds (*e.g.*, benzene, methanol, ethanol), or even solid polymeric materials (*e.g.*, polyethylene- or polystyrene-based).[30] The introduction of these carbon precursors into the heated chamber initiates a sequence of chemical reactions, often assisted by the catalytic effect of the substrate. This facilitates the breakdown of carbon-containing molecules into smaller species – atoms or simple molecules – which are dissolved at high temperature inside the Cu

crystal. As the temperature is gradually lowered, the solubility of C atoms decreases, they migrate towards the surface and, thanks to the crystal plain exposed on the surface of Cu, precipitate in the form of graphene.[23,124] The low solubility of C in Cu accounts for the self-limiting character of this process, which enables the synthesis of single-layer graphene.[24] Changing parameters such as the substrate, its crystal structure, its cleaning procedure, the temperatures involved in the process and the cooling rate, or adding preliminary steps, such as intentional seeding, can drastically change the outcome of the synthesis in terms of layer thickness, homogeneity, grain size and purity. [124]

Remarkably, CVD methods are not limited to graphene. By appropriately choosing the precursors and tuning process parameters (such as pressure, temperature profiles, and reaction time), researchers can synthesize a broad spectrum of 2D materials, including transition metal dichalcogenides (TMDs),[141–143] *h*-BN,[144–146] and other layered compounds.[147,148] As in all growth processes, the temperature of the substrate, the heating ramp rate, and the total growth duration are key considerations for achieving high-quality 2D crystals.[149] Also in this cases, subtle variations in these parameters can result in differences in grain size, layer thickness, and overall crystallinity, enabling fine control over the properties of the final product.

Despite its undeniable advantages – namely, the ability to produce ultra-pure, low-defect 2D films – CVD does face certain limitations.[23] One of the most significant challenges lies in the considerable cost of the equipment and the high energy demands for maintaining the precise temperature and pressure conditions necessary for the growth process.[150] This cost factor poses hurdles for large-scale commercialization and mass production of 2D materials, as the economics of operating such systems may prove prohibitive for industrial-scale outputs, when high amounts of material are required. Another issue arises from the post-growth procedures: the removal of the substrate and the transfer of the fragile 2D film onto a target substrate can introduce defects or contamination,[151] further complicating the production flow.[152,153] These extra steps may limit the applicability of CVD in certain sectors in which rapid and inexpensive processing is essential.

Nonetheless, CVD continues to be a premier technique for obtaining 2D materials with exceptional quality and well-defined properties. Ongoing research seeks to address cost and transfer challenges – such as developing reusable substrates or refining transfer-free growth setups – in order to broaden CVD utility in advanced electronic,[154–156] photonic,[157–159] and energy-storage applications.[160–162] Through continued innovation, CVD holds promise as a cornerstone method for the scalable large-area production of the next generation of 2D materials.

Section 1.3.2 Molecular beam epitaxy

Among the various bottom-up techniques proposed for the fabrication of graphene and other 2D materials, MBE distinguishes itself as a particularly robust thin-film deposition method. Historically, MBE has played a major role in the production of epitaxial structures of exceptional quality, especially within the realm of III–V and II–VI semiconductor systems.[163] By carefully controlling the deposition conditions, MBE enables researchers to tailor structural and electronic properties with remarkable precision – a key consideration in cutting-edge electronics and optoelectronics.

Similarly to CVD, MBE fundamentally revolves around the physical evaporation of material precursors. However, while CVD typically uses gaseous chemical reactions (*e.g.*, decomposition of hydrocarbons at elevated temperatures), MBE for graphene production draws on the sublimation of solid carbon sources. An electron beam evaporator is commonly used to heat and vaporize a carbon precursor,[35] allowing the condensation of carbon atoms onto a heated substrate.[164] Under these conditions, high-quality single-layer graphene could theoretically form. However, it is often accompanied by other carbon-based materials, depending on the precise growth parameters and substrate characteristics.[165]

Despite these similarities, significant distinctions set MBE apart from CVD. In MBE, the generation of atomic beams involves directing the constituent elements – in this case, carbon for graphene – toward the substrate under ultra-high-vacuum (UHV) or near-UHV conditions.[23] This focused stream of atoms can lead to uneven coverage, given that deposition might continue over already-formed graphene regions. Therefore, since MBE is a thermal process, a substantial fraction of incoming carbon species can form amorphous or nanocrystalline carbon phases on the substrate, rather than contributing to the growth of a uniform, crystalline graphene layer.[23] Over time, few-layer graphene (FLG) or related layered materials synthesized using MBE may exhibit a notable diversity in domain sizes and a relatively large density of defects. Such imperfections stem from the challenge of maintaining precise control over nucleation dynamics and the subsequent crystal growth processes.[166]

Ensuring that graphene or other 2D materials produced via MBE possess the desired uniformity, minimal defect density, and consistent interface quality remains a non-trivial task.[167] In fact, while the concept of evaporating a carbon source under vacuum and directing it onto a substrate appears straightforward, the technical reality is considerably more complex. Growth protocols must be optimized in terms of substrate temperature, beam flux, evaporation rates, and background pressure. Moreover, similarly to CVD, impurities within the source materials or slight fluctuations in vacuum level can severely affect the structural and electronic properties of the as synthesized film.[167]

Interestingly, MBE exhibits excellent compatibility with in-situ diagnostic techniques.[124,167] Instruments such as X-ray photoelectron spectroscopy (XPS) or scanning tunnelling microscopy (STM) can be integrated directly into the MBE chamber. This seamless coupling allows scientists to monitor the growth process in real time, investigating surface chemistry, morphology, and electronic properties as layers form atom-by-atom. Insights gained from these real-time measurements can drive immediate adjustments to growth parameters (*e.g.*, substrate temperature or beam flux), thus refining the deposition process and more accurately steering material characteristics.

Section 1.3.3 Micromechanical cleavage

Micromechanical cleavage, often referred to as mechanical exfoliation, describes a process in which layers of 2D materials of differing thicknesses are physically peeled from their original bulk crystals. Although this practice was already in use among crystallographers and crystal growers as early as the 1960s,[168] it became particularly significant in 2004 when A. Geim and K.S. Novoselov – later awarded the Nobel Prize for their work – successfully isolated FLG from graphite through this very method.[2] Crucially, they utilized Scotch tape as the cleavage agent,[127] applying it to a piece of highly oriented pyrolytic graphite and exerting sufficient normal force to detach a few-atom-thick layer of graphene, eventually succeeding in obtaining single-layer crystals.[9] This deceptively simple innovation came to be widely known as the "Scotch tape method" and served as a foundational step in the burgeoning field of graphene research.

Figure 1.5 Photographs of illustrative procedure of mechanical exfoliation.[127]

As illustrated in Figure 1.5, the general MC procedure for obtaining single-layer nanoflakes involves repeatedly placing adhesive tape onto a bulk crystal and peeling it away, thereby overcoming the relatively weak van der Waals bonds between individual layers. With each successive peel-off operation, flakes of varying thicknesses may be produced due to the progressive delamination of the crystal.[127] In practice, this approach can be applied to a wide array of layered materials – beyond just graphite – to obtain small-scale samples suitable for fundamental investigations.[9] Because the process is physically driven and imposes minimal chemical or thermal stress on the sample, the resulting sheets exhibit very few defects and closely preserve their intrinsic material properties.

However, while MC yields high-quality 2D crystals ideally suited for research probing electronic, optical, and mechanical characteristics, the method suffers from a low production rate, making it unfeasible for large-volume or commercial-scale applications.[167] The small flake size, together with the lack of automated control, limits its capacity to generate uniform, large-area films in a reliable manner. Consequently, despite being invaluable for proof-of-concept demonstrations and pioneering studies, micromechanical cleavage remains impractical for mass manufacturing of 2D materials. Nevertheless, MC continues to hold an important place in the broader 2D-materials toolbox, particularly when researchers seek pristine, defect-free nanosheets for fundamental experiments or prototype device fabrication.

Section 1.3.4 Liquid-phase exfoliation

Among the top-down strategies devised for producing graphene and other 2D materials in liquid environments, LPE remains one of the most accessible and versatile methods for generating stable colloidal dispersions of exfoliated flakes.[18] By applying LPE, researchers can transform bulk crystals dispersions into inks loaded with 2D materials that lend themselves to various industrially relevant processes, making this approach particularly appealing for large-scale or high-throughput applications. In general, LPE comprises three sequential steps: the dispersion of the bulk crystal in a suitable solvent or solution, the application of mechanical energy (via sonication or shear) to drive exfoliation, and a final purification stage to isolate the exfoliated material from unexfoliated fragments (Figure 1.6).[25,169,170] One fundamental aspect that needs to be addressed both for the dispersion of the bulk material and for the subsequent exfoliation in its 2D form is the choice of the solvent or solution. A solvent that closely matches the surface energy of the bulk crystal minimizes interfacial tension (γ) and stabilizes the resulting exfoliated flakes, thereby preventing their reaggregation into thicker structures.[25]

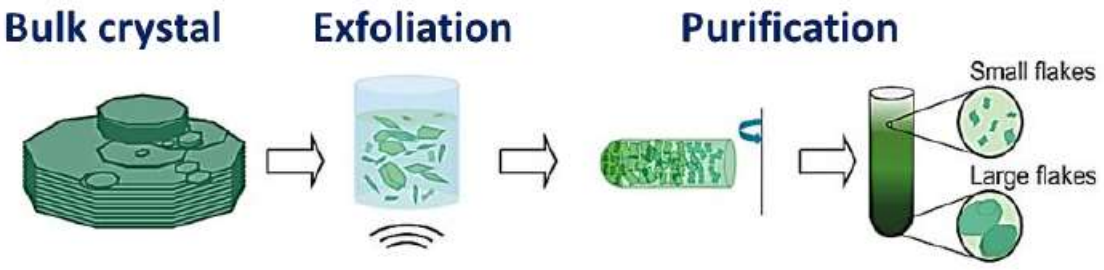

Figure 1.6 Schematic representation of the different steps involved in the LPE process.[169]

For the specific case of graphite exfoliation into graphene, solvents exhibiting surface energies in the range of ~70-80 mJ m^{-2} (equivalent to a surface tension of ~40-50 mN m^{-1}) facilitate effective

delamination.[171] In addition to surface tension considerations, solubility parameters – namely the Hildebrand and Hansen solubility parameters – play a pivotal role in solvent selection.[18] The Hildebrand parameter (δ_{Hild}) is derived from the cohesive energy density, calculated as $\delta = [(\Delta H_v - RT)/V_m]^{0.5}$, where ΔH_v is the enthalpy of vaporization, R the universal gas constant, and V_m the molar volume.[18] While δ_{Hild} is useful for gauging solvent compatibility, it does not fully capture the effects of hydrogen bonding or polar interactions, leading to the development of the Hansen model.[18] According to Hansen theory, the total solubility parameter is split into dispersion (δ_D), polar (δ_P), and hydrogen bonding (δ_H) contributions, satisfying ${\delta_{Hild}}^2 = {\delta_D}^2 + {\delta_P}^2 + {\delta_H}^2$.[18] In practice, identifying a solvent system that aligns well with given layered material parameters is essential for maximizing exfoliation yields. Notable examples include N-Methyl-2-pyrrolidone (NMP) and Dimethylformamide (DMF), both of which exhibit suitable surface tension values (40-50 mN m^{-1}) and Hansen parameters ($\delta_D \approx 18$ MPa$^{0.5}$, $\delta_P \approx 10$ MPa$^{0.5}$, $\delta_H \approx 7$ MPa$^{0.5}$) that facilitate stable graphene dispersions.[124,169] Despite their efficacy, NMP and DMF are hampered by toxicity issues and high boiling points,[172] thus driving interest in more benign solvents – such as isopropanol[18] or acetone[173] – often bolstered by stabilizing agents that help preserve the stability of dispersions.[167]

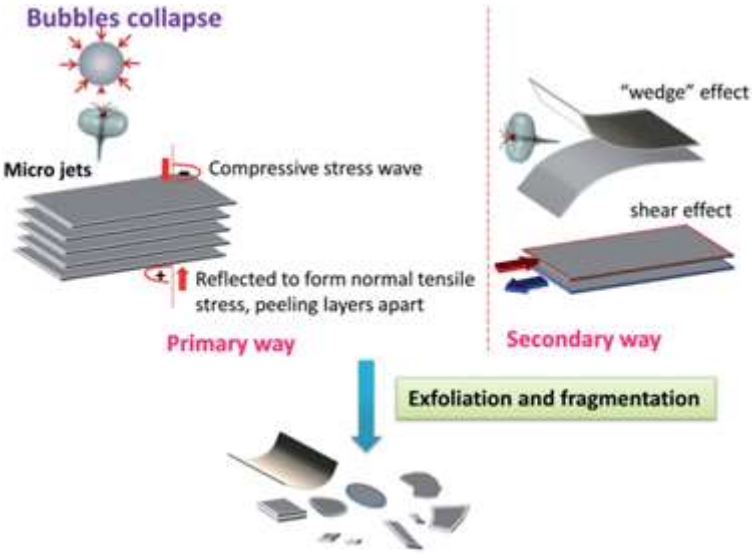

Figure 1.7 Illustration of the mechanical mechanism for exfoliation via sonication.[127]

Various techniques have been developed based on the overarching principle of LPE. One prominent example is ultrasonication-assisted exfoliation,[18] wherein bulk crystals dispersed in a solvent are subjected to ultrasonic waves delivered either through a direct tip or by immersion in a bath sonicator.[124] In tip sonication, the ultrasonic energy is transferred more directly, enabling higher throughput and relatively brief processing times (for TMDs, sonication times are longer by a factor ~20 in bath compared to tip sonication)[124] and higher reproducibility of results with respect to bath

sonication, albeit at the cost of expensive equipment maintenance, potential localized sample heating and contamination from the tip.[124] Bath sonication, conversely, imparts energy more uniformly through water-coupled ultrasound; it is more economical (from a capital – CAPEX – operational – OPEX – and maintenance point of view) and tends to produce fewer structural defects in the resulting 2D flakes.[124,174] The exfoliation arises from cavitation – the formation, expansion, and eventual collapse of microscopic bubbles – which generates localized mechanical shocks, as well as from shear forces that help detach individual layers from the parent crystal (Figure 1.7). Purification is then carried out by sedimentation-based separation (SBS), commonly involving ultracentrifugation in a density-gradient or uniform medium to remove thicker, unexfoliated particles.[175,176] During centrifugation, the Svedberg equation governs the time required for flakes to sediment:

$$s = \frac{m(1 - \vartheta'\rho)}{f} \tag{1.1}$$

where m is the flake mass, ϑ' the partial specific volume, ρ the solvent density, and f the frictional coefficient. By modulating centrifugation time or speed and repeating the process multiple times, different flake thicknesses and lateral dimensions can be selectively isolated, through a process often referred to as "liquid cascade centrifugation" (Figure 1.8). [175]

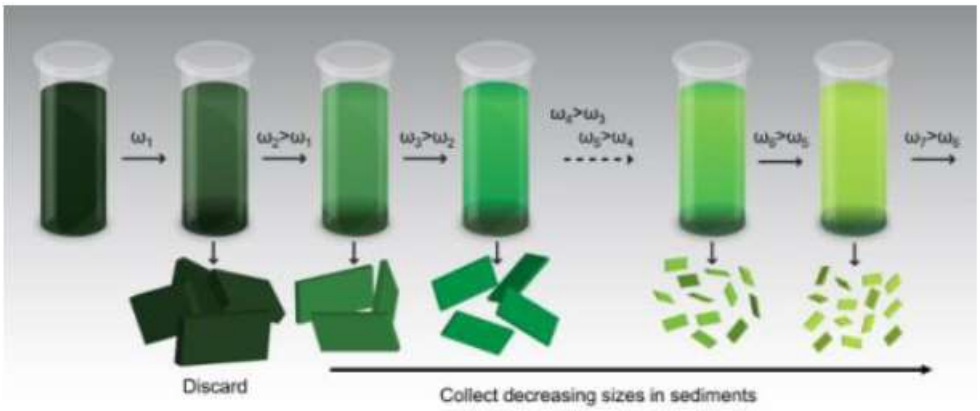

Figure 1.8 Schematic illustration of SBS together with the liquid cascade centrifugation for a size selecting of exfoliated flakes.[175]

Another LPE approach is wet-jet milling (WJM), a high-pressure technique patented for the exfoliation of 2D crystals by the Istituto Italiano di Tecnologia (WO2017/089987A1).[177] Unlike ultrasonication, which applies acoustic forces for extended durations, WJM forces the solvent-crystal mixture through constricted nozzles or channels at pressures of 180-250 MPa, provoking high shear-rate effects in very short pulses (milliseconds to microseconds).[177,178] A typical WJM apparatus is depicted in Figure 1.9. This method can achieve production rates of ~60 g min^{-1} per single apparatus with nearly 100% exfoliation yields,[177,179] culminating in dispersions with concentrations as high as

30 g L^{-1}. An additional advantage is that WJM tends to preserve the basal plane integrity, limiting the formation of defects and thus maintaining the core electrical and mechanical properties of the parent crystal – unlike chemical or thermal reduction methods that give rise to derivatives such as reduced graphene oxide.[124,177,180] WJM has also proven adaptable to other layered materials, including *h*-BN, TMDs, and metal matrix composites (MMCs).[177] Because the flake exposure to high stress is brief, stabilization can proceed in a separate step, opening the door to a broader range of solvents with varied boiling points, viscosities, and toxicity levels.

One of the chief attractions of LPE is its ability to produce single- and few-layer 2D materials in liquid dispersion, which can then be processed into functional "inks" and deposited using solution-based or printing methodologies (*e.g.*, spray coating, spin coating, inkjet printing).[181–187] Such approaches are conducive to a variety of emerging technologies, including flexible electronics,[185] energy storage and conversion devices,[181,183,188–192] and composite materials with enhanced mechanical or thermal properties.[193] While LPE offers valuable benefits – namely simplicity, relatively low overhead costs, and broad applicability – certain drawbacks limit its universal adoption. For instance, the exfoliation mechanism necessarily fractures the crystal in random ways, producing flakes with diverse thicknesses and lateral dimensions.[194,195] Longer exfoliation times can amplify such fragmentation and introduce more edge defects, ultimately degrading performance properties.[196] Therefore, refining the protocol – be it adjusting sonication power, optimizing solvent choice, or fine-tuning centrifugation parameters – remains essential for generating higher-yield, uniform, and minimally defective 2D materials.

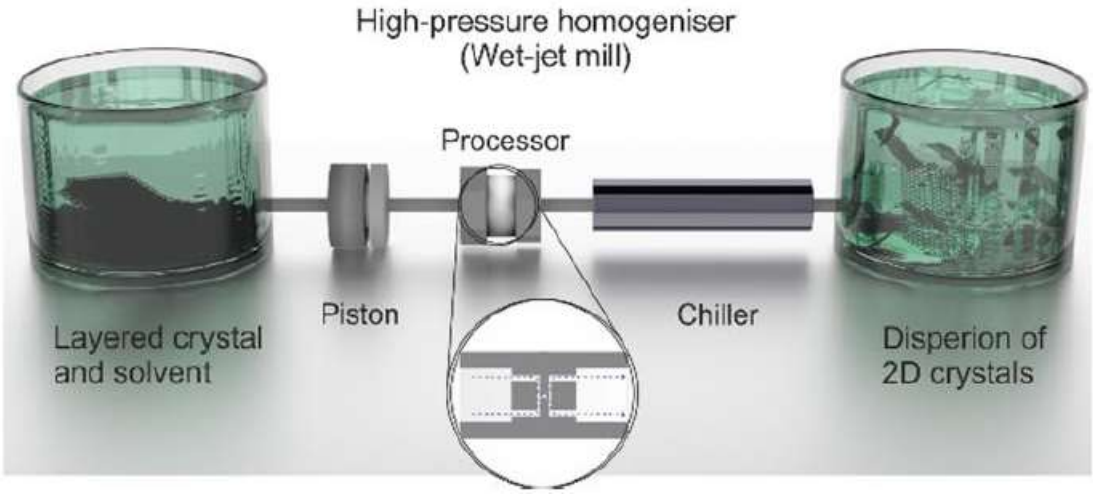

Figure 1.9 Representation of schematic setup of high–pressure homogenizers, wet-jet mill.[177]

Despite these challenges, LPE continues to stand as a cornerstone technique in the effort to scale up 2D material production to the industrial level. Its combination of relatively low cost, and adaptability

to potentially all layered crystals underscores its importance in both fundamental research and industrial processes.[124] By exploring greener solvents, more effective stabilizers, and improved exfoliation setups, researchers aim to address limitations related to flake size, thickness uniformity, and solvent toxicity, thus paving the way for large-volume manufacturing of advanced 2D-material-based devices and components.

Section 1.4 Biocompatibility and biological applications

Biocompatibility is the capacity of materials to interact with cells, tissues, or living organisms without generating a stressful response.[197] Evaluations of the biocompatibility of 2D nanomaterials through cytotoxicity assays which take into account variations in their composition, size, layer number, or degree of functionalization provide crucial insights into the mechanisms underlying potential toxic effects.

In 2013, Pinto *et al.* systematically reviewed existing literature on the biocompatibility of graphene-based materials (GBMs, *i.e.*, graphene, GO, reduced graphene oxide – RGO – and functionalized graphene),[198] noting that several studies indicated a slight to moderate decrease in bacterial and mammalian cell viability upon exposure to GBMs. However, systematic investigations about the influence of particle size on cell viability remained scarce. Furthermore, the understanding of the long-term cytotoxic effects of GBMs and their influence on cell signaling was still at an initial stage. Other studies demonstrated that pristine and functionalized graphene induced negligible hemolysis (below 0.2%) in red blood cells at concentrations up to 75 μg mL^{-1},[199] while another investigation explored CVD-synthesized graphene on copper substrates for promoting cardiomyogenic differentiation of mesenchymal stem cells, revealing no cytotoxic effects alongside an upregulation of cardiomyogenic signaling molecules.[200] Further studies have established CVD graphene[201] and GO papers[202] as suitable substrates for neuronal and mammalian cell growth without observable cytotoxicity.

Other studies analyzed the biocompatibility potential in biological applications of the different synthesis methods for GBMs, yet underscoring the necessity for further toxicity versus biocompatibility tests, particularly employing *in vivo* models.[203] In addition, a recent review conducted by Fadeel *et al*. systematically assessed GBMs biocompatibility,[204] highlighting that these materials should be distinguished based on physicochemical parameters, particularly layer number, lateral dimensions, and carbon-to-oxygen atomic ratio, factors that significantly influence their toxicity profiles, confirming previous hypotheses.[205,206]

Surface functionalization, which is often dictated and influenced by synthesis methodologies, significantly impacts the biocompatibility of nanomaterials, affecting cellular uptake and biological interactions. For example, RGO, functionalized with hydrophilic biocompatible polymers, demonstrated favorable cytocompatibility towards endothelial cells at concentrations up to 100 μg mL^{-1}.[207] Another study reported graphene nanoplatelets modified with similar polymers, such as poly(vinyl alcohol) (PVA), hydroxyethyl cellulose (HEC), and poly(ethylene glycol) (PEG), exhibited minimal hemolysis at concentrations up to 500 μg mL^{-1}, with improved biocompatibility particularly observed with PVA modification, due to reduced cellular interaction and internalisation.[208] *In vivo* studies demonstrated that PEGylation of FLG significantly mitigated histological abnormalities compared to the non-functionalized material,[209] while intravenously administered and radiolabeled thin (<2 nm) GO sheets displayed rapid urinary excretion without causing renal damage,[210] suggesting the role of sheet thickness and surface chemistry in biodistribution and pharmacokinetics.[211]

Similarly to GBMs, the atomic composition, exfoliation processes, and lateral dimensions are crucial for the biocompatibility of other 2D materials, including TMDs, *h*-BN, and black phosphorus (BP).[212–215] Studies have linked TMDs cytotoxicity with their chemical reactivity and the release of chalcogen atoms, with selenium and vanadium being notably associated with increased toxicity, and ditellurides exhibiting greater cytotoxic effects than disulfides.[212,216–218] As in the case of GBMs, the functionalization of these 2D materials with suitable functionalities, as exemplified by MoS_2 sheets modified with lipoic acid-linked PEG, can significantly enhance physiological stability and reduce cytotoxicity.[219,220]

Additionally, the concentration of nanomaterials in the culturing medium, their morphology, and the specific cell lines employed in the tests markedly influence cytotoxicity, with several reports confirming dose-dependent toxicity patterns across diverse cell types.[221] For instance, BP sheets exhibited dose-dependent cytotoxic effects in human lung carcinoma epithelial cells,[222] while BP quantum dots triggered a negligible inflammatory response.[223]

Most *in vivo* studies have focused on functionalized 2D crystals as their functional materials. For example, iron oxide-decorated and PEGylated MoS_2 nanosheets utilized for multimodal imaging-guided photothermal therapy demonstrated good biocompatibility and favorable pharmacokinetics.[224] Similarly, PEGylated BP nanosheets loaded with therapeutic agents confirmed robust pharmacokinetic profiles, significant biocompatibility, and effectiveness against cancer *in vitro* and *in vivo*.[225]

Contextually, several 2D materials have demonstrated promising results concerning biocompatibility with neurons.[226] Graphene and GBMs have been extensively studied, showing minimal inflammatory response, promoting neuronal development, and exhibiting long-term biocompatibility and seamless integration with neural tissue.[227–234] Moreover, BP has been found to degrade into biocompatible phosphates with low toxicity and to be biocompatible in *in vitro* and *in vivo* studies, including when incorporated into composite patches or nanoscaffolds.[235–239] Metal-organic frameworks (MOFs) and covalent organic frameworks (COFs) show degradability in biological environments, with COFs generally displaying lower toxicity compared to MOFs.[226] Studies involving nickel- 2,3,6,7,10,11-hexahydroxytriphenylene ($Ni_3(HHTP)_2$)-based materials[240] and COFs based on 2,4,6-trihydroxybenzene-1,3,5-tricarbaldehyde and p-phenylenediamine[241] reported excellent biocompatibility with negligible inflammation and no tissue damage.[242,243] MXenes are recognized for their exceptional biocompatibility and functionality,[244] validated through neural recordings *in vivo*,[245,246] along with the capability to modulate immune activity and promote nerve recovery.[247] Finally, TMDs have been shown to enhance their biological properties via surface functionalization[248] and have exhibited good biocompatibility in cellular and histological experiments, along with notable tissue integration through van der Waals interactions.[249–251]

In summary, many research efforts have been made to comprehend the mechanisms and material parameters responsible for tissue damage induced by 2D materials, but a full systematic characterization still needs to be assessed. In particular, a complete understanding of the potential health risks associated with these materials and their composite or hybrid forms is essential, particularly in relation with the specific production process used.[252–254]

The most promising biological applications for 2D materials include biosensing for highly sensitive and selective biomarker detection,[255] biomedical imaging for early diagnosis – including fluorescence imaging,[256–259] computed tomography (CT),[260–263] photoacoustic (PA),[263–265] magnetic resonance (MR)[266–268] and positron-emission tomography (PET)[224,269,270] – and a broad variety of therapeutic interventions.[271] In therapy, 2D materials function as drug- and therapeutic-agent delivery platforms owing to their high cargo capacity and controlled-release profiles,[268,272,273] as photothermal (PTT)[274–276] or photodynamic (PDT)[277,278] transducers able to convert near-infrared (NIR) light into heat[279,280] or generate reactive oxygen species (ROS),[281–283] and as components of other modalities such as sonodynamic therapy (SDT),[284,285] chemodynamic therapy (CDT),[286,287] radiotherapy (RT)[288–290] and immunotherapy,[291–293] often used synergistically to enhance efficacy.[271] Another key area is tissue engineering and regenerative medicine,[294] where 2D materials provide a high surface area for cellular attachment, proliferation and tissue repair – supporting bone regeneration,[295] wound healing,[296,297]

and neural repair,[245,298] and even facilitating drug passage across the blood-brain barrier (BBB).[299] These technologies based on 2D materials are being explored for the treatment of diverse pathological conditions, including neurological disorders (epilepsy, depression, Alzheimer's and Parkinson's diseases),[226] as well as cardiovascular,[300,301] orthopaedic,[294,302,303] and inflammatory diseases.[304] Specific materials, such as GBMs, MXenes, TMDs, MOFs, COFs, BP and others, exhibit outstanding performance across these applications.[226,271,305,306]

Section 1.4.1 Biocompatibility of *h*-BN

For the scope of this work, a brief insight into the properties and applications of *h*-BN nanosheets (*h*-BNNSs) in the biological and biomedical field is here presented.

As for other 2D materials, several studies indicate that variables such as cell type or concentration, aspect ratio, and crystallinity influence the toxicity profiles of *h*-BNNSs. For example, Lu *et al.*[307] examined *h*-BNNs of 30-60 nm lateral dimensions and observed that concentrations up to 100 μg mL^{-1} did not significantly affect the viability of HEK-293T or Chinese hamster ovary (CHO) cells, as confirmed by MTT assays over 48 h. Similarly, Kivanç *et al.*[308] used MTT, sulforhodamine B (SRB), and PicoGreen assays to demonstrate that *h*-BNNs averaging a lateral size of 121 nm could be used at concentrations up to 100 μg mL^{-1} with Madin-Darby Canine Kidney (MDCK) and human normal skin fibroblast (CRL 2120) cells without causing cytotoxicity, suggesting potential suitability for oral care products. Li *et al.*,[309] however, studied *h*-BNNs with a 50-60 nm lateral size with LNCaP and DU145 prostate cancer cells using WST-8, annexin V-FITC/PI, and LDH assays over 3 and 6 days, revealing that higher concentrations and extended incubation times decreased viability and induced apoptosis, potentially due to an increased boron release from more crystalline *h*-BNNs, and suggesting a possible therapeutic role in prostate cancer. Mateti *et al.*[214] further employed MTS and 2,2-diphenyl-1-picrylhydrazyl (DPPH) assays to examine the toxicity of *h*-BNNs of varying sizes on the Saos-2 osteosarcoma cell line, revealing that micrometer-scale nanosheets at 1 mg mL^{-1} showed good biocompatibility, whereas sub-micrometer flakes generated reactive oxygen species and reduced viability. These results were supported by bright-field microscopy images, where larger *h*-BNNs (~1 μm diameter, ~100 nm thickness) proved to be more compatible than smaller nanosheets (~100 nm diameter, ~3 nm thickness). Similar observations were made for nanoparticle-sized *h*-BNNs in the range of 10-40 nm, suggesting that shape and surface characteristics play a critical role. Nurunnabi *et al.*[310] tested hydroxyl-functionalized *h*-BNNs (*h*-BN-OH) with lateral sizes of 50-100 nm on KB (human cervix carcinoma) cells at concentrations up to 500 μg mL^{-1} and observed no toxicity after 24 h, supporting their application in imaging and detection. Despite these encouraging results, all existing studies are *in vitro* and collectively indicate that *h*-BNNs are generally non-toxic under

specific conditions, but that their safety depends on factors such as their lateral size and crystallinity, the presence of surfactants, their concentration, and the cell type. While no substantial adverse effects on proliferation, metabolism, or viability have been documented, a comprehensive study including other cell types (such as neurons) and *in vivo* assessments remain paramount for establishing definitive biocompatibility profiles and guiding the use of *h*-BNNSs in clinical and therapeutical applications.

Section 1.5 Barrier and protective properties of *h*-BN

Hexagonal boron nitride has emerged as a key 2D material for various applications due to its exceptional barrier properties.[311,312] Its crystalline structure and high chemical stability make it particularly effective in protecting materials from corrosion and oxidation.[311]

Hexagonal boron nitride is inherently impermeable to many gases and liquids, making it ideal for applications where preventing the diffusion of corrosive substances is essential. Its chemical and thermal stability allows it to maintain its protective properties even in aggressive environments and at high temperatures.[313] Due to its 2D nature, *h*-BN shows a high surface area, enabling even small amounts of the material to provide significant protection in composite coatings.[314] Furthermore, its flexibility and mechanical strength allow for a seamless integration into various polymeric matrices without compromising or even improving the mechanical properties of the composite material.[312]

Many studies present the performance of *h*-BN as protective coating to prevent metal corrosion. For instance, a single layer of *h*-BN (SL-*h*-BN) can protect copper (Cu) from oxidation in oxidative environments up to 200°C.[104,105] In this regard, the fraction of Cu surface subjected to corrosion is much lower when a h-BN coating is applied with respect to when bare Cu is exposed to the same environment. Additionally, monolayer *h*-BN has proven effective in inhibiting microorganism-induced corrosion.[104] Electrochemical tests show that the polarization resistance (R_p) in an SL-*h*-BN-Cu cell is three times higher than that of a bare Cu cell, indicating greater corrosion resistance. Furthermore, impedance analyses confirm that the overall corrosion resistance in the SL-*h*-BN-Cu cell is approximately 49% higher than in the bare Cu cell.

Moving to composite systems, the incorporation of *h*-BN into polymeric matrices, has been widely demonstrated to improve the barrier properties of the coatings.[315] The dispersion of *h*-BN nanosheets in a commonly used matrix, such as an epoxy, can significantly enhance the corrosion resistance of the underlying metal substrate.[316] Another example shows that the addition of *h*-BN nanosheets functionalized with poly(ethyleneimine) (PEI-*h*-BNNSs) to a waterborne epoxy (WEP) coating

increased the impedance by four orders of magnitude compared to the pure WEP coating, demonstrating exceptional long-term corrosion resistance.[317] The properties of *h*-BN in anticorrosive coatings will be further investigated and studied in Chapter 3.

Hexagonal boron nitride can also be utilized in the fabrication of nanometer-thick atomic-level membranes (NATM) for gas and liquid separation, offering great potential for reducing the energy intensity and costs of separation processes.[312] The mass transport resistance through a membrane was found to be proportional to its thickness and pore tortuosity and inversely proportional to its porosity.

Thanks to its high thermal and chemical stability, *h*-BN is also well-suited for applications in oxygen-rich or atomic oxygen-containing environments, where it can protect materials from corrosion and oxidation without losing performance due to the aggressive environment.[311]

Finally, it is important to consider that the presence of defects in *h*-BN can reduce its effectiveness as a barrier, due to a lower impermeability of the crystals. However, studies have shown that atomic oxygen can repair defects, enhancing its ability to prevent corrosion in time.[311] Furthermore, it is crucial to achieve a uniform dispersion of *h*-BN in the matrix, in order to maximize its barrier properties and avoid the formation of defects in the continuity of the matrix, as nanoparticle agglomeration can compromise performance.[317–319] Additionally, the functionalization of *h*-BN with other materials or chemical moieties, such as GO or poly(ethyleneimine) (PEI), has been shown to be an effective way to improve its dispersion and adhesion within the matrix, further enhancing its barrier properties.[316–318]

Chapter 2 Production and characterization of 2D *h*-BN

Section 2.1 Production of 2D materials by wet-jet milling

Wet-jet milling is a liquid-phase mechanical process developed as a novel method for mixing, dispersion, and filler manipulation across various fields, including chemical engineering,[320] food technology,[321] and the ceramics[322] and pharmaceutical industries.[323–327] In this process, a dispersion containing particles is pumped and made to collide under high pressure and velocity, typically within a dedicated collision unit or through perforated discs with adjustable-diameter openings known as nozzles.[322–324,328] The primary mechanism of WJM relies on the generation of high-velocity turbulent and shear flows, driven by rapid injection into the specialized channel of the equipment.[322,324,328,329] For layered materials such as *h*-BN and graphite, it has been observed that the high impact energy and shear forces mainly act along the thickness direction of the particles, achieving effective exfoliation without significantly reducing their lateral dimensions.[177,323,330] In the case of pulverizing agglomerates, such as Al_2O_3 or other ceramics, particle size reduction is primarily attributed to inter-particle collisions within high-pressure flows.[177,331]

Wet-jet milling offers several advantages over conventional grinding methods, including ball milling,[322] planetary homogenization,[323] and ultrasonication.[177] These benefits include short processing times, as WJM can pulverize raw materials down to primary particle sizes within a relatively brief period;[322,324,328] effective exfoliation of layered materials, with high yields and preserved flake quality demonstrated for *h*-BN and graphite;[177,183,323] lower contamination risks, thanks to the absence of milling media such as balls or beads;[322] preservation of initial particle surface conditions – unlike ball milling, WJM tends to maintain the original particle surfaces, leading to fewer OH groups on materials such as Al_2O_3 and thus enhancing dispersion stability;[322,324,328,332] lower and more stable viscosity, indicating better dispersion and reduced re-flocculation over time;[322,324,328,332] and scalability, since the process has been proven to give repeatable results up to the ton scale.[177,183]

The WJM process fundamentally relies on the use of high-pressure liquid flows to induce collisions among suspended particles.[177,183,323,328,329] This process generates intense shear forces and high impact energies, which lead to the disaggregation of agglomerates, the exfoliation of layered materials, or the homogeneous mixing of components.[177,183,323] A key technical aspect is the pumping and pressure system, in which a high-pressure pump is used to drive the colloidal suspension or dispersion through the apparatus.[322,323] Operational pressures can be extremely high - up to 250 MPa - and are crucial

for generating the high-velocity flows necessary to achieve the desired level of particle collision and energy transfer.[183]

The collision unit, or collision chamber, and the nozzles constitute the core of the WJM equipment. This chamber typically contains one or more narrow-diameter nozzles through which the high-pressure dispersion is forced, converting pressure into high-velocity kinetic energy.[177,183] In certain designs, opposing nozzles are arranged so that the particle-laden jets meet head-on, maximizing impact energy.[323] Other configurations involve perforated discs with calibrated holes, and the nozzle diameter can be adjusted to optimize the process for different starting materials and target outcomes.[177] For example, when exfoliating large graphite crystals (+100 mesh), operators often begin with larger nozzles (*e.g.*, 0.30 mm) to reduce clogging, then gradually switch to smaller diameters (*e.g.*, 0.15 mm or 0.10 mm) to achieve greater size reduction while minimizing the risk of clogging.[177,183]

High-velocity injection through these nozzles produces intense shear flows in the liquid.[323] For layered materials such as *h*-BN and graphite, these shear forces help partially separate the layers without significantly damaging the structure or reducing the lateral size of the flakes.[183,323] Subsequently, high-energy collisions between particles – driven by the high-pressure flows – deliver strong impacts along the thickness direction of the material, enabling effective exfoliation into thin nanosheets with a high aspect ratio, while preserving lateral dimensions.[323] In contrast, mechanical methods such as vortex fluid, planetary homogenizer, and ultrasonication can apply shear energies that overly reduce or even destroy the lateral dimensions of exfoliated particles.[323]

Several process parameters can be regulated to optimize the WJM process. For example, increasing the operating pressure generally yields more substantial impact energies and shear forces, enhancing disaggregation or exfoliation efficiency.[183,323] The number of passes through the collision unit can be increased if a higher degree of processing is required, with a greater collision frequency resulting in reduced sediment height and lower packing density.[183,323,331] Suspension concentration also affects the frequency and intensity of collisions, while the viscosity of the dispersing liquid influences flow generation and process effectiveness.[177,183,329] In some cases, dispersants can be added to improve the initial dispersion and stabilize particles after processing.[329,332] Finally, nozzle size determines flow velocity and impact energy, highlighting the importance of selecting appropriate diameters to accommodate both the starting material and the intended final product.[177,183]

Section 2.2 Theoretical model of wet-jet milling exfoliation

The following theoretical description of the exfoliation process of hexagonal boron nitride through wet-jet milling is derived from that of graphite proposed by Del Rio *et al.*[177] As stated in the paper, the approached can be extended to any layered material, thus including *h*-BN.

Among the liquid-phase methods used to exfoliate layered crystals, micro-fluidization is most comparable to WJM, as both drive the entire fluid volume through a localized region in which turbulent flow develops.[178,333,334] In micro-fluidization, this region is a microchannel, whereas in WJM it occurs at the channel junctions before and after the nozzle.[177] Within this region, the turbulence generates a large velocity gradient perpendicular to the main flow direction, leading to a high shear rate.[177]

This shear stress acting on the dispersed flakes promotes sliding of the 2D crystal planes and initiates exfoliation. For *h*-BN, shear rates exceeding 10^4 s^{-1} have been shown to be sufficient to induce exfoliation,[18,335,336] and such rates can be achieved in laminar-flow shear mixers,[335,337] but even more efficiently in the turbulent flow of micro-fluidizers[178] and WJMs.

One key difference between WJM and the other LPE methods is the significant drop in pressure that the crystallites experience over time as they travel through the nozzle. Here, the high production yield (up to 100%)[177] of WJM can be primarily ascribed to a geometry-induced enhancement of shear-driven exfoliation, ruling out the possibility that the steep pressure drop triggers an alternative mechanism. To justify this, Del Rio *et al.*[177] developed a straightforward model to estimate the pressure required to peel off a single layer from its bulk. Although these calculations focus on graphite and graphene, the approach can be extended to other layered materials, such as *h*-BN. A graphene sheet at the crystal surface experiences an attractive force from its neighboring layer, captured by the Lennard-Jones potential.[338,339]

$$U(x) = 4A\varepsilon_0\left[\left(\frac{\sigma}{x}\right)^{12} - \left(\frac{\sigma}{x}\right)^{6}\right] \tag{2.1}$$

in which A is the sheet area, x is the interlayer separation, ε_0 is the depth of the potential well and σ is the distance for which the potential is null. The equilibrium distance is $x_0 = 2^{1/6}\sigma$, while $\varepsilon_G = -U(x_0)/A$ can be defined as the energy per unit area needed for expansion,[339] ignoring any solvent contribution to the free energy. A graphene layer oscillates rigidly around x_0 with an angular frequency calculated as:

$$\Omega = \sqrt{\frac{36\varepsilon_G A_0}{m_C {x_0}^2}} \tag{2.2}$$

in which m_C is the mass of a carbon atom, and A_0 is the real-space area of a primitive cell of graphene.

To examine how the pressure drop across the nozzle affects graphite particles, the pressure *P(t)* is represented by an exponential decay:

$$P(t) = P_f + e^{-t/\tau}\left(P_i - P_f\right) \tag{2.3}$$

in which τ is the transit time related to the nozzle length L and the fluid speed v through $\tau = L/v$. P_i and P_f are the pressures before and after the nozzle, respectively. The equation of motion can then be solved for the interlayer distance x in the Lennard-Jones potential,[339] considering the force given by the pressure:[177]

$$\ddot{x}(t) = -\Omega^2[x(t) - x_0] - \frac{A_0}{2m_C} \cdot P(t) \tag{2.4}$$

In order to assure a null total force at $t = 0$, the following initial condition must be imposed:[177]

$$x_i = x_0 - \frac{A_0 P_i}{2m_C \Omega^2} \tag{2.5}$$

Because the pressure performs work on the flakes, $U(x_i)$ exceeds $U(x_0)$. As the flake progresses through the nozzle and the pressure declines, the layer relaxes toward x_0, dissipating energy into the solvent. The total dissipated work is:[177]

$$W = \int dW = \int AP\, dx = \int AP\dot{x}\, dt \tag{2.6}$$

Since the oscillation frequency is much larger than $1/\tau$, one obtains a simplified expression for the work dissipated per unit area:[177]

$$\frac{W}{A} = \frac{A_0}{4m_C} \frac{\tau^2}{1 + (\Omega\tau)^2} \tag{2.7}$$

Out-of-plane expansion ensues if the difference between the potential energy and the dissipated work exceeds the potential energy of two non-interacting layers (taken as zero), *i.e.*, if $U(x_i) - W > 0$.[177] This can be recast as a limit on the allowable rate of pressure decrease in time. Under the assumptions $P_i \gg P_f$ and $\Omega\tau \gg 1$, the limit recites as follows:[177]

$$\dot{P} \sim \frac{P_i}{\tau} > \Omega^2 \sqrt{\frac{4m_C}{A_0}} \sqrt{\varepsilon_G} \tag{2.8}$$

Using m_C = 2.04 · 10^{-26} kg, A_0 = 0.051 nm^2, ε_G = 71 mJ m^{-2}, and x_0 = 0.34 nm, one would find $\Omega/2\pi \approx 1.2\,THz$, similar to the ZO′ vibrational mode observed in FLG,[340,341] confirming the correctness of this theoretical approach.

From the nozzle diameter and dispersion flux, the flow speed is roughly 10^3 km h^{-1}.[177] With a nozzle length of L = 0.95 mm, this corresponds to $\tau \approx$ 3.4 µs, implying $P_i > 6 \cdot 10^{16}$ Pa. Such a high value indicates that out-of-plane delamination cannot be achieved under actual WJM conditions – in which the maximum pressure is on the order of 2.5 · 10^8 Pa. Consequently, these results confirm that shear forces, rather than pressure-driven expansion, govern the exfoliation process in WJM.[177]

Section 2.3 Industrial production of wet-jet milling exfoliated *h*-BN

In this work, 2D *h*-BN was industrially produced by BeDimensional S.p.A. through a patented (WO2017/089987A1)[177] WJM exfoliation process of bulk *h*-BN powder. The powder was dispersed in NMP at a concentration of 30 g L^{-1} (3 wt%) and processed through the wet-jet milling apparatus. In this phase, the dispersion is pressurized through two microfluidic channels at a pressure of 200 MPa and becomes a liquid jet stream, flowing by laminar flow (Re ~10^2).[342] The stream then goes through the interaction chamber (Figure 2.1) and collide with each other determining a turbulent flow (Re >10^4) that generates shear stresses (shear rate >10^4 s^{-1}) responsible of the exfoliation process.[177] After the exfoliation, the flow is again divided into two channels, where the linear jet streams become vortex jet streams, further increasing the exfoliation and enhancing the homogeneity of the dispersion.[343]

The dispersion then flows through a chiller to avoid excessive overheating and a possible degradation.[331,344,345] The wet-jet milling process is repeated 5 times to achieve the desired degree of exfoliation. A schematic of the entire wet-jet milling apparatus is depicted in Figure 2.2. As a consequence of the industrial scale-up of production, the actual system in use nowadays has been modified, particularly as the interaction chamber is concerned. Still, the chamber depicted in Figure 2.2b was used during the pilot tests, as described in various publications,[177,330] and gives a close idea of the real apparatus. The industrial exfoliation system is able to process for one pass around 250 L h^{-1} of dispersion, which means that – considering the number of passes and the technical time for loading and unloading the material – the total productivity of completely exfoliated material is around

40 L h^{-1} of dispersion, corresponding to 1.2 kg h^{-1} of *h*-BN. Noteworthy, this productivity is not currently achieved if the dried material is considered, due to the slower drying procedure, as described in the following paragraphs.

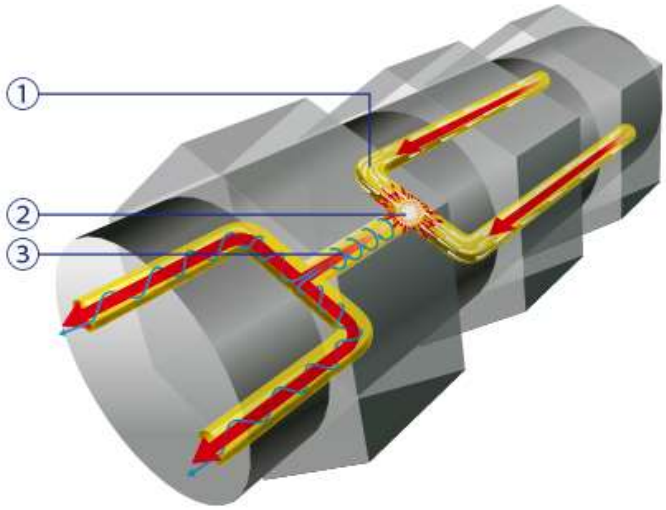

Figure 2.1 Image of an interaction chamber similar that used by BeDimensional S.p.A. in its patented wet-jet milling apparatus. (1) Generation of the parallel liquid phase jet streams. (2) Particles collision and a flow-through linear effect. (3) Vortex jet stream.[346]

The 2D *h*-BN dispersion was finally dried using a proprietary modified industrial spray drier operating under nitrogen flow. The operating parameters are proprietary of BeDimensional S.p.A.

This drying method, which replaced lyophilization with the scale-up from the laboratory scale, allows for an efficient solvent removal and prevents particle aggregation in the powder form. A schematic representation of a generic industrial spray dryer similar to that used by BeDimensional S.p.A. is depicted in Figure 2.3.

In greater detail, the exfoliated *h*-BN dispersion is injected and atomized into the drying chamber through a flow of cold nitrogen, while another inlet injects hot nitrogen, responsible for the drying process. A venting valve is present on top of the drying chamber for safety reasons. The resulting solid-gas mixture is then transported to the cyclone, in which the largest particles are collected – usually representing about 85 wt% of the total material. At this stage, the NMP remains in the vapor phase, dissolved in the nitrogen atmosphere. The remaining fine powder is conveyed to the bag filter to capture the residual solids. The NMP/N_2 vapor mixture is directed through a vent to a condenser and subsequently recycled in successive production batches. Any uncondensed NMP still dissolved in nitrogen is removed via a scrub, and the purified nitrogen is recirculated in the system. Usually, just 5% of the solvent is lost during each drying cycle and must be replenished with clean NMP.

A two-valve system is placed downstream of both the cyclone and the bag filter for collecting the dried powder. This configuration isolates the drying unit from atmospheric humidity and allows more precise control over the discharge of the powders into their final containers.

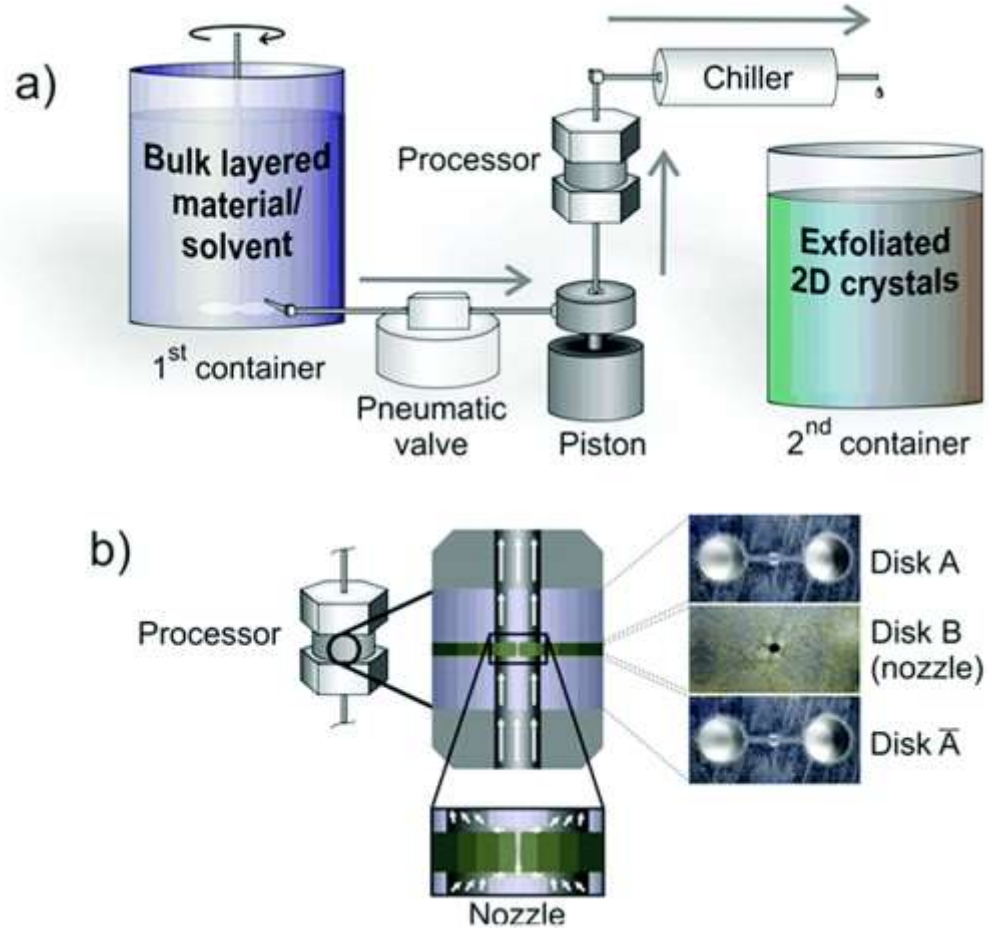

Figure 2.2 (a) Scheme of the wet-jet mill system, the arrows indicate the flow of the solvent through WJM, and (b) close-up view of the processor. The zoomed-in image in (b) shows the channel configuration and the disk arrangement. The solvent flow is indicated by the white arrows. On the right side is a top view of the holes and channels on each disk. The disks A and Ā have two holes of 1 mm in diameter, separated by a distance of 2.3 mm from center to center and joined by a half-cylinder channel of 0.3 mm in diameter. The thickness of the A and Ā disks is 4 mm. Disk B is the core of the system; it can be changed to 0.10, 0.20, and 0.30 mm nozzle diameter disks according to the size of the bulk layered crystals. The thickness of the B disk is 0.95 mm.[177]

BeDimensional S.p.A. is nowadays capable of producing up to 800 g h^{-1} or 3000 kg $year^{-1}$ of exfoliated material in powder form, being it FLG or *h*-BN.

Other specifications and parameters regarding the production of 2D materials are an industrial secret owned by BeDimensional S.p.A.

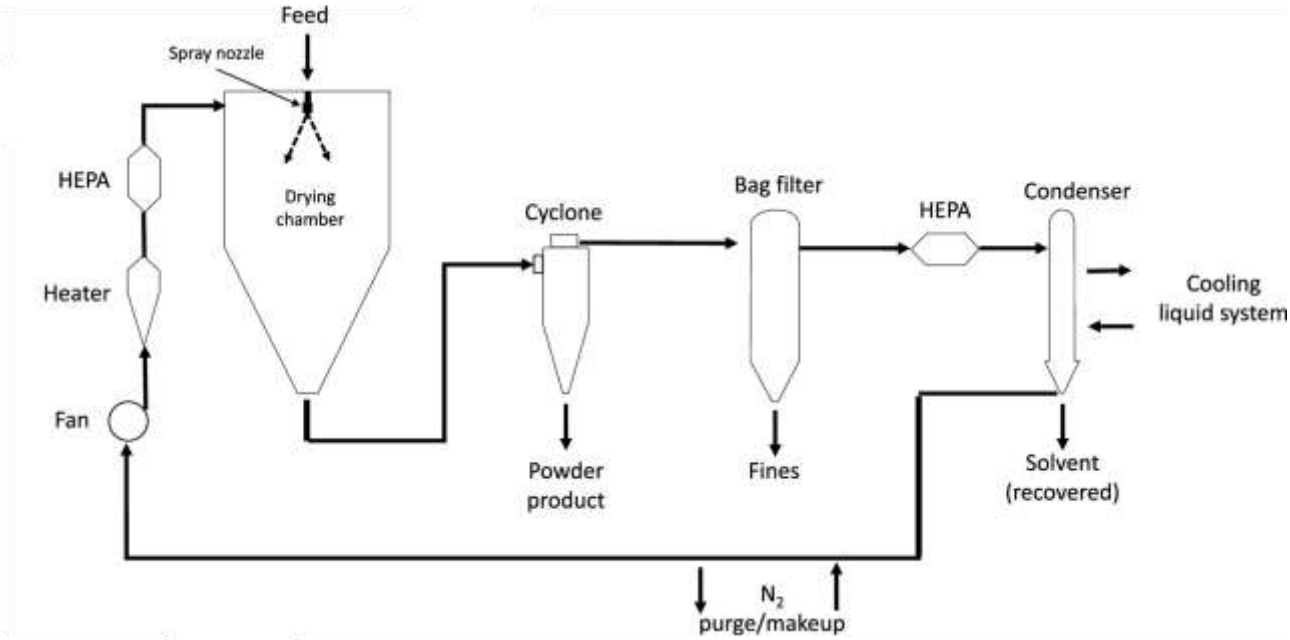

Figure 2.3 Schematic diagram of a generic industrial spray dryer. Adapted from [347].

Section 2.4 Characterization methods

The morphological characteristics of the WJM-produced *h*-BN flakes were characterized via transmission electron microscopy (TEM) using a JEOL Jem-1011 (Jeol) microscope operated at 100 kV. Samples were prepared by drop-casting *h*-BN dispersions diluted 1:50 in weight in NMP (≥ 99.0%, ACS reagent, Merck) onto ultrathin C-film on holey carbon 400 mesh Cu grids (Ted Pella Inc.) and subsequently storing them under vacuum at RT to remove residual solvent. The lateral dimensions of the *h*-BN flakes were determined from TEM images, and statistical analysis of 100 flakes was performed in OriginPro 2020 by fitting the data with a log-normal distribution.

The thickness of the *h*-BN flakes was examined by atomic force microscopy (AFM) using an NX10 AFM (Park System) in non-contact mode with a PPP-NCHR 10 M cantilever (resonance frequency ~330 kHz, force constant 42 N m^{-1}). To prepare these samples, the WJM-produced *h*-BN dispersions were diluted 1:100 in isopropyl alcohol (≥ 99.5%, ACS reagent, Merck), drop-cast onto mica sheets (Ted Pella, Inc.), and heated at 250 °C for 20 min to remove remaining solvent. Images were acquired over 35 × 35 μm^2 areas (512 × 512 data points) at a scan rate of 0.30 Hz, maintaining a working set point of ~6 nm. The images and height profiles were processed using Gwyddion (64 bit), and statistical data from 100 flakes were analyzed with OriginPro 2020.

Thermogravimetric analysis (TGA) was conducted on a TA Instruments STD650 under a nitrogen atmosphere (flow rate 100 mL min^{-1}) from 30 °C to 700 °C at a ramp of 10 °C min^{-1}.

X-ray diffraction (XRD) measurements were performed on a PANalytical Empyrean diffractometer equipped with a 1.8 kW CuKα ceramic x-ray tube and a PIXcel3D 2 × 2 area detector, operating at 45 kV and 40 mA. The patterns were recorded in air at RT using a parallel-beam geometry and symmetric reflection mode.

Section 2.5 Results

The morphological characteristics of the as-produced *h*-BN flakes were examined by TEM and AFM. The inset to Figure 2.4a presents a representative TEM image showing *h*-BN flakes with rounded edges and lateral dimensions ranging from approximately 25 to 1000 nm. Their size distribution follows a log-normal profile, with a peak at 105.2 nm (Figure 2.4a). The inset to Figure 2.4b depicts an AFM image of representative *h*-BN flakes.

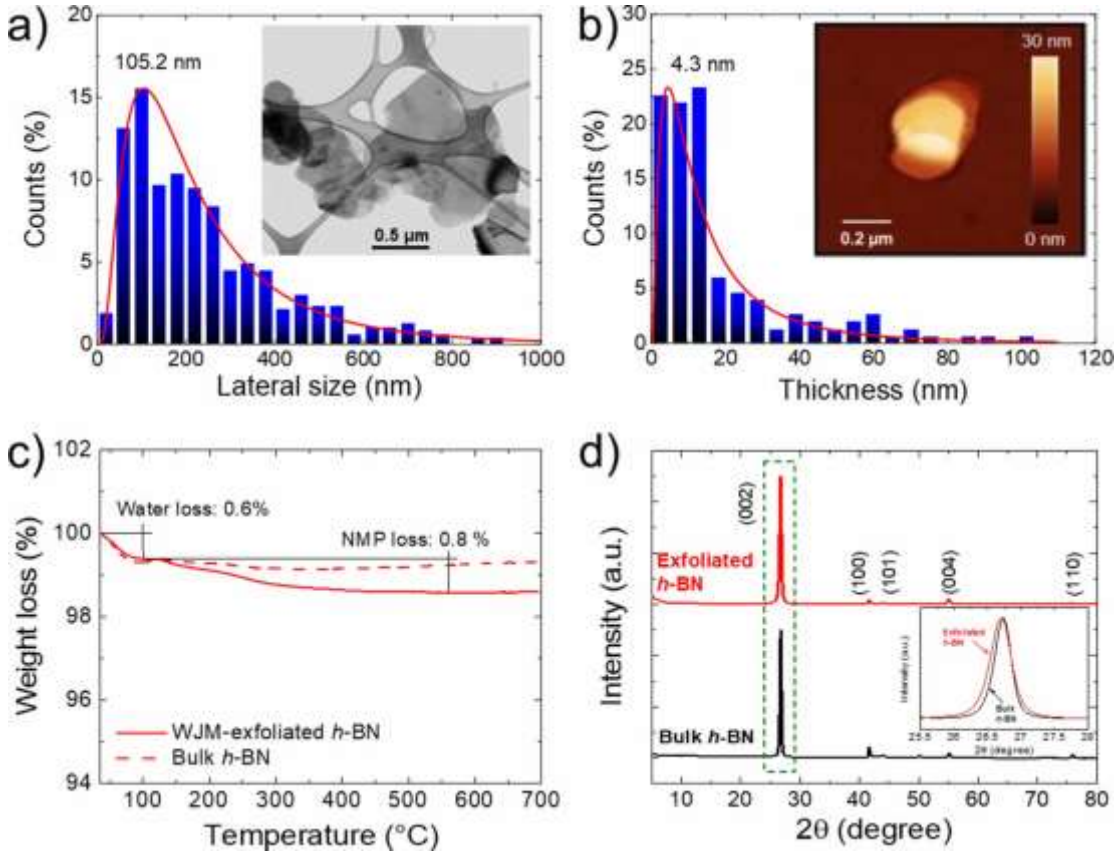

Figure 2.4 (a) Statistical analysis of the lateral size of h-*BN flakes obtained from TEM images (inset: TEM image of representative* h-*BN flakes). (b) Statistical analysis of the thickness of* h-*BN flakes obtained from AFM images (inset: AFM image of representative* h-*BN flakes). (c) TGA analysis of exfoliated* h-*BN powder (red solid line) versus bulk* h-*BN (red dashed line). (d) XRD patterns of bulk and exfoliated* h-*BN (inset: enlarged view of crystallographic (002) plane region).*[348]

Statistical analysis of the flake thickness indicates that data follow a log-normal distribution centered at 4.3 nm, with over 75% of the flakes exhibiting a thickness below 20 nm (Figure 2.4b). Given the

h-BN interlayer spacing of 0.33 nm,[75] the AFM data suggest that the exfoliated *h*-BN sample predominantly consists of few-layer (≤10) *h*-BN flakes.

The solvent residues in the as-produced *h*-BN flakes were evaluated via TGA. As shown in Figure 2.4c, minimal quantities of water (0.6 wt%) and NMP (0.8 wt%) remained in the dried exfoliated *h*-BN powder. A comparison of TGA curves between exfoliated and bulk *h*-BN confirms that the solvent employed during the WJM process is effectively removed in the exfoliated product.

The crystalline structures of both the exfoliated *h*-BN and the original bulk material were probed by XRD, with the results presented in Figure 2.4d. The XRD pattern of the exfoliated *h*-BN shows a high degree of crystallinity, highlighted by a prominent peak at 26.7° corresponding to the (002) plane of *h*-BN.[349] Alignment of this peak with that of bulk *h*-BN reveals a similar diffraction angle and shape, indicating that the exfoliation procedure does not alter the crystalline structure of the parent material. Contextually, the broadening of the peak for the exfoliated *h*-BN sample confirms the successfulness of the exfoliation process.[350,351] The weaker peaks detected in both samples at 2θ values of 41.6°, 43.9°, 55.1°, and 76.0° are attributed to the (100), (101), (004), and (110) planes, respectively.[352]

Chapter 3 Anticorrosion coatings based on *h*-BN

In this chapter, the barrier properties of industrially produced few-layer *h*-BN are examined for anticorrosion applications in marine environments. The material is incorporated into anticorrosive coatings to evaluate its efficacy in corrosion prevention, and the impact of its loading on overall performance is assessed. Although the barrier properties of *h*-BN are well established (as discussed in Section 1.5 and Section 3.1), it is crucial to investigate the behavior of this specific wet-jet milled grade, industrially produced by BeDimensional S.p.A., when used in composite coatings and encapsulants. This study serves as a fundamental preliminary investigation that underpins the practical applications presented in Chapter 4 and Chapter 5. The results shown in this chapter have been published by Molina-Garcia *et al.*[348] and the final application has been patented worldwide under the international publication number WO 2022/243949 A1.[353]

Section 3.1 *h*-BN in corrosion engineering

Corrosion of metallic parts and surfaces remains a critical issue across multiple industries – most notably in the petroleum, energy, and biomedical sectors – where metal components frequently encounter fluctuating temperatures, high humidity, and chemical pollutants.[354–356] These environmental stressors accelerate corrosion through chemical and electrochemical pathways,[355,357–359] thereby compromising structural integrity and operational safety while also imposing considerable financial burdens in terms of maintenance, repairs, and replacements. Hou et al.[354] estimate that corrosion-related losses in China alone approach USD 310 billion, whereas Koch[356] reports a global cost of approximately USD 2.5 trillion, corresponding to 3.4% of the global GDP.

Traditional organic and metallic coatings often exhibit inadequate durability under severe conditions, prompting the search for advanced protective materials. Two-dimensional materials[167] have recently garnered attention for use in anticorrosion coatings, with graphene standing out for its impressive mechanical properties and impermeability to gases and ions.[360,361] Early investigations by Chen *et al.*[362] and Prasai *et al.*[363] demonstrated that pristine graphene layers substantially reduce corrosion rates on metal surfaces. However, graphene's high electrical conductivity can exacerbate galvanic corrosion over prolonged operational periods, particularly if defects are present.[364–366] In such scenarios, differing corrosion potentials between dissimilar metals, combined with the presence of a conductive medium (*e.g.*, humid air or an electrolyte), lead to preferential anodic oxidation. Even

minor coating flaws permit electrolyte penetration, creating electrochemical pathways that accelerate corrosion.[367] Conductive materials such as graphene can thus serve as cathodic sites, intensifying galvanic corrosion. This realization has fueled interest in electrically insulating materials such as *h*-BN, which can thwart galvanic cell formation and enhance corrosion resistance over extended durations.[368–370] Additionally, the challenges of synthesizing and transferring continuous, defect-free graphene films at an industrial scale further constrain its widespread application in anticorrosion coatings.[371]

The exploitation of *h*-BN monolayers in anticorrosive coatings poses several challenges related predominantly to scalability, cost, and quality, which hinder their industrial application. In contrast, polymers are generally favored for large-scale use owing to their straightforward processing, robust barrier performance, low cost, and strong adhesion to metallic surfaces.[372–374] Nonetheless, during both the fabrication and service life of polymer-based coatings, cracks and pores can emerge,[374] thereby permitting corrosive species to penetrate and initiate corrosion.[348,375,376]

Incorporating *h*-BN or other 2D materials as fillers within these polymer matrices presents a promising approach. Whereas *h*-BN monolayers provide a physical barrier or help repair cracks and pores, polymeric substrates reduce fabrication costs and lessen the need for extensive, defect-free *h*-BN films. Despite these advantages, certain issues remain unresolved. For example, the hydrophobic nature of *h*-BN induces flake agglomeration in polar solvent-based paints, thereby diminishing the coatings ability to act as a physical barrier.[373] Furthermore, a uniform dispersion of *h*-BN flakes is essential to ensure optimal anticorrosive behavior.[374,375]

In polymer coatings, the impermeability of *h*-BN nanosheets impedes the ingress of corrosive species, extending their diffusion path before reaching the metallic surface. Husain *et al.*[377] used exfoliated *h*-BN flakes as fillers for polyvinyl alcohol-based coatings on stainless steel, achieving a corrosion rate of 0.0013 mm $year^{-1}$ upon immersion. Although *h*-BN/polymer composite coatings have been repeatedly shown to confer beneficial protection,[319,378–381] their efficacy strongly depends on the uniformity of *h*-BN dispersion within the polymer.[374] Achieving the "maze effect" critical to corrosion inhibition requires evenly distributed 2D materials; however, *h*-BN's inherent hydrophobicity and its van der Waals interlayer interactions foster aggregation in water or polar solvents.[17] To address this challenge, chemical modification and functionalization of *h*-BN flakes have been explored to enhance dispersibility.[316,382–390] Non-covalent functionalization, often facilitated by π–π interactions, is a common strategy. For instance, Cui *et al.*[391] functionalized *h*-BN flakes with carboxylated aniline trimer, thereby improving their dispersion and enabling epoxy coatings with enhanced water resistance. Wu *et al.*[318] modified *h*-BN with GO for WEP systems; adding 0.3 wt% GO/*h*-BN

significantly boosted both barrier and anticorrosion properties, owing to the complementary impermeability of *h*-BN and GO. Zhao *et al.*[392] used *h*-BN quantum dots to non-covalently functionalize *h*-BN, embedding these hybrid flakes into WEP coatings for Q235 steel. This approach notably improved dispersibility and corrosion resistance at loadings of just 0.1-0.5 wt% quantum dots. Wang *et al.*[393] similarly leveraged strong π–π interactions between polystyrene microspheres and *h*-BN, resulting in BNNS-PS composite coatings within a waterborne polyurethane matrix. Their facile latex-blending approach raised the coating impedance by four orders of magnitude after 28 days of immersion, underscoring the improved corrosion protection.

Alongside non-covalent modification, covalent strategies have also been widely investigated.[318,384,394–396] A primary concern in covalent functionalization lies in introducing functional groups without substantially disrupting the *h*-BN lattice. Common methods include surface decoration with hydroxyl groups, organic moieties, or carbon dots.[319,397,398] Tang *et al.*[394] carried out in situ polymerization of aniline on *h*-BN nanosheets to produce *h*-BN/polyaniline (PANI) nanocomposites, subsequently integrating them into WEP at various loadings. Their results revealed that 2 wt% *h*-BN/PANI nanocomposites offered the best anticorrosion performance, likely due to the synergistic enhancement of *h*-BN dispersion and extended diffusion path. Li *et al.*[395] oxidized *h*-BN with acids and grafted silane onto its surface via a condensation reaction, improving the bond between *h*-BN and epoxy and diminishing micropores. Consequently, corrosion current decreased, and polarization resistance rose by an order of magnitude relative to unmodified *h*-BN/epoxy coatings. Wu *et al.*[399] functionalized *h*-BN with branched PEI, permitting uniform integration in WEP and markedly better corrosion inhibition on mild steel. Wan *et al*.[396] decorated *h*-BN nanosheets with carbon dots, which not only boosted dispersion within the WEP matrix but also extended the duration of corrosion protection in a saltwater immersion test to 40 days.

h-BN can also make the composite coating more hydrophobic,[318,378,382] although an excessive *h*-BN fraction may lead to aggregation and creation of surface defects and porosity.[348] Appropriate filler content and functionalization mitigate this risk by balancing the surface properties of *h*-BN, allowing the achievement of higher loadings and higher levels of hydrophobicity with respect to pristine *h*-BN. Zhang *et al.*[381] incorporated *h*-BN functionalized with polydopamine and decorated with Fe_3O_4 into an epoxy matrix, demonstrating highly effective anticorrosion properties and enhanced hydrophobicity. Similarly, Wang *et al.*[389] produced superhydrophobic coatings by reacting *h*-BN with benzoxazine, reaching a contact angle of 158.2°, and maintained this property after one month of immersion in 3.5 wt% NaCl. Wu *et al.*[318] similarly used GO-functionalized *h*-BN in WEP, with *h*-BN contributing to hydrophobic traits alongside its fundamental barrier function.

Finally, combining *h*-BN with polymers can enhance mechanical strength, thermal stability, and wear resistance – attributes derived from the intrinsic physical and chemical robustness of *h*-BN. Kumar *et al.*[351] demonstrated that TiO_2-decorated *h*-BN nanosheets in a PEDOT matrix not only inhibited corrosion on 316L stainless steel but also improved wettability for biomedical applications, while the pure *h*-BN-loaded PEDOT coating displayed a higher contact angle. Yan *et al.*[385] have shown that oxidized carbon fiber combined with silane-functionalized *h*-BN in epoxy coatings increased both thermal conductivity and corrosion protection with respect to the base resin, although excessive carboxyl functionalities limited performance. Taken together, these studies underscore the versatility of *h*-BN-based fillers in polymer coatings, revealing diverse chemical and structural modifications that optimize anticorrosive performance for a broad range of industrial applications.

Although functionalization of *h*-BN nanosheets can enhance their dispersibility, interfacial adhesion, and compatibility within polymer matrices, this strategy is generally considered impractical at an industrial scale due to its high costs and processing complexities. The chemical reactions required for functionalization often entail hazardous reagents and stringent reaction conditions, necessitating specialized equipment that increases production expenses. Furthermore, adapting these laboratory-scale methods to the large volumes demanded by commercial manufacturing remains challenging, as any slight variability in process parameters can compromise product consistency. Consequently, while functionalization may offer notable improvements in niche applications, it does not currently present an economically viable or industrially efficient solution.

In order to achieve the best performance, the selection of the polymeric matrix for the composite coating fabrication is of critical importance. Various polymeric materials, including polyvinyl butyral (PVB),[400] polydimethylsiloxane,[401] polyurethane,[402] PANI,[403] polypyrrole (PPy),[404] and polythiophene,[405] have been investigated as protective coatings against metal corrosion. Among these, poly(isobutylene) (PIB) has received significant attention since its invention in 1930,[406] owing to its versatility and broad applicability in adhesives,[407] sealants,[408] multiblock copolymeric materials,[409] personal care products,[410] and fuel additives.[411] Notably, PIB demonstrates unique air tightness, gas impermeability, and excellent weathering resistance, alongside good flexibility even at mild sub-ambient temperatures.[406] These characteristics, combined with its low cost, non-toxicity, and the ability to modulate its properties by varying its molecular weight, render PIB an ideal candidate for polymeric coatings intended for metal corrosion protection. Despite the advantages offered by PIB and other polymeric coatings in this context, several challenges must be addressed to ensure reliable and efficient long-term performance,[412] particularly with regard to chemical degradation under environmental conditions.[413]

In this chapter, wet-jet milled *h*-BN was used as a barrier filler to produce anticorrosive coatings based on PIB as the polymeric matrix.[348] Different loadings of *h*-BN were tested in order to study the trend of the barrier performance of the composite and the effect of filler aggregation. Due to the low polarity and high hydrophobicity of the polymer and to the industrial aim of the work, 2D *h*-BN was used in its pristine non-functionalized form, as industrially produced by BeDimensional S.p.A. The coating was tested on structural carbon steel and characterized in terms of morphological, mechanical and electrochemical properties.

Section 3.2 Materials and methods

Section 3.2.1 Materials

Poly(isobutylene) was provided in the form of Oppanol® N80 (average molecular weight – MW – 800000) by BASF Italia S.p.A. Toluene (purity >99.7%) was supplied by Merck. *N*-methyl-2-pyrrolidone was provided by ThermoFisher Scientific. All reagents were used without further purification. Few-layer *h*-BN flakes were produced in the industrial plant of BeDimensional S.p.A. as previously described in Chapter 2.

Section 3.2.2 Preparation of *h*-BN/PIB composite coatings

The *h*-BN/PIB composites were prepared as follows. First, solid PIB was dissolved in toluene at a PIB/toluene weight ratio of 1:8 and stirred at 80 °C and 800 rpm for 12 h until a homogeneous solution was obtained. Subsequently, WJM-produced *h*-BN flakes were introduced at various mass loadings, and the mixtures were processed in a Thinky ARE-250 Mixing and Degassing Machine (planetary centrifugal mixer) at 1000 rpm for 5 min to yield *h*-BN/PIB composite resins containing 2.5, 5, 10, and 20 wt.% *h*-BN. The resulting resins were deposited onto cylindrical S355 steel substrates via doctor blading. The coatings were then dried at RT for 1 h, followed by 15 h at 60 °C to eliminate residual solvent. The thickness of the pristine PIB and *h*-BN/PIB coatings on the S355 steel substrates was measured using a Trotec BB20 thickness gauge based on magnetic induction.

Section 3.2.3 Material and coating characterization

The morphological characteristics of the WJM-produced *h*-BN flakes were examined as reported in Chapter 2.

The surface roughness of coatings containing various amounts of *h*-BN were investigated through AFM using an NX10 AFM (Park System) operated in non-contact mode with a non-contact PPP-NCHR 10 M cantilever (resonance frequency ~330 kHz, force constant 42 N m^{-1}). Images were

collected from 35 × 35 μm^2 regions (512 × 512 data points) at a scan rate of 0.30 Hz, maintaining a working set point of ~6 nm. The acquired AFM images and corresponding height profiles were processed using Gwyddion (64 bit).

Thermogravimetric analysis was carried out using a TA Instruments STD650 under an N_2 atmosphere (flow rate: 100 ml min^{-1}) with a heating rate of 10 °C min^{-1} from 30 °C to 700 °C. X-ray diffraction patterns were recorded with a PANalytical Empyrean diffractometer equipped with a 1.8 kW CuKα ceramic x-ray tube and a PIXcel3D 2 × 2 area detector, operated at 45 kV and 40 mA. Measurements were performed in air at RT, using parallel-beam geometry in symmetric reflection mode.

Scanning electron microscopy data were acquired on a JEOL JSM-6490LA SEM (low-vacuum) with a thermionic electron gun (tungsten source) after coating the samples with a 10 nm gold layer. The hydrophobic behavior of the composites was investigated by contact angle (CA) measurements, in which a 10 μl water droplet was placed on each composite and imaged using an OSSILA L2004A1 CA goniometer.

The molecular structure of the coatings was characterized by Fourier-transform infrared (FTIR) spectroscopy. Thin films (~4 μm) of each composite were deposited on CaF_2 substrates (Crystran) by doctor blading and analyzed in transmission mode on a PerkinElmer Frontier FTIR spectrometer equipped with an N_2 purge. Spectra were collected from 4000 to 600 cm^{-1} at a 4 cm^{-1} resolution, and 128 scans were accumulated to enhance the signal-to-noise ratio. A pristine CaF_2 substrate served as the blank reference. Raman spectroscopy was performed using a Renishaw InVia micro-Raman spectrometer with a 100× objective (numerical aperture – NA – 0.85), operating at 514 nm excitation and an incident power below 1 mW to avoid sample overheating. Finally, optical microscopy images of the steel substrate before and after the long-term immersion test were acquired with a Leica optical microscope using a 100× objective (NA 0.85).

Section 3.2.4 Electrochemical characterization

Electrochemical measurements were performed using a BioLogic VMP3 Multichannel Potentiostat in a three-electrode 1 L electrochemical cell at RT in a 3.5 wt.% NaCl aqueous solution, in agreement with the ASTM G5-14 standard. A KCl-saturated Ag/AgCl Radiometer Analytical REF201 Red Rod Reference Electrode (Biologic) served as the reference electrode, and a graphite rod was used as the counter electrode. The standard working electrode assembly consisted of a cylindrical steel substrate sample (0.785 cm^2 area) coated with PIB or *h*-BN/PIB composites; the sample was drilled and tapped with a 3–48 UNC thread and secured onto a support rod. A polytetrafluoroethylene compression

gasket ensured a leak-tight seal. The open-circuit voltage (OCV) was monitored for 30 min prior to acquiring potentiodynamic anodic polarization data at a scan rate of 10 mV min^{-1}.

The corrosion performance of the coatings was evaluated by potentiodynamic anodic polarization measurements and subsequent Tafel analysis, as detailed in ASTM G5-14, to determine the corrosion current density (i_{corr}) and corrosion potential (E_{corr}).[414,415] The linear polarization resistance values were determined following ASTM G59-97 from the slope of the polarization curve at E_{corr},[416] *i.e.*:

$$R_p = \left(\frac{dE}{dI}\right)_{E_{corr}} \tag{3.1}$$

The corrosion rate (CR, in mm yr^{-1}) was calculated from i_{corr} using the Faraday law:

$$CR = \frac{K \cdot W_{eq} \cdot i_{corr}}{D} \tag{3.2}$$

where $K = 3.27 \cdot 10^{-3}$, $W_{eq} = 27.9$ g eq^{-1} (the equivalent weight of iron in ferrous compounds), i_{corr} is given in µA cm^{-2}, and $D = 7.85$ g cm^{-3}.[417] The inhibition efficiency (η_p) of the composites was derived from the following equation:[418]

$$\eta_p\% = \frac{i^0_{corr} - i_{corr}}{i^0_{corr}} \cdot 100 \tag{3.3}$$

where i^0_{corr} and i_{corr} are the corrosion current densities in the absence and presence of inhibitors (*i.e.*, *h*-BN flakes).

Electrochemical impedance spectroscopy (EIS) was carried out in potentiostatic mode at OCV with a sinusoidal AC amplitude of 10 mV over a 0.1 Hz - 200 kHz frequency range, following ASTM G106-89. Cyclic potentiodynamic polarization measurements were acquired at 0.6 V h^{-1} in accordance with ASTM G61-86. A long-term immersion test in 3.5 wt.% NaCl solution was subsequently conducted for 1000 h continuously, following the ASTM G31-72 protocol.

Section 3.3 Characterization of PIB/*h*-BN composite coatings

Hexagonal boron nitride flakes were incorporated into PIB at loadings ranging from 2.5 to 20 wt.% with respect to the polymer, following the procedure detailed in Section 3.2.2. The resulting resins were then cast onto structural S355 steel substrates (Figure 3.1), producing coatings with an average thickness of 58.4 ± 6.8 µm. The composite coatings are denoted hereafter as *h*-BN/PIB 2.5%, *h*-

BN/PIB 5%, *h*-BN/PIB 10%, and *h*-BN/PIB 20%, according to their respective *h*-BN content. A pristine PIB coating was also prepared as a reference.

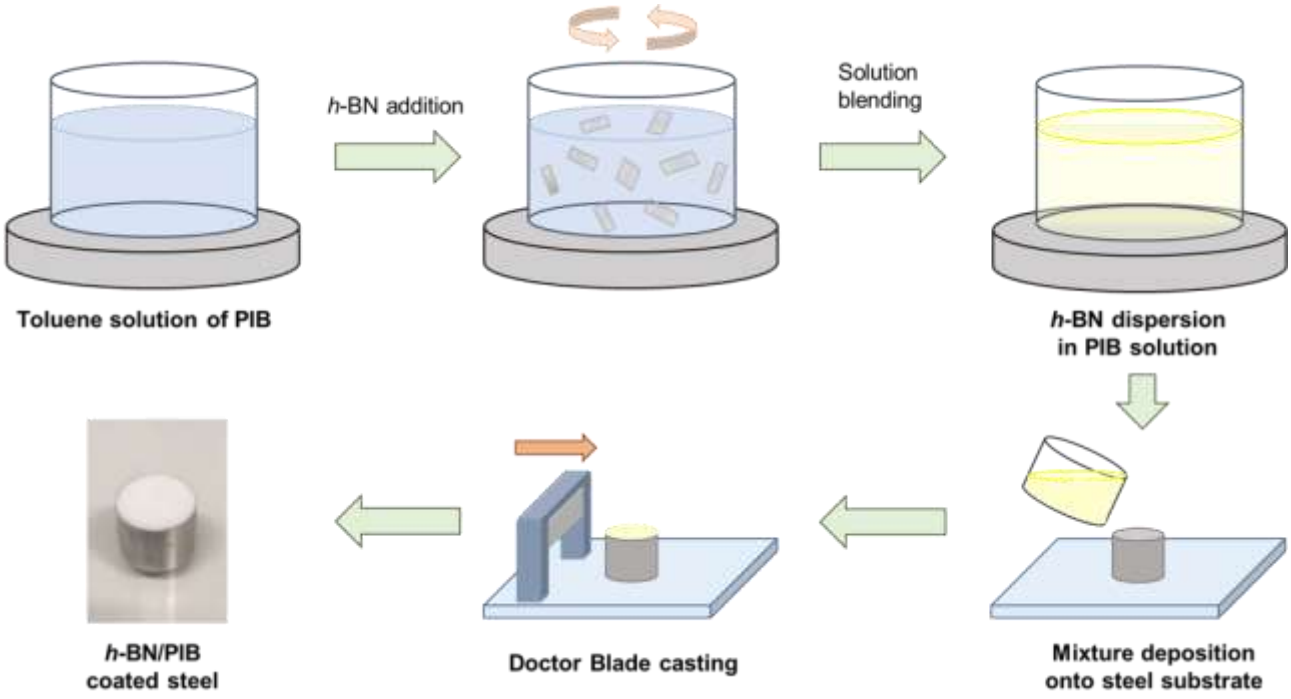

Figure 3.1 Set of procedures used for h-*BN/PIB composite formulation and deposition on structural steel substrates.*[348]

The morphology of the *h*-BN/PIB composites at various *h*-BN loadings was examined by SEM and compared with that of pristine PIB. As shown in Figure 3.2a, the pristine PIB exhibits a homogeneous polymeric structure devoid of fillers. In contrast, the SEM images of the *h*-BN/PIB composites (Figure 3.2b-e) reveal a uniform distribution of the *h*-BN flakes within the polymeric matrix at all tested loadings. Notably, no flake agglomeration was detected, indicating the effective dispersion of the 2D *h*-BN nanofillers achieved using the method outlined in Figure 3.1.

Thermogravimetric analysis was then conducted on pristine PIB and the *h*-BN/PIB composites (Figure 3.2f). All samples displayed comparable thermal responses, with a pronounced mass loss observed at approximately 340 °C, which corresponds to PIB decomposition. Beyond 430 °C, the weight stabilized, indicating the final residual mass.

Table 3.1 presents the temperatures corresponding to 10% ($T_{-10\%}$) and 50% ($T_{-50\%}$) weight loss. These values are similar across all samples, indicating that the incorporation of *h*-BN flakes does not influence the thermal stability of the composites. The residual mass values are approximately in agreement with the *h*-BN weight fraction in each composite.

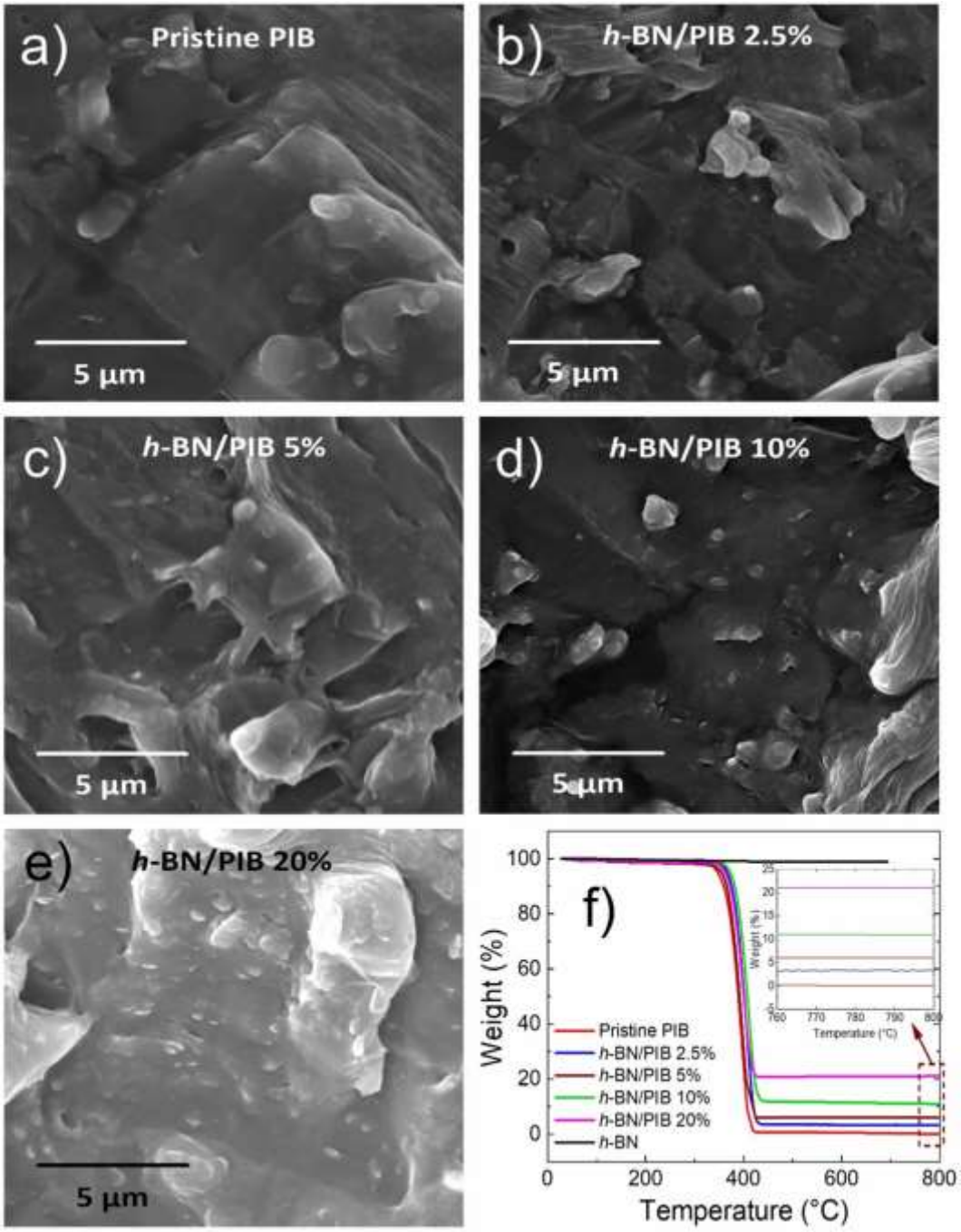

Figure 3.2 SEM images of (a) pristine PIB, (b) h-*BN/PIB 2.5%, (c)* h-*BN/PIB 5%, (d)* h-*BN/PIB 10%, and (e)* h-*BN/PIB 20% composites. (f) TGA curves for pristine PIB and* h-*BN/PIB composites as a function of temperature, measured in N_2 atmosphere. Inset: TGA curve at 760 °C - 800 °C region, showing the mass residues of each sample.*[348]

Surface roughness plays a critical role in determining coating hydrophobicity, which in turn strongly affects the overall anticorrosion performance.[419] To assess the impact of *h*-BN loading on coating roughness, AFM measurements were carried out. As shown in Figure 3.3a,c, the pristine PIB sample exhibits a smooth surface with a root mean square (RMS) roughness of 1.2 nm over a 35 × 35 µm^2 area. Upon incorporating 2.5 wt.% *h*-BN (*h*-BN/PIB 2.5%), the RMS roughness increases to 10.9 nm,

attributable to the occasional presence of *h*-BN flakes on the surface. Further increases in *h*-BN content yield larger roughness values: 41.4, 60.6, and 186.5 nm for the *h*-BN/PIB 5%, 10%, and 20% samples, respectively. Figure 3.3c shows the linear relationship between the *h*-BN loading and surface roughness.

Table 3.1 Parameters obtained from the TGA analysis for pristine PIB and h-BN/PIB composites.[348]

Sample	$T_{-10\%}$ (°C)	$T_{-50\%}$ (°C)	Residual weight (%)
PIB	359.1	389.1	0.01
***h*-BN/PIB 2.5%**	375.9	401.0	3.27
***h*-BN/PIB 5%**	365.4	391.8	6.04
***h*-BN/PIB 10%**	381.9	407.6	10.93
***h*-BN/PIB 20%**	372.1	400.2	21.05

The influence of *h*-BN content on coating wettability was subsequently investigated via water CA measurements. A high CA (>90°) indicates a hydrophobic behavior, which impedes electrolyte penetration through the coating.[419] Representative images of water droplets on the various composite surfaces are presented in Figure 3.3b, while Figure 3.3d plots the measured CA values against *h*-BN content. Pristine PIB exhibits a CA of 88.3° ± 0.4°, close to the 90° threshold for hydrophobic materials. Incorporating *h*-BN increases the CA beyond 90°, consistently with the hydrophobic nature of *h*-BN flakes.[420,421] The highest CA (100.5° ± 0.5°) was observed in the *h*-BN/PIB 10% composite, whereas increasing the *h*-BN content to 20 wt.% reduced the CA to 96.6° ± 0.5°. This decrease likely reflects local aggregation of *h*-BN flakes, as indicated by AFM. Therefore, producing highly hydrophobic surfaces requires both sufficient *h*-BN content (2.5-15 wt.%) and a homogeneous dispersion of the flakes. Overall, *h*-BN/PIB composites with intermediate *h*-BN loadings (5-10 wt.%) achieve the greatest hydrophobicity and thus potentially the most enhanced barrier properties.

Fourier-transform IR spectroscopy was performed between 4000 and 600 cm^{-1} to confirm the incorporation of *h*-BN into the PIB matrix. Figure 3.3e displays the FTIR spectra of the pristine and *h*-BN/PIB 5% samples. In the PIB spectrum, the characteristic bands at 2961 and 2916 cm^{-1} correspond to asymmetric stretching of CH_3 and CH_2 groups, respectively.[422] The peak at 1471 cm^{-1} is associated with CH_2 groups[422] or -CH bending,[423] while the double peak at 1389 and 1361 cm^{-1} arises from CH_3 symmetric bending.[422] The band at 1231 cm^{-1} is attributed to C-H bending, and the weak peaks at 949 and 923 cm^{-1} correspond to C=C bending originating from trace amounts of unpolymerized isobutylene.[424]

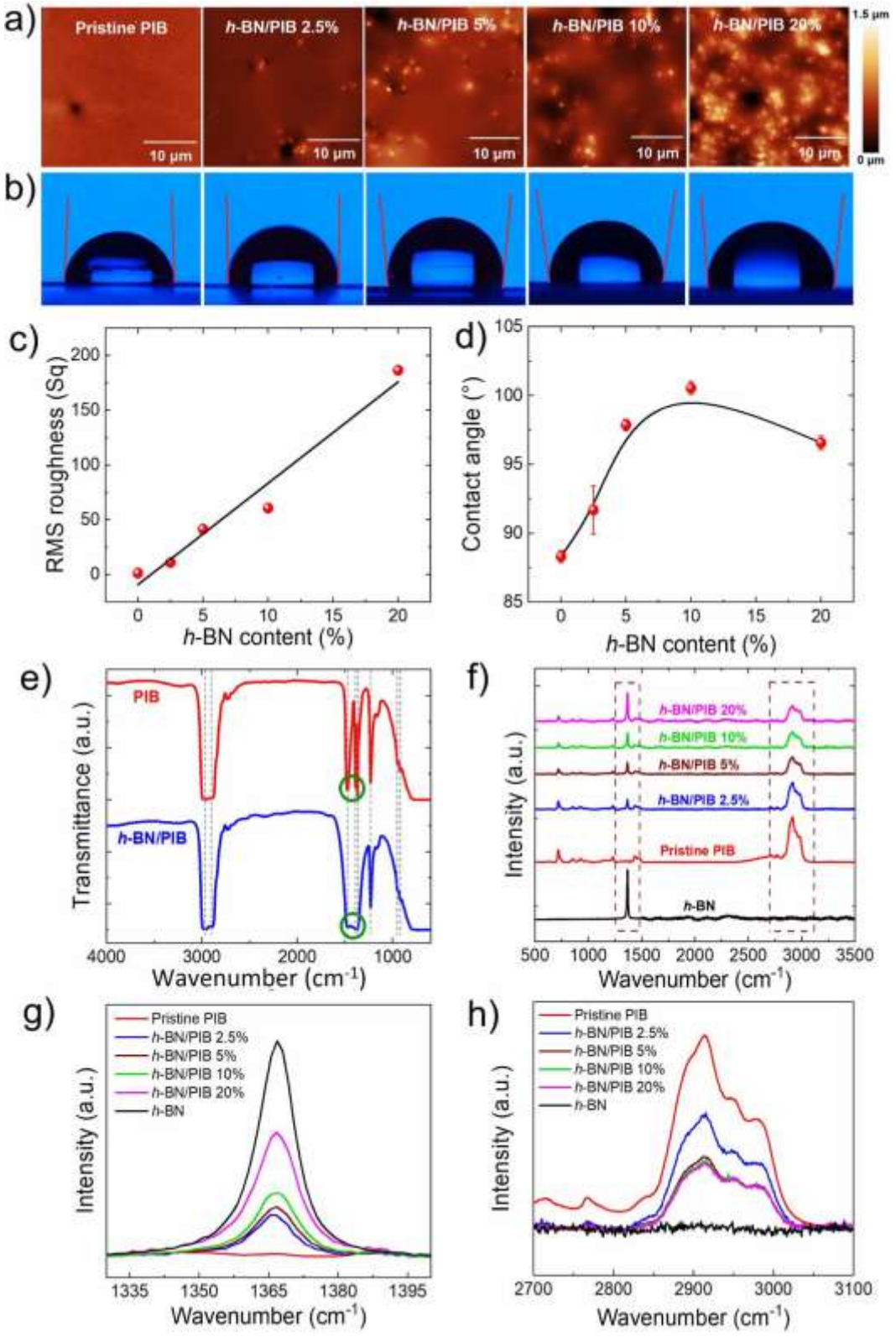

Figure 3.3 (a) AFM images and (b) water contact angle measurements of pristine PIB, h-*BN/PIB 2.5%,* h-*BN/PIB 5%,* h-*BN/PIB 10% and* h-*BN/PIB 20%. (c) Plot of measured RMS roughness of the investigated coatings versus their* h-*BN content, showing the corresponding B-spline fitting. (d) Plot of water contact angle was measured for the investigated coatings versus their* h-*BN content, showing the corresponding B-spline fitting. (e) FTIR spectra of pristine PIB and a representative composite coating (*h-*BN/PIB 5%). Raman spectra of pristine PIB and* h-*BN/PIB composites with different* h-*BN content at (f) full range, (g) 1330–1400, and (h) 2700–3100 cm^{-1} regions, using an excitation wavelength of 514 nm.* [348]

In the FTIR spectra of *h*-BN/PIB 5% (taken as representative for all *h*-BN loaded coatings), notable differences appear between 1471 cm^{-1} and 1361 cm^{-1} compared to pristine PIB (green circles in Figure 3.3e). Specifically, an additional broad band superimposed on the PIB peaks can be attributed to the in-plane ring B-N stretching vibration (E_u mode) of *h*-BN at 1396 cm^{-1},[274,381,425–430] confirming the effective incorporation of *h*-BN flakes into the polymer matrix. Complementary Raman spectra of pristine PIB and all *h*-BN/PIB composites were then obtained, as shown in Figure 3.3f. The pristine PIB Raman spectrum features a broad band in the 2810-3060 cm^{-1} range with a maximum at 2914 cm^{-1}, corresponding to a combination of symmetric and asymmetric C-H modes.[431] Additional minor peaks are also observable at 717 cm^{-1} and 925 cm^{-1}, assigned to the methylene rocking mode $\gamma_r(CH_2)$[431] and out-of-plane CH deformation,[432] respectively.

A sharp peak at 1365 cm^{-1}, attributed to the E_{2g} phonon mode characteristic of *h*-BN,[433] is present in both the pristine *h*-BN and *h*-BN/PIB composite spectra but is absent in pristine PIB, as depicted in Figure 3.3g. Its intensity increases progressively in the composite samples with higher *h*-BN content. Meanwhile, the broad feature at 2914 cm^{-1}, characteristic of PIB, is shown in Figure 3.3h. As expected, its relative intensity with respect to the peak attributed to *h*-BN decreases with increasing *h*-BN content.

Section 3.4 Electrochemical properties of PIB/*h*-BN composite coatings

The principal parameters describing the corrosion performance of the coatings can be obtained from potentiodynamic anodic polarization measurements and corresponding Tafel analyses, in agreement with ASTM G5-14 and ASTM G59-97. Figure 3.4a presents the anodic polarization curves acquired for the *h*-BN/PIB composite coatings, the pristine PIB coating, and the uncoated structural steel substrate. Table 3.2 summarizes the key corrosion metrics determined from these measurements.

All the coatings provide corrosion protection to the bare steel substrate. In particular, the measured E_{corr} of the uncoated structural steel (-0.604 V versus Ag/AgCl) shifts to values between -0.020 and 0.187 V upon application of the polymeric coatings, highlighting their protective function. Notably, the *h*-BN/PIB composite coatings exhibit higher E_{corr} values than pristine PIB, indicating additional anticorrosion benefits conferred by the *h*-BN flakes. However, the E_{corr} values of the *h*-BN/PIB composites do not follow a systematic trend with varying *h*-BN loading.

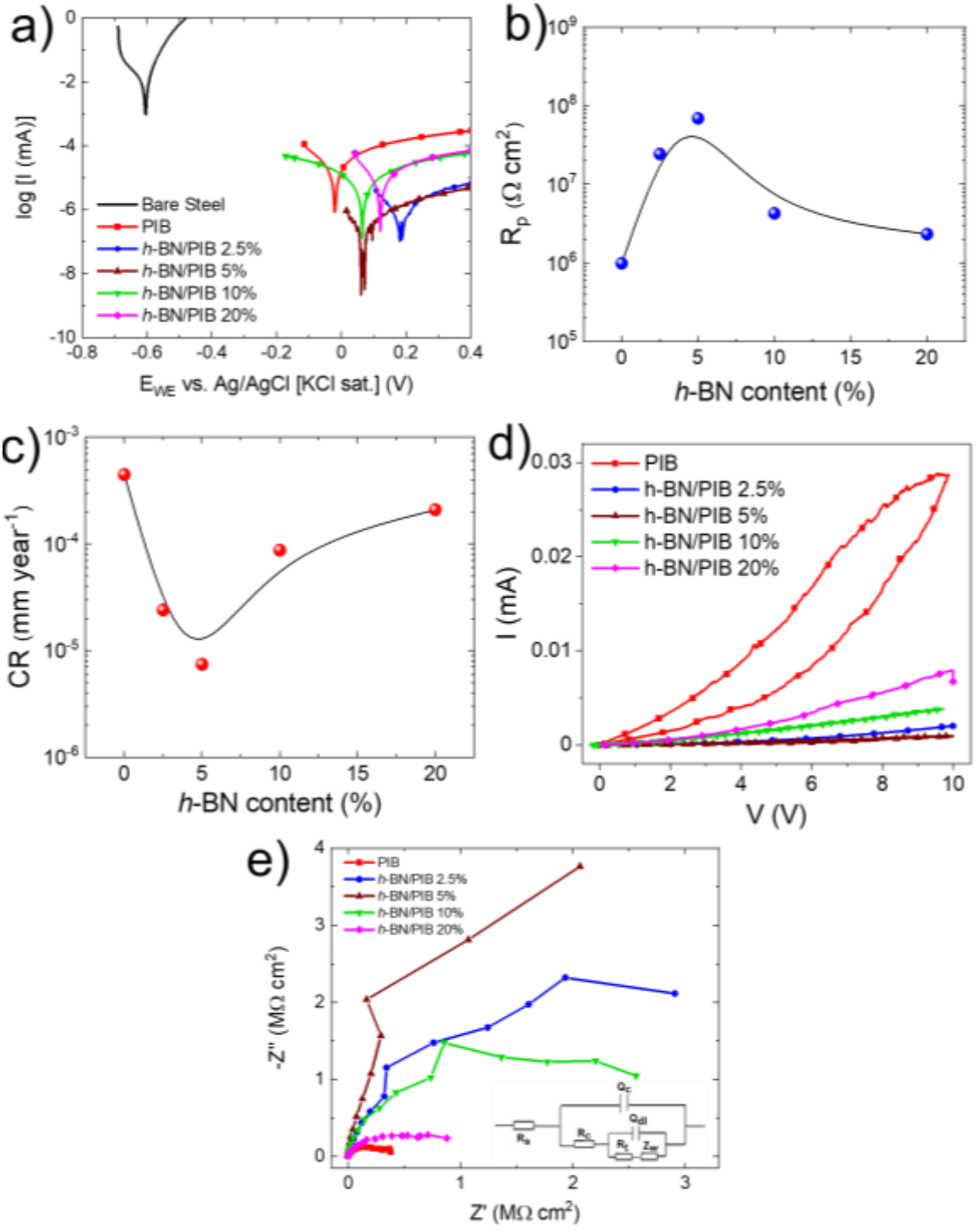

Figure 3.4 (a) Anodic polarization curves (Tafel plots) of pristine PIB- and h-*BN/PIB composite-coated structural steel. The Tafel plot measured for uncoated structural steel is also shown for comparison. (b) Measured* R_p *and (c) calculated CR measured for pristine PIB- and* h-*BN/PIB composite-coated structural steel versus* h-*BN content, showing the corresponding B-spline fitting. (d) Cyclic voltammograms of pristine PIB- and* h-*BN/PIB composite-coated structural steel. (e) Nyquist plots of pristine PIB- and* h-*BN/PIB composite-coated structural steel (inset: equivalent circuit diagram of coated structural steel substrates).*[348]

In contrast, i_{corr} decreases with increasing *h*-BN content up to 5 wt.% (reaching a minimum of $6.4 \cdot 10^{-4}$ μA cm^{-2} in the *h*-BN/PIB 5% composite) but rises again at higher *h*-BN loadings. A similar trend has been reported previously in a PPy/graphene system in which adding a modest amount of graphene enhanced barrier properties, whereas excessive graphene loading caused agglomeration and localized defects.[434] As shown in Figure 3.4b, the highest R_p value, $6.9 \cdot 10^7$ Ω cm^2, is achieved in the *h*-BN/PIB 5% composite.

Figure 3.4c displays the CR of each steel/coating system as a function of *h*-BN content. Consistent with the i_{corr} data, the *h*-BN/PIB 5% coating shows the lowest CR ($7.4 \cdot 10^{-6}$ mm yr^{-1}) among all samples, corresponding to an excellent η_p of 98.36%. Table 3.3 reveals that this CR value is lower than those reported for 2D-material-based coatings of comparable thickness in recent literature. Furthermore, cyclic voltammetry measurements (ASTM G61-86) confirm that none of the investigated coatings undergo pitting corrosion (Figure 3.4d).

Electrochemical impedance spectroscopy measurements, carried out following ASTM G106-89, were then used to investigate interfacial and bulk electrochemical properties.[435] The data can be visualized using Nyquist plots or Bode plots, with the standard equivalent circuit for corrosion (inset of Figure 3.4e) describing the system through solution resistance (R_s), coating capacitance (Q_c), coating resistance (R_c), the double-layer constant phase element (Q_{dl}), and electron-transfer resistance (R_t).[436] In Bode plots, the impedance modulus (|Z|) at low frequency (~0.1 Hz) is related to R_c.[436,437]

Figure 3.4e shows the Nyquist plots for pristine PIB and *h*-BN/PIB composite coatings on structural steel. Each plot reveals a distorted high-frequency semicircle linked to the barrier property of the coating; larger semicircle radii indicate superior corrosion protection.[400] These results support those obtained from the Tafel analysis, showing that the semicircle radius (and thus corrosion resistance) increases from 0 wt.% to 5 wt.% *h*-BN containing coatings. Increasing the *h*-BN content from 5 wt.% to 20 wt.% significantly reduces the semicircle radius, indicating diminished protection. The enhanced performance in *h*-BN/PIB composites relative to pristine PIB arises from the physical barrier provided by *h*-BN flakes, which prolongs the diffusion pathways for corrosive species, as illustrated in Figure 3.5. Importantly, *h*-BN does not exhibit the galvanic coupling reported for graphene, whose barrier properties have also been extensively studied.[361]

In order to evaluate the long-term behavior of the protective coatings, structural steel samples coated with *h*-BN/PIB 5% composite and pristine PIB were immersed in a 3.5 wt.% NaCl solution for 1000 h, while continuously monitoring their E_{corr} values in accordance with ASTM G31-72. As shown in Figure 3.6, the initial E_{corr} was approximately 0.09 V versus Ag/AgCl for the *h*-BN/PIB 5% coating

and 0.03 V for the pristine PIB. Although some fluctuations in E_{corr} were observed during immersion, both coatings remained stable throughout the test. After 1000 h, the measured E_{corr} was around 0.08 V for *h*-BN/PIB 5% and 0.04 V for pristine PIB.

Table 3.2 Electrochemical parameters of bare steel, pristine PIB and h-*BN/PIB composite coatings with different* h-*BN contents, obtained from the Tafel analysis.* [348]

Sample	E_{corr} (V)	i_{corr} (μA cm^{-2})	R_p (Ω cm^2)	CR (mm yr^{-1})	η_p (%)
Bare steel	−0.604	$4.8 \cdot 10^{1}$	$1.3 \cdot 10^{3}$	$5.6 \cdot 10^{-1}$	N/A
PIB	−0.020	$3.9 \cdot 10^{-2}$	$9.9 \cdot 10^{5}$	$4.5 \cdot 10^{-4}$	N/A
***h*-BN/PIB 2.5%**	0.187	$2.1 \cdot 10^{-3}$	$2.4 \cdot 10^{7}$	$2.4 \cdot 10^{-5}$	94.67
***h*-BN/PIB 5%**	0.072	$6.4 \cdot 10^{-4}$	$6.9 \cdot 10^{7}$	$7.4 \cdot 10^{-6}$	98.36
***h*-BN/PIB 10%**	0.065	$7.5 \cdot 10^{-3}$	$4.3 \cdot 10^{6}$	$8.7 \cdot 10^{-5}$	80.67
***h*-BN/PIB 20%**	0.121	$1.8 \cdot 10^{-2}$	$2.3 \cdot 10^{6}$	$2.1 \cdot 10^{-4}$	53.33

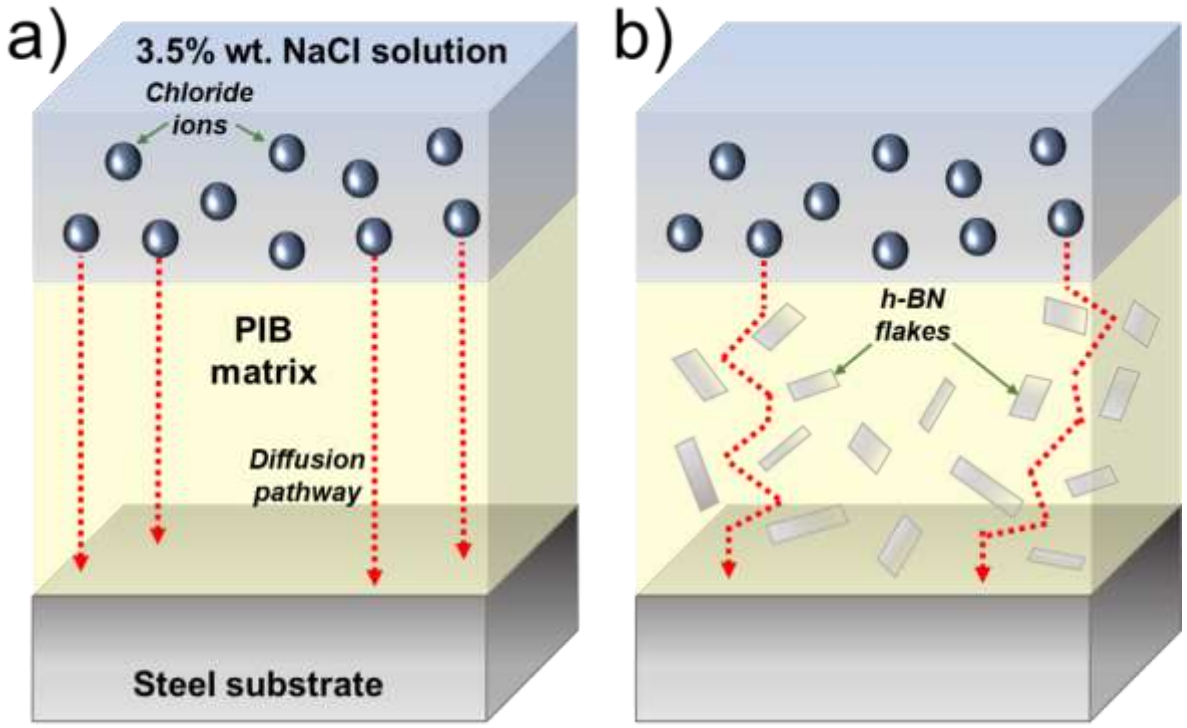

Figure 3.5 Schematic diagrams of diffusion pathways followed by chloride ions through (a) pristine PIB and (b) h-*BN/PIB composite coatings from the NaCl aqueous solution to the surface of the steel substrate.*[348]

Table 3.3 Performance comparison of h-*BN/PIB 5% coating with literature in terms of corrosion rate.*[348]

Filler	Matrix	Loading (wt.%)	Thickness (µm)	CR (mm yr^{-1})	References
***h*-BN**	PIB	5	58 ± 7	$7.4 \cdot 10^{-6}$	This work
f-BNNS-PPy	Epoxy	0.5–3	40	$1.5 \cdot 10^{-5}$	[390]
B-doped graphene	PU	0.5	25 ± 2	$1.6 \cdot 10^{-5}$	[438]
PPyNG	Epoxy	2	20	$8.9 \cdot 10^{-5}$	[439]
BNNDs@GNSs	Epoxy	0.1	20	$6.3 \cdot 10^{-5}$	[440]
F*h*-BN, SZP	Epoxy	0.5, 0.5	30 ± 2	$2.3 \cdot 10^{-4}$	[316]
GNSs	PMMA	0.5	10 ± 1	$8.6 \cdot 10^{-3}$	[441]

To further evaluate the impact of immersion on the steel substrate structural integrity, optical microscopy images were captured after delaminating the coatings (insets, Figure 3.6). Following 1000 h of immersion in a 3.5 wt.% NaCl solution, the bare steel substrate surface appeared severely corroded (Figure 3.6b) relative to its initial condition (Figure 3.6a). In contrast, the pristine PIB coating provided clear protection against oxidation (Figure 3.6c), although some areas still exhibited corrosion. By comparison, the *h*-BN/PIB 5% composite coating preserved the substrate surface entirely free of oxidation products (Figure 3.6d), closely resembling the as-received steel. These findings confirm the superior corrosion resistance offered by the composite coating, whereas the lower protection afforded by pristine PIB allows limited ingress of corrosive species.

The evolution of the anticorrosion properties of the coatings during immersion was investigated by EIS. Figure 3.7 presents the Bode plots measured for pristine PIB and *h*-BN/PIB 5% on structural steel over 26 days of immersion. As shown in Figure 3.7a,c, the uncoated steel substrate exhibits the lowest $|Z|_{0.1\,Hz}$ value (~$10^3\,\Omega\,cm^2$). After a 2.5 h preconditioning period, initial $|Z|_{0.1\,Hz}$ values of $5.6 \cdot 10^5\,\Omega\,cm^2$ and $3.5 \cdot 10^6\,\Omega\,cm^2$ were measured for pristine PIB and *h*-BN/PIB 5%, respectively, indicating the superior anticorrosive properties of the composite. During the first 10 days, the Bode plots exhibited some changes commonly observed in early immersion studies of anticorrosion coatings.[400,434,442,443] However, these shifts do not necessarily reflect a loss in coating efficacy if

$|Z|_{0.1\,Hz}$ remains high. Coating failure is instead signaled by a pronounced change in E_{corr} toward the value of the bare substrate (*e.g.*, -0.604 V vs. Ag/AgCl for uncoated steel).

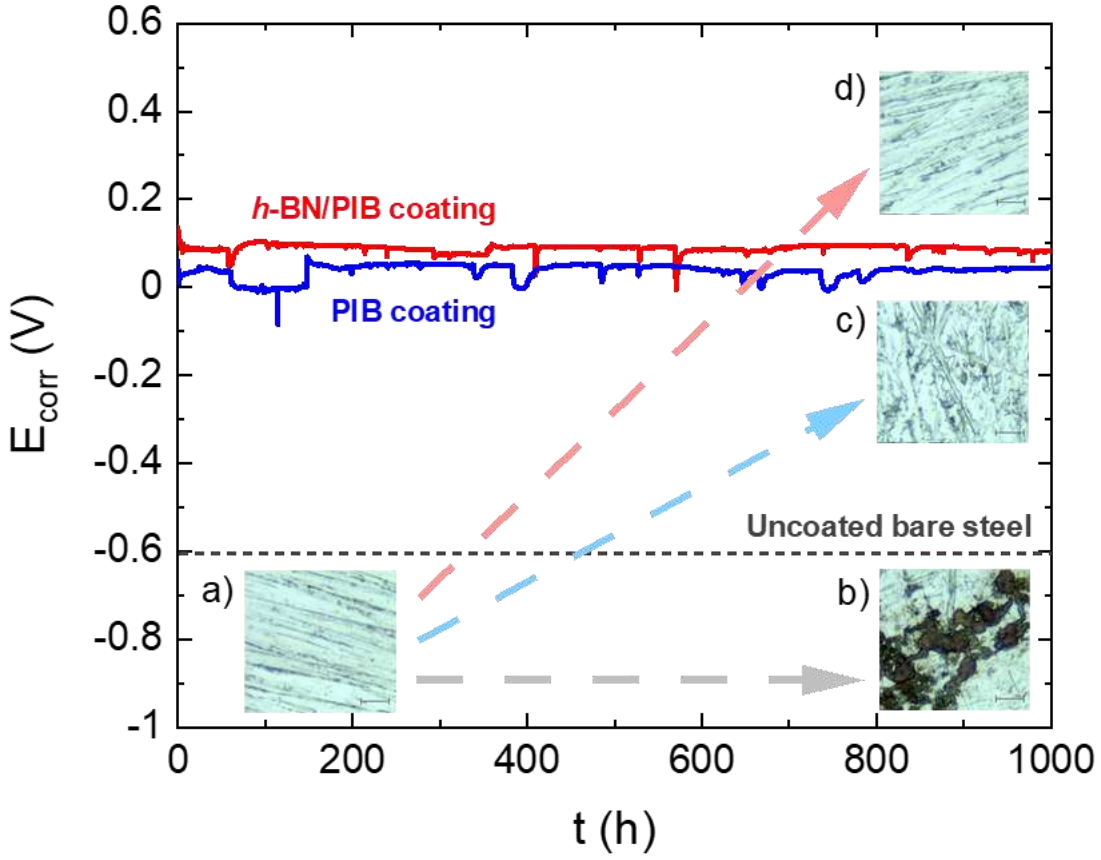

Figure 3.6 E_{corr} over 1000 h of immersion in 3.5 wt.% NaCl aqueous solution of structural steel substrates coated with pristine PIB and h-*BN/PIB 5%. The insets show optical microscopy images of bare steel substrate (a) before and (b) after 1000 h of immersion in 3.5 wt.% NaCl aqueous solution and steel substrate coated with (c) pristine PIB and (d)* h-*BN/PIB 5% composite coatings after 1000 h of immersion in the same saline solution.*[348]

Coating failure is commonly indicated by a progressive decrease in $|Z|_{0.1\,Hz}$ over time, eventually converging to values characteristic of the bare substrate. In this study, the E_{corr} of PIB-based coatings remained virtually unchanged after 1000 h of uninterrupted immersion. Even after 48 h, the *h*-BN/PIB 5%-coated steel exhibited a $|Z|_{0.1\,Hz}$ value of $6.2 \cdot 10^5\,\Omega\,cm^2$, exceeding that of the steel protected solely by pristine PIB. At day 10, the $|Z|_{0.1\,Hz}$ values for the pristine PIB and *h*-BN/PIB 5% coatings were $1.7 \cdot 10^4$ and $2.9 \cdot 10^4\,\Omega\,cm^2$, respectively. Beyond the 10-day mark, no further variations in $|Z|_{0.1}$ Hz were recorded in either system, indicating stable anticorrosion performance over time.

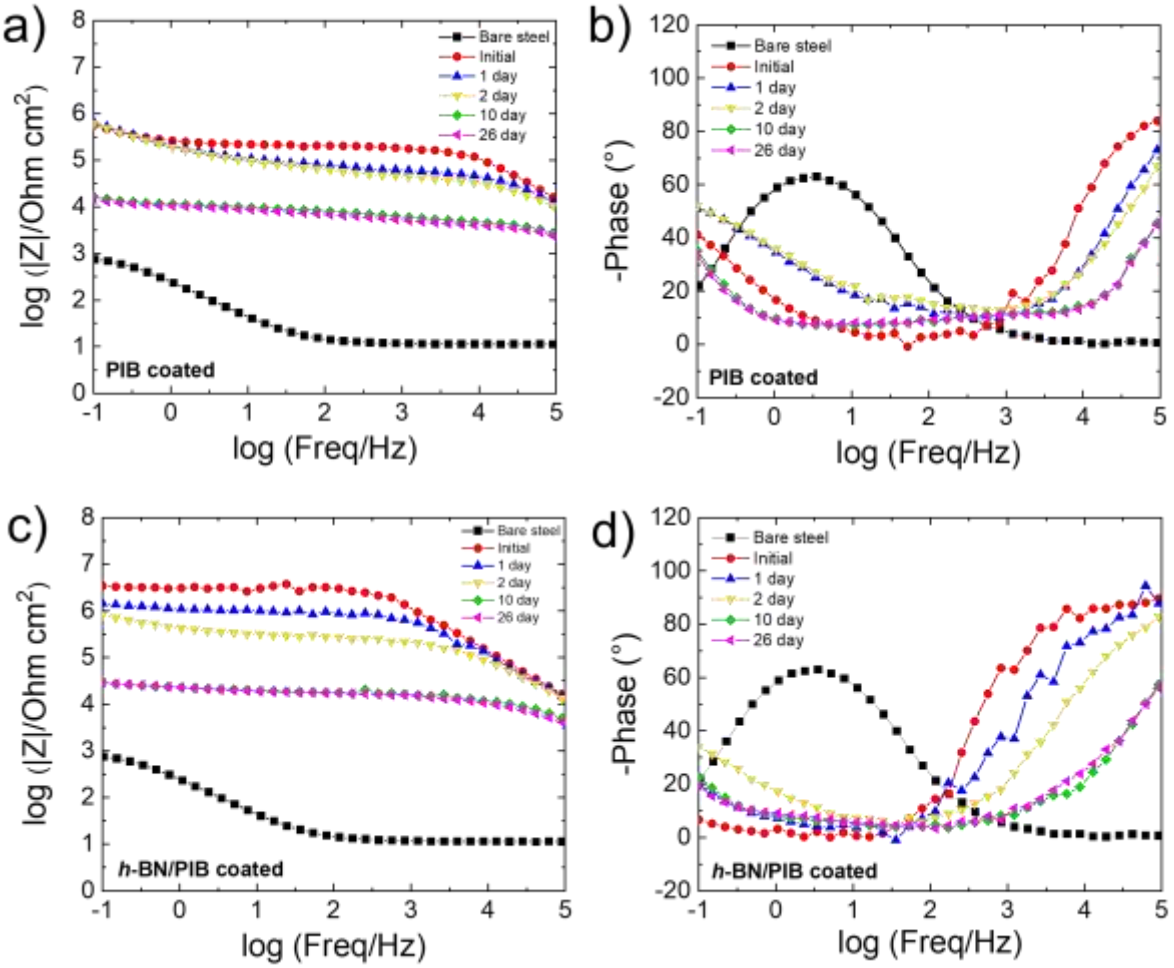

Figure 3.7 Bode plots of (a), (b) pristine PIB- and (c), (d) h-BN/PIB 5%-coated structural steel substrates.[348]

Section 3.5 Conclusions

In this chapter, the barrier effect of 2D *h*-BN industrially produced by wet-jet milling has been investigated. A composite formulation has been developed by embedding few-layer *h*-BN flakes in a PIB matrix for use as an anticorrosion coating on steel substrates in aqueous saline environments. The surface roughness of the resulting composite coatings was found to increase proportionally to the content of *h*-BN, while the highest hydrophobicity was attained at 10 wt% *h*-BN with a water contact angle of 101° with respect to 88° for pristine PIB. Raising the *h*-BN content beyond this level decreases the coating hydrophobicity, probably due to filler aggregation. The anticorrosion performance of the coatings was systematically evaluated at different *h*-BN loadings, and these results were correlated with the physicochemical properties of the coated samples. In 3.5 wt% NaCl solution, the coating containing 5 wt% *h*-BN achieved a minimum corrosion rate of $7.4 \cdot 10^{-6}$ mm yr^{-1}, which is nearly two orders of magnitude lower than that of the pristine PIB coating. The embedded hydrophobic *h*-BN flakes serve as an additional barrier against electrolyte penetration, thus enhancing

substrate protection with respect to the unfilled polymer. Also in this case, increasing the loading of h-BN results in higher corrosion rates, probably due to filler aggregation, as demonstrated through SEM images. The stability of the *h*-BN/PIB 5% coating was assessed through E_{corr} measurements over 1000 h of immersion in 3.5 wt% NaCl solution. Combined EIS data and optical microscopy images revealed that this composite coating maintains long-term anticorrosion stability. Overall, *h*-BN flakes are shown to be effective nanofillers for improving the corrosion resistance of polymeric coatings in marine environments.

Chapter 4 Encapsulation of perovskite solar cells and modules with *h*-BN based composites

This chapter demonstrates how the barrier properties and high thermal conductivity of few-layer *h*-BN can enhance the performance of polymeric encapsulants for PSCs and perovskite solar modules (PSMs), thereby improving their stability to meet multiple standard solar cell tests. The results described in Chapter 2 serve as a reference for formulating the encapsulant, which will then be tested on several state-of-the-art PSC configurations and one PSM as a proof-of-concept for large-scale industrial applications. The work shown in this chapter was performed in collaboration with the University of Roma "Tor Vergata" and the results have been published by Mariani *et al*.[192]

Section 4.1 Perovskite solar cells

Since the 1950s, photovoltaic (PV) technology has been recognized as one of the most powerful solutions for meeting global energy demands, laying the groundwork for a green economy. The central mechanism of a solar cell (SC) relies on the photovoltaic effect, whereby photons with energies exceeding the semiconductor bandgap are absorbed by the photoactive layer, generating electron-hole pairs or excitons.[444] In certain semiconductors, excitons dissociate under an internal electric field, releasing free carriers that migrate through the cell structure until collected by selective contacts or lost through recombination – thereby dissipating energy as heat.[188] Ideally, these contacts should collect only one type of charge carrier. In practice, n-type semiconductors, which exhibit high electron conductivity but lower hole conductivity, collect electrons, whereas p-type semiconductors selectively transport holes (Figure 4.1).[445]

Building on this mechanism, numerous photoactive materials have been investigated for SCs, leading to diverse PV architectures.[446] Among these, PSCs have recently gained prominence as innovative, low-cost, and easily processable PV systems, achieving certified power conversion efficiencies (PCEs) above 25%.[447] Perovskite semiconductors form a broad class of materials sharing the calcium titanate ($CaTiO_3$) crystal structure, typically described by the formula ABX_3, where A is a monovalent cation, B is a divalent metal cation, and X is a halide anion (*e.g.*, F^-, Cl^-, Br^-, I^-).[448,449] In these materials, the A cation is coordinated by 12 halogen anions in a cube–octahedral configuration, while the B cation sits centrally, coordinating six halogen anions in an octahedral arrangement (Figure

4.2).[188,450] This structure allows the incorporation of large cations, such as organic molecules, to form organic–inorganic hybrid perovskites.

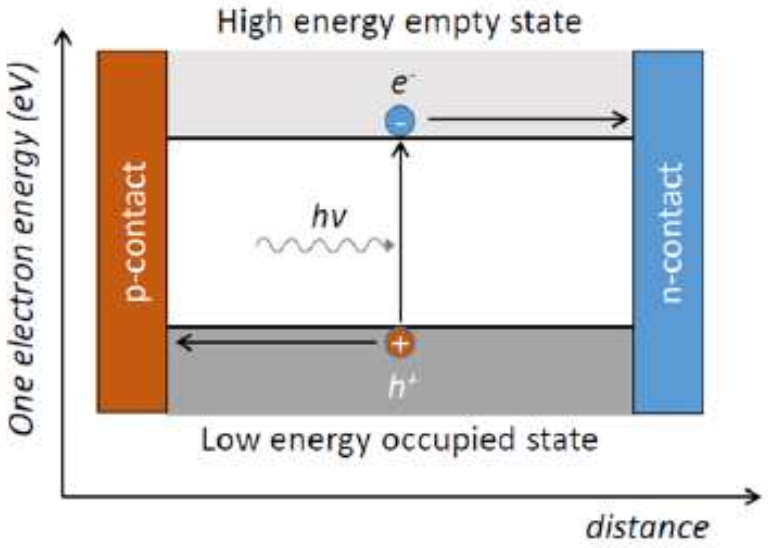

Figure 4.1 Schematic illustration of the photovoltaic principle in solar cells.[451]

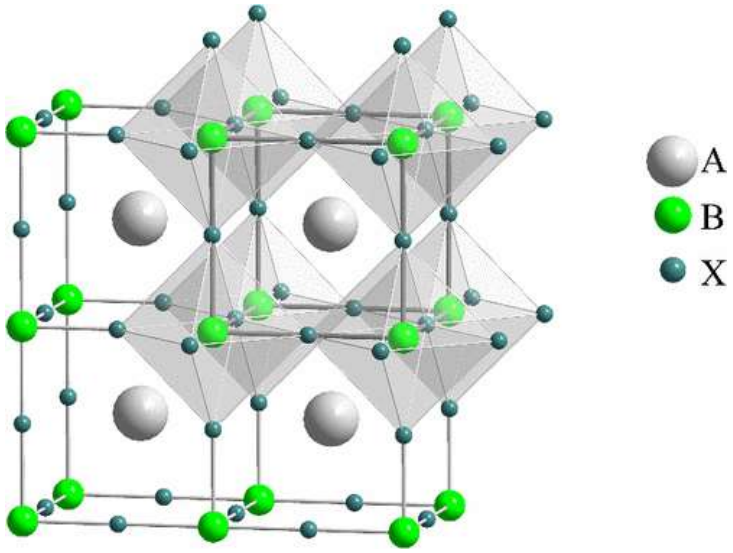

Figure 4.2 Perovskite crystal structure. In PSCs A is a large organic cation, B is a small metallic cation, and X is a halogen ion.[450]

In PSCs, the most prevalent organic-inorganic perovskites are organometallic halides, wherein A is typically a large organic cation (*e.g.*, methylammonium (MA) or formamidinium (FA)), B is a small divalent metal cation (commonly Pb^{2+}, though Sn^{2+}, Ge^{2+}, or Bi^{2+} may substitute it), and X is generally I^- or Br^-.[188,449] A key advantage of these materials is their ionic nature, which allows precursor compounds to be dissolved in common solvents, thereby enabling low-temperature solution processing and facilitating industrial scalability.[452] Additionally, perovskites exhibit absorption

coefficients greater than 10^4 cm^{-1}, surpassing those of crystalline silicon. As a result, a thin absorber layer (300-600 nm) can capture most incident photons, reducing charge-carrier recombination and improving the OCV along with overall device performance.[452,453]

Within PV devices, perovskite materials serve as photoactive absorbers that generate charge carriers subsequently transferred to electron-transporting (ETL) or hole-transporting (HTL) layers. In most PSC architectures, electrons migrate to the ETL and then to the anode, commonly fluorine-doped tin oxide (FTO), whereas holes pass into the HTL and eventually reach a metal cathode (*e.g.*, Au or Ag).[454] The device structure strongly influences performance, giving rise to two main configurations: the conventional (n–i–p) or the inverted (p–i–n), depending on whether incident light first contacts the ETL or the HTL.[188,454] Furthermore, PSCs can feature a mesoporous layer (often the ETL), into which the perovskite is infiltrated, or a planar stack of flat layers (Figure 4.3). These distinctions entail different processing requirements, materials, and performance outcomes; thus, careful selection of the absorber, ETL, and HTL – alongside an appropriate device layout – is critical for achieving high PSC efficiency.[188,454] Beyond PVs, perovskites also show promise in sensing,[455] photodetection,[456] light-emitting devices,[457] and lasing.[458] However, their limited thermal and chemical stability currently impedes large-scale market deployment, as factors such as oxygen and moisture ingress,[459] elevated temperatures,[460] and UV irradiation[460,461] can degrade perovskite films. Various approaches, including interfacial engineering and encapsulation, are under investigation to mitigate these issues.[462]

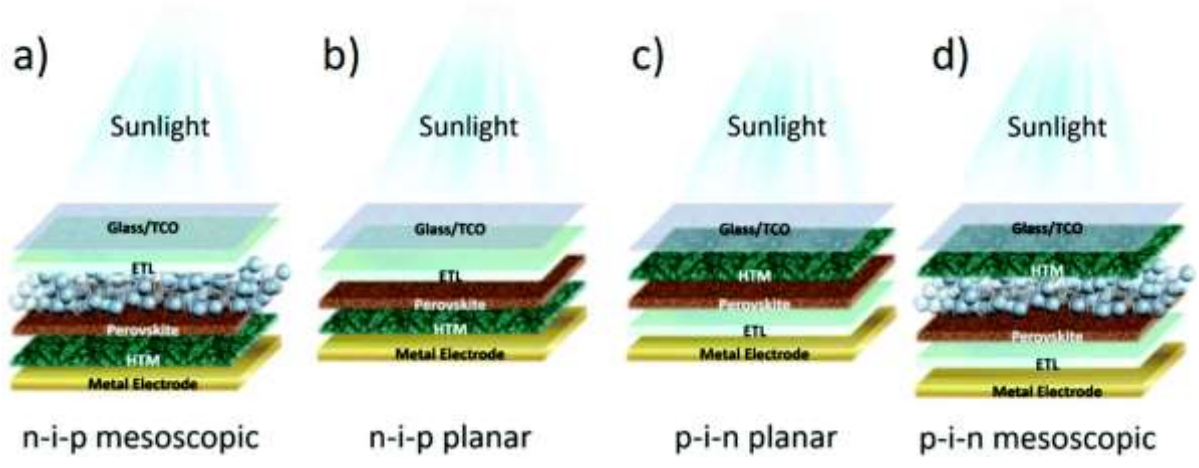

Figure 4.3 Different architecture of perovskite solar cells: (a) regular mesoscopic, (b) regular planar, (c) inverted planar, (d) inverted mesoscopic.[188]

Having achieved PCEs as high as 26.1% in single-junction and 33.9% in tandem configurations,[463–466] PSCs promise to revolutionize the PV sector. These exceptional performance levels, combined with cost-effectiveness stemming from readily available precursors and scalable solution-based

production, position PSCs as next-generation PV contenders.[467,468] However, achieving a Levelized Cost of Energy (LCoE) comparable to commercial crystalline silicon (c-Si) cells (*i.e.*, less than USD 0.05/kWh)[469] requires long-term stability – a challenge exacerbated at the module level, where additional failures such as potential-induced degradation and reverse bias effects must be considered.[470,471] In general, PSCs lifetimes depend on intrinsic (*e.g.*, polymorphism, defects, lattice strains, ion migration) and extrinsic (*e.g.*, moisture, oxygen, heat, UV exposure, reverse bias) factors.[472,473] Common degradation pathways include phase segregation within perovskite films or charge-transport layers (CTLs),[474,475] often accompanied by morphological changes.[473,476] Ion migration and outgassing of volatile species at grain boundaries and interfaces frequently initiate these processes,[477,478] which may be intensified by lattice defects,[479] strains,[480] and mismatches in thermal expansion coefficients (TECs) among the cell materials.[153] Proposed stabilizing strategies include compositional[481] and dimensional[482,483] engineering, defect passivation,[484,485] grain boundary modifications,[486,487] and interface engineering,[191,488] frequently combined to bolster PSCs' intrinsic stability.[472,473,476,489]

Moisture and oxygen can react directly with perovskite absorbers, ultimately causing decomposition. Water forms hydrogen bonds with organic cations, weakening the interaction between these cations and Pb-halide octahedra.[490] The released proton may transfer to halide ions (*e.g.*, I^-) via water molecules, generating volatile species (*e.g.*, CH_3NH_2, HI, PbI_2). Meanwhile, oxygen can fill halide vacancies, and photoexcitation of the perovskite leads to charged superoxide species that trigger acid–base reactions with organic cations, forming further volatile byproducts.[461,491] Intrinsic factors such as lattice defects, combined with extrinsic drivers like moisture, oxygen, and temperature, collectively govern PSC stability.[472] Elevated temperatures and temperature fluctuations,[492] as well as illumination and reverse bias conditions,[493] exacerbate intrinsic degradation, with photodissociation occurring more readily at high temperatures.[477]

Encapsulation protocols are widely recognized as critical for ensuring operational longevity of PSCs and related modules under outdoor conditions (≥20 years).[472,494–496] However, typical encapsulation strategies designed for commercial PV technologies may not meet the specific requirements of PSCs, and encapsulation practices for these cells are still evolving.[472,494,497] An ideal encapsulant should fulfil the following criteria:[472,494,498] (1) chemical inertness and compatibility with underlying layers, avoiding release of damaging byproducts (*e.g.*, acetic acid in ethylene vinyl acetate (EVA)[499] or methacrylic acid in Surlyn);[500,501] (2) low water-vapor transmission rate (WVTR $\leq 10^{-4}$ g m^{-2} day^{-1}) and oxygen transmission rate (OTR $\leq 10^{-3}$ cm^3 m^{-2} day^{-1} atm^{-1}) to prevent moisture/oxygen ingress and curtail outgassing of volatile species;[502] (3) UV-radiation stability, preventing degradation (*e.g.*,

yellowing); (4) thermal stability up to 85 °C and low-temperature (≤120 °C) processability, aligning with the PSC thermal budget and stability of common CTLs; (5) optical transparency (≥90% from 400 to 1100 nm) for front-side encapsulants; (6) high electrical insulation (resistivity >10^{13} Ω·cm) to avert leakage current and reduce potential-induced degradation; and (7) suitable mechanical properties (*e.g.*, flexibility with a low Young's modulus <20 MPa at 25 °C and adhesion strength >0.1 MPa) to tolerate thermo-mechanical stress from daily temperature cycles.[495] Presently, a combination of glass/pressure-tight polymer/glass encapsulation – sandwiching the PSC or module between two glass sheets via an adhesive layer – is often employed to produce highly stable devices.[472,494,495] Examples of such adhesives include EVA, ionomers (Surlyn, Bynel, Jurasol), PIB, polyolefins (POEs), polyurethanes (PUs), thermoplastic polyurethanes (TPUs), and edge sealants made of PIB-based butyl rubbers, UV-curable polymers, epoxy resins, silicones, or glass frits.[503,504] Early studies have reported small-area PSCs passing accelerated aging tests in line with International Electrotechnical Commission (IEC) 61215 standards and ISOS (International Summit on Organic PV Stability) protocols,[472,494] such as damp heat (≥1000 h at 85 °C, 85% RH – PCE retention >80%) and thermal cycling (≥200 cycles between -40 °C and 85 °C – PCE retention >80%),[492,495,502,505–512] as well as humidity-freeze testing.[502,513] However, many of these achievements have not yet been fully demonstrated in PSMs, highlighting a gap between laboratory-scale studies and market-ready technologies.[513]

Overall, limited studies have used high-throughput, commercially viable processes for PSM encapsulation, and comprehensive aging tests have seldom been conducted outside of direct outdoor performance measurements.[190,495] For industrial-scale PSM fabrication, encapsulants must be compatible with rapid (minute-scale), cost-effective production.[495,514] Compared with conventional PV encapsulants, PSC-specific materials may also require thermal management capabilities, reflecting the low thermal conductivity of perovskite absorbers,[495,515] as well as Pb-sequestration capacity due to the high solubility of Pb-containing degradation byproducts (~40 µg kWh^{-1} of Pb release)[516] and the large solubility product constants of common Pb-halide phases (*e.g.*, K_{sp} of PbI_2 is $4.4 \cdot 10^{-9}$ M, which is about 11 orders of magnitude higher than for PbS or PbSe).[517,518] Furthermore, lower Young's modulus encapsulants are generally preferred to mitigate delamination issues arising from mismatched TECs.[506] Finally, encapsulants must minimize cell-to-module losses by limiting the width of edge seals to under 1 cm in meter-scale panels – an aspect not always addressed in small-scale stability demonstrations, which often utilize encapsulant areas larger than the device's photoactive area.[497,502,506,507] Accordingly, these findings still require validation in practical device architectures that deliver competitive LCoEs.[469]

In this chapter, the intrinsic instability of perovskites is addressed by proposing a novel, industrially viable encapsulation strategy employing a low molecular weight PIB-based encapsulating material loaded with wet-jet milled *h*-BN nanosheets. The approach was tested on solar cells and modules based on a well-known perovskite chemistry, passing standardized aging tests, such as thermal stress (ISOS-D-2), light soaking (ISOS-L-1), thermal shock, and a modified humidity freeze test. The barrier properties of the encapsulating composites are also examined.[192]

Section 4.2 Materials and methods

Section 4.2.1 Materials

TiO_2 paste (30 NR-D), formamidinium iodide (FAI), methylammonium bromide (MABr), methylammonium chloride (MACl), and phenylethylammonium chloride (PEACl) were obtained from GreatCell Solar. Lead(II) iodide (PbI_2), lead(II) bromide ($PbBr_2$), and cesium iodide (CsI) were purchased from TCI. Cesium bromide (CsBr) beads, titanium(IV) isopropoxide (TIP), diisopropoxytitanium bis(acetylacetonate) ($Ti(AcAc)_2$), acetylacetone (AcAc), phenethylammonium iodide (PEAI), tris(2-(1H-pyrazol-1-yl)-4-tert-butylpyridine)cobalt(III) tri[bis(trifluoromethane)sulfonimide] (FK209 Co(III) TFSI), bathocuproine (BCP), copper (Cu) beads, ethanol (EtOH) (anhydrous, ≥99.8%), acetone (≥99.5%), acetonitrile (ACN) (≥99.8%), DMF (≥99%), dimethyl sulfoxide (DMSO) (>99%), chlorobenzene (CB) (99.8%), 1,2-dichlorobenzene (DCB) (99%), toluene (>99.7%), NMP (>97%), 2-propanol (IPA) (anhydrous, 99.5%), ethyl acetate (anhydrous, 99.8%), tert-butylpyridine (tBP), and lithium bis(trifluoromethane)sulfonimide (LiTFSI) were obtained from Sigma-Aldrich. The SnO_2 dispersion (15% in water) was purchased from Alfa Aesar. Poly[bis(4-phenyl)(2,4,6-trimethylphenyl)amine] SOL2426M (average molecular weight 105 kDa) was procured from Solaris Chem, and [6,6]-phenyl-C_{61}-butyric acid methyl ester (PCBM) was acquired from Solenne. A graphene dispersion in ethanol (0.9 mg mL^{-1}) was supplied by BeDimensional S.p.A.

A highly viscous (Brookfield viscosity >100000 mPa·s at 10 rpm and <120 °C) PIB (LMW-80, average molecular weight 95000, viscosity average) was provided by TER Chemicals. All reagents were used as received unless otherwise indicated. Fluorine-doped tin oxide-coated glass substrates (sheet resistance, R_{SH} = 7 Ω sq^{-1}) were purchased from NSG-Pilkington, and indium–tin oxide (ITO)-coated glass substrates (R_{SH} = 7 Ω sq^{-1}) were obtained from Kintec. Silver (Ag) paste (7713) was purchased from Dupont, and the ITO sputtering target was provided by TestBourne Ltd.

Section 4.2.2 Encapsulant preparation

Two types of encapsulants were prepared for the encapsulation of PSCs and PSMs. The first encapsulant consisted of a highly viscous, low-molecular-weight PIB, liquid at RT, whereas the second one is an opaque composite of the same PIB and 2D *h*-BN flakes, hereafter referred as PIB:*h*-BN.

To prepare homopolymer PIB encapsulants, PIB was first dissolved in toluene at a 1:1.5 (PIB:toluene) weight ratio and subjected to vigorous stirring (500 rpm) at 80 °C for 12 hours at 800 rpm, yielding a homogeneous solution.

For preparing PIB:*h*-BN encapsulants, few-layer *h*-BN flakes were produced using the patented WJM method developed by BeDimensional S.p.A., as described in Chapter 2.[177,344,348] After drying, WJM-produced *h*-BN flakes were incorporated into the PIB solution and mixed in a planetary centrifugal mixer (Thinky ARE-250 Mixing and Degassing Machine) at 1000 rpm for 5 minutes, producing *h*-BN/PIB composite resins containing 5 wt% *h*-BN (with respect to the total solid content). This *h*-BN concentration was previously determined through electrochemical evaluations compliant with ASTM G5-14, ASTM G59-97, ASTM G61-86, and ASTM G106-89 standards, with the aim of maximizing the barrier properties of the resulting *h*-BN-containing encapsulants (see Chapter 3).[348]

To produce encapsulant films, the PIB and PIB:*h*-BN resins were doctor-bladed onto 1 mm-thick glass substrates for glass/pressure-tight polymer/glass device encapsulation. The resulting films were dried at RT for 1 hour and then further dried at 60 °C for 15 hours to remove any residual solvent.

Section 4.2.3 Encapsulants characterization

The thickness of the resulting homopolymer PIB or PIB:*h*-BN films was 600-700 µm, as determined using a Trotec BB20 thickness gauge. For these measurements, the encapsulant films were deposited onto metallic substrates following the same procedure and parameters employed for glass deposition. The water contact angle of the PIB and PIB:*h*-BN films was measured using an OSSILA L2004A1 goniometer by imaging a 10 µL water droplet on the sample surface. To evaluate the barrier performance of these encapsulants, both electrochemical tests and calcium (Ca) corrosion tests were conducted.

Electrochemical measurements were performed at RT using a BioLogic VMP3 Multichannel Potentiostat in a three-electrode cell (1 L) containing 3.5 wt% NaCl aqueous solution, in accordance with ASTM G5-14, as previously described in Section 3.2.4. The reference electrode was a KCl-saturated Ag/AgCl (Biologic REF201 Red Rod), and a graphite rod served as the counter electrode.

For the working electrode assembly, a cylindrical S355 structural steel substrate coated with PIB or PIB:*h*-BN film was drilled and tapped (3-48 UNC thread) for secure attachment to the support rod. The films were produced by doctor blading the respective resins, followed by drying for 1 h at RT and then 15 h at 60 °C to eliminate residual solvents. Film thickness was approximately 60 µm, measured with a Trotec BB20 magnetic-induction thickness gauge. A Teflon compression gasket was used to ensure a leak-free seal. Open-circuit potential was tracked for 30 min, after which the corrosion behavior was assessed by means of potentiodynamic anodic polarization and Tafel analysis, per ASTM G5-14. This analysis determined i_{corr} and E_{corr}.[414,415] The corrosion rate (mm yr^{-1}) was derived from the measured i_{corr} by applying Faraday's law:

$$CR = \frac{K \cdot W_{eq} \cdot i_{corr}}{D} \tag{4.1}$$

where $K = 3.27 \cdot 10^{-3}$, $W_{eq} = 27.9$ g eq^{-1} (equivalent weight of iron in ferrous compounds), i_{corr} is in µA cm^{-2}, and $D = 7.85$ g cm^{-3} (steel density).[417] The corrosion inhibition efficiency of the composites was calculated from i_{corr} using:

$$\eta_p\% = \frac{i^0_{corr} - i_{corr}}{i^0_{corr}} \tag{4.2}$$

where i^0_{corr} and i_{corr} are the corrosion current densities in the absence and presence of inhibitors, respectively.[418]

Ca corrosion tests were conducted on samples prepared by depositing a Ca film onto etched FTO-coated glass substrates (25 mm × 25 mm). These were subsequently laminated onto glass substrates coated with the encapsulants using a heated press at ~100-150 °C in an N_2-filled glove box. Figure 4.4c,d illustrates the layout of the sample configuration. The FTO layer was etched over a central 25 mm × 5 mm strip. A Ca film (5 mm × 15 mm) was thermally evaporated to cover part of the FTO-etched region as well as an adjacent FTO-coated region, the latter serving as an electrical contact. The Ca film was then sealed under the encapsulant (25 mm × 18 mm). The water-vapor transmission rate across the encapsulants was determined via electrical (quantitative)[519] and optical (qualitative)[520] evaluations of Ca corrosion.

Thermal management capabilities were assessed by monitoring the maximum temperature of glass/encapsulant/glass assemblies using a FLIR A655sc thermal camera positioned ~50 cm from the sample. Samples were fabricated through a lamination protocol analogous to that employed for PSC and PSM encapsulation (see subsequent details). Following heating at 90 °C on a hot plate with a lid, the samples were transferred to an aluminum platform at 25 °C, and their temperature was tracked

during cooling. The thermal camera was operated and the data processed using FLIR ResearchIR Max software.

Section 4.2.4 Perovskite solar cells and modules fabrication

Mesoscopic n-i-p PSCs

Mesoscopic PSCs (active area: 1 cm^2) were fabricated on FTO-coated glass substrates (25 mm × 25 mm). The FTO layer was first patterned by laser etching with an Nd:YVO_4 pulsed UV laser system (BrightSolutions, Luce 40) to electrically separate the photoelectrode from the counter electrode. The substrates were then cleaned by gently brushing with a 2:98 vol/vol Hellmanex:water solution, followed by ultrasonic treatment in acetone and IPA (10 minutes each) and air drying. Any residual organic contaminants were removed by UV/O_3 treatment in a PSD Pro Series Digital UV Ozone System (Novascan).

A compact TiO_2 (*c*-TiO_2) layer was deposited onto the patterned FTO via spray pyrolysis. A dispersion of 0.16 M $Ti(AcAc)_2$ and 0.4 M AcAc in EtOH was sprayed at 465 °C, using air (1.6 bar) as the carrier gas. The nozzle was oriented at 45° relative to the substrate and moved in a serpentine path for 12–13 cycles (one every 10 s), yielding a ~50 nm-thick layer (as determined by profilometry with a Deektak Veeco 150). The substrates were held at 465 °C for 15 minutes, then slowly cooled to RT.

A mesoporous TiO_2 (*m*-TiO_2) layer was formed by diluting 30NR-D TiO_2 paste in anhydrous EtOH (1:5 w/w). After stirring overnight (>12 h), 1 vol% of a graphene dispersion in EtOH was added to this diluted TiO_2 paste.[190] A 120 µL aliquot of this paste was spin-coated onto the c-TiO_2 at 3000 rpm for 30 s (acceleration 1500 rpm s^{-1}). The resulting layer was sintered via a multi-step program: (1) ramp from RT to 150 °C over 5 min, 5 min dwell; (2) ramp from 120 to 325 °C over 15 min, 5 min dwell; (3) ramp from 325 to 375 °C over 5 min, 5 min dwell; (4) ramp from 375 to 490 °C over 15 min, 30 min dwell. To improve wetting properties, the graphene-containing *m*-TiO_2 was subjected to UV treatment for 30 min using 5000-EC UV curing lamps (Dymax). The substrates were then transferred into a N_2-filled glove box.

The perovskite precursor solution – comprising FAI (1 M), PbI_2 (1.2 M), $PbBr_2$ (0.2 M), CsI (0.1 M), and MABr (0.2 M) dissolved in a 1:4 vol/vol DMF:DMSO mixture – was prepared to yield a $Cs_{0.08}FA_{0.80}MA_{0.12}Pb(I_{0.88}Br_{0.12})_3$ composition. After overnight stirring, 90 µL of this solution was spin-coated using a two-step program: (1) 2000 rpm, 10 s, acceleration 400 rpm s^{-1}; (2) 5000 rpm, 20 s, acceleration 2000 rpm s^{-1}. Fifteen seconds before the end of the program, 100 µL of chlorobenzene was added as an antisolvent to induce perovskite nucleation. The substrates were then annealed at 100 °C for 45 min. A thin perovskite-passivating PEAI layer was deposited by spin-coating 100 µL

of a 5 mg mL^{-1} PEAI solution in IPA at 2500 rpm for 30 s (acceleration 1250 rpm s^{-1}) and annealing at 100 °C for 10 min.

The HTL was then deposited. A poly[bis(4-phenyl)(2,4,6-trimethylphenyl)amine] (PTAA) solution in toluene (10 mg mL^{-1}), doped with 7 µL mL^{-1} of tBP and 10 µL mL^{-1} of a LiTFSI stock solution in ACN (170 mg mL^{-1}), was spun at 3000 rpm for 20 s (acceleration 1500 rpm s^{-1}). Alternatively, 2,2′,7,7′-tetrakis[N,N-di(4-methoxyphenyl)amino]-9,9′-spirobifluorene (spiro-OMeTAD) was employed by spin-coating 90 µL of a 73.5 mg mL^{-1} spiro-OMeTAD solution in CB, doped with tBP (26.8 µL mL^{-1}), LiTFSI (16.6 µL mL^{-1}; from a 520 mg mL^{-1} stock in ACN), and FK209 Co(III) TFSI (7.2 µL mL^{-1}), at 4000 rpm for 1 min (acceleration 1000 rpm s^{-1}). Finally, a 100 nm-thick gold (Au) electrode was thermally evaporated in a high-vacuum chamber (~10^{-6} mbar).

Planar n-i-p PSCs

Planar n-i-p PSCs (active area: 1 cm^2) were fabricated following the same procedure as the mesoscopic devices, except for the ETL. Here, 100 µL of a 15% SnO_2 aqueous dispersion was spin-coated onto the FTO (UV-treated for 30 min) at 6000 rpm for 35 s (acceleration 3000 rpm s^{-1}). The substrates were then annealed at 150 °C for 1 h, forming a SnO_2 layer ~70-80 nm thick.

Inverted p-i-n PSCs

Inverted p-i-n PSCs were fabricated on ITO-coated glass substrates patterned by an Nd:YVO_4 pulsed UV laser (BrightSolutions, Luce 40), then cut into 25 mm × 25 mm pieces. The patterned samples underwent sequential ultrasonic cleaning (15 min each) in diluted Hellmanex (2:98 vol/vol), acetone, and IPA, followed by air drying. After a 15 min UV/ozone treatment (PSD Pro Series Digital UV Ozone System, Novascan), the samples were transferred to a N_2-filled glove box.

A PTAA solution (2 mg mL^{-1} in toluene) was spin-coated at 5000 rpm for 20 s and annealed at 100 °C for 10 min. After cooling, a film containing PbI_2 and CsBr (10:1 ratio) was thermally co-evaporated onto the substrates. A solution of FAI (0.48 M), MABr (0.09 M), and MACl (0.09 M) in EtOH was then spin-coated in a flow box under dry air (RH < 10%). The resulting films were annealed in air (RH 30-40%) at 150 °C for 15 min. Next, PEACl (1.5 mg mL^{-1} in EtOH) was spun at 4000 rpm, followed by annealing at 100 °C for 10 min. A PCBM solution (27 mg mL^{-1} in 3:1 CB:DCB) was deposited at 1350 rpm for 20 s and annealed at 100 °C for 5 min. BCP (0.5 mg mL^{-1} in IPA) was spin-coated at 2300 rpm for 20 s without further thermal drying. A 100 nm-thick copper (Cu) layer was thermally evaporated through a shadow mask to form the top electrode.

Semi-transparent PSCs

Semi-transparent PSCs (active area: 1 cm^2) were fabricated by first depositing the *c*-TiO_2 layer on FTO-coated glass as described for mesoscopic devices. Before the perovskite deposition, the samples were treated under UV light for 10 min. In an N_2 atmosphere, 80 µL of a 1 M FaBr and 1 M $PbBr_2$ solution in DMSO was spin-coated onto the 60 °C-preheated substrates at 4000 rpm for 20 s (acceleration 2000 rpm s^{-1}). After 10 s of spinning, 200 µL of anhydrous ethyl acetate was dropped to induce $FaPbBr_3$ crystallization, followed by annealing at 85 °C for 10 min.

Once cooled to RT, 90 µL of a PTAA solution in toluene (10 mg mL^{-1}), doped with 10 µL mL^{-1} of tBP and 5 µL mL^{-1} of a LiTFSI solution in ACN (170 mg mL^{-1}), was spin-coated using the same parameters as for the perovskite. Afterwards, a 200 nm-thick ITO top electrode was sputtered at low temperature (KENOSISTEC S.R.L., KS 400 In-Line) at $1.1 \cdot 10^{-3}$ mbar and 90 W RF power with 40 sccm of Ar flow. The samples were passed under the ITO target 200 times at a speed of 120 cm min^{-1}, achieving a sheet resistance of 25 Ω sq^{-1} (verified by a four-probe unit in the Arkeo Platform, Cicci Research S.r.L.).

Mesoscopic PSMs

Mesoscopic PSMs were fabricated similarly to mesoscopic PSCs, except for the amounts of solutions and the three additional laser ablation steps (P1, P2, P3) required to define a series-connected layout with an active area of 10 cm^2 (five cells of 2 cm^2 each).[521] The FTO substrate measured 56 mm × 56 mm. The volumes of the *m*-TiO_2 solution, perovskite precursor, CB (antisolvent), PEAI solution, and PTAA solution were 600 µL, 450 µL, 400 µL, 450 µL, and 500 µL, respectively, for each module.

- **P1** patterned the FTO for isolating the five cells (width = 20 µm; cell spacing = 0.5 mm; cell width = 5 mm; cell length = 40 mm).
- **P2** cleaned the FTO interconnection areas after depositing PTAA (width = 160 µm).
- **P3** defined inter-cell isolation after thermal evaporation of 100 nm Au (width = 90 µm).

These processes yield a geometric fill factor of ~91%.[522] Silver busbars (width = 4 mm) were screen-printed near the substrate edges (2 mm from each edge), parallel to the long side of the cells. The busbars were dried on a hot plate at 120 °C for 10 min, then sintered during c-TiO_2 deposition.

Section 4.2.5 Perovskite solar cells and modules lamination

Both PSCs and PSMs were encapsulated by a multi-step differential-pressure lamination process at low temperature (90 °C), using an automated two-chamber solar panel laminator (CORE – Model 2,

Rise Technology srl). This system includes a cooling feature to ensure high reproducibility of the lamination procedure and to minimize the materials' exposure time at temperatures that could cause degradation. Specifically, the entire device surface was covered with the PIB- or PIB:*h*-BN-coated glass, achieving glass/pressure-tight polymer/glass encapsulation (*i.e.*, a blanket-cover approach). The assembled laminates were placed in the lower chamber of the laminator, which applied the differential pressure between the upper and lower chambers.

Once sealed, both chambers were evacuated to a moderate vacuum (~1 mbar), while the laminate temperature was raised from RT to 50 °C over 215 s (~7 °C min^{-1}). The upper chamber was then pressurized to attain a final pressure of 30 mbar on top of the substrates, requiring 500 s for stabilization. Next, the laminate temperature was increased from 50 to 90 °C over 500 s (4.8 °C min^{-1}) and held at 90 °C for 600 s. The laminate was subsequently cooled back to 50 °C over 500 s (4.8 °C min^{-1}). (5) Lastly, the chamber pressure was restored to 1000 mbar in approximately 1 s, and the laminator was opened to retrieve the encapsulated devices.

Section 4.2.6 Device characterization

J-V measurements were conducted on a Class-A Sun Simulator (ABET 2000) with an AM1.5 G filter (ABET). The simulator was calibrated to 1 Sun illumination using a silicon-based reference cell (RR-226-O, RERA Solutions). All J-V data were acquired under both forward and reverse voltage scans using the Arkeo platform (Cicci Research S.r.l.), with a voltage step of 20 mV s^{-1} and a scanning rate of 200 mV s^{-1}.

A Shimadzu UV-2550 spectrophotometer equipped with an integrating sphere was used to record transmittance spectra for encapsulant optical characterization in both Ca tests and semi-transparent device assessments. During the calcium test, the sheet resistance of the Ca films was monitored via a four-probe measurement using a Keithley 2620 source meter (Tektronix). The average visible transmittance (AVT) of semi-transparent PSCs was calculated in accordance with ISO 9050:2003, based on the following equation:

$$AVT = \frac{\int_{380}^{780} D(\lambda) \cdot T(\lambda) \cdot V(\lambda) d\lambda}{\int_{380}^{780} D(\lambda) \cdot V(\lambda) d\lambda} \tag{4.3}$$

where $D(\lambda)$ is the incident light spectrum, $V(\lambda)$ is the human eye sensitivity factor, and $T(\lambda)$ is the transmittance.

ISOS-L-1 testing was carried out in air using an Arkeo-multichannel system (Cicci Research S.r.l.) featuring 32 fully independent source meter units (±10 V at ±250 mA) and a low-mismatch LED-

based ARKEO light soaker (VIS version, 400-750 nm). A standard Perturb & Observe algorithm was employed to track the maximum power point, with a full J-V scan recorded every 4 min.

ISOS-D-2 testing was performed in a Lenton WHT4/30 oven (Hope Valley). For thermal shock evaluation, the samples were cycled between -40 °C and +85 °C with abrupt transitions from RT to +85 °C and from RT to -40 °C. After 200 cycles, a modified humidity freeze test was conducted by subjecting the devices to 10 additional thermal shock cycles (-40 °C to +85 °C), each beginning with immersion in water at RT. A Lenton WHT4/30 oven and a domestic freezer were used to maintain the +85 °C and -40 °C conditions, respectively.

Inductively coupled plasma optical emission spectroscopy (ICP-OES) analyses were conducted on a ThermoFisher iCAP 7600 DUO spectrometer to determine Pb leakage in the modules submerged in water. Samples of the water solution were collected at various intervals over a total immersion time of 24 h.

Section 4.3 Protective performance

Two types of encapsulants were prepared for the encapsulation of PSCs and PSMs, as described in Section 4.2. The first encapsulant consists of a highly viscous, low-molecular-weight (95000) PIB liquid at RT, whereas the second one is an opaque composite of the same PIB and 2D *h*-BN flakes. The 2D *h*-BN flakes were produced via WJM exfoliation of bulk *h*-BN crystals, as reported in Chapter 2.[177,344,348]

Despite its amorphous, semi-solid/liquid nature in the -40/+85 °C temperature range, the selected PIB homopolymer displays tightly packed molecular chains, imparting high barrier properties.[348,523] In addition, PIB has a resistivity of ~10^{16} Ω cm, exceeding that of EVA (10^{13}-10^{15} Ω cm),[494] which can potentially confer resistance to induced degradation.[494,524] Previous studies and the results reported in Chapter 3 have shown that incorporating 2D *h*-BN flakes into the PIB matrix effectively enhances its barrier properties against water and other corrosive species.[348,391] This improvement is generally attributed to the high-specific surface area of 2D *h*-BN (*e.g.*, 1488 m^2 g^{-1} for monolayer *h*-BN),[525] its hydrophobic nature,[526] and the delocalized dense cloud of overlapping π-orbitals in the *h*-BN structure, which serves as a physical barrier preventing molecular or ionic penetration.[527] Furthermore, 2D *h*-BN flakes exhibit excellent thermal conductivity (>700 W m^{-1} K^{-1} for monolayer *h*-BN and >100 W m^{-1} K^{-1} for few-/multi-layer *h*-BN),[528,529] thereby improving the thermal management properties of polymers used as matrices or binders.[495]

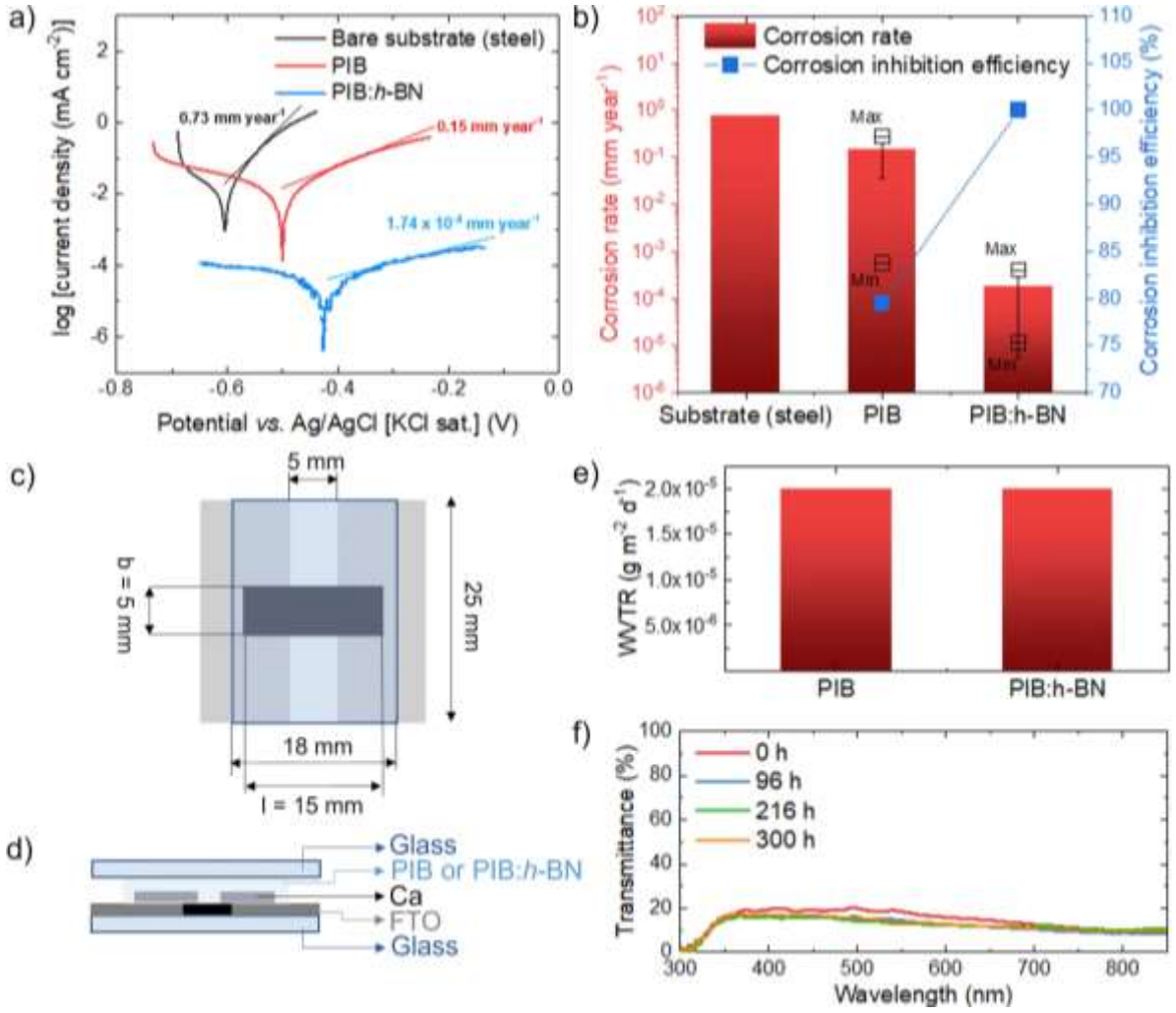

*Figure 4.4 (a) Anodic polarization curves (Tafel plots) of steel protected by PIB (LMW-80) and PIB:*h*-BN encapsulants (data acquired for the samples showing the highest corrosion rate among different replicas). The Tafel plot measured for bare steel is also shown for comparison. (b) Statistical analysis of the corrosion rates of the investigated systems and average corrosion inhibition efficiencies of the encapsulants. (c), (d) Schematics (top-view and cross-section, respectively) of the sample configuration used for the Ca test. (e) WVTR measured through the encapsulants in the glass/pressure-tight polymer/glass encapsulation systems through the Ca test.(f) UV-vis transmittance spectra of the samples measured through the Ca film at different times of environmental exposure.*[192]

On the basis of the work presented in Chapter 3, the barrier properties of the low-molecular-weight semi-solid/liquid PIB proposed in this study were first evaluated using electrochemical methods. Figure 4.4a presents the potentiodynamic anodic polarization curves and Tafel analyses for representative PIB- and PIB:*h*-BN-coated steels immersed in 3.5 wt.% NaCl solution (bare steel served as a reference). These measurements were performed according to ASTM G5-14, as described in Section 4.2. Both PIB and PIB:*h*-BN films significantly reduced the corrosion rate (from $7.3 \cdot 10^{-1}$ mm year^{-1} for uncoated steel to $1.5 \cdot 10^{-1}$ mm year^{-1} and $1.7 \cdot 10^{-4}$ mm year^{-1} for PIB- and PIB:*h*-BN-coated steels, respectively, as shown in Figure 4.4b). Notably, the presence of 2D *h*-BN flakes in the PIB matrix enhanced both the anticorrosion efficiency and the reproducibility of PIB films, as

evidenced by minimal corrosion rates of $5.6 \cdot 10^{-4}$ mm year^{-1} (PIB) and $1.2 \cdot 10^{-5}$ mm year^{-1} (PIB:*h*-BN). Overall, PIB:*h*-BN films exhibited superior barrier properties (average corrosion inhibition efficiency = 99.97%) compared to homopolymer PIB (79.53%). This behavior mirrors that of homopolymer and composite films prepared with high-molecular-weight PIB (see Chapter 3) and is attributed to the additional hydrophobicity conferred by 2D *h*-BN flakes (water contact angles of 88.3° ± 0.4° and 97.9° ± 0.4° for solid PIB and PIB:*h*-BN films, respectively, as reported in Section 3.3).[348]

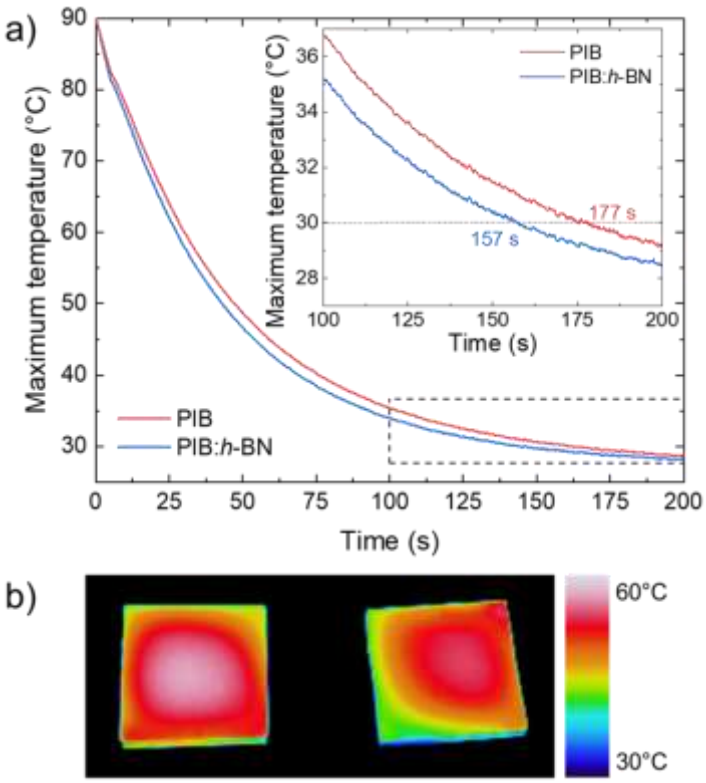

*Figure 4.5 (a) Maximum temperature over time measured for the glass/PIB/glass and glass/PIB:*h*-BN/glass systems (area = 56 mm × 56 mm) first heated at 90°C (t = 0 s) and then transferred to an Al platform at 25°C. The internal panel shows the magnification of the figure in the 100-200 s time interval. (b) Infrared thermal images of glass/PIB/glass (left) and glass/PIB:*h*-BN/glass (right) systems acquired after 60 s of cooling.*[192]

The WVTR of the proposed encapsulants was determined using a glass/pressure-tight polymer/glass configuration in a calcium corrosion test (Ca test)[519,530] (Figure 4.4c,d). This setup simulates the encapsulation concept (blanket-cover approach) employed for PSCs and PSMs, where moisture can only penetrate from the device edges through the encapsulant,[520] rather than through the glass. Both the PIB- and PIB:*h*-BN-based encapsulants displayed a WVTR of approximately $2 \cdot 10^{-5}$ g m^{-2} d^{-1} (Figure 4.4e). The nearly unchanged UV-vis transmittance spectra of the encapsulated Ca films over 15 days confirmed negligible Ca oxidation and, thus, negligible moisture ingress (Figure 4.4f).

The influence of 2D *h*-BN flakes on thermal management was evaluated via infrared thermal imaging of glass/PIB/glass and glass/PIB:*h*-BN/glass laminates (56 mm × 56 mm). These samples were produced using the same lamination protocol adopted for encapsulating PSCs and PSMs (see Section 4.2). After heating to 90 °C and quickly transferring onto a 25 °C aluminum platform, the maximum sample temperature was recorded over time using an infrared camera. As shown in Figure 4.5, incorporating 2D *h*-BN flakes facilitated heat dissipation compared to bare PIB, reducing by 11.2% the time required to cool to 30 °C.

Section 4.4 Characterization of encapsulated PSCs

The encapsulants were initially evaluated in mesoscopic n-i-p PSCs (active area = 1 cm^2) based on the $Cs_{0.08}FA_{0.80}MA_{0.12}Pb(I_{0.88}Br_{0.12})_3$ perovskite and a PTAA HTL, following ISOS-D-2 (at 85 °C) and ISOS-L-1 protocols (after 240 h of ISOS-D-1 preconditioning).[531] PTAA was chosen because of its superior thermal stability compared to other common HTLs, such as spiro-OMeTAD, which is used in state-of-the-art PSCs.[532] In addition, this specific perovskite composition and the overall cell architecture were selected because of the high PCE demonstrated at the module/farm scale.[190]

The device structure was FTO/*c*-TiO_2/graphene-incorporating *m*-TiO_2/ $Cs_{0.08}FA_{0.80}MA_{0.12}Pb(I_{0.88}Br_{0.12})_3$/PEAI/PTAA/Au (Figure 4.6a), as described in Section 4.2. Graphene was introduced into the *m*-TiO_2 to enhance electron extraction in the mesoscopic ETL[189,190,533,534] and to improve the stability of MA-based perovskites.[535] Furthermore, PEAI was employed as an ultrathin perovskite passivation layer, as shown in previous works.[536,537] Figure 4.6b illustrates the cell layout, designed such that the encapsulant entirely covers all non-compact layers while two flat metallic ribbons (commercial tape-like charge collectors) provide external electrical contacts. The encapsulants were then applied using an industrially compatible, high-throughput lamination protocol (total duration <45 min; see Section 4.2). Figure 4.6c displays a photograph of a representative device encapsulated with PIB:*h*-BN, while Figure 4.6d presents the J-V curves (reverse voltage scan) of a representative PSC before and after encapsulation with PIB:*h*-BN; the J-V curve obtained after the 240 h ISOS-D-1 preconditioning (prior to the ISOS-D-2 test) is also included.

The as-prepared mesoscopic n-i-p PSCs employing PTAA HTLs reach PCEs of up to ~18.8%. Although this value is lower than the record certified PCE achieved on small-area devices (26.1% on 0.057127 cm^2),[465,466] it is significant for PSCs with a 1 cm^2 active area – whose record certified PCE of 21.6% has remained unchallenged since 2019.[538] A recent report indicates a record PCE of 24.35% for a 1.007 cm^2 device by the NUS/SERIS group,[466] but further details are not yet disclosed.[538] As demonstrated below, either mesoscopic n-i-p architectures incorporating spiro-OMeTAD HTLs or

planar n-i-p geometries can further improve the PCE of our PTAA-based mesoscopic n-i-p PSCs, achieving maximum PCEs of ~20.2% (for spiro-OMeTAD-based mesoscopic n-i-p PSCs) and therefore moving closer to record certified PCEs for large-area PSCs.

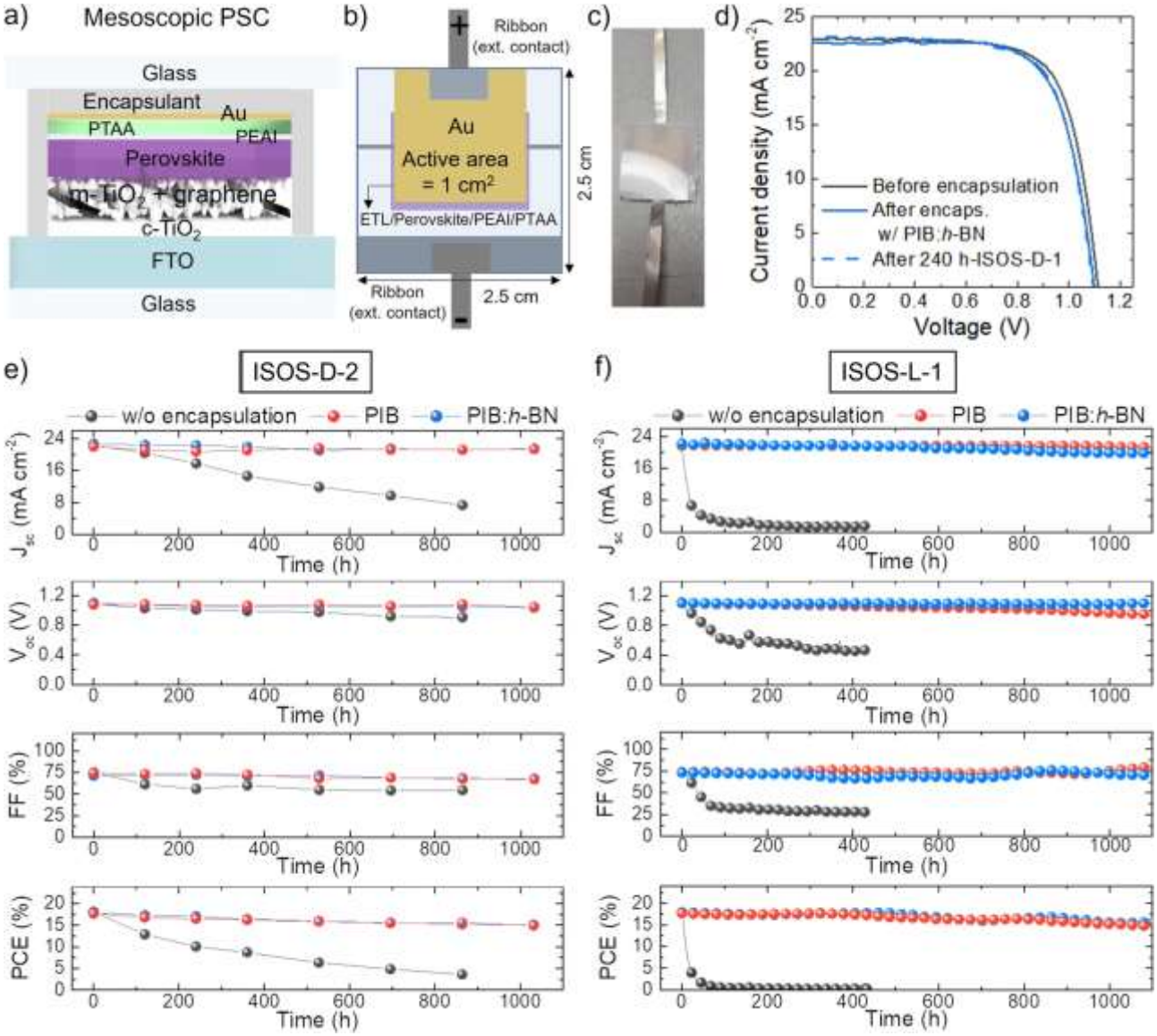

Figure 4.6 (a) Sketch of the structure of the mesoscopic n-i-p PSCs based on $Cs_{0.08}FA_{0.80}MA_{0.12}Pb(I_{0.88}Br_{0.12})_3$ *perovskites and PTAA HTLs. (b) Schematic of the cell layout (active area = 1 cm²), in which the non-compact layers of the device are fully covered by the encapsulant. Two flat metallic ribbons are connected to the cell terminals to bring the electrical contacts externally. (c) Photograph of a representative mesoscopic PSC encapsulated with PIB:*h-*BN. (d) J-V curves (reverse voltage scan) measured for a representative mesoscopic PSC before and after encapsulation with PIB:*h-*BN (before and after 240 h-ISOS-D1). (e), (f) PV parameters of the mesoscopic PSCs without encapsulation and with PIB and PIB:*h-*BN encapsulants, acquired over >1000 h of ISOS-D-2 and ISOS-L-1 tests.*[192]

Upon encapsulation, the lamination process had only a minor impact on cell performance (absolute PCE drop <1%, irrespective of the encapsulant type). During the ISOS-D-1 test (*i.e.*, dark storage at ambient temperature and RH) over 240 h, the devices preserved their performance (absolute PCE

drop <1%), confirming their shelf-life stability. Subsequently, the cells were subjected to ISOS-D-2 and ISOS-L-1 tests, and their PV parameters were tracked for more than 1000 h. As illustrated in Figure 4.6e,f, unencapsulated devices degraded rapidly in both aging tests, showing a T_{80} (time to reach 80% of the initial PCE, extracted from multi-order polynomial fitting with $R^2 > 0.999$) of <70 h under ISOS-D-2 and <5 h under ISOS-L-1. Conversely, all encapsulated devices exhibited T_{80} values >1000 h, regardless of the encapsulant. Crucially, this high stability was achieved without the use of edge sealants, demonstrating the excellent barrier properties of the studied primary encapsulants under operational conditions. Moreover, stability was retained in the presence of interconnection ribbons, underscoring the practical reliability of these encapsulants for ribbon-interconnected PV modules. Finally, although interconnected ribbons may complicate lamination in small-area cells, the highly viscous liquid encapsulants effectively dissipated thermomechanical stress, resulting in a strain-free encapsulation process.

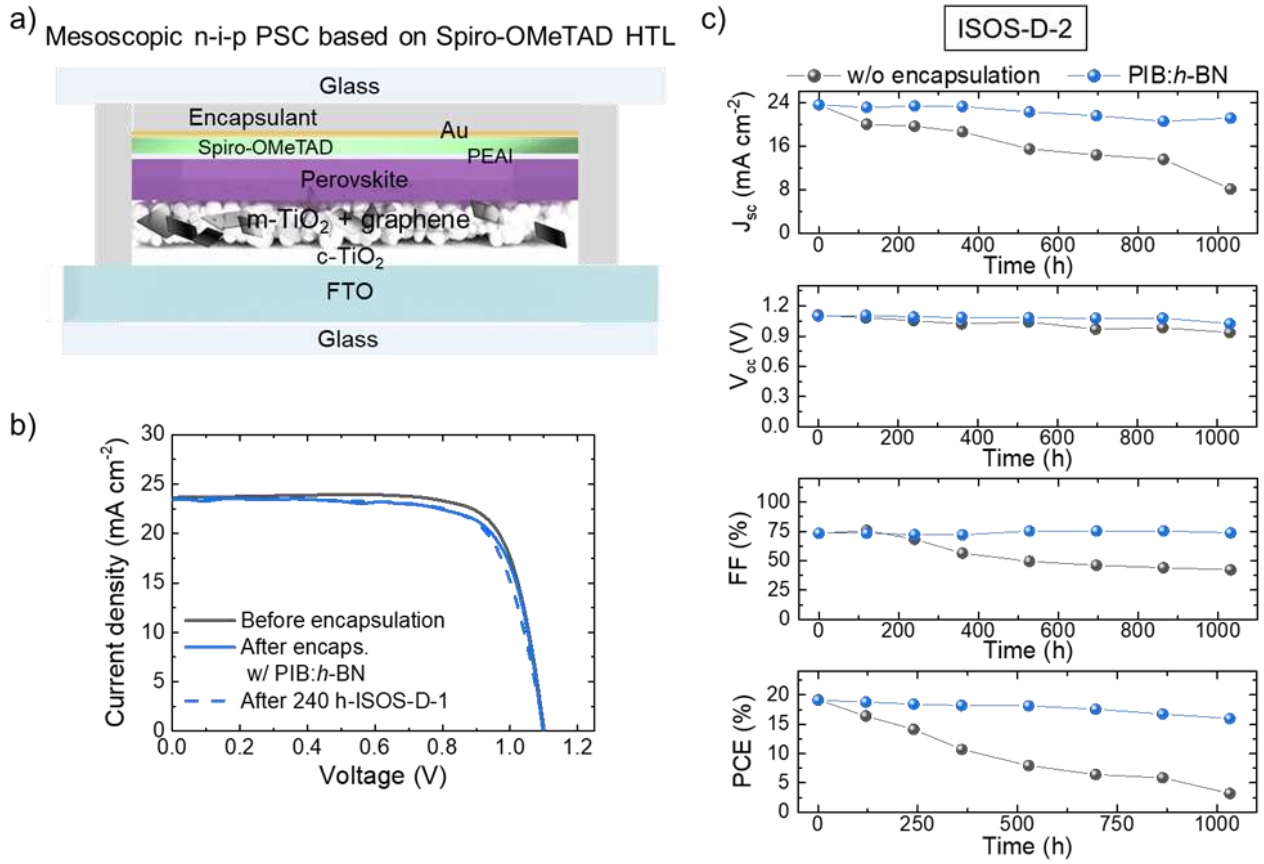

Figure 4.7 (a) Sketch of the structure of the large-area (1 cm²) mesoscopic n-i-p PSCs based on $Cs_{0.08}FA_{0.80}MA_{0.12}Pb(I_{0.88}Br_{0.12})_3$ *perovskites and spiro-OMeTAD HTLs. (b) J-V curves measured for the as-fabricated mesoscopic n-i-p PSCs based on spiro-OMeTAD HTLs before and after encapsulation with PIB:*h*-BN (before and after 240 h-ISOS-D-1). (c) PV parameters of the investigated mesoscopic n-i-p PSCs based on spiro-OMeTAD HTLs acquired over >1000 h of ISOS-D-2 test.*[192]

As previously discussed, the encapsulation protocol was also evaluated in mesoscopic n-i-p PSCs employing spiro-OMeTAD, thereby confirming that this lamination procedure is compatible with HTLs that are more temperature-sensitive than PTAA. As illustrated in Figure 4.7, the application of the PIB:*h*-BN encapsulant minimally impacts device performance (absolute PCE drop <1%), consistently with the results obtained for PTAA-based mesoscopic n-i-p PSCs (see Figure 4.6d). Subsequently, a 240 h ISOS-D-1 test verified the shelf-life stability of the examined cells. During the ISOS-D-2 test, the unencapsulated device underwent rapid degradation (T_{80} < 240 h), while the encapsulated cells exhibited excellent stability (T_{80} > 1000 h).

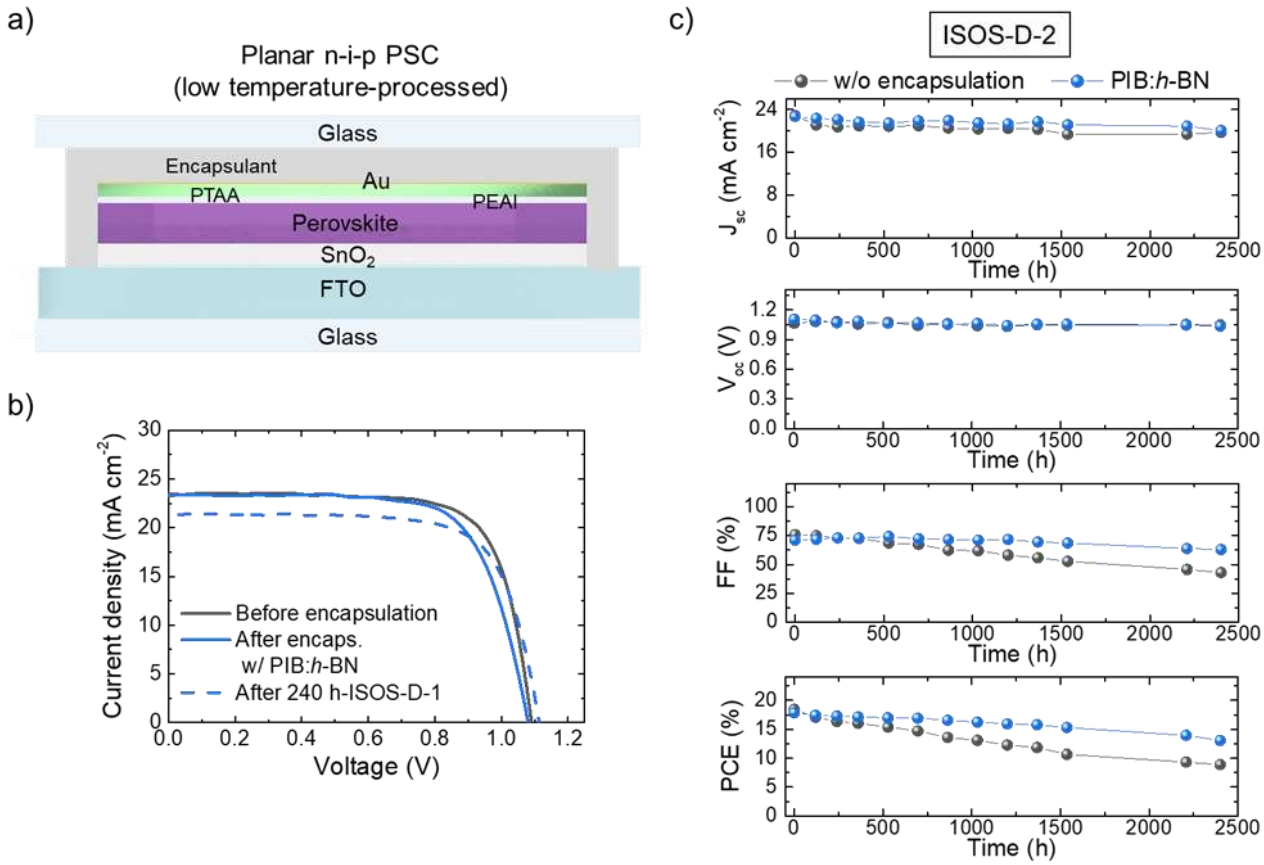

*Figure 4.8 (a) Sketch of the structure of the low temperature-processed large-area (1 cm^2) planar n-i-p PSCs based on $Cs_{0.08}FA_{0.80}MA_{0.12}Pb(I_{0.88}Br_{0.12})_3$ perovskites. (b) J-V curves measured for the as-fabricated planar n-i-p PSCs before and after encapsulation with PIB:*h*-BN (before and after 240 h-ISOS-D-1). (c) PV parameters of the investigated planar n-i-p PSCs acquired over >2000 h of ISOS-D-2 test.*[192]

In general, the hygroscopic character of LiTFSI and the volatility of tBP, which are used to dope spiro-OMeTAD, facilitate the ingress of moisture and induce morphological changes in both the perovskite and spiro-OMeTAD layers.[532] These processes become more pronounced at elevated temperatures, promoting the formation of pinholes that accelerate iodine migration toward iodine-sensitive device components (*e.g.*, metal electrodes) and can create direct connections between charge-transporting layers (leading to shunting pathways), ultimately causing PCE losses.[532] In this

regard, these results suggest that combining advanced PIB-based encapsulants – which mitigate moisture intrusion – with ultrathin perovskite passivation layers (*e.g.*, PEAI) is a viable route to preserve the stability of spiro-OMeTAD-based PSCs under high-temperature conditions. Specifically, PEAI effectively passivates defects and trap states at the perovskite/spiro-OMeTAD interface,[539] enabling these spiro-OMeTAD-based devices to endure lamination at 90 °C for 10 min. Nonetheless, the reported data confirm that reliable encapsulants providing robust protection against air/moisture ingress are essential to prevent the oxidation-induced degradation of doped spiro-OMeTAD.[540] These findings align with previous reports on the excellent thermal stability of spiro-OMeTAD-based PSCs.[541–543]

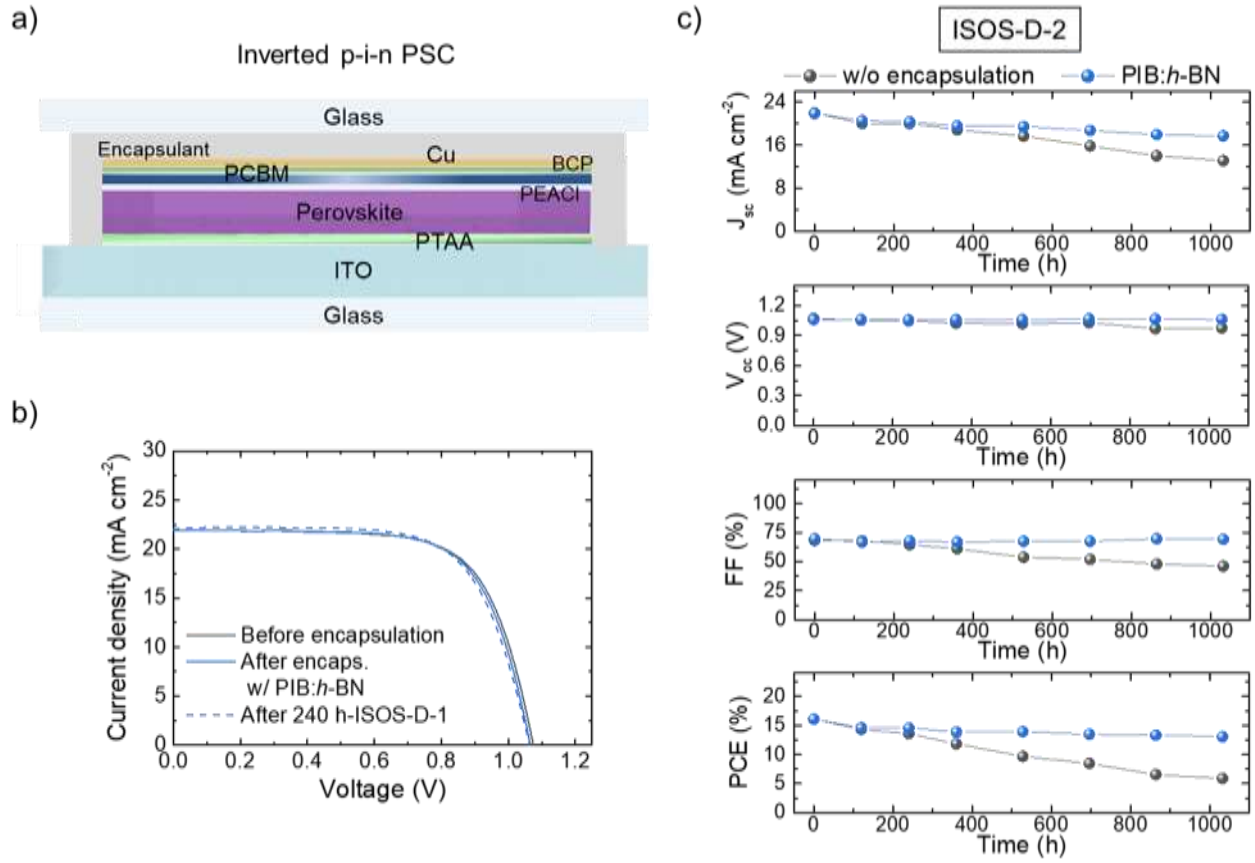

*Figure 4.9 (a) Sketch of the structure of the large-area (1 cm^2) inverted p-i-n PSCs based on PTAA HTLs and PCBM ETLs. (b) J-V curves measured for the as-fabricated inverted p-i-n PSCs before and after encapsulation with PIB:*h*-BN (before and after 240 h-ISOS-D-1). (c) PV parameters of the investigated inverted p-i-n PSCs acquired over >1000 h of ISOS-D-2 test.*[192]

The efficacy of PIB:*h*-BN encapsulants was further demonstrated using 1 cm^2-active-area planar n-i-p PSCs incorporating low-temperature-processed SnO_2 as the ETL. As presented in Figure 4.8, the as-fabricated devices attained a maximum PCE of ~19.0%. Following encapsulation with PIB:*h*-BN, the cells achieved $T_{80} \approx 2000$ h during ISOS-D-2 testing, whereas the unencapsulated counterparts exhibited a shorter T_{80} of ~700 h. Although substituting TiO_2 with SnO_2 in planar PSCs can eliminate

the photo-induced degradation typically associated with TiO_2-based mesoscopic structures,[472,473] planar architectures still exhibit lower reproducibility at the module scale than mesoscopic devices. The latter have recently been integrated with PTAA-based HTLs into a 4.5 m^2 stand-alone solar farm infrastructure[190,544] and were therefore chosen for the fabrication of the PSMs described herein.

Finally, the versatility of the encapsulation methodology reported in this work was validated in 1 cm^2-active-area inverted (p-i-n) configurations that employ PTAA as the HTL and PCBM as the ETL. In these cells, the PEACl long-chain alkylammonium salt was used for perovskite surface treatment to simultaneously passivate the grain boundaries and the perovskite/PCBM interface.[545] As shown in Figure 4.9, these devices maintained their performance following PIB:*h*-BN encapsulation, demonstrating T_{80} > 1000 h during ISOS-D-2 testing. In contrast, the unencapsulated cells showed T_{80} < 360 h.

Section 4.5 Validation of the encapsulant in PSMs

The PIB and PIB:*h*-BN encapsulants were subsequently evaluated in mesoscopic n-i-p PSMs based on PTAA HTLs. These modules consisted of five series-connected cells, each with an active area of 2 cm^2, for a total active area of 10 cm^2, as described in Section 4.2. Figure 4.10a presents the layout of the encapsulated mesoscopic n-i-p PSMs. The encapsulants were applied following the same lamination protocols used for PSCs, ensuring complete coverage of the porous layers of the module structure. As in the case of PSCs, no edge sealants were employed alongside the primary encapsulants. The PSMs were specifically designed to avoid the need for metallic ribbons to contact the positive and negative module terminals; instead, two silver busbars were printed along the module edges, extending beyond the encapsulant. Consequently, unlike the case of PSCs, thermomechanical stress from the presence of the ribbon (during both encapsulation and operation) was eliminated. Figure 4.10b,c show photographs of a representative PSM before encapsulation (front and rear sides) and after encapsulation (rear side) with PIB:*h*-BN. Figure 4.10d displays the J-V curves (reverse voltage scan) of two representative PSMs before and after encapsulation with PIB and PIB:*h*-BN, respectively; these curves also include measurements taken after a 240 h ISOS-D-1 test performed prior to subsequent aging.

The PSMs prepared in this work achieved a maximum PCE of 17%, a value pertinent for module configurations validated at solar farm level,[190] where material scalability and reproducibility must be assured alongside high manufacturing yields. Prospectively, this encapsulant approach can also be evaluated on more efficient PSM configurations, which now demonstrate record PCE values up to 19.9% on a 10 cm^2 active area.[547] As with the PSCs, the encapsulation process had only a minor

impact on overall module performance (absolute PCE drop <1%), which remained stable over 240 h of ISOS-D-1 testing (absolute PCE drop <1%) regardless of the encapsulant. By contrast, unencapsulated PSMs degraded rapidly under ISOS-D-2 and ISOS-L-1 tests (Figure 4.10e,f), showing T80 <100 h and <3 h, respectively, consistent with the instability observed in unencapsulated PSCs. In contrast, the encapsulated PSMs exhibited T80 >1000 h.

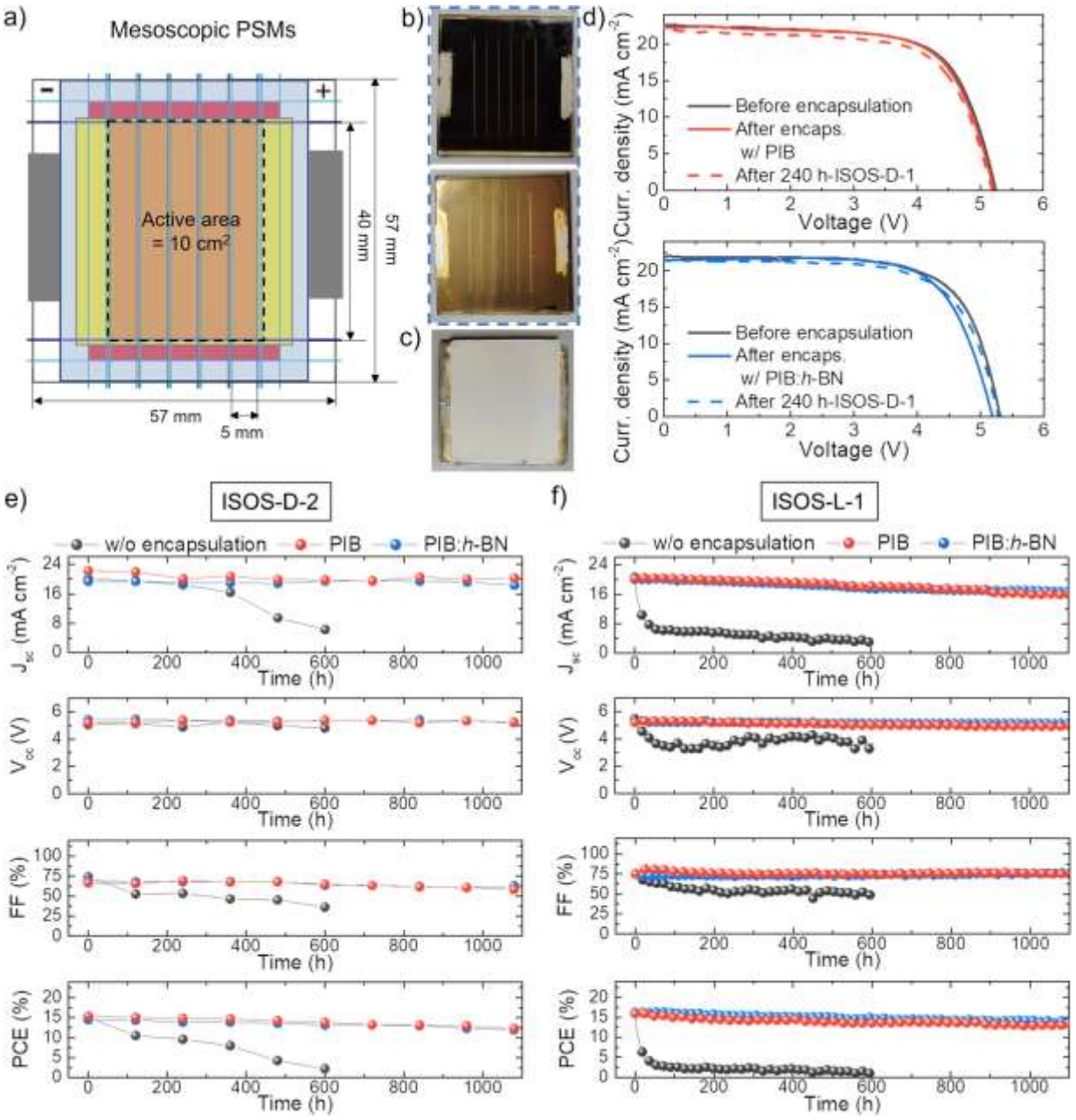

*Figure 4.10 (a) Schematic of the mesoscopic n-i-p PSM layout (cell active area = 2 cm²; total active area = 10 cm²), in which the non-compact layers are entirely covered by the encapsulant. (b) Photograph of a representative mesoscopic n-i-p PSM as fabricated (front and read sides: top and bottom picture, respectively), and (c) after encapsulation (rear side) with PIB:*h-*BN. (d) J-V curves (reverse voltage scan) measured for the as-fabricated mesoscopic n-i-p PSMs before and after encapsulation with PIB (top panel) and PIB:*h-*BN (bottom panel) (before and after 240 h-ISOS-D1). (e), (f) PV parameters of the PSMs without encapsulation and with PIB and PIB:*h-*BN encapsulants acquired over >1000 h of the ISOS-D-2 and ISOS-L-1 tests.*[192]

To further assess the reliability of these encapsulants and to investigate the barrier and thermal management functions of 2D *h*-BN flakes as encapsulant additives, encapsulated PSMs were subjected to two custom accelerated aging tests: a thermal shock test (cycling between -40 °C and +85 °C) and a modified humidity freeze test. Figure 4.11a,b depict the temperature profiles and environmental conditions (water immersion and air exposure) for these tests, while Figure 4.12 compares them with the IEC 61215 thermal cycling and humidity freeze protocols. Crucially, the cycle durations in the proposed tests (20 min for thermal shock and 25 min for humidity freeze) are substantially shorter than those required in IEC 61215 (>2.5 h for thermal cycling and >22 h for humidity freeze).

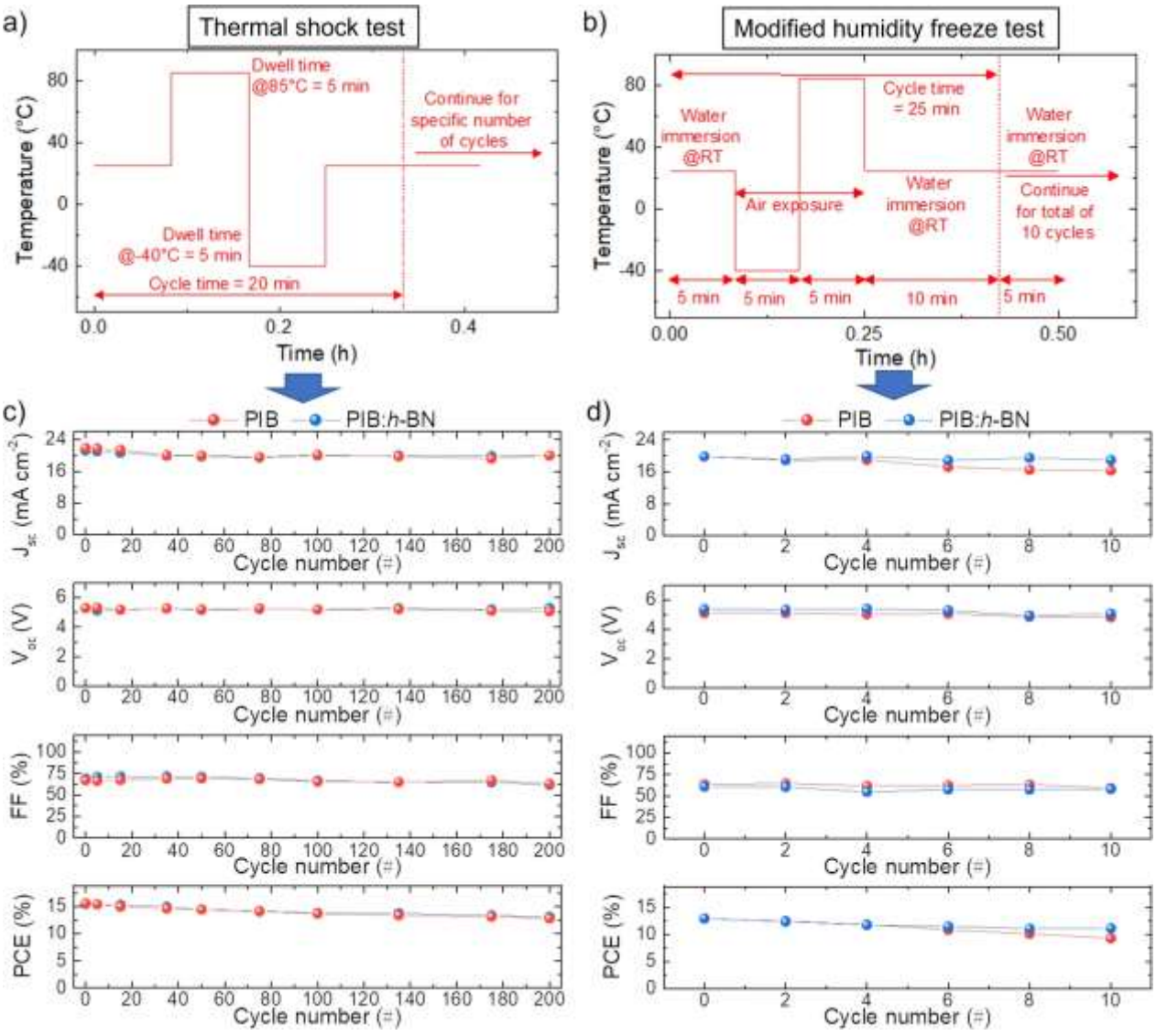

*Figure 4.11 (a) Temperature profile of the thermal shock test performed on the mesoscopic n-i-p PSMs encapsulated with PIB and PIB:*h-*BN. (b) Temperature profile and environmental exposure conditions of the humidity freeze test performed on the mesoscopic n-i-p PSMs encapsulated with PIB and PIB:*h-*BN. (c) PV parameters of the mesoscopic n-i-p PSMs encapsulated with PIB and PIB:*h-*BN acquired over >200 cycles of the thermal shock test. (d) PV parameters of the mesoscopic n-i-p PSMs encapsulated with PIB and PIB:*h-*BN acquired over >10 cycles of the customized humidity freeze test.*[192]

Accordingly, these more abrupt temperature changes are expected to impose severe thermomechanical stress from the differing thermal expansion coefficients of the various materials, potentially compromising interlayer adhesion and electrical interconnections.[548] A previous work on Si passivated emitter rear cells has established that accelerated thermal cycling can serve as an effective tool for rapid prototyping of new photovoltaic materials and module designs, revealing degradation pathways that may not be activated during standard IEC 61215 thermal cycling.[549] Moreover, in the proposed humidity freeze test, immersion in water after heating the module to +85 °C – followed by cooling to -40 °C – replaces the prolonged (>20 h) high-humidity (+85 °C, 85% RH) step of IEC 61215, thereby testing the module's ability to resist moisture ingress.

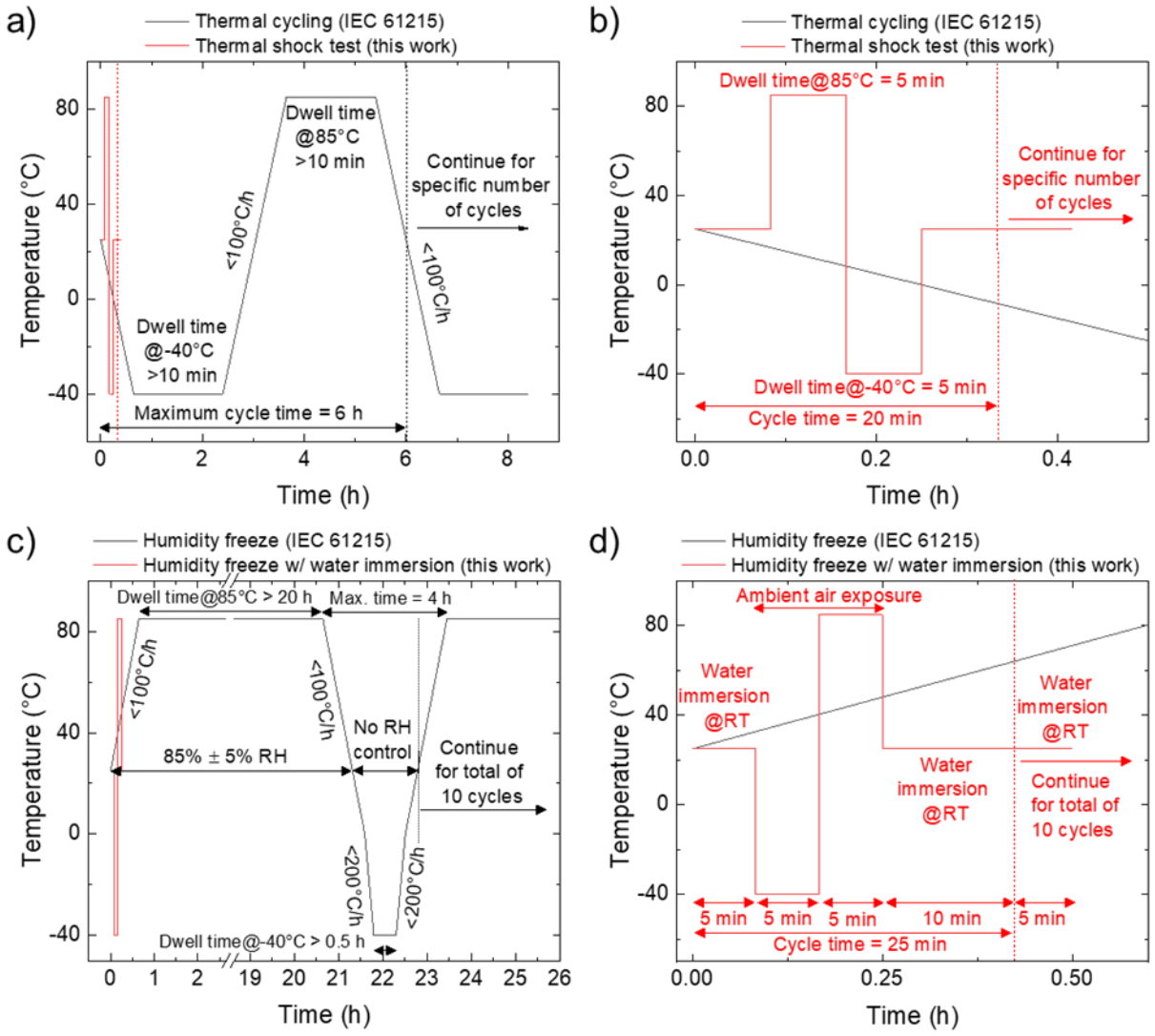

Figure 4.12 (a) Comparison between the temperature profiles of the IEC 61215 thermal cycling and the proposed thermal shock test. (b) Enlargement of the temperature profiles shown in panel a), evidencing the first cycle of the proposed thermal shock test. (c) Comparison between the temperature and RH profiles of the IEC 61215 and the proposed humidity freeze tests. (d) Enlargement of the temperature profiles and other environmental conditions (water immersion or ambient air exposure) shown in panel (a), evidencing the first cycle of our humidity freeze test, including a water immersion step.[192]

As shown in Figure 4.11c, the PSM encapsulated with PIB:*h*-BN withstood 200 thermal shock cycles, retaining 84.5% of its initial PCE. The PSM encapsulated with PIB retained 82.1% of its initial PCE after 200 cycles. These data indicate that incorporating 2D *h*-BN flakes as thermally conductive additives in encapsulants can substantially enhance PSM thermal management by conferring passive cooling properties, in line with the measured thermal characteristics of these encapsulants (Figure 4.5). Following the thermal shock test, the PIB- and PIB:*h*-BN-encapsulated PSMs were further stressed by the humidity freeze test, retaining 72.1% and 86.0% of their pretest PCE after 10 cycles, respectively (Figure 4.11d). Overall, PIB:*h*-BN outperformed homopolymer PIB slightly under both tests, as expected given its oustanding barrier and thermal management properties.

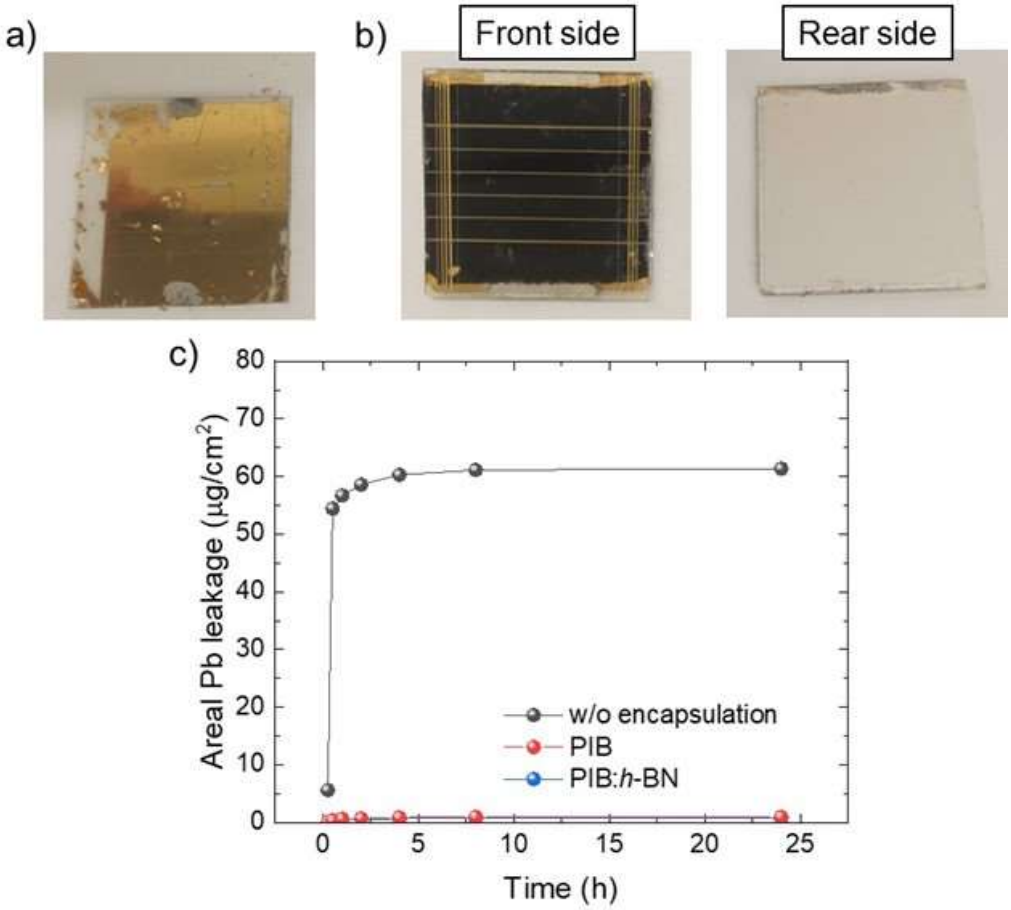

*Figure 4.13 (a), (b) Photograph of the unencapsulated PSM (rear side) and a PSM encapsulated with PIB:*h-*BN (rear and front side) after 24 h of immersion in water. (c) Areal Pb leakage from the investigated PSMs over water immersion time. The Pb leakage from a perovskite film encapsulated with PIB was also measured.*[192]

Finally, the ability of PIB:*h*-BN to protect PSMs from external degradation factors was demonstrated by measuring Pb leakage from encapsulated PSMs immersed in water, using ICP-OES (Figure 4.13). After water immersion, the unencapsulated PSM degraded rapidly, exhibiting yellowing caused by perovskite decomposition into PbI_2. Due to its high solubility (340 mg L^{-1}; solubility product constant

= 4.4 · 10^{-9} M),[517,518] PbI_2 dissolved quickly, leading to cracks in the Au rear electrode. The observed Pb leakage (>60 µg cm^{-2} after 24 h) is in agreement with the Pb content typically found in perovskites (0.1-1 g m^{-2}).[516] By contrast, the perovskite layer in the encapsulated PSMs maintained its original color and phase, resulting in Pb leakage values below 1 µg cm^{-2} after 24 h. This minimal Pb contamination presumably stems from residual perovskite located near the encapsulant edges, rather than from the active area.

Section 4.6 Conclusions

This chapter demonstrates how the integration of 2D *h*-BN flakes within a low-molecular-weight PIB matrix leads to a markedly improved encapsulant suitable for PSCs and PSMs. The beneficial effect of *h*-BN is evident in different areas, including improved barrier properties and better thermal management. These factors collectively drive better overall performance during long-term operation.

Corrosion-inhibition tests in saline water showed how the presence of *h*-BN increases the efficacy of PIB barrier films, resulting in corrosion rates that are orders of magnitude lower than those measured for either bare steel or pristine PIB, as suggested by the results collected in Chapter 3. The inclusion of *h*-BN also raised the water contact angle, further validating the hydrophobic nature of the composite. At the device level, this barrier properties was confirmed in Ca corrosion tests, where negligible changes to calcium film transmittance and resistivity during extended exposure were noted, indicating minimal moisture ingress when PIB:*h*-BN was used as the primary encapsulant, allowing to calculate a WVTR as low as 2·10^{-5} g m^{-2} d^{-1}.

Furthermore, the thermal management properties of PIB were improved by the addition of *h*-BN. This is a key requirement for PSCs and PSMs that must operate reliably under temperature fluctuations. Infrared imaging revealed that glass/PIB:*h*-BN/glass laminates can dissipate heat more efficiently than their pristine PIB counterparts, cooling faster and thereby reducing thermal stress. This is particularly important given the inherent thermomechanical challenges associated with perovskite-based devices, particularly PSMs, which can degrade under sustained or abrupt temperature gradients.

Looking from a device-oriented perspective, these characteristics manifested in excellent long-term stability results for *h*-BN-encapsulated devices. When subjected to multiple accelerated aging protocols (*i.e.*, ISOS-D1, ISOS-D2, and ISOS-L1) encapsulated PSCs and PSMs consistently maintained more than 80% of their initial PCE. Moreover, under customized thermal shock cycles (-40 °C to +85 °C) and modified humidity-freeze tests (with protocols derived from IEC 61215), *h*-BN-

containing encapsulants outperformed the pristine polymer, showing superior resistance to the severe stressors of a real-world application. This high tolerance derives not only from the improved barrier properties and thermal conductivity of *h*-BN flakes but also from PIB's inherent viscoelasticity and low module, which accommodates thermomechanical strain without developing cracks or interfacial failures.

Finally, the composite encapsulant was tested on its ability to reduce Pb leakage, which is a significant environmental concern for lead-based perovskites. Inductively coupled plasma optical emission spectroscopy measurements confirmed that PIB:*h*-BN encapsulated PSMs can work immersed in water without undergoing substantial structural degradation or Pb release. In contrast, unencapsulated devices quickly degraded and leached high amounts of Pb into the solution, highlighting the critical protective role of PIB:*h*-BN.

These findings highlight the potential of 2D *h*-BN as a powerful additive for improving encapsulant performance in perovskite-based photovoltaics. By providing good compatibility, high barrier properties, enhanced heat dissipation, and improved mechanical resistance, PIB:*h*-BN composites can help to address many degradation pathways that have historically limited the commercial viability of perovskite technologies.[473] Notably, no secondary edge sealants were used in this work, simplifying the encapsulation process further.

In conclusion, the PIB:*h*-BN composite encapsulant was demonstrated to be a promising advancement in the development of high-throughput, low-temperature, and mechanically friendly processes able to keep PSCs and PSMs performant under accelerated aging conditions. This approach significantly narrows the gap between laboratory-scale demonstrations and industrial manufacturing, moving the field another step closer to delivering cost-effective and durable perovskite photovoltaics on a large scale.

Chapter 5 Encapsulation of neural sensors for chronic applications

In this chapter, a preliminary study is reported on the use of *h*-BN composite coatings as encapsulants for neural sensors. As discussed in Chapter 3 and Chapter 4, *h*-BN enhances the barrier properties, mechanical performance, and thermal dissipation of composite coatings, making it an ideal filler for encapsulation. The goal is to develop an encapsulating layer that facilitates the use of novel neural sensors in chronic applications, by improving their chemical, thermal, electrical, and mechanical stability and providing a robust external structure that prevents material loss if sensor rupture occurs inside the brain. This work was carried out in collaboration with the Istituto Italiano di Tecnologia, Corticale srl, and the University of "Roma Tre".

Section 5.1 Neural sensors

Neural sensors, sometimes also called neural interfaces or neural probes, are medical devices designed to measure and/or modulate the electrical signals generated by neurons.[550,551] Their primary function is to facilitate a bidirectional exchange of information with the nervous system: they can record electrical activity (*i.e.*, action potentials or local field potentials) and, in some cases, deliver stimulation to modulate neural activity.[552] These devices are of fundamental importance to both basic neuroscience, since they can enable the comprehension of brain function and neural communication, and clinical applications, including the treatment of neurological disorders and the development of advanced prosthetics.[552,553]

Neural sensors often consist of one or more microelectrodes arranged on a thin substrate.[550,554] The electrodes are made from conductive materials (*e.g.*, metals or conductive polymers) and are insulated everywhere except on the active surface.[555,556] The substrate may be composed of rigid materials (*e.g.*, Si) or flexible polymers (*e.g.*, polyimide), depending on the requirements of the specific application. Many designs incorporate on-board electronics – such as amplifiers and multiplexers – to improve the signal-to-noise ratio, and these microdevices may be located either on the implant itself or integrated closely within its housing.[550,555,557] Apart from improving signal quality, electronics can enable real-time data acquisition and sometimes wireless data transmission.[555]

Neural sensors are able to detect every minute voltage changes produced by neuronal activity on the surface of their electrodes. When a neuron activates, it generates what is called an action potential, which propagates an electrical waveform with a typical amplitude in the order of microvolts to

millivolts.[558] This signal can be detected by the microelectrodes and the associated circuitry processes and interprets the data, which are then sent to a software. Meanwhile, in devices that also support stimulation, electrodes are also able to deliver controlled electrical pulses back into the tissue to modulate network activity, enabling treatments such as deep brain stimulation for Parkinson's disease or essential tremor.[552] Thanks to their functionality and structure, neural sensors represent a growing research field for the advancement of both our fundamental understanding of the brain and the therapeutic options available for neurological disorders.[550–552,554,555]

The continuous evolution of our understanding of neural pathways demands ever-more flexible, reconfigurable devices capable of adapting to emerging therapeutic approaches.[559] One representative example is the concept of the "neural coprocessor," such as the Summit RC+S device, which brings the computational power of a microprocessor into an implantable neuroprosthesis.[559] Built on the experience with the Activa PC+S research tool, the Summit RC+S aims at enhancing both sensing and stimulation performance for a more robust bidirectional communication with the nervous system. Furthermore, it incorporates rechargeable technology to extend device longevity and exploits MICS-band telemetry to share data management and algorithm development. These features definitely improve the device's performance and the user experience with respect to older technologies, allowing it to support advanced neuromodulation research in human subjects while minimizing patient risk.[559] Other progresses have also been made in developing integrated wireless systems for neural signal acquisition by employing an embedded compressed-sensing processor to substantially reduce the data transmission rate, thereby enabling the system to handle a larger number of recording channels without significantly increasing power consumption.[560] This approach can be particularly valuable in chronic neural monitoring scenarios where durability is fundamental and energy resources are limited and preventing tissue heating is a priority.

In order to increase the space and time resolution of the recordings, the most advanced solution was found to be that of microelectrode arrays (MEAs), which remain an essential technology for recording extracellular potentials from excitable cell cultures and are widely used in both fundamental research and applied electrophysiology.[561,562] In this configuration a large number of electrodes is created on a substrate in the form of an array, with each electrode being potentially able to provide a different signal in a different position on the sensor. Their applications range from studying signal propagation and information processing, to investigating learning and memory, and screening drugs for toxicity.[561,562] To maximize the number of effective recording sites, research has focused on methods such as patterning cellular networks on MEAs or introducing large numbers of closely spaced electrodes addressed via light-addressable potentiometric sensors (LAPS).[561] In active-pixel-sensor

(APS)-based MEAs, amplifiers reside directly beneath each electrode, enabling continuous recordings from thousands of electrode-pixels with sub-millisecond temporal resolution and micrometer-scale spatial resolution over large brain areas, rather than acquiring signals from a group of electrodes at a time through external electronics.[557,563,564] One example is the SiNAPS Complementary Metal-Oxide-Semiconductor (CMOS)-based APS probe, initially validated *in vivo* and capable of recording broadband bioelectrical signals over sizable brain regions with high spatiotemporal resolution.[557] Future improvements include on-probe analog-to-digital converters, digital multiplexing circuits, and high-speed wireless interfaces for chronic implantation in freely behaving animals.[557]

Despite these advances, the achievement of stable, high-quality, long-term (chronic) neural recordings remains a substantial challenge, as brain tissue responses to neural implants, such as foreign body reactions, glial activation, scar formation, and potential electrode-tissue interface degradation, significantly affect signal sensitivity and implant longevity.[564–569] Mechanical rigidity and mismatch between the implant and brain tissue contribute to chronic inflammatory responses, suggesting the use of more compliant, flexible polymers (*e.g.*, Parylene-C, polyimide) to mitigate strain and deformation *in vivo*.[564,569] The size and architecture of the implanted probes also play a role: for instance, probes with subcellular cross-sections or mesh-like structures can diminish foreign body responses and the speed and geometry of insertion further impact acute tissue damage.[564,569]

Material-based strategies to improve biocompatibility and long-term performance include the use of biocompatible or bioactive coatings designed to reduce reactive gliosis.[566,569] For example, surface-immobilized neuronal adhesion molecules have been shown to boost compatibility and diminish astrogliosis, while peptide sequences that target astrocytes and anti-inflammatory drugs such as dexamethasone, delivered via coatings or controlled-release systems, can help against curtail inflammation.[564,568] Conductive polymers like PPy and poly(3,4-ethylenedioxythiophene) (PEDOT), often doped with polystyrene sulfonate (PSS), improve the electrode-tissue interface by reducing impedance and increasing surface area.[569] Meanwhile, CNTs and graphene are gained interest for their promising mechanical, electrical, and biological properties in chronic neural interfaces.[557,569] Furthermore, the tuning of the surface permeability of an implant can further regulate inflammatory factors at the electrode-tissue interface, thereby improving biocompatibility.[569]

Finally, non-conventional probe designs have been investigated in order to offer additional routes for overcoming the limitations of rigid shanks.[570] Some examples include multi-sided arrays, mesh-like or filamentous architectures, tubular or cylindrical probes, folded probes, and self-softening or self-deploying devices, as well as nanostructured architectures.

The field of neural sensors is thus marked by rapid innovation directed toward creating more effective, biocompatible, and durable interfaces for neuroscience research and advanced clinical interventions in neurological disorders and pathologies. Progresses in the understanding of the interactions between implants and brain tissue, together with advancements in materials science and device architecture, will dictate the future of neuroprosthetics and brain-machine interfaces,[564,568–570] by hopefully holding the promise of improving therapeutic outcomes and deepening the knowledge of the nervous system in health and disease.[567,569]

Section 5.2 Encapsulation of neural sensors

As previously discussed, the encapsulation of neural sensors is a critical factor in the development of long-term implantable neural interfaces for research or therapeutic use. This process addresses several fundamental requirements to ensure the functionality and safety of the devices once they are introduced into the body. One primary motivation is to protect the sensor's electronic components from the physiological environment, which is warm, humid, and dynamic, all conditions that can reduce the durability of electrodes and substrates.[571–574] Encapsulation thereby acts as a protective barrier against moisture, bodily fluids, and corrosive chemicals, ultimately prolonging the lifespan of the device and possibly improving the interaction with tissues.[572,575] It also provides electrical insulation by preventing short circuits and ensuring an accurate transmission of neural signals.[571,574] In this context, using dielectric materials with appropriate properties is indispensable for reducing the signal-to-noise ratio and enhancing the selectivity of the interactions of each electrode with the neuronal tissue.[571] This is particularly relevant for emerging high-density microelectrode arrays with ever-shrinking dimensions, where a reliable encapsulation is crucial for protecting and isolating individual electrode sites.[577] Another key consideration is the biocompatibility of the encapsulating materials, which must not cause traumatic or toxic reactions in the surrounding tissues, thus minimizing foreign body responses and gliosis and promoting a long-term integration with the nervous system.[571,573,574,576]

The materials used for neural sensors encapsulation must therefore meet a set of specific requirements for implantable and chronic applications. First, they must be biocompatible to avoid excessive inflammatory responses and ensure a long-term tolerance of biological tissues.[571,573,574,576] They also need to be conformable, adapting to the complex geometries of three-dimensional architectures, such as those used in MEAs-based sensors.[571,573] Furthermore, long-term dielectric stability is essential to maintain insulation properties in the physiological environment over the whole expected lifetime of the device, while low permeability to moisture and ionic substances is critical for preventing corrosion

and malfunction of electronic components.[574] Depending on the application, the encapsulant should exhibit an appropriate balance of flexibility and mechanical robustness, allowing it to accommodate natural tissue movements without losing structural integrity, thus reducing inflammatory response caused by friction with tissues and guaranteeing the reliability of the whole sensor during insertion and extraction.[574] Finally, a strong adhesion to the sensor surface is also necessary to prevent delamination and infiltration.[578]

A variety of polymeric and inorganic materials have been investigated for neural sensor encapsulation, each with distinct advantages and disadvantages. Parylene C is widely regarded as the golden standard for neural and biomedical implants encapsulation due to its excellent biocompatibility, electrical and chemical stability, low moisture absorption, and conformability.[571,573–576,578–580] It can in fact be deposited as a conformal coating by CVD and selectively removed to expose the active electrode areas via oxygen plasma etching.[571] Among the others, silicon nitride and polyimide have been employed as encapsulating materials for the Utah Electrode Array (one of the most common Si-based MEAs),[571,574] while silicon carbide (SiC) has shown promise for extending the long-term stability of neural implants due to its superior barrier properties.[573] Other materials, such as glass,[579] epoxy resins,[579] silicone rubber,[575] poly(L-lactic acid) (PLLA),[581] and ultra nanocrystalline diamond,[571,581] have also been explored with good performance. Ongoing research includes the development of composite micro/nanostructured coatings that combine nanometric silane layers as an adhesion promoter with micrometric parylene C films to enhance both adhesion and barrier performance,[578] as well as the exploration of flexible polymers such as liquid crystal polymers (LCP) for both probe fabrication and encapsulation.[574,582]

Research on neural sensor encapsulation remains a central subject for the development of long-lasting, safe, and performing implantable devices. In general. efforts include the development of new encapsulant materials with greater chemical, electrical, and mechanical stability, enhanced biocompatibility, and improved barrier properties to extend the functional lifetime of chronical neural implants.[573] Together with biocompatibility, there is also growing attention to minimizing foreign body responses, which is essential for ensuring stable and performing neural interfaces over extended periods.[580,581,583] Additional challenges involve the encapsulation of high-density MEAs,[577] due to their highly resolved architecture, improving the adhesion between the encapsulant and the sensor to prevent delamination, guaranteeing a sufficient resolution of the etching process, and designing ultra-thin, flexible coatings for specialized applications such as implantable pressure sensors.[578] Researchers are also investigating composite materials and nanomaterials to optimize mechanical, electrical, and biological properties,[578] as well as exploring additional and complementary strategies

such as sensor surface modifications and local drug release to reduce tissue response.[576,580] Furthermore, the geometry of the neural probe itself and the insertion protocol remain important factors in mitigating chronic tissue responses.[580]

In summary, encapsulation is a fundamental requirement for the success of implantable neural interfaces. Ongoing research and the development of innovative materials and encapsulation techniques are essential for achieving more reliable, biocompatible, and high-performing devices over the long term, which could be employed for chronical treatment of neurological disorders and pathologies or extensive research studies.

Section 5.3 Materials and methods

Section 5.3.1 Materials

PIB was provided in the form of Oppanol® N80 (average molecular weight – MW – 800000) by BASF Italia S.p.A. Polyvinyl butyral was provided in the form of Mowital® B45H by Kuraray Co. Toluene (purity >99.7%) and IPA (purity >99.5%) were supplied by Merck. All reagents were used without further purification. Few-layer *h*-BN flakes were produced in the industrial plant of BeDimensional S.p.A. as previously described in Chapter 2.

Regarding the materials for cultures, Poly-D-Lysine, NEUROBASAL™ Medium (1X) liquid B-27™ Supplement (50X, serum free), Penicillin-Streptomycin solution (10,000 U/mL), and GlutaMAX™ Supplement were supplied by Thermo Fisher Scientific. Dulbecco's modified Eagles medium (DMEM, high glucose) and Fetal Bovine Serum (FBS) were supplied by Merck.

Phosphate buffered solution (PBS, pH 7.4) and Normal Goat Serum (NGS) were supplied by Thermo Fischer Scientific, while Triton™ X-100 and paraformaldehyde (PFA) were supplied by Merck.

As for the antibodies for immunostaining, GFAP Polyclonal Antibody (cat. PA1-10004), Goat anti-Chicken IgY (H+L) Secondary Antibody (Alexa Fluor™ 546, cat. A11040), Donkey anti-Rabbit IgG (H+L) Highly Cross-Adsorbed Secondary Antibody (Alexa Fluor™ 488, cat. A21206), and Goat anti-Mouse IgG (H+L) Highly Cross-Adsorbed Secondary Antibody (Alexa Fluor™ 647, cat. A21236) were supplied by Thermo Fisher Scientific. Anti-NeuN Antibody (rabbit, from rabbit, purified by affinity chromatography, cat ABN78) was supplied by Merck. Purified anti-Tubulin β 3 (TUBB3) Antibody (cat. Covance MMS-435P) was supplied by BioLegend. Finally, ProLong™ Gold Antifade Mountant with DNA Stain DAPI (cat. P36935) was supplied by Thermo Fisher Scientific and used as a mounting media.

Section 5.3.2 Encapsulant preparation

Two families of encapsulants were prepared using two polymeric matrices. As described in Chapter 3 and Chapter 4, PIB is a low-polarity homopolymeric polyolefin available in various molecular weights. The high-molecular-weight PIB used in this work displays a highly viscous, semi-solid behavior, similar to an elastomer. This polymer offers exceptional impermeability to gases and moisture, high damping and excellent chemical and oxidative resistance,[523,584] making it a perfect choice for encapsulant applications. Polyvinyl butyral, on the other hand, is widely employed in applications such as safety glass lamination, photovoltaic encapsulation, and adhesives.[585] It is synthesized via the reaction of vinyl alcohol and butyraldehyde – sometimes combined with acetaldehyde – and is produced in grades differing in molecular weight, hydroxyl content, and degree of acetalization.[585] The specific grade used here contains 18-21 wt% vinyl alcohol, 1-4 wt% vinyl acetate, has a glass transition temperature of 69 °C, and a water uptake of 4-6 wt%. The chemical formula of the two polymers is shown in Figure 5.1.

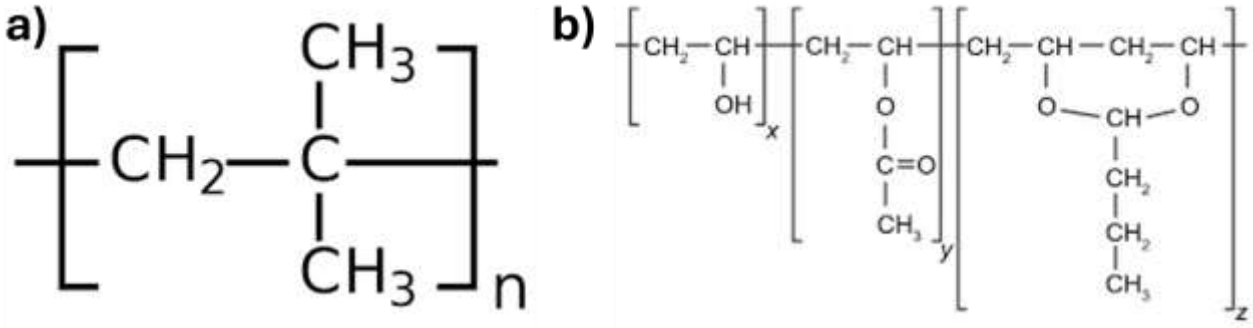

Figure 5.1 (a) Chemical formula of PIB and (b) generic chemical formula of PVB.

To prepare the PIB solution (following a procedure similar to that described in Chapter 3), the polymer was dissolved in toluene at 10 wt%, then stirred at 800 rpm for 12 h at 80 °C in a sealed container until a homogeneous solution was obtained. The PVB solution was prepared in a similar manner by dissolving the polymer in IPA at 10 wt%, followed by stirring at 800 rpm for 12 h until homogeneous.

PIB/*h*-BN and PVB/*h*-BN composites were produced by dispersing WJM-produced *h*-BN powder into the respective polymer solutions. A Thinky ARE-250 Mixing and Degassing Machine (planetary centrifugal mixer) was used at 2000 rpm for 5 min to disperse *h*-BN loadings of 0.5, 2, and 5 wt% relative to the total solid content. The resultant composites are hereafter denoted as PIB0.5, PIB2.0, PIB5.0, PVB0.5, PVB2.0, and PVB5.0.

All characterization experiments other than corrosion tests were conducted on samples prepared by blade-coating the encapsulants onto silicon wafers of (100) orientation with a thickness of 525 μm. The wafers were first treated with plasma (100% O_2, 100 W) in a Gambetti Tucano low-pressure plasma chamber to enhance the adhesion of the encapsulants and prevent delamination during immersion in water or biological fluids. The encapsulants were then applied using a doctor blade set to a thickness of 100 μm and allowed to dry under ambient conditions for 1 h. Finally, the samples were dried in a vacuum oven at 60 °C and 200 mbar for 4 h to ensure complete solvent removal.

Samples for corrosion tests were prepared by blade coating the encapsulants on carbon steel panels (Q-Panels QD-46) with a wet thickness of 100 μm and drying them as described in the previous paragraph.

Section 5.3.3 Encapsulant characterization

Scanning electron microscopy data were acquired on a JEOL JSM-6490LA SEM (low-vacuum) with a thermionic electron gun (tungsten source) after coating the samples with a 10 nm gold layer. The hydrophobic behavior of the composites was investigated by CA measurements, in which a 10 μl water droplet was placed on each composite and imaged using an OSSILA L2004A1 CA goniometer. The measurement was repeated three times for each sample, and the average value will be reported.

Profilometry analyses were performed with a Leica DCM 3D optical (confocal) profilometer. The confocal mode of the Leica DCM 3D was used to measure the topography of the surfaces and the thickness of the coatings. To achieve high surface sensitivity, the samples were made planar using a goniometer, and the following parameters were set: 10x lens magnification, blue LED illumination, and the acquisition of 7 images using the stitching technique. For each topography obtained, 5 profiles were then processed with the Leicamap software, and the difference in Z between the silicon substrate and the coatings was evaluated.

To evaluate the dynamic viscoelastic response of PVB- and PIB-based coatings through nanoindentation testing, an Agilent KLA G200 Nanoindenter with a DCM II-style actuator was used. By applying a sinusoidal loading, it was possible to define the conservative and dissipative components of the dynamic modulus, E′ and E″ respectively,[586–590] where E′ is defined as the storage modulus, representing the material's ability to store energy, and E″ is the loss modulus, representing the energy dissipated.

In all cases, the values of E′ and E″ were calculated for 10 different frequencies in a range between 150 Hz and 1 Hz with an oscillation amplitude of 50 nm. The compression and the nanoindentation tests were performed with a flat-end cone diamond indenter with a diameter of 5 μm. Using a flat

punch has the advantage that the contact area can be directly measured, but the drawback is that it is impossible to mount it perfectly perpendicular, resulting in a small angle between the face of the indenter and the sample surface.[588,591] Therefore, it is necessary to identify a condition of full contact with the sample surface. A pre-test compression is defined to start the data recording after full contact is achieved. Several tests were conducted with different pre-test compressions ranging from 100 nm to 500 nm, achieving full contact with a precompression of 400 nm for the PVB samples and 300 nm for the PIB samples. The pre-compression was kept shallow to avoid any influence from the substrate, being considered the measured thicknesses. Eventually, any substrate effect is, in any case, sorted out within a pure comparison upon the eight tested samples.

The specimens were mounted onto the nanoindentation stub using super glue at RT. At least four tests were conducted at a temperature of 31 ± 0.6 °C under medium and high humidity conditions, respectively at 40% RH and 60% RH. The frame stiffness has been corrected using a Berkovich tip calibrated on the reference fused quartz prior to testing. Moreover, the reference sample has been mounted under the same conditions as the samples tested.

Similarly to the description reported in Section 3.2, electrochemical measurements were performed using a BioLogic VMP3e Multichannel Potentiostat in a three-electrode 50 mL Biologic coating cell (exposed surface area 15.2 cm^2) at RT in a 3.5 wt.% NaCl aqueous solution, in accordance with the ASTM G5-14 standard. A KCl-saturated Ag/AgCl Radiometer Analytical REF201 Red Rod Reference Electrode (Biologic) served as the reference electrode, and a graphite rod was used as the counter electrode. The OCV was monitored for 30 min prior to acquiring potentiodynamic anodic polarization data at a scan rate of 10 mV min^{-1}.

The corrosion performance of the coatings was evaluated by potentiodynamic anodic polarization measurements and subsequent Tafel analysis, as detailed in ASTM G5-14, to determine i_{corr} and E_{corr}.[414,415] The R_p values were determined following ASTM G59-97 from the slope of the polarization curve at E_{corr},[416] *i.e.*:

$$R_p = \left(\frac{dE}{dI}\right)_{E_{corr}} \tag{5.1}$$

The corrosion rate (mm yr^{-1}) was calculated from i_{corr} using the Faraday law:

$$CR = \frac{K \cdot W_{eq} \cdot i_{corr}}{D} \tag{5.2}$$

where $K = 3.27 \cdot 10^{-3}$, $W_{eq} = 27.9\ g\ eq^{-1}$ (the equivalent weight of iron in ferrous compounds), i_{corr} is given in $\mu A\ cm^{-2}$, and $D = 7.85\ g\ cm^{-3}$.[417] The inhibition efficiency of the composites was derived from the following equation:[418]

$$\eta_p\% = \frac{i^0_{corr} - i_{corr}}{i^0_{corr}} \cdot 100 \quad (5.3)$$

where i^0_{corr} and i_{corr} are the corrosion current densities in the absence and presence of inhibitors (*i.e.*, *h*-BN flakes).

Electrochemical impedance spectroscopy was carried out in potentiostatic mode at OCV with a sinusoidal AC amplitude of 10 mV over a 0.1 Hz - 200 kHz frequency range, following ASTM G106-89.

The molecular structure of the coatings was characterized by FTIR spectroscopy. The samples were analyzed using a Thermo Fisher Scientific Nicolet 380 equipped with an Attenuated Total Reflectance (ATR) module. Spectra were collected from 4000 to 400 cm^{-1} at a 4 cm^{-1} resolution, and 100 scans were accumulated to enhance the signal-to-noise ratio. Air was taken as the background before each measurement. Spectra were elaborated through Omnic 9.2.86 by Thermo Fisher Scientific.

Section 5.3.4 Biocompatibility tests

Cytotoxicity tests were performed both on HEK293 cells (a cell line exhibiting epithelial morphology isolated from the kidney of a human embryo) and on cortical neurons. The protocols adopted for the tests are reported in the following.

Before each assessment, samples were sterilized under a UV light for 30 minutes at 30 W. The choice of this sterilization method over ethanol sterilization was performed considering the solubility of PVB in the solvent, as declared by the producer.

To perform cytotoxicity tests on HEK293 cells, the samples were firstly coated with poly-D-Lysine (0.1 mg/mL in water) and placed over night inside a CO_2 incubator (humidity around 85%, 37 °C and 5% CO_2). After one day, HEK293 cells were plated both on the samples and on Petri dishes (Corning Incorporated) as a reference. The culture medium was DMEM high glucose supplemented with 10% FBS and 1% Penicillin streptomycin solution. The cells were finally let to grow for three days (Day in-vitro 3 - DIV3) inside the incubator at the same previous conditions (humidity 85%, 37 °C and 5% CO_2).

The adhesion and growth of the cells on the reference substrate was checked after DIV3 through an optical microscope and the survival of cell grown on the samples was checked after DIV4 through optical images in the brightfield.

Neurotoxicity tests were performed both in standard cultures plating the neuronal cells directly on the samples and in co-cultures, plating the neuronal cells on reference standard substrates and exposing the culture medium to the samples to be tested, in order to evaluate the possible release of toxic substances from the samples when in contact with the medium. Following both approaches, neurons were firstly plated on the substrate of interest (sample or glass coverslip prepared following a standard protocol). In the case of co-culturing, the glass coverslip was moved in the same dish as the samples after two hours of adhesion. Then, the culture medium was added to the Petri dishes, and they were placed in a CO_2 incubator (humidity 85%, 37 °C and 5% CO_2). After DIV5, the viability of cultures was checked through optical microscopy. The cultures then continued until DIV14, and immunofluorescence was used for a further assessment of viability, using the following protocol for immunofluorescence staining. After incubation, the cell culture medium was removed, and the cells were washed in PBS. Then, they were fixed with PFA (4% in PBS) and incubated for 20 min at RT under a chemical hood and subsequently washed four times with PBS and stored overnight at 4 °C. The day after, the cells were washed with PBS and made permeable with Triton X-100 (0.1% in PBS – PBST) for 5 minutes at RT, incubated for 45 minutes with blocking buffer (5% normal goat serum in PBST – NGS solution) and incubated overnight at 4°C with the following primary antibodies: Chicken anti-GFAP (1:500 in NGS solution); Rabbit anti NeuN (1:500 in NGS solution), Purified anti-Tubulin β 3 Antibody (1:500 in NGS solution). On the following day, the cells were washed three times with PBST and incubated for 45 minutes at RT using the following secondary antibodies: Goat anti-Chicken (Alexa Fluor™ 546, 1:500 in NGS solution), Donkey anti-Rabbit (Alexa Fluor™ 488, 1:500 in NGS solution), and Goat anti-Mouse (Alexa Fluor™ 647, 1:500 in NGS solution). Finally, the samples were washed 3 times with PBST and once with PBS, and the cells were mounted on glass slides using Prolong Gold antifade reagent with DAPI at 4 °C overnight and sealed with nail polish.

An Axio Observer widefield fluorescence inverted microscope from Zeiss was used to acquire images of the samples with 40x magnification.

Section 5.4 Barrier, chemical and mechanical properties of the encapsulants

Initially, the thickness of the encapsulating layers deposited on the silicon wafer was assessed to determine whether it met the stringent dimensional requirements of Corticale's sensors. Given that

the SiNAPS sensors incorporate electrodes that are 20 µm wide and a shaft measuring around 100 µm in width,[557] the encapsulant should ideally not exceed a thickness of 10 µm. A thickness of a few micrometers is also usually reported for Parylene C encapsulating layers.[571,575,578] The thickness of the deposited encapsulants was measured once per sample using an optical profilometer and the results are reported in Table 5.1.

Table 5.1 Thickness of the different coatings obtained through optical profilometry analysis.

Sample	Thickness (µm)
PVB	2.69 ± 0.05
PVB0.5	2.59 ± 0.07
PVB2.0	2.64 ± 0.10
PVB5.0	2.78 ± 0.17
PIB	3.48 ± 0.13
PIB0.5	3.54 ± 0.13
PIB2.0	3.05 ± 0.06
PIB5.0	3.11 ± 0.14

The surface morphology and homogeneity of the deposited layers was investigated by SEM. Images depicted in Figure 5.2 and Figure 5.3 show an evenly distributed amount of *h*-BN, increasing with increasing nominal loading, with larger aggregates being depicted in PIB-based samples with respect to PVB-based ones. A higher roughness of the samples containing higher *h*-BN loading is also clearly visible.

Chemical analyses were performed by FTIR spectroscopy to study the possible interactions between the polymeric matrix and wet-jet milled *h*-BN and the effective incorporation of the material in the polymeric matrices. The spectra acquired in an ATR configuration are reported in Figure 5.4a,b. As reported in Section 3.3, in the PIB spectrum, the characteristic bands at 2961 and 2916 cm^{-1} correspond to asymmetric stretching of CH_3 and CH_2 groups, respectively.[422] The peak at 1471 cm^{-1} is associated with CH_2 groups[422] or -CH bending,[423] while the double peak at 1389 and 1361 cm^{-1} arises from CH_3 symmetric bending.[422] The band at 1231 cm^{-1} is attributed to C-H bending, and the weak peaks at 949 and 923 cm^{-1} correspond to C=C bending originating from trace amounts of unpolymerized isobutylene.[424] On the other hand, the spectra of PVB are characterized by the

following features: the peaks between 3000 cm^{-1} and 2850 cm^{-1} can be attributed to CH_3, CH_2 and CH stretching,[422] the broad signals around 1400 cm^{-1} are associated to CH_3, CH_2 and CH bending and deformation,[422] and the peak at 1240 cm^{-1} is connected to CH bending.[424] Finally, the band at 1100-1150 cm^{-1} is related to C-O-C stretching,[592] that at 950-1000 cm^{-1} to CO stretching and breathing of the acetal cycle,[593] and the peak at 1050 cm^{-1} is attributable to CO stretching in -OH groups,[594] as well as the broad band above 3000 cm^{-1}.[595] The shift of this last band from the usual position at 3600 cm^{-1} to 3450 cm^{-1} can be explained by the presence of intermolecular hydrogen bonding.[595]

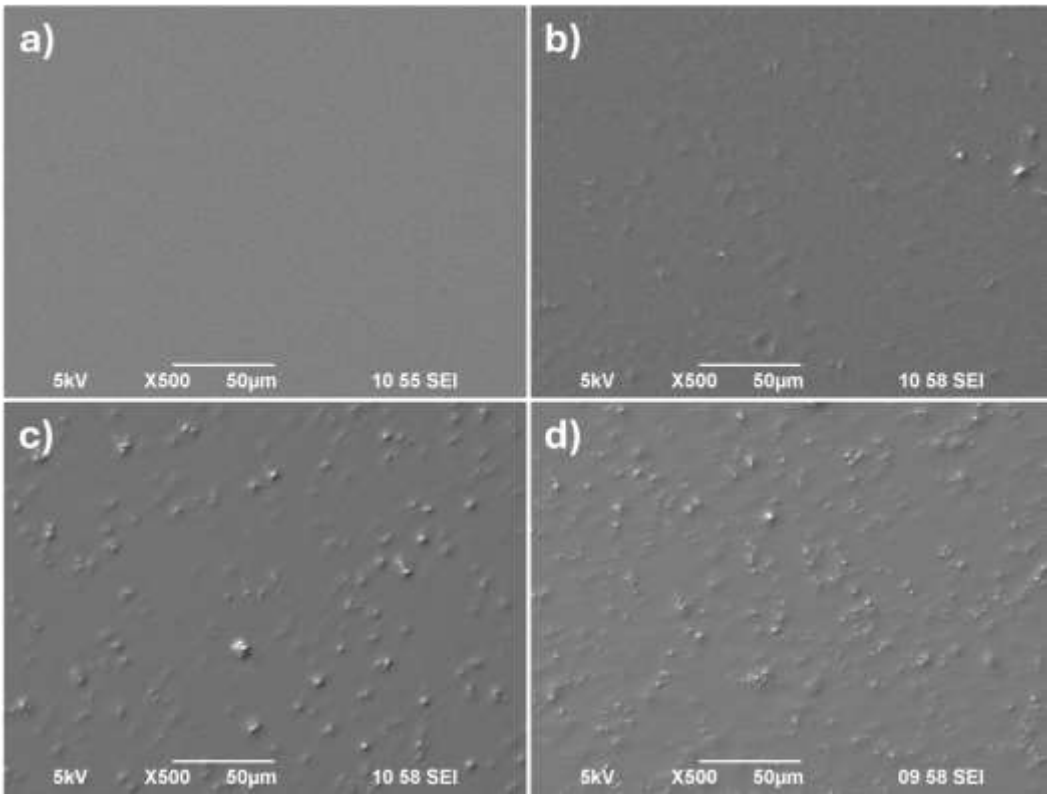

Figure 5.2 SEM images acquired at 500x magnification of (a) PIB, (b) PIB0.5, (c) PIB2.0, and (d) PIB5.0.

In both PIB- and PVB-based composite samples, two distinctive features are visible and attributable to the presence of *h*-BN. In particular, an additional broad band – superimposed on the PIB peaks in spectra acquired from PIB-based samples – can be attributed to the in-plane ring stretching vibration (E_u mode) of *h*-BN at 1372 cm^{-1},[274,381,425–430] while an isolated peak arising at 810 cm^{-1} can be associated with B-N stretching. The two characteristic signals of *h*-BN are highlighted in yellow in Figure 5.4a,b. The intensity increase of the band associated with -OH stretching above 3000 cm^{-1} can also be attributed to the loading of *h*-BN, due to the presence of hydroxyl and amine groups on the edges of the flakes, which could also contribute to hydrogen bonds.[594,596]

As a further confirmation of the composition of the composite encapsulants, the ratio between the intensities of the peak attributed to B-N stretching (810 cm^{-1}, black dashed lines in Figure 5.4a,b) and

of one representative peak of each polymeric matrix (blue dashed lines in Figure 5.4a,b) was calculated. The results plotted in Figure 5.4c show an almost linear increase in the intensity ratio with increasing nominal loading of *h*-BN, demonstrating how FTIR could be used as a quantitative analysis for this kind of materials.

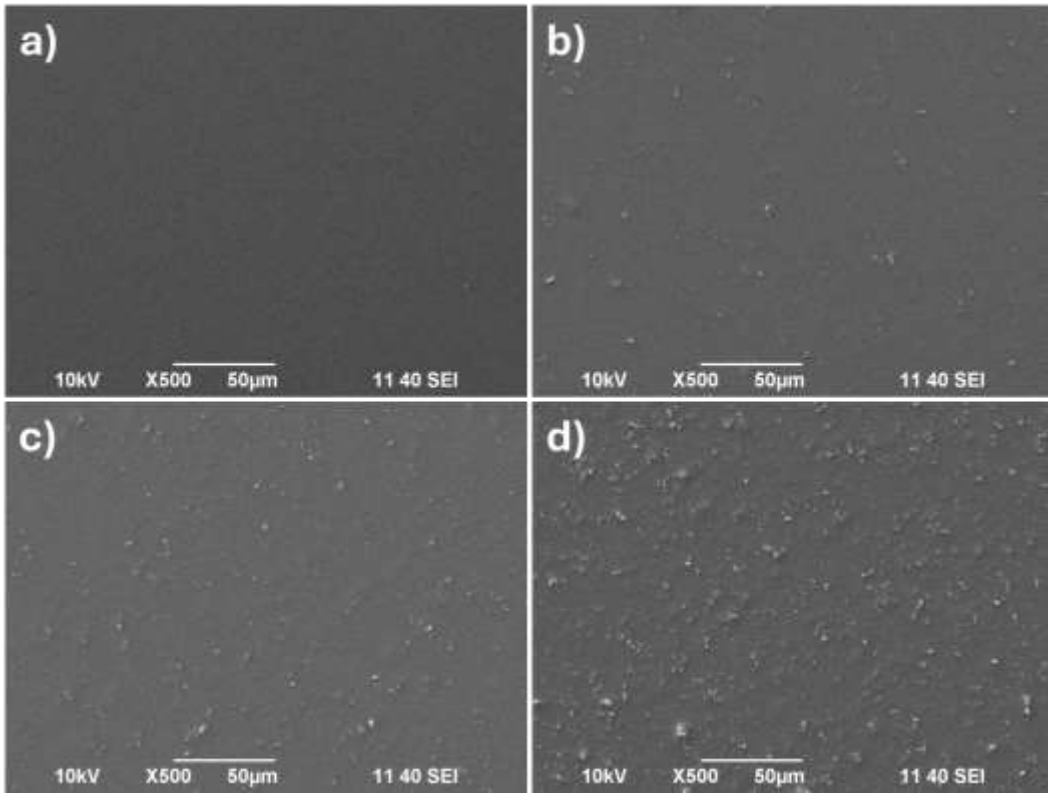

Figure 5.3 SEM images acquired at 500x magnification of (a) PVB, (b) PVB0.5, (c) PVB2.0, and (d) PVB5.0.

The wettability and hydrophobicity of the encapsulant was evaluated through water CA measurements. The results reported in Figure 5.5 show a slight increase in the value of the water contact angle with an increase in the loading of *h*-BN for PVB-based samples, with the measurement going from 74.3° to 80.3° for PVB and PVB5.0 samples, respectively. This behavior denotes the hydrophobic effect that *h*-BN can impart to polymeric matrices when used as a filler, as reported Chapter 3in literature.[318,381,389,421] Differently, the recorded contact angle values for PIB-based samples do not shown a significative variation upon changing the loading of *h*-BN, with the difference between PIB and PIB5.0 being as low as 0.6°, varying from 102.7° to 102.1°, respectively. The behavior of the pristine polymers is similar to that found in literature,[597,598] and is expected by the different polarities of the building blocks of PIB and PVB (Figure 5.1), while the dissimilarities with the results reported in Section 3.3 for PIB-based samples can be ascribed to the really low thickness of these encapsulants, which could affect both the drying step of deposition and the surface morphology of the film.

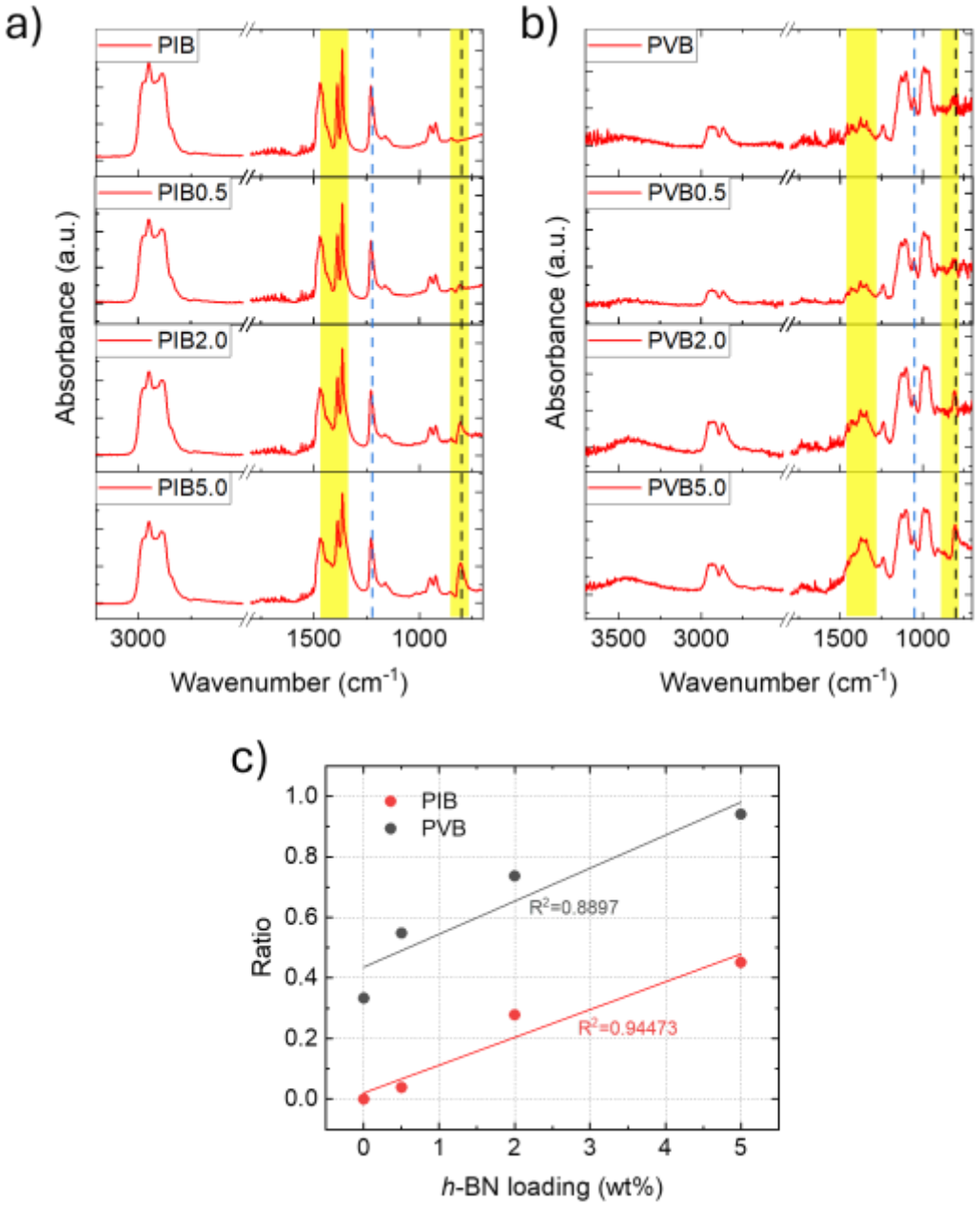

Figure 5.4 FTIR ATR spectra of (a) PIB-based composite encapsulants and (b) PVB-based composite encapsulants. Highlighted in yellow are the two major features associated with h-*BN, while the black and blue dashed lines indicate the peaks used are reference for* h-*BN and the matrix, respectively, for the calculation of the intensity ratios. (c) Plot of the ratios between the intensities of the aforementioned peaks against the nominal loading of* h-*BN in the composite layers.*

The barrier properties of the encapsulant were evaluated through corrosion tests similar to those reported in Section 3.2.4. A standard test protocol for marine corrosion was employed (ASTM G5-14), considering the conditions of a 3.5% NaCl aqueous solution to be comparable to those encountered in biological environments, if not harsher. Furthermore, a higher conductivity of the electrolytic solution improves the signal-to-noise ratio of the measurements, providing more precise analyses. The corrosion rate of the steel substrates coated with the various encapsulant formulations

was calculated from the corrosion current extrapolated from the Tafel polarization curves, and electrochemical impedance spectroscopy – performed according to ASTM G106-89 – was used to study interfacial and bulk electrochemical properties. The acquired curves are displayed in Figure 5.6, while the various metrics are reported in Table 5.2.

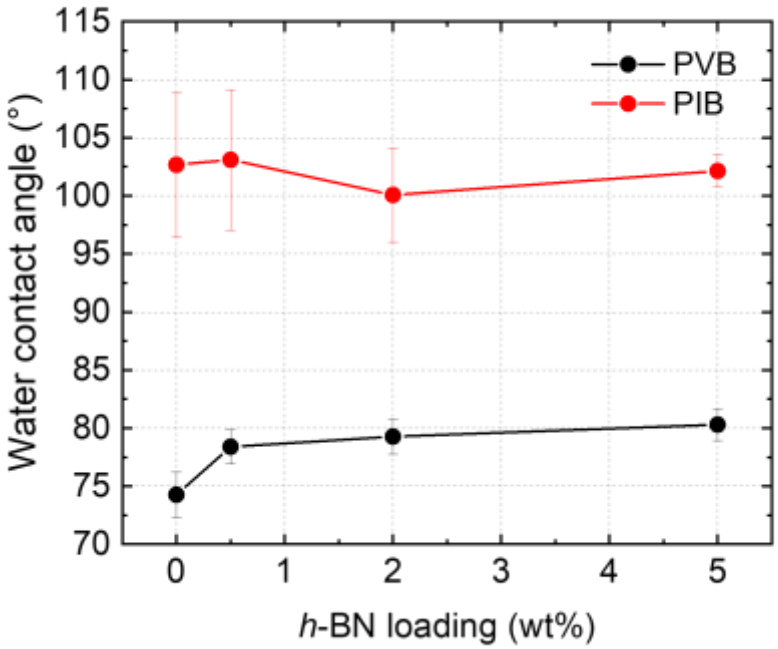

Figure 5.5 Water contact angle values of samples containing different loading of h-*BN.*

All the coatings provide corrosion protection to the steel substrate. The measured E_{corr} is shifted from that of bare steel (-0.6 V vs Ag/AgCl),[348] to values ranging from -0.500 V to -0.180 V vs Ag/AgCl, with the *h*-BN-loaded samples providing even higher protection than pristine polymers (E_{corr} higher than -0.308 V vs Ag/AgCl). This behavior is a first confirmation on the ability of *h*-BN flakes to confer corrosion protection and barrier effect to polymeric composites.

Contextually, the corrosion current densities and corrosion rates of the different samples, reported in Table 5.2 and Figure 5.6e, show a diverging trend for samples based on PIB and on PVB. The corrosion rate of steel plates protected by PIB-based encapsulants decreases for PIB0.5 with respect to PIB, reaching the lowest value of $1.49 \cdot 10^{-5}$ mm yr^{-1} but increases again for higher *h*-BN loadings. This behavior deviates from that reported in Chapter 3 for similarly loaded samples probably due to the low thickness of these encapsulants and to the higher probability of aggregates to have an impact on the permeability of the coatings. On the contrary, corrosion rates calculated for PVB-based samples decrease monotonically with increasing amount of *h*-BN, providing the lowest corrosion rate of $2.31 \cdot 10^{-6}$ mm yr^{-1} for PVB5.0. Table 5.2 also reports the corrosion inhibition efficiency of *h*-BN

loaded samples calculated with respect to the pristine matrix of reference. The barrier effect provided by *h*-BN guarantees an improvement in corrosion protection of 95.63% for PIB0.5 with respect to PIB and of 99.51% for PVB5.0 with respect to PVB.

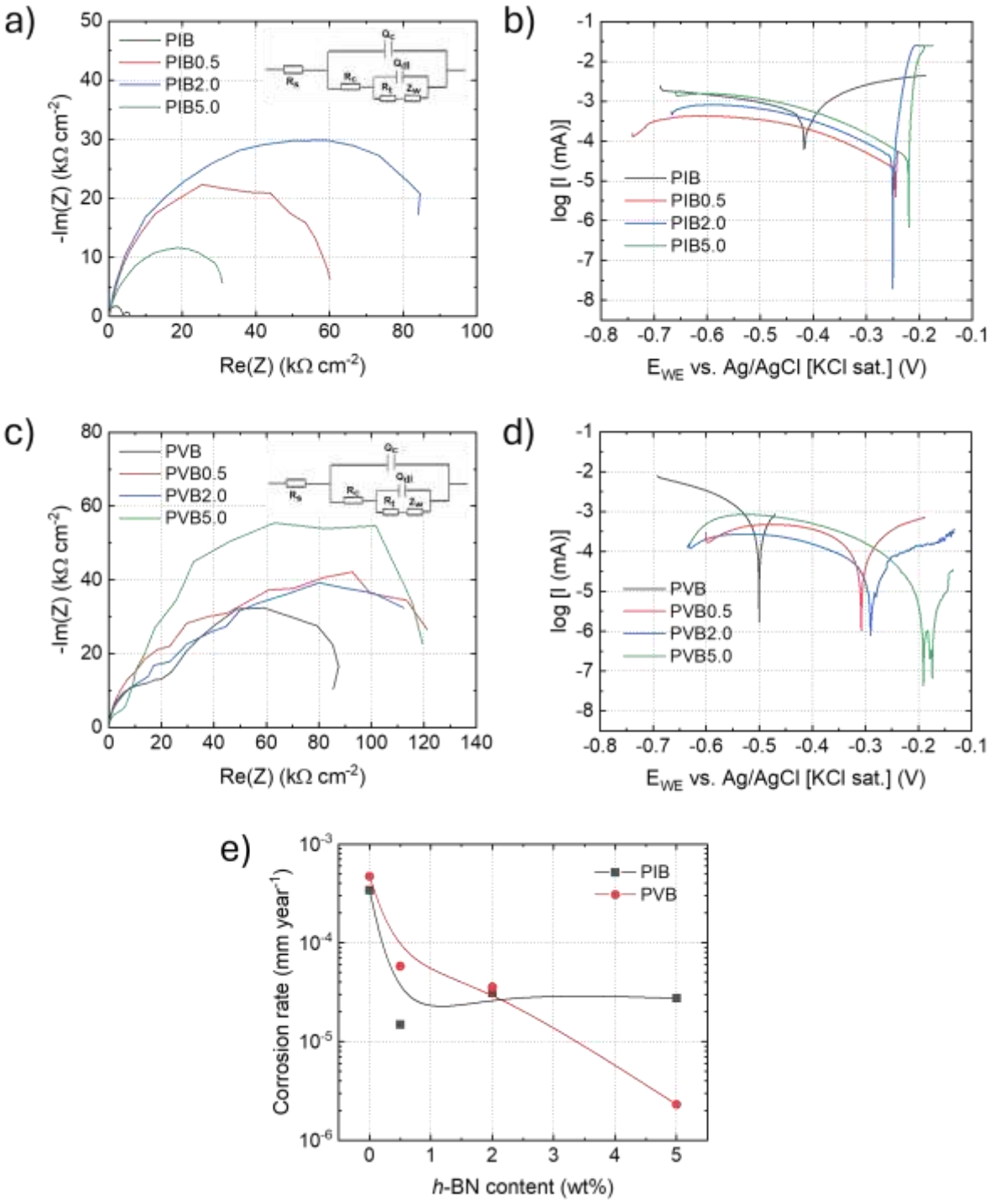

Figure 5.6 Nyquist plots of steel panels coated with (a) PIB-based composite encapsulants and (c) PVB-based encapsulants (inset: equivalent circuit diagram of coated steel substrates). Anodic polarization curves (Tafel plots) of steel panels coated with (b) PIB-based composite encapsulants and (d) PVB-based encapsulants. (e) calculated CR measured for steel panels coated with PIB- and PVB-based encapsulants versus h-*BN content, showing the corresponding B-spline fitting.*

Figure 5.6a,c display the Nyquist plots recorded for PIB- and PVB-based samples, respectively. The standard equivalent circuit for corrosion studies in case of coated samples is shown in the insets of Figure 5.6a,c and is described by R_s, Q_c, R_c, Q_{dl}, and R_t.[436] Each plot reveals a distorted high-frequency semicircle linked to the barrier property of the coating; larger semicircle radii indicate superior corrosion protection.[400] The results partially reflect those obtained calculating the corrosion rates from Tafel plots, with the best samples being PIB2.0 (instead of PIB0.5) and PVB5.0 for PIB- and PVB-based coatings, respectively.

Table 5.2 Electrochemical parameters of PIB- and PVB-based composite encapsulant coatings with different h-*BN contents, obtained from the Tafel analysis.*

Sample	**E_{corr} (V)**	**i_{corr} (µA cm^{-2})**	**CR (mm yr^{-1})**	**η_p (%)**
PIB	−0.417	$2.94 \cdot 10^{-2}$	$3.41 \cdot 10^{-4}$	N/A
PIB0.5	−0.244	$1.28 \cdot 10^{-3}$	$1.49 \cdot 10^{-5}$	95.63
PIB2.0	-0.250	$2.68 \cdot 10^{-3}$	$3.11 \cdot 10^{-5}$	90.88
PIB5.0	-0.221	$2.36 \cdot 10^{-3}$	$2.74 \cdot 10^{-5}$	91.96
PVB	-0.500	$4.06 \cdot 10^{-2}$	$4.71 \cdot 10^{-4}$	N/A
PVB0.5	-0.308	$4.99 \cdot 10^{-3}$	$5.80 \cdot 10^{-5}$	87.70
PVB2.0	-0.289	$3.08 \cdot 10^{-3}$	$3.58 \cdot 10^{-5}$	92.41
PVB5.0	-0.180	$1.99 \cdot 10^{-4}$	$2.31 \cdot 10^{-6}$	99.51

The mechanical properties of the encapsulants were investigated through nanoindentation as reported in Section 5.3.3. Experiments were performed under both medium and high relative-humidity conditions to simulate biological environments and to elucidate how moisture influences their mechanical response. A frequency-dependent trend is observed for E' and E" in both the PVB-based and PIB-based samples, Figure 5.7 and Figure 5.9 show the trend of E' and E" for the PVB samples tested under medium and high humidity, respectively. Specifically, E' exhibits a parabolic trend, increasing with rising frequency, while E" shows a particularly noticeable minimum point around 9 Hz for all PVB-based samples. Figure 5.8 and Figure 5.10, on the other hand, show the trends of E' and E" for the PIB-based samples under the same environmental conditions (31 °C, 40% RH and 60% RH, respectively). These samples exhibit the same parabolic trend of E', while E" shows an absolute minimum point at a frequency of 3 Hz.

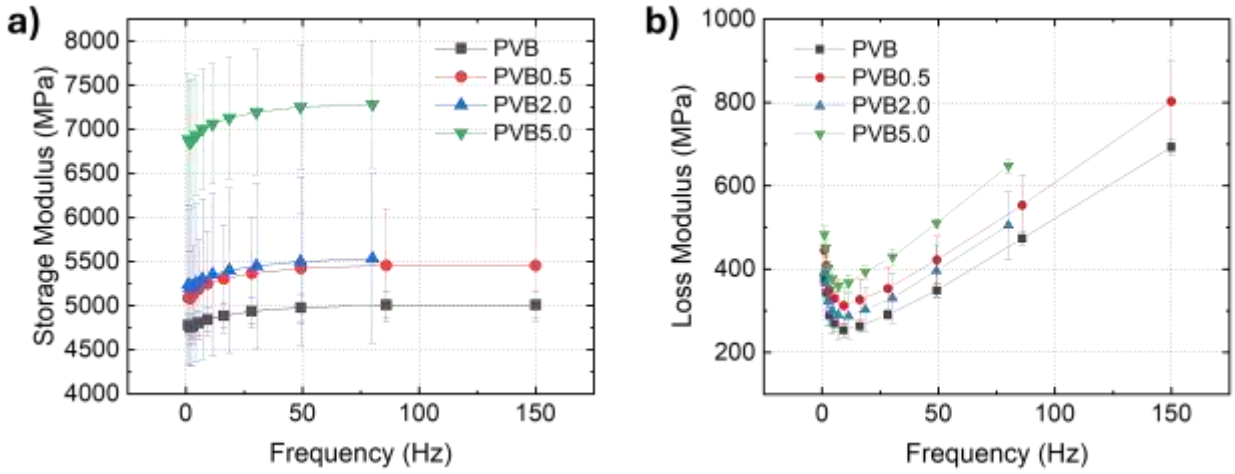

Figure 5.7 Trend of E' (a) and E'' (b) as a function of frequency for PVB-based samples at 40% RH.

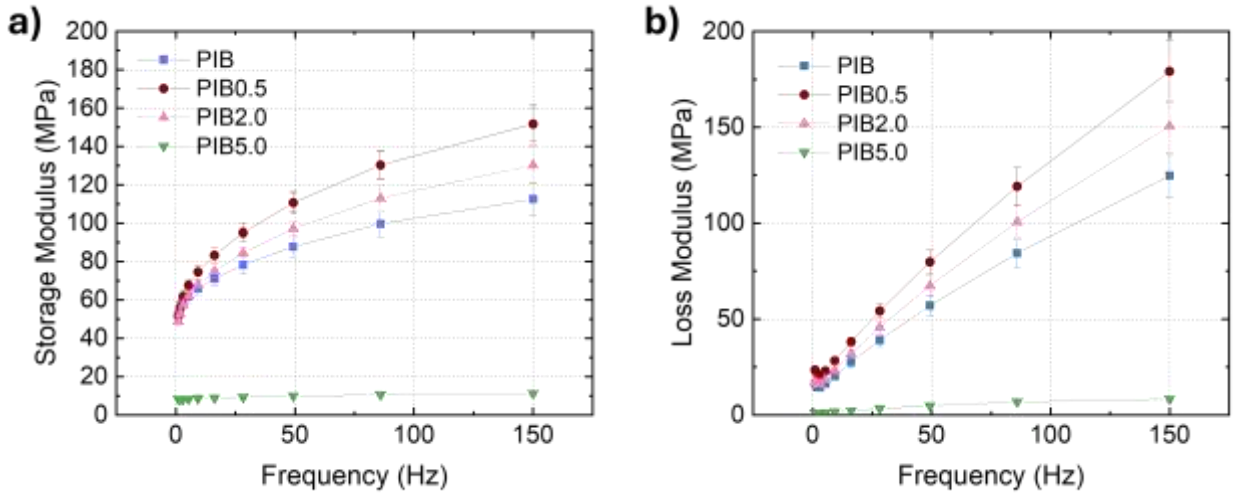

Figure 5.8 Trend of E' (a) and E'' (b) as a function of frequency for PIB-based samples at 40% RH.

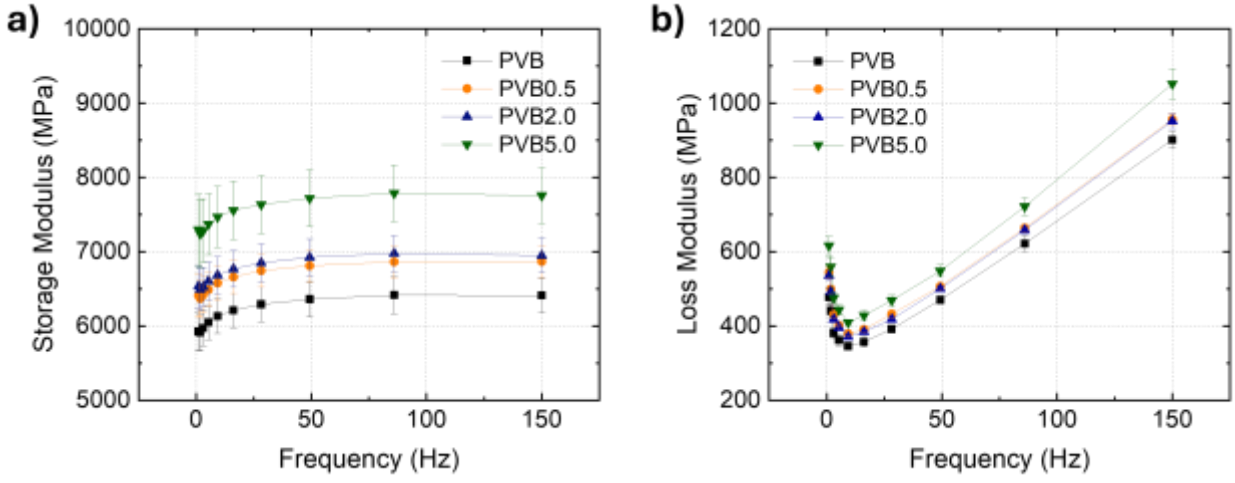

Figure 5.9 Trend of E' (a) and E'' (b) as a function of frequency for PVB-based samples at 60% RH.

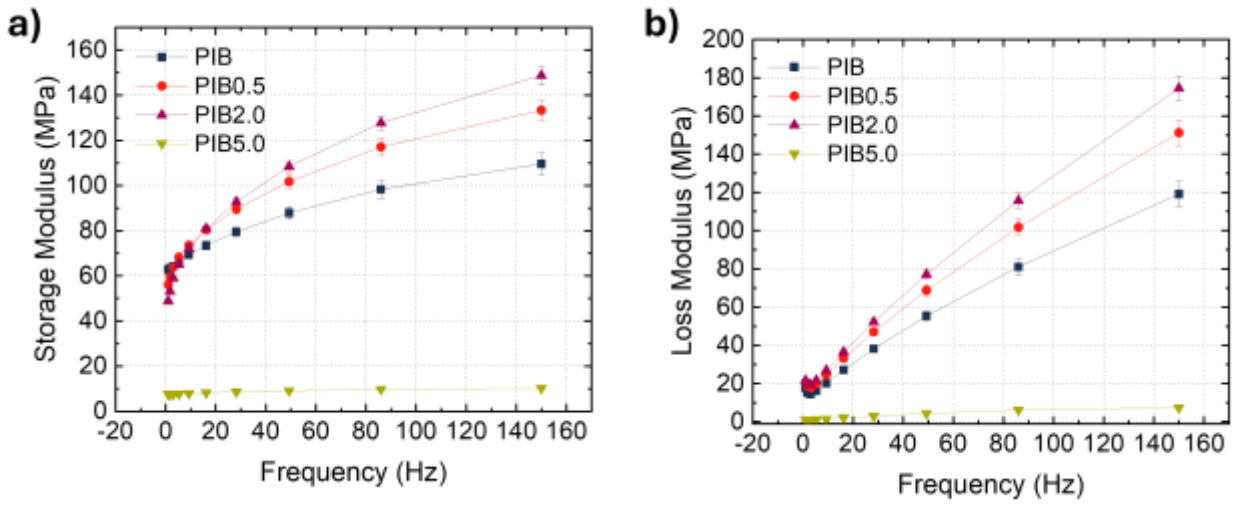

Figure 5.10 Trend of E' (a) and E'' (b) as a function of frequency for PIB-based samples at 60% RH.

Some variation in the E' and E'' values was also observed with changes in humidity. Figure 5.11, Figure 5.12, Figure 5.13, and Figure 5.14 present a direct sample-by-sample comparison of E' and E'' under the tested humidity conditions of 40% RH and 60% RH. With the increase in humidity, a clear difference in the viscoelastic response of the PVB-based samples is observed. Both E' (Figure 5.11) and E'' (Figure 5.12) exhibit increased values under higher humidity conditions. Despite this increase, E' maintains the same parabolic trend, while E'' continues to show a minimum at approximately 9 Hz.

The trends of the curves remain consistent for the PIB-based samples as well. However, these samples exhibit higher values for both E' (Figure 5.13) and E'' (Figure 5.14) only at the highest frequencies. Under moderate humidity conditions (40% RH), the E' values are generally elevated across most samples, except for PIB2.0, where higher values are observed at 60% RH.

Analyzing the results, significant differences in the viscoelastic responses of PVB- and PIB-based encapsulants have been observed. Generally, both at medium and high humidity levels, PVB-based samples exhibit better mechanical properties rather than PIB samples, as shown in Figure 5.15 and Figure 5.16, where PVB samples demonstrate higher values for both E' and E''. A frequency-dependent trend is observed for E' and E'' in both the PVB-based and PIB-based samples, with a parabolic trend for E' while the E'' curve exhibits a minimum point. Specifically, PIB samples reach their minimum value of energy dissipation at 3 Hz, while PVB samples show this effect at 9 Hz, indicating different frequency-dependent behaviors between the materials.

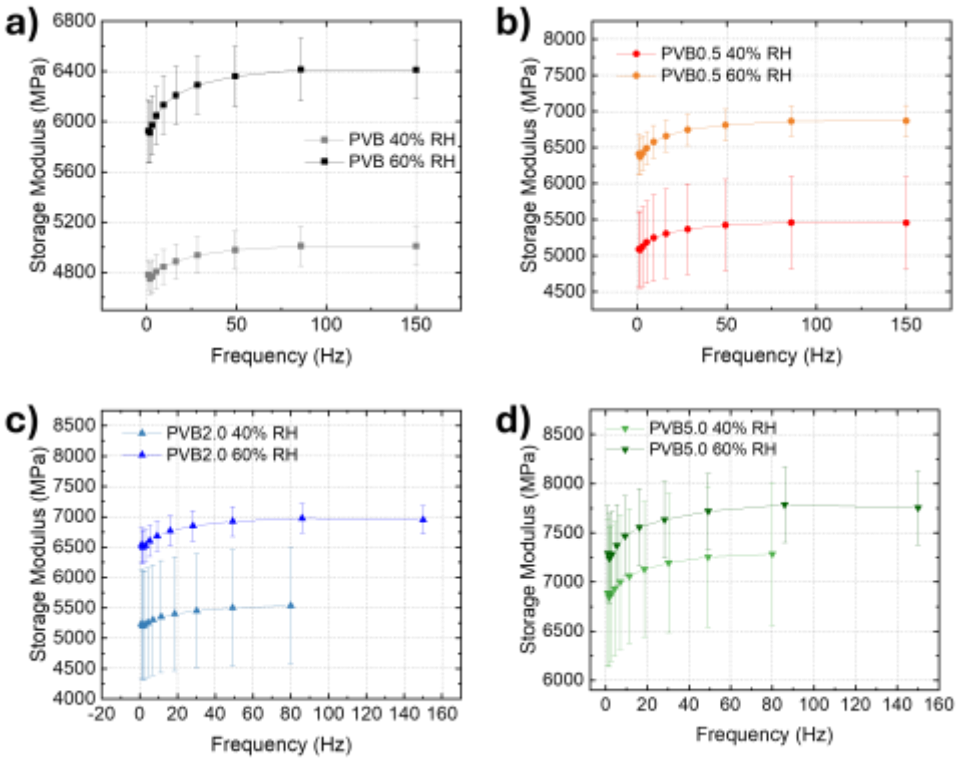

Figure 5.11 Comparison of the E' trends at 60% RH and 40% RH: (a) PVB, (b) PVB0.5, (c) PVB2.0, (d) PVB5.0.

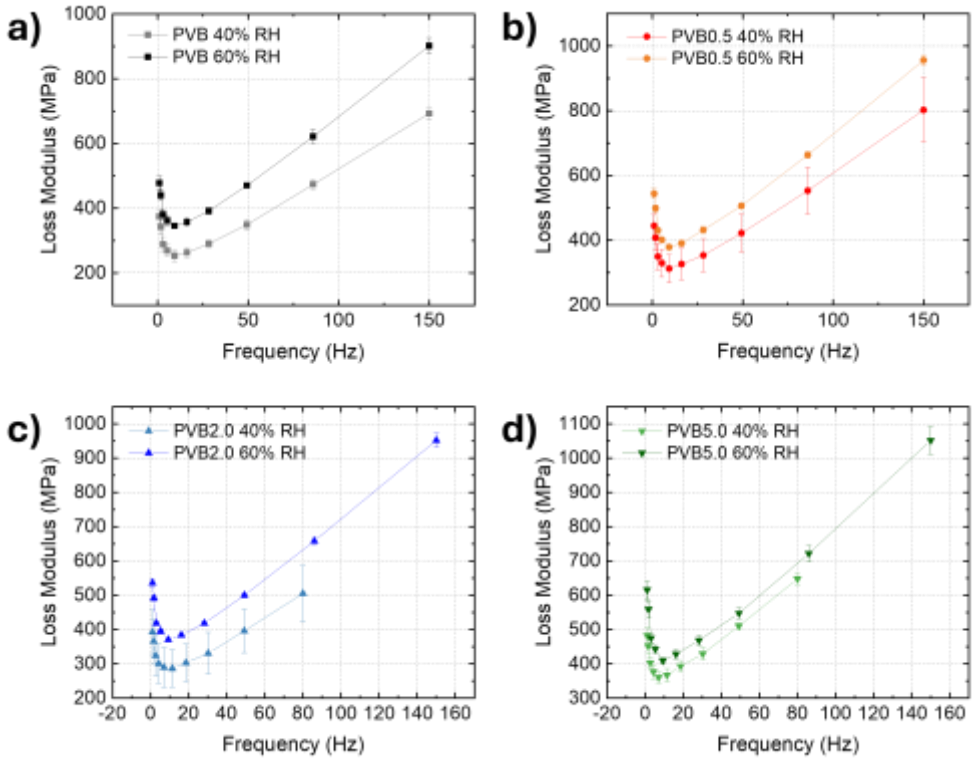

Figure 5.12 Comparison of the E'' trends at 60% RH and 40% RH: (a) PVB, (b) PVB0.5, (c) PVB2.0, (d) PVB5.0.

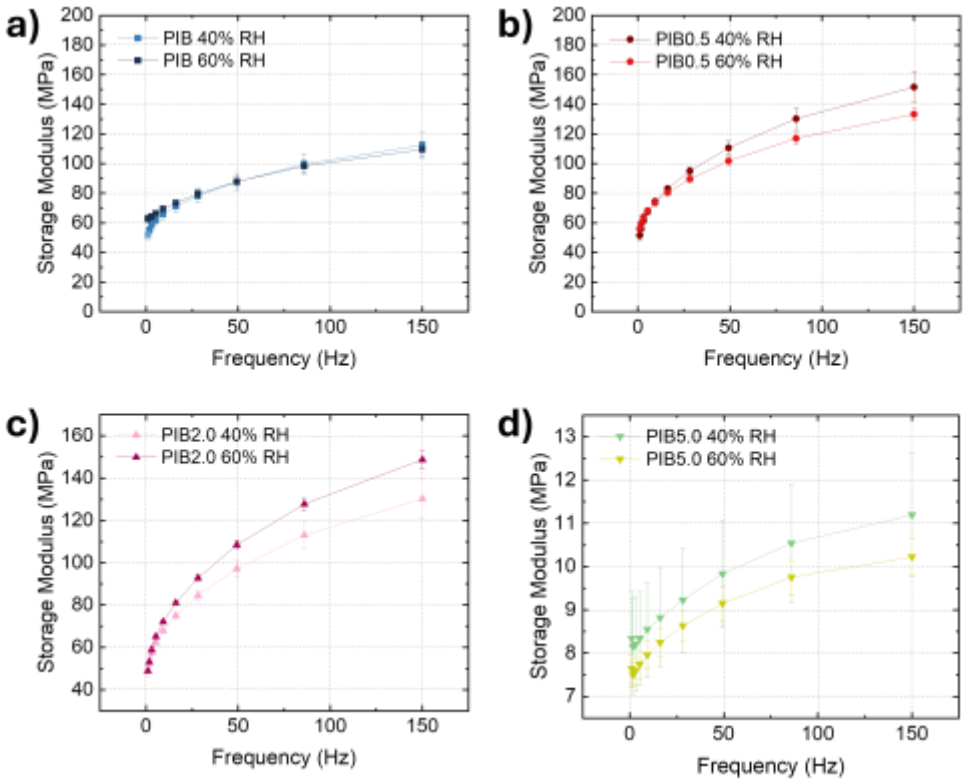

Figure 5.13 Comparison of the E' trends at 60% RH and 40% RH: (a) PIB, (b) PIB0.5, (c) PIB2.0, (d) PIB5.0.

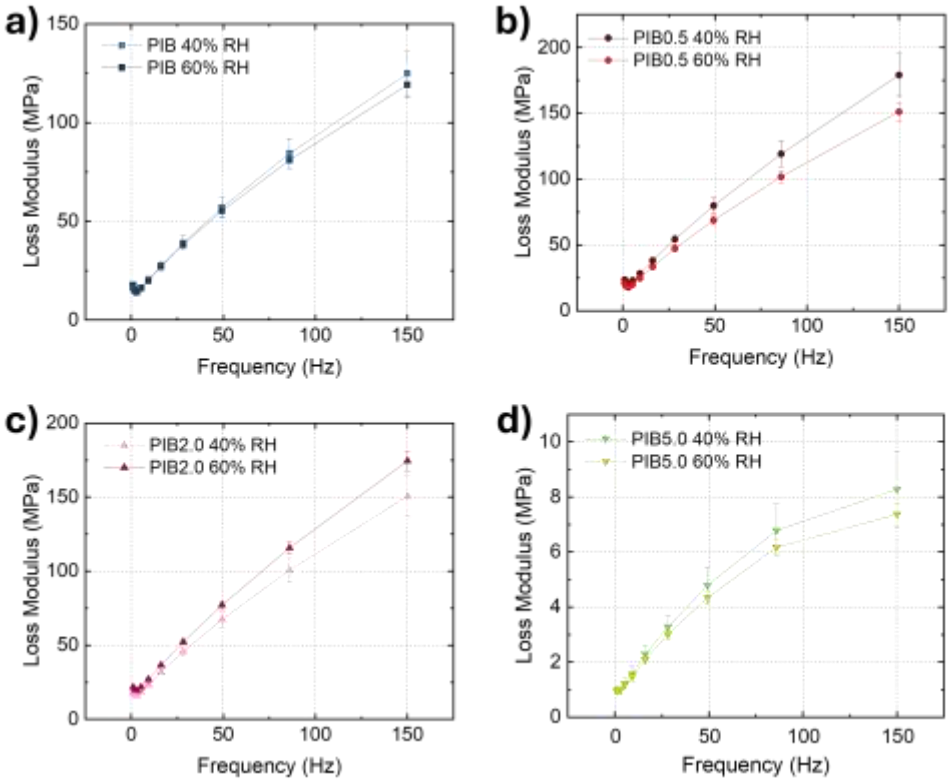

Figure 5.14 Comparison of the E'' trends at 60% RH and 40% RH: (a) PIB, (b) PIB0.5, (c) PIB2.0, (d) PIB5.0.

The performance of the materials also varies with humidity. PVB-based samples generally perform better at higher humidity levels (60% RH), showing enhanced storage and dissipation capabilities. In contrast, for PIB-based samples, the effect of humidity on E' and E" is less evident at low frequencies. However, at high frequencies, all PIB-based samples, except for PIB2.0, show higher E' and E" values at 40 RH% compared to 60 RH%. It is noteworthy that all tests conducted at high humidity exhibit lower dispersion around the mean values, indicating a more consistent material response under these environmental conditions. For PVB-based samples, this increased consistency shows a clearer link between the rise in E' and E" and higher *h*-BN concentrations. This effect is more noticeable when comparing PVB2.0 to PVB5.0, rather than the change from PVB0.5 to PVB2.0, as shown in Figure 5.9. The PVB5.0 sample demonstrates the highest energy storage and dissipation capabilities among the PVB-based samples, at both 40% RH and 60% RH.

Furthermore, in PIB-based samples, a trend of increasing E' and E" with *h*-BN concentration is observed at high humidity levels, a behavior not evident at 40% RH. Interestingly, this trend is notable only when increasing from 0 wt% to 0.5 wt% and then to 2 wt% *h*-BN loading. Indeed, PIB5.0 consistently shows very low values for E' and E", with a E" approximately ten times lower than that of PIB, PIB0.5 and PIB2.0 (Figure 5.10). This trend showing a decrease in performance with increasing the *h*-BN content above 2 wt% is consistent with the results obtained in corrosion tests and is probably linked to a deterioration of the composite caused by the presence of an excessive number of aggregates of *h*-BN.

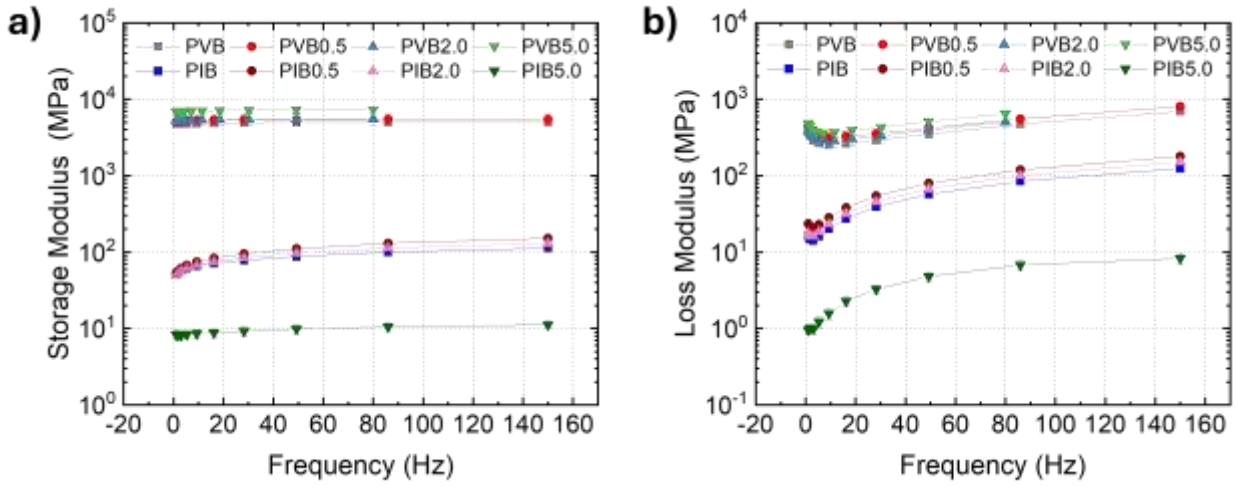

Figure 5.15 Trend of E' (a) and E" (b) at 40% RH for PVB- and PIB-based samples.

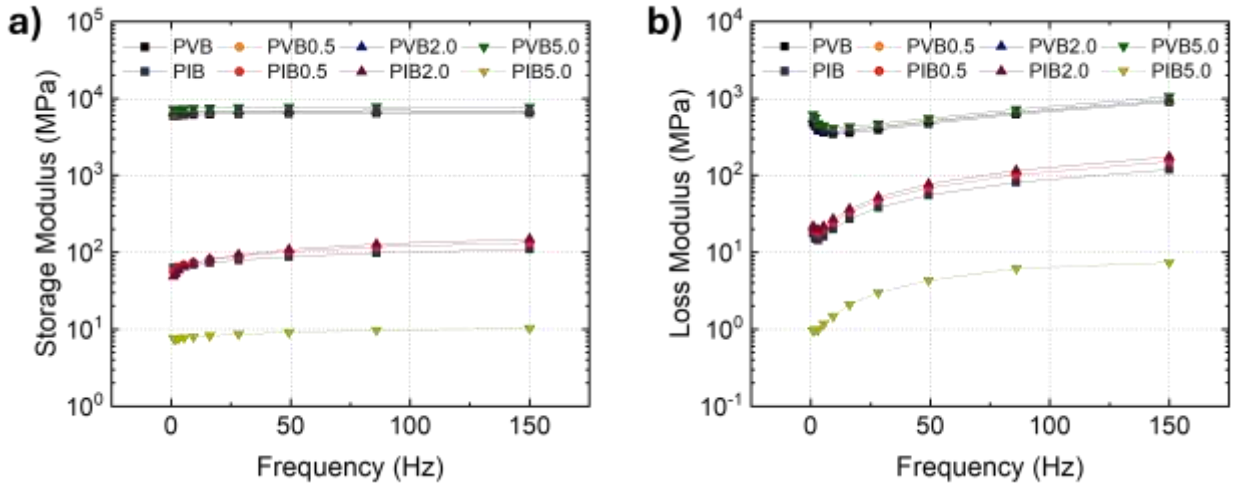

Figure 5.16 Trend of E' (a) and E'' (b) at 60% RH for PVB- and PIB-based samples.

Section 5.5 Effect of UV sterilization

The effect of the sterilization protocol on the performance of the encapsulants has been investigated. The choice to use a UV sterilization protocol was made due to the incompatibility of PVB-based samples with ethanol. The samples were subjected to UV irradiation at 30 W for 30 minutes and were then tested through FTIR analyses, water contact angle measurements and nanoindentation. Despite the demonstrated sensitivity of PIB to long exposures to UV irradiation,[599–602] the test with doses as low as those coming from the sterilization protocol is interesting as it could prove the usability of this polymer after being subjected to certain degrading conditions. Several applications of PIB, from photovoltaics encapsulation[192] to transparent adhesives, suggest that its degradation mechanisms could not lead to a detrimental loss in performance. For this reason, many manufacturers propose transparent pristine PIB homopolymers claiming their high UV resistance. Similarly, PVB was found to degrade upon prolonged exposure to UV irradiation,[603–606] but its large use as adhesive for safety glass lamination adhesive[585] indicate its suitability for environmental conditions subjected to UV exposures.

The FTIR ATR subtraction spectra reported in Figure 5.17c shows no chemical effect of the sterilization process on both PIB- and PVB-based samples. In this case, PIB5.0 and PVB5.0 were taken as examples for all the other *h*-BN-loaded samples. Contextually, the spectra acquired for all the samples are depicted in Figure 5.17a,b and show the same features as those acquired for non-treated samples (Figure 5.4a,b). In particular, no development of peaks related to oxidative groups is detected. A small difference in the broad band related to CH_3, CH_2 and CH stretching[422] is revealed, but hardly connected to degradation processes, rather than to a starting difference in the two samples.

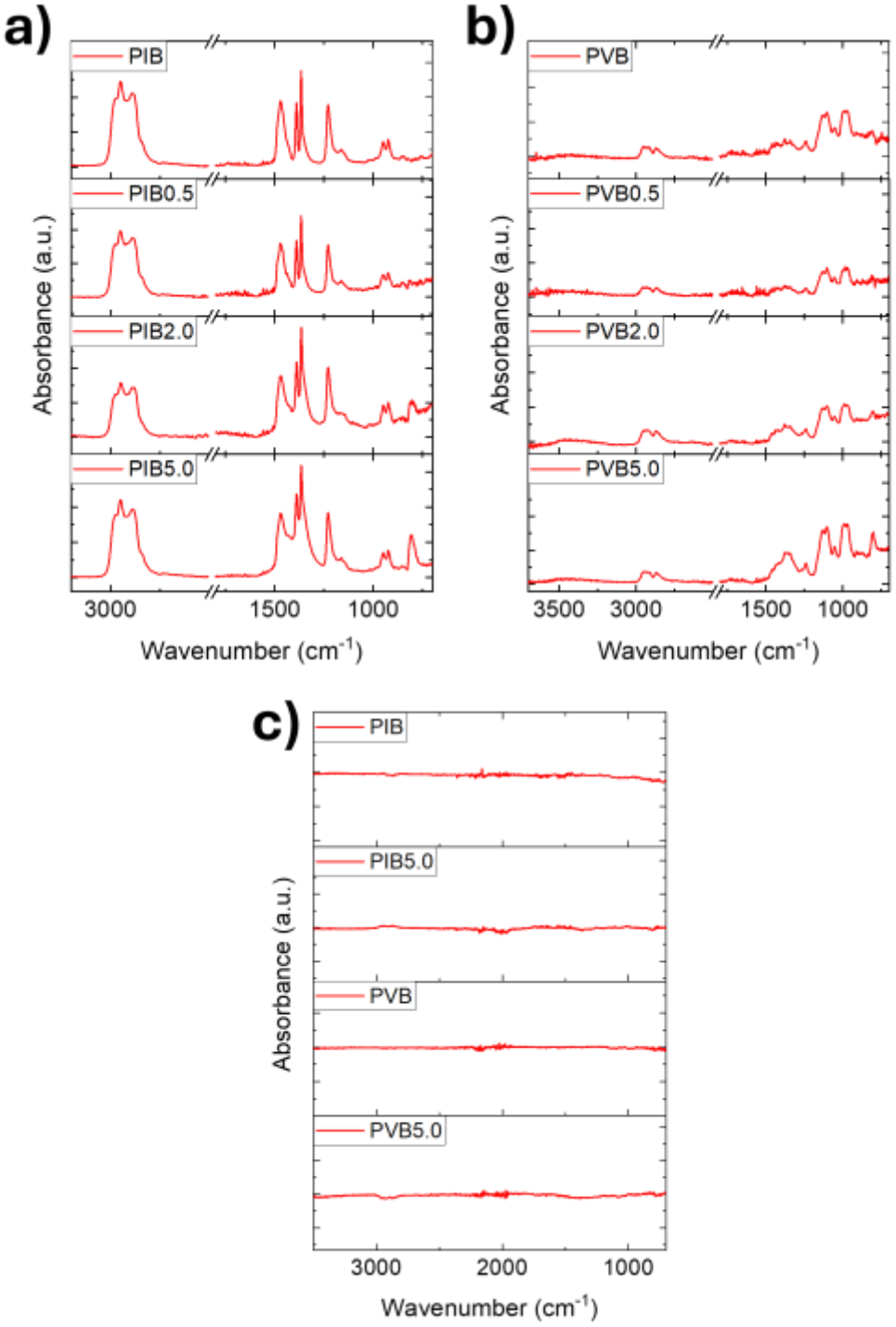

Figure 5.17 FTIR ATR spectra of (a) PIB-based and (b) PVB-based samples after undergoing the UV sterilization protocol. (c) FTIR ATR subtraction spectra of PIB, PIB5.0, PVB, and PVB5.0 samples, where the spectra acquired on non-treated samples were subtracted from the ones acquired on UV-treated samples.

Water CA measurements were also performed on UV-treated samples to evaluate potential surface modifications that could have changed the wettability of the samples. Figure 5.18 reports the contact angle value measured on treated and non-treated samples as a function of the loading of *h*-BN in the composite encapsulant. Almost no change in CA was detected for PVB-based samples, with the

values keeping the slightly ascending trend with increasing loading of *h*-BN. On the other hand, a general increase in water contact angle was noticed for all PIB-based samples, while the general trend relative to the amount of *h*-BN was maintained. This behavior is not expected after a potentially oxidative process, since the generation of oxidated moieties on the surface would have increased water wettability and thus decreased the CA. The most likely explanation lays in a removal of surface impurities present on the non-treated samples, which could have slightly lowered the water contact angle for the as-deposited samples.

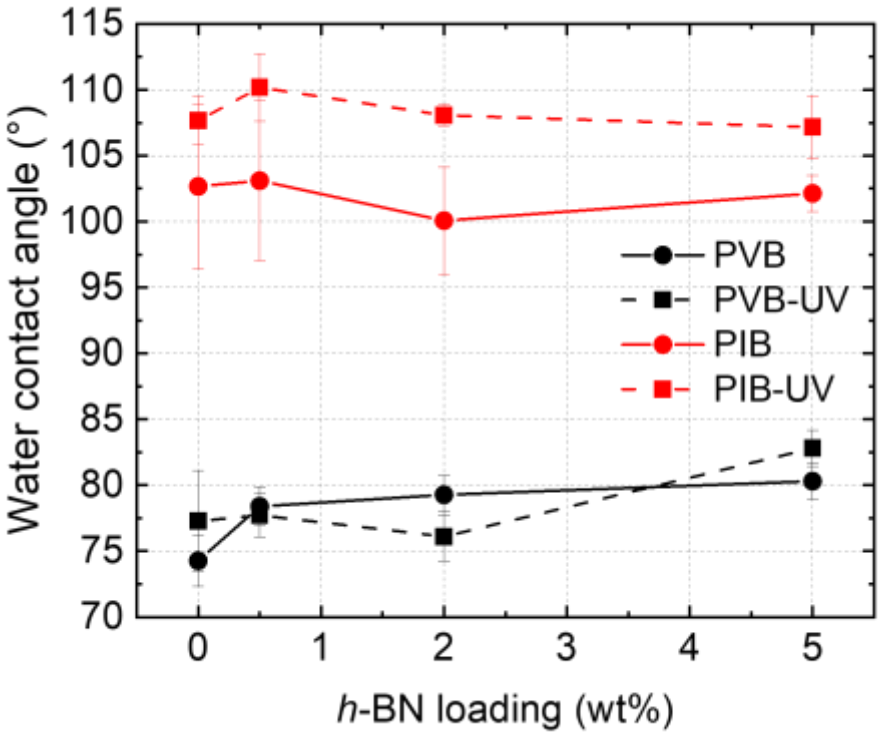

Figure 5.18 Water CA values of samples containing different loading of h-*BN, as deposited and after the UV sterilization treatment.*

Finally, the effect of the UV treatment on the mechanical properties of the encapsulants was studied through nanoindentation. The tests have been performed only at high (60%) RH, in order to account for the final application in a biological environment. Figure 5.19 and Figure 5.20 display the curves measured for PVB- and PIB-based samples, respectively, while Figure 5.21 reports the percentage variation of E' against the frequency of treated samples with respect to non-treated ones. Results show that, regarding PVB-based samples, no significant changes were observed in the E' of the tested specimens. Although a slight decrease was detected (in all samples except PVB2.0), the reduction was less than 10% and therefore does not constitute a critical alteration of the material's mechanical properties. This finding is consistent with the literature, which indicates that PVB retains stable

mechanical characteristics for exposure times of up to 912 h.[607] Similarly, the measured E" did not change after the UV treatment, nor as the curve shape, nor as the absolute values are concerned. On the other hand, major differences were detected for PIB-based samples. Relative to the as deposited specimens, a pronounced reduction in both E' and E" was measured for every formulation except PIB5.0. Thus, it can be stated that this kind of UV exposure alters the mechanical behavior of PIB, producing a softening effect. Moreover, the E" curves become monotonically increasing, and the local minimum previously observed at ≈3 Hz disappears. Given the previous results regarding possible chemical modifications to the polymeric matrices after the treatment, the most probable cause for the deterioration of the mechanical performance of PIB-based samples is that of a strong reduction in molecular weight, which is hardly detectable though FTIR and CA analyses.

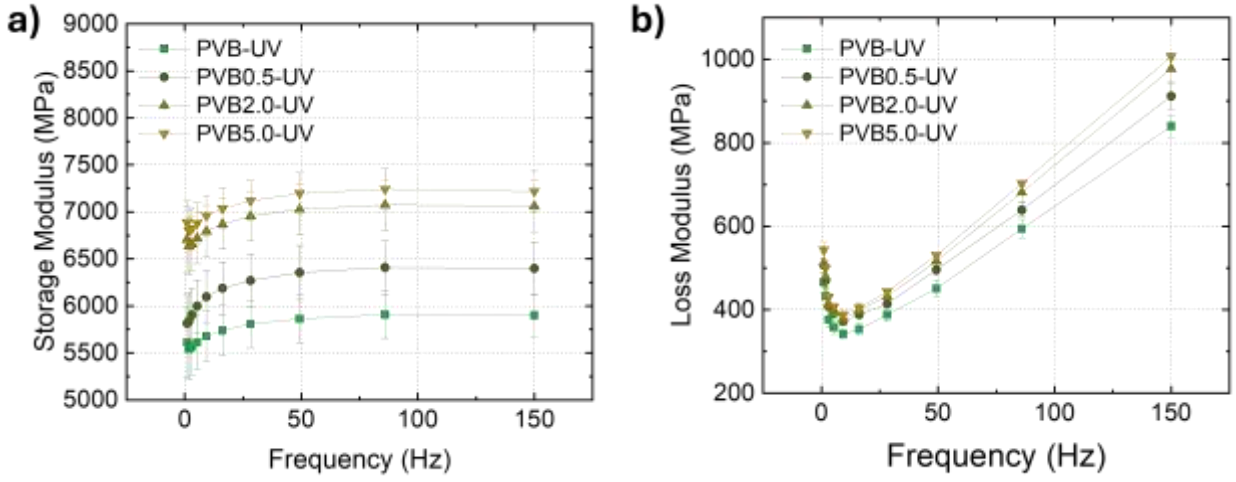

Figure 5.19 Trend of E' (a) and E" (b) as a function of frequency for PVB-based samples after the UV sterilization process.

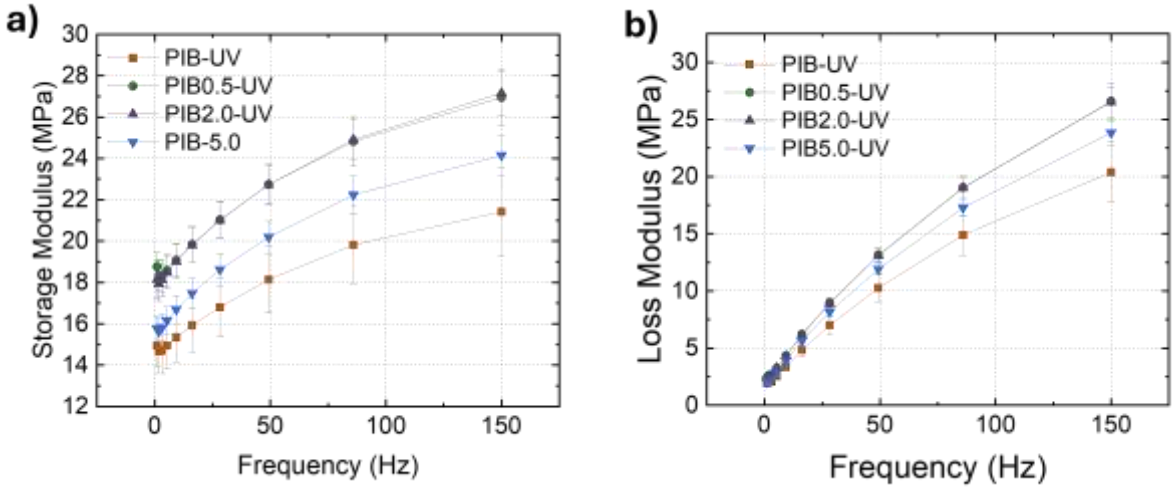

Figure 5.20 Trend of E' (a) and E" (b) as a function of frequency for PIB-based samples after the UV sterilization process.

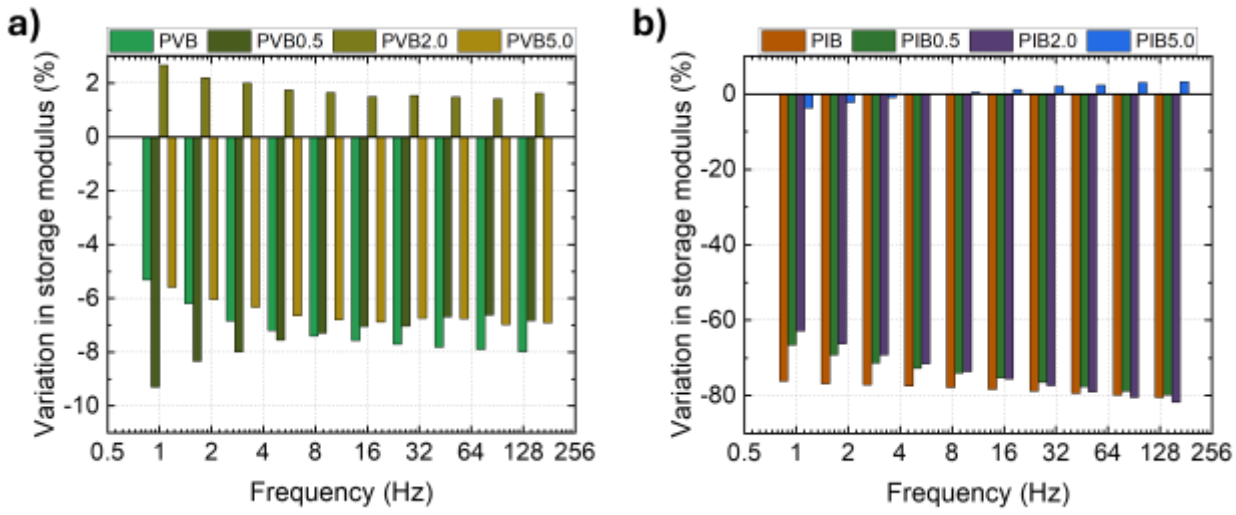

Figure 5.21 Variation in E' among as deposited and UV-treated a) PVB-based and b) PIB-based samples.

Section 5.6 Biocompatibility

The biocompatibility and cytotoxicity of the composite encapsulants was studied to assess whether these materials were suitable for applications in biological environments. Firstly, the two pristine polymers were tested with epithelial cells, then both the pristine polymers and the samples loaded with 5 wt% *h*-BN, taken as worst-case scenarios for all the other formulations, were tested with cortical neurons.

Both PVB and PIB have already been extensively studied for biomedical applications and their biocompatibility with a variety of cell types have been widely demonstrated.[608–612] On the contrary, to the knowledge of the candidate, no evidence of their compatibility with neuronal cells has been produced. Similarly, as already mentioned in Section 1.4.1, *h*-BN has been proven to be widely usable in bio applications, while no reference to its compatibility with neurons has been found.

Despite the known biocompatibility of the materials employed in this work, it was important to understand whether the preparation method – *i.e.*, solution blending and solvent evaporation – could modify the properties of the encapsulating layers and render them cytotoxic, *e.g.* by release of unevaporated solvent in the culturing medium.

Compatibility tests were carried out on PIB and PVB samples with epithelial cells. The tests were protracted up to DIV4 and confirmed the non-cytotoxicity of these materials, since no significant loss of viability was detected with respect to the reference substrate, as shown in Figure 5.22. Conversely, poor adhesion of the cells on the polymeric surfaces and a non-homogeneous growth were denoted. This characteristic did not prevent the cells from surviving but made it impossible to proceed with a

fixation protocol and acquire photoluminescence images. Nonetheless, having a poor adhesion of biological material to the encapsulant can be an advantageous factor since it could prevent or weaken the phenomena of foreign body response and gliosis, which usually deteriorate signal acquisition in chronical implants.[613,614]

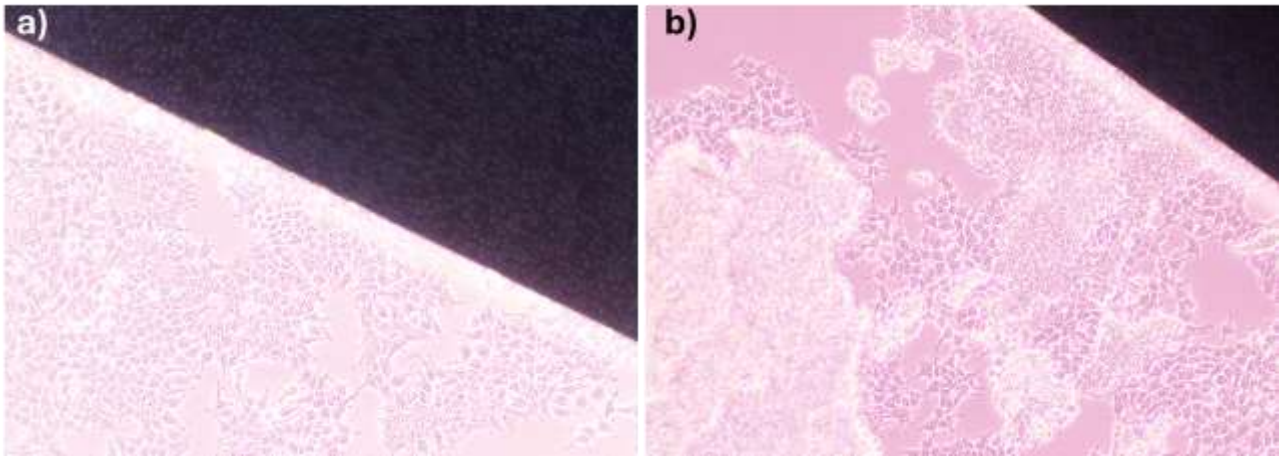

Figure 5.22 Brightfield images of epithelial cell cultures on (a) PIB and (b) PVB samples at DIV4.

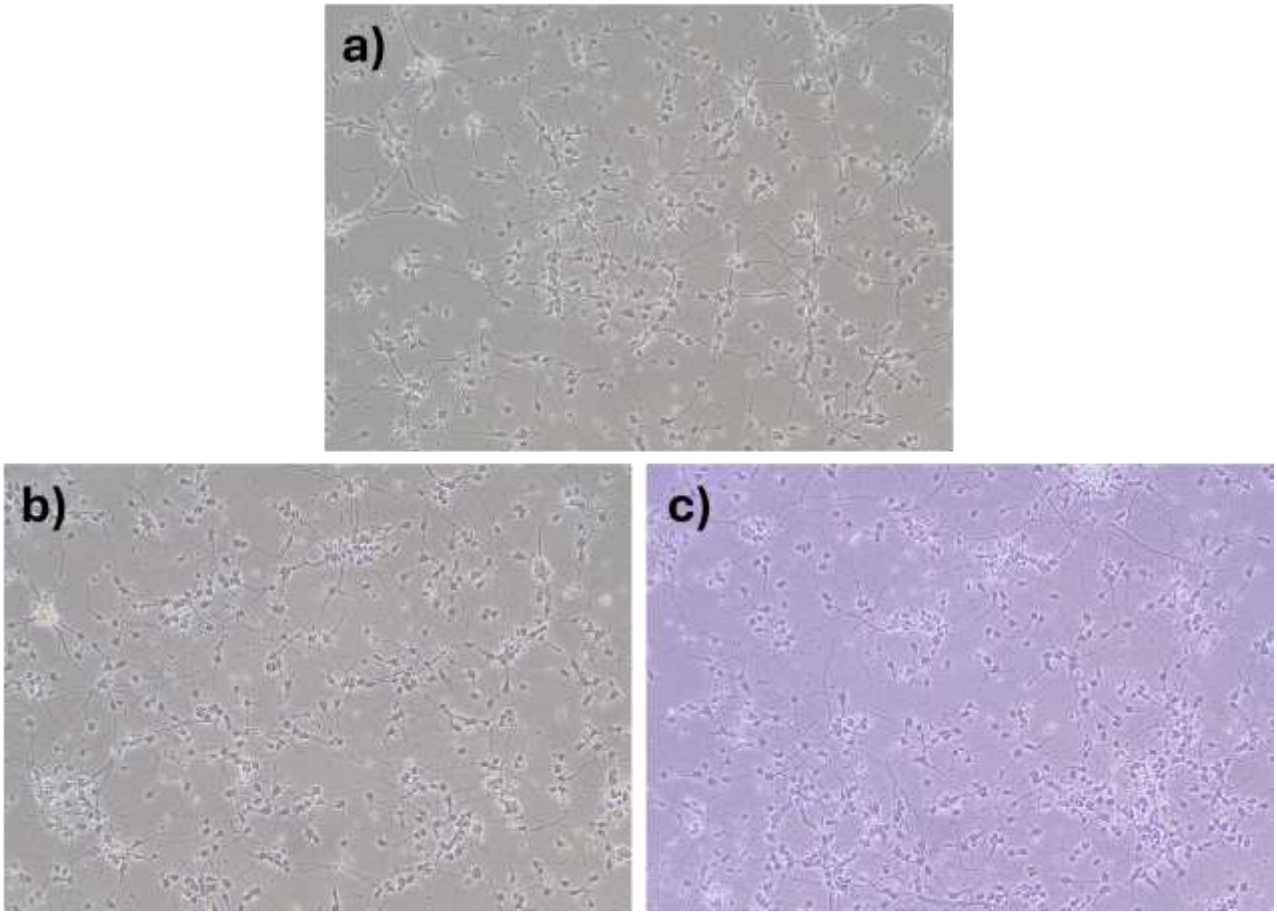

Figure 5.23 Brightfield images taken at DIV5 of the neuronal cultures on the reference substrate (a) alone, (b) co-cultured with PIB, and (c) co-cultured with PVB.

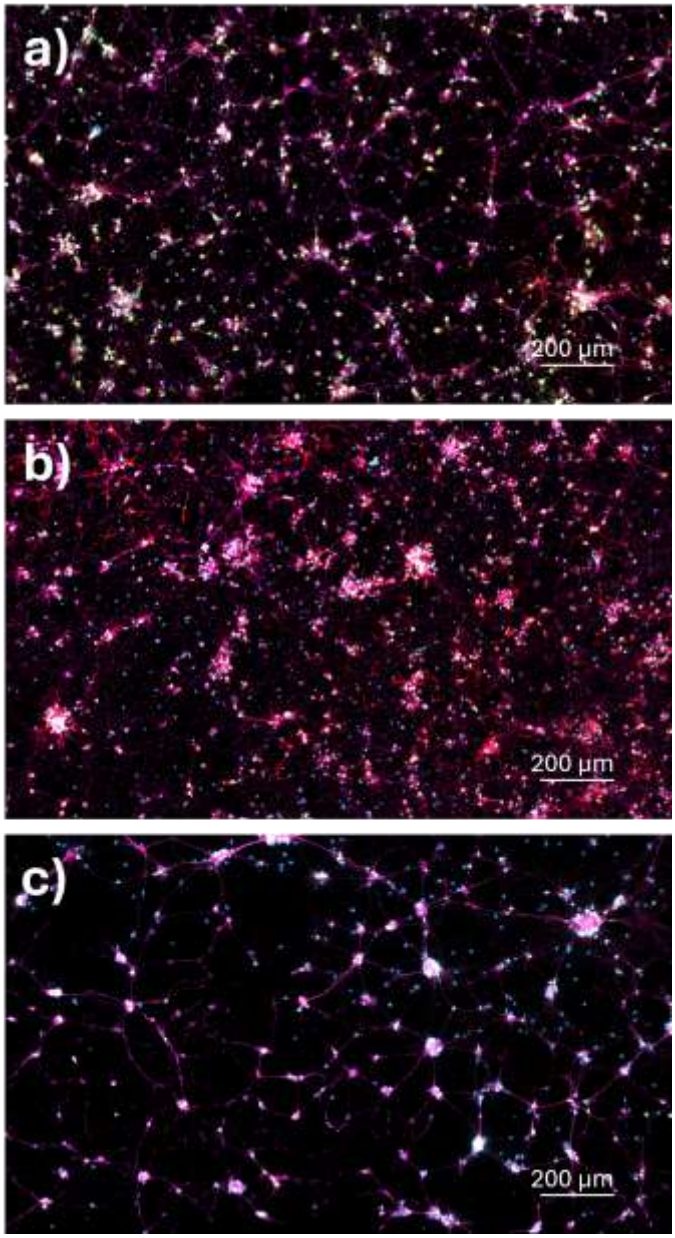

Figure 5.24 Immunofluorescence images taken at DIV15 of the neuronal cultures on the reference substrate (a) alone, (b) co-cultured with PIB, and (c) co-cultured with PVB.

The same samples were also tested culturing primary cortical neurons. Initial tests evidenced the same lack of adhesion on the substrates, which in this case prevented the neuron from creating a proper network and surviving. For this reason, the test protocol was modified to a co-culture, in which the neuronal cells were grown on a standard substrate with the sample of interest immersed in the same culturing medium. This allowed to evaluate whether the possible release of toxic substances from the studied encapsulants could be detrimental for the viability of neurons. Figure 5.23 depicts brightfield images taken at DIV5 of the neuronal cultures on the reference substrate alone, with PIB, and with PVB, while Figure 5.24 shows immunofluorescence images of the same taken at DIV15. The cells formed healthy networks both in control condition and when co-cultured with PIB and PVB samples,

indicating that these materials do not release cytotoxic compounds that alter their viability and functionality. In all the samples, neurons and astrocytes were alive and connected to form a network, indicating a healthy state. Some clamping of cells can be observed in all samples, but it is consistent with the relatively long duration of the culture (15 days). Based on these results, it can be concluded that PIB and PVB are biocompatible, and they do not interfere with the viability and functionality of in-vitro neuronal cell cultures.

Lastly, the same test protocol was employed using CD1 mouse embryonic hippocampal neurons to study the neurotoxicity of *h*-BN-loaded samples. The samples with the highest loading – *i.e.*, PIB5.0 and PVB5.0 – were taken as example and worst-case scenario. Figure 5.25 depicts brightfield images taken at DIV10 of neurons grown on a standard substrate alone and co-cultured with PIB5.0 and PVB5.0 samples. Results show that neurons co-cultured with both PIB5.0 and PVB5.0 substrates are partially compromised by DIV4 compared with the controls; by DIV10, neurons co-cultured with either PIB5.0 or PVB5.0 are completely degraded relative to the controls. The presence of *h*-BN in the samples therefore appears to be cytotoxic *in vitro*. The cause for this behavior could be searched in either the intrinsic neurotoxicity of *h*-BN or in the possible release of the residual solvent of the industrially produced *h*-BN in the culturing medium. In either case, this effect precludes the use of these composite encapsulants as they are for applications in neural environments.

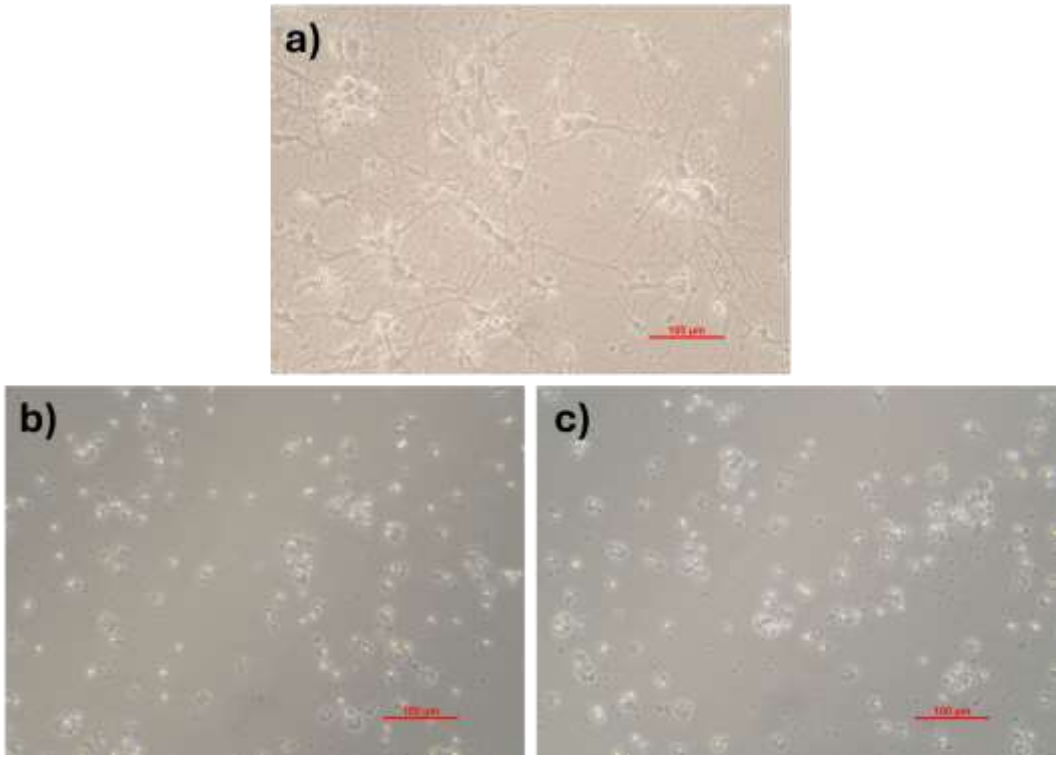

Figure 5.25 Brightfield images taken at DIV10 of the neuronal cultures on the reference substrate (a) alone, (b) co-cultured with PIB5.0, and (c) co-cultured with PVB5.0.

Section 5.7 Conclusions

This chapter sets out a preliminary study to determine whether PIB and PVB coatings reinforced with few-layer *h*-BN flakes can serve as thin, compliant, long-lived encapsulants for next-generation neural probes. Films just 2.6-3.5 µm thick – well below the 10 µm limit imposed by Corticale's SiNAPS architecture – were produced by doctor-blading. Spectroscopy and electron microscopy confirmed uniform polymer coverage and progressive incorporation of *h*-BN, although some major agglomeration appeared in PIB matrices at loadings higher than 2 wt%. All formulations shifted the E_{corr} of carbon steel coupons toward nobler values, but PVB/*h*-BN out-performed PIB analogues: the PVB film with 5 wt% *h*-BN suppressed the corrosion rate by ~99.5% relative to neat PVB and showed the largest impedance semicircle, whereas PIB achieved optimal protection at only 0.5 wt% filler loading. Dynamic nano-indentation revealed that PVB composites also store and dissipate more mechanical energy than their PIB counterparts across relevant frequencies and humidity levels; conversely, excessive *h*-BN (>2 wt%) in PIB reduced the storage modulus by an order of magnitude, underscoring the need for controlled dispersion.

A short UV sterilization protocol (30 min, 30 W) left PVB chemistry, wettability, and mechanics virtually unchanged – consistently with its commercial use in UV-exposed glass laminates – whereas PIB softened markedly, suggesting chain scission and signaling that alternative less harsh sterilization methods may be necessary for PIB-based systems. Biocompatibility assays brought further information: neat PIB and PVB were harmless to HEK-293 cells and supported cortical neuron networks for 15 days in co-culture, but 5 wt% *h*-BN composites compromised neurons by DIV4 and caused complete degradation by DIV10. Whether this neurotoxicity stems from the flakes themselves or from residual solvent coming from industrial production, it precludes immediate use of the present *h*-BN-loaded formulations for chronic neural implants.

Overall, PVB/*h*-BN coatings combine sub-10 µm thickness, excellent moisture and ion barriers, mechanical robustness, and UV-sterilization resilience, making them the most promising encapsulant platform identified in this work. Before clinical translation, however, the *h*-BN component must be purified or functionalized to remove cytotoxic impurities, filler loadings and architectures must be tuned to achieve the best performance, and long-term *in vivo* studies are required. Poly(isobutylene), meanwhile, should be revisited only after strategies to mitigate UV sensitivity and filler agglomeration are in place. Resolving these challenges will pave the way toward reliable, flexible, and truly chronic neural interfaces encapsulated by *h*-BN-enhanced hybrid films.

Conclusions and outlook

The goal of this thesis is to summarize the PhD activity focused on the transfer of few-layer hexagonal boron nitride (*h*-BN) from ton-scale industrial manufacture to serviceable, multifunctional barrier films and to demonstrate their value in three widely separated application spaces: anticorrosion coatings for steel in saline media, encapsulants for perovskite photovoltaics and candidate protective layers for chronic neural interfaces. In the opening chapters the extraordinary in-plane bonding, 6 eV band gap, chemical inertness and high phonon-mediated thermal conductivity that set *h*-BN apart from graphene and oxide glasses were surveyed. A detailed account of wet-jet-milling has shown how the production process used by BeDimensional S.p.A. could turn bulk powders into flakes that are mostly thinner than 10 layers, with a lateral size mode of about 100 nm, while running at a continuous production rate of ~1.2 kg h^{-1}. X-ray diffraction revealed the expected (002) reflection at 26.7°, but with a broadened full width at half maximum, while transmission-electron and atomic-force microscopy analyses confirmed the morphology of the flakes. Thermogravimetric characterization indicated solvent residue below 1.5 wt % and an oxidation onset well above 800 °C, proving that the industrial powder retained laboratory-grade crystallinity and purity.

Starting from these results, the thesis first tackled corrosion of carbon steel. Few-layer *h*-BN flakes were dispersed in a high-viscosity poly-isobutylene (PIB) binder and cast as 60 µm coatings. Increasing the filler content to 5 wt% raised the water contact angle from 88° to 101°, imparting hydrophobicity to the coatings. Electrochemical polarization tests in 3.5 % NaCl (according to ASTM G5-14 standard) have shown that the corrosion current density drops from $3.9 \cdot 10^{-2}$ µA cm^{-2} for neat PIB to $6.4 \cdot 10^{-4}$ µA cm^{-2} for the 5 wt% composite, translating into a corrosion rate of $7.4 \cdot 10^{-6}$ mm yr^{-1} – two orders of magnitude lower than the polymer alone and better than the state-of-the-art reported in literature for similar systems. Impedance spectra displayed semicircles whose diameters grew with the *h*-BN loading, and 1000 h immersion tests left the 5 wt% unaltered, while the pristine polymer has shown incipient pitting. Thus, a minimal quantity of *h*-BN sufficed to lengthen the diffusional path for chloride ions and water and to deliver marine-grade protection without sacrificial pigments.

The investigation then shifted to perovskite solar cells, in which instability toward moisture, oxygen and heat still prevents commercial deployment. A low molecular weight, liquid PIB was blade-cast into 600 µm interlayers, either pristine or loaded with 5 wt% *h*-BN, and laminated between float glass sheets at only 90 °C. Calcium corrosion experiments on glass/encapsulant/glass mock-ups gave a water-vapor transmission rate of $2 \cdot 10^{-5}$ g m^{-2} d^{-1} for the composite: an order of magnitude better than

the plain polymer. Infra-red thermography has shown that the presence of *h*-BN accelerated cool-down by 11%, confirming a useful lateral heat-spreading function. When mesoscopic 1 cm^2 CsFA/MA triple-cation cells were laminated, power conversion efficiency fell by less than 1%, and under ISOS-D-2 (85 °C in the dark) and ISOS-L-1 (one-sun light soaking) the encapsulated devices retained more than 80% of their initial efficiency for over 1000 hours, whereas unprotected references failed within a few tens of hours. Five-cell, 10 cm^2 modules followed the same trend: after 200 thermal shocks between -40 and +85 °C the composite retained 85% of its initial performance, survived 10 modified humidity-freeze cycles that included immersion in water, and released less than 1 µg cm^{-2} of lead into a water bath compared with more than 60 µg for bare modules. These results constitute a demonstration that a printable, edge-sealant-free encapsulant can satisfy International Electrotechnical Commission (IEC)-analogous stress tests on large-area perovskites.

After the aforementioned enabling tests, the work explored whether sub-10 µm thick encapsulants could be adapted to neural microelectrodes whose shafts are only 100 µm wide. Doctor-bladed films on silicon wafers were 2.6 µm thick for polyvinyl butyral (PVB) matrices and 3.5 µm for PIB, well below the geometric ceiling imposed by Corticale's SiNAPS probes. Dynamic nano-indentation under high humidity has shown that PVB increased both storage and loss moduli when reinforced with 5 wt% *h*-BN, whereas PIB softened above 2 wt%, likely because of flake agglomeration. Steel panels coated with PVB/*h*-BN exhibited corrosion rates as low as $2.3 \cdot 10^{-6}$ mm yr^{-1} and a calculated inhibition efficiency of 99.5 %. Epithelial HEK-293 cultures adhered poorly but remained viable on the pristine polymers, and co-cultured cortical neurons formed healthy networks up to DIV15. However, when 5 wt% loaded composites were tested in co-culture, neurons began to degenerate after DIV4 and collapsed by DIV10, pointing to residual solvent or inherent material toxicity. A standard brief ultraviolet sterilization process left PVB chemistry and mechanics unchanged, but probably induced chain scission in PIB, further recommending PVB as the more robust host.

Taken together, the thesis establishes that industrially exfoliated *h*-BN can endow thin, flexible polymers with enhanced impermeability, galvanic inertness and improved thermal conductivity while remaining compatible with low-temperature, roll-to-roll processing. A filler content of only 5 wt% is sufficient to unlock marine anticorrosion properties, IEC-compliant perovskite encapsulation and mechanically credible coatings for neural electronics. The principal limitations encountered were the agglomeration-induced softening of PIB at high loadings and the unexpected neurotoxicity observed for unpurified *h*-BN composites.

This work thus demonstrated the applicability of industrially produced *h*-BN according to the method developed by BeDimensional S.p.A. in encapsulating systems for both metal protection in marine

environments and perovskite solar cells and modules. Results have shown how this material is suitable for high technology readiness level (TRL) applications in industrial fields, while it is still to be fully studied in biological applications. Due to the industrial focus of this PhD work, the preliminary study performed in the field of neural sensors was taken as a clear indication that its use in biological and neurological environment is not recommended without a joint development involving both the material itself and its production process, aimed at improving its biocompatibility and performance.

Future work should therefore target the purification and possible edge functionalization of wet-jet-milled flakes to remove residual N-methyl-pyrrolidone and to passivate reactive defect sites, which could be detrimental for the biocompatibility of the material. The refine of dispersion chemistry would help increase the agglomeration threshold for PIB and improve the overall performance. As already mentioned, in order to maintain a high TRL for these applications, a new process development at the industrial scale is needed to provide the material with the required chemical properties and biocompatibility performance. A study of this extent was not in the focus of this PhD and was not therefore undertaken.

In addition, a deeper characterization of encapsulated neural implants would be needed once the biocompatibility of the material has been addressed. Chronic implantation studies extending beyond six months *in vivo* will be essential to quantify foreign-body response and long-term signal integrity, while insertion and extraction tests both in dummy substrates and real brain tissue is needed to define the suitability of the encapsulant as an interface between the sensor and the biological tissue and as a reinforcing layer able to guarantee a safe extraction at the end-of-life of the sensor.

Finally, the study of perovskite solar cells could be implemented with accelerated outdoor exposure of meter-scale perovskite panels to establish lifetime energy yields and lead-containment performance. Additionally, the circularity of PIB/*h*-BN encapsulants could be demonstrated through tests on the solventless delamination of spent layers, which could cement *h*-BN composites as sustainable barrier solutions for the encapsulation of even more environmentally friendly solar modules.

References

1. Geim AK, Novoselov KS. The rise of graphene. *Nat Mater*. 2007;6(3):183-191. doi:10.1038/nmat1849
2. Novoselov KS, Geim AK, Morozov S V, et al. Electric Field Effect in Atomically Thin Carbon Films. *Science (80-)*. 2004;306(5696):666-669. doi:10.1126/science.1102896
3. Nicolosi V, Chhowalla M, Kanatzidis MG, Strano MS, Coleman JN. Liquid Exfoliation of Layered Materials. *Science (80-)*. 2013;340(6139):1226419. doi:10.1126/science.1226419
4. Wang H, Yuan H, Sae Hong S, Li Y, Cui Y. Physical and chemical tuning of two-dimensional transition metal dichalcogenides. *Chem Soc Rev*. 2015;44(9):2664-2680. doi:10.1039/C4CS00287C
5. Kaul AB. Two-dimensional layered materials: Structure, properties, and prospects for device applications. *J Mater Res*. 2014;29(3):348-361. doi:10.1557/jmr.2014.6
6. Miró P, Audiffred M, Heine T. An atlas of two-dimensional materials. *Chem Soc Rev*. 2014;43(18):6537-6554. doi:10.1039/C4CS00102H
7. Ellis JK, Lucero MJ, Scuseria GE. The indirect to direct band gap transition in multilayered MoS2 as predicted by screened hybrid density functional theory. *Appl Phys Lett*. 2011;99(26):261908. doi:10.1063/1.3672219
8. Chhowalla M, Shin HS, Eda G, Li L-J, Loh KP, Zhang H. The chemistry of two-dimensional layered transition metal dichalcogenide nanosheets. *Nat Chem*. 2013;5(4):263-275. doi:10.1038/nchem.1589
9. Novoselov KS, Jiang D, Schedin F, et al. Two-dimensional atomic crystals. *Proc Natl Acad Sci*. 2005;102(30):10451-10453. doi:10.1073/pnas.0502848102
10. Bolotin KI, Sikes KJ, Jiang Z, et al. Ultrahigh electron mobility in suspended graphene. *Solid State Commun*. 2008;146(9-10):351-355. doi:10.1016/j.ssc.2008.02.024
11. Mayorov AS, Gorbachev R V, Morozov S V, et al. Micrometer-Scale Ballistic Transport in Encapsulated Graphene at Room Temperature. *Nano Lett*. 2011;11(6):2396-2399. doi:10.1021/nl200758b
12. Antonatos N, Ghodrati H, Sofer Z. Elements beyond graphene: Current state and perspectives of elemental monolayer deposition by bottom-up approach. *Appl Mater Today*. 2020;18:100502. doi:10.1016/j.apmt.2019.100502
13. Addou R, Colombo L. Introduction. In: Addou R, Colombo L, eds. *Defects in Two-Dimensional Materials*. Elsevier; 2022:1-5. doi:10.1016/B978-0-12-820292-0.00007-0
14. Jayakumar A, Mathew S, Radoor S, Kim JT, Rhim J-W, Siengchin S. Recent advances in two-dimensional nanomaterials: properties, antimicrobial, and drug delivery application of nanocomposites. *Mater Today Chem*. 2023;30:101492. doi:10.1016/j.mtchem.2023.101492
15. Cain JD, Hanson ED, Shi F, Dravid VP. Emerging opportunities in the two-dimensional chalcogenide systems and architecture. *Curr Opin Solid State Mater Sci*. 2016;20(6):374-387. doi:10.1016/j.cossms.2016.06.001
16. Hess P. Bonding, structure, and mechanical stability of 2D materials: the predictive power of the periodic table. *Nanoscale Horizons*. 2021;6(11):856-892. doi:10.1039/D1NH00113B
17. Bonaccorso F, Bartolotta A, Coleman JN, Backes C. 2D-Crystal-Based Functional Inks. *Adv Mater*. 2016;28(29):6136-6166. doi:https://doi.org/10.1002/adma.201506410
18. Coleman JN, Lotya M, O'Neill A, et al. Two-Dimensional Nanosheets Produced by Liquid Exfoliation of Layered Materials. *Science (80-)*. 2011;331(6017):568-571. doi:10.1126/science.1194975
19. Turunen M, Brotons-Gisbert M, Dai Y, et al. Quantum photonics with layered 2D materials. *Nat Rev Phys*. 2022;4(4):219-236. doi:10.1038/s42254-021-00408-0
20. Ahn EC. 2D materials for spintronic devices. *npj 2D Mater Appl*. 2020;4(1):17. doi:10.1038/s41699-020-0152-0
21. Aftab S, Hussain S, Al-Kahtani AA. Latest Innovations in 2D Flexible Nanoelectronics. *Adv Mater*. 2023;35(42):2301280. doi:10.1002/adma.202301280
22. Zhao Z, Fang Z, Han X, et al. A general thermodynamics-triggered competitive growth model to guide the synthesis of two-dimensional nonlayered materials. *Nat Commun*. 2023;14(1):958. doi:10.1038/s41467-023-36619-5
23. Bonaccorso F, Lombardo A, Hasan T, Sun Z, Colombo L, Ferrari AC. Production and processing of graphene and 2d crystals. *Mater Today*. 2012;15(12):564-589. doi:https://doi.org/10.1016/S1369-7021(13)70014-2
24. Li X, Cai W, An J, et al. Large-Area Synthesis of High-Quality and Uniform Graphene Films on Copper Foils. *Science (80-)*. 2009;324(5932):1312-1314. doi:10.1126/science.1171245
25. Hernandez Y, Nicolosi V, Lotya M, et al. High-yield production of graphene by liquid-phase exfoliation of graphite. *Nat Nanotechnol*. 2008;3(9):563-568. doi:10.1038/nnano.2008.215

26. Meyer JC, Geim AK, Katsnelson MI, Novoselov KS, Booth TJ, Roth S. The structure of suspended graphene sheets. *Nature*. 2007;446(7131):60-63. doi:10.1038/nature05545

27. Kroto HW, Heath JR, O'Brien SC, Curl RF, Smalley RE. C60: Buckminsterfullerene. *Nature*. 1985;318(6042):162-163. doi:10.1038/318162a0

28. Allen MJ, Tung VC, Kaner RB. Honeycomb Carbon: A Review of Graphene. *Chem Rev*. 2010;110(1):132-145. doi:10.1021/cr900070d

29. Iijima S. Helical microtubules of graphitic carbon. *Nature*. 1991;354(6348):56-58. doi:10.1038/354056a0

30. Lee HC, Liu W-W, Chai S-P, et al. Review of the synthesis, transfer, characterization and growth mechanisms of single and multilayer graphene. *RSC Adv*. 2017;7(26):15644-15693. doi:10.1039/C7RA00392G

31. Cooper DR, D'Anjou B, Ghattamaneni N, et al. Experimental Review of Graphene. *ISRN Condens Matter Phys*. 2012;2012:1-56. doi:10.5402/2012/501686

32. Orlita M, Faugeras C, Plochocka P, et al. Approaching the Dirac Point in High-Mobility Multilayer Epitaxial Graphene. *Phys Rev Lett*. 2008;101(26):267601. doi:10.1103/PhysRevLett.101.267601

33. Castro Neto AH, Guinea F, Peres NMR, Novoselov KS, Geim AK. The electronic properties of graphene. *Rev Mod Phys*. 2009;81(1):109-162. doi:10.1103/RevModPhys.81.109

34. Weiss NO, Zhou H, Liao L, et al. Graphene: An Emerging Electronic Material. *Adv Mater*. 2012;24(43):5782-5825. doi:https://doi.org/10.1002/adma.201201482

35. Bonaccorso F, Sun Z, Hasan T, Ferrari AC. Graphene photonics and optoelectronics. *Nat Photonics*. 2010;4(9):611-622. doi:10.1038/nphoton.2010.186

36. Morozov S V, Novoselov KS, Katsnelson MI, et al. Giant Intrinsic Carrier Mobilities in Graphene and Its Bilayer. *Phys Rev Lett*. 2008;100(1):016602. doi:10.1103/PhysRevLett.100.016602

37. Akturk A, Goldsman N. Electron transport and full-band electron-phonon interactions in graphene. *J Appl Phys*. 2008;103(5):53702. doi:10.1063/1.2890147

38. Sun Y, Sun M, Xie D. Graphene Electronic Devices. In: Zhu H, Xu Z, Xie D, Fang YBT-G, eds. *Graphene*. Elsevier; 2018:103-155. doi:10.1016/B978-0-12-812651-6.00005-7

39. Wu Y, Farmer DB, Xia F, Avouris P. Graphene Electronics: Materials, Devices, and Circuits. *Proc IEEE*. 2013;101(7):1620-1637. doi:10.1109/JPROC.2013.2260311

40. Sood AK, Lund I, Puri YR, et al. Review of Graphene Technology and Its Applications for Electronic Devices. In: Ebrahimi F, ed. *Graphene - New Trends and Developments*. InTech; 2015. doi:10.5772/61316

41. Dash GN, Pattanaik SR, Behera S. Graphene for Electron Devices: The Panorama of a Decade. *IEEE J Electron Devices Soc*. 2014;2(5):77-104. doi:10.1109/JEDS.2014.2328032

42. Yung KC, Wu WM, Pierpoint MP, Kusmartsev FV. Introduction to graphene electronics – a new era of digital transistors and devices. *Contemp Phys*. 2013;54(5):233-251. doi:10.1080/00107514.2013.833701

43. Wang X-L, Dou SX, Zhang C. Zero-gap materials for future spintronics, electronics and optics. *NPG Asia Mater*. 2010;2(1):31-38. doi:10.1038/asiamat.2010.7

44. Britnell L, Gorbachev R V, Jalil R, et al. Field-Effect Tunneling Transistor Based on Vertical Graphene Heterostructures. *Science (80-)*. 2012;335(6071):947-950. doi:10.1126/science.1218461

45. Sung C-Y, Lee J. The ultimate switch. *IEEE Spectr*. 2012;49(2):32-59. doi:10.1109/MSPEC.2012.6139231

46. Mehr W, Dabrowski J, Scheytt JC, et al. Vertical Graphene Base Transistor. *IEEE Electron Device Lett*. 2012;33(5):691-693. doi:10.1109/LED.2012.2189193

47. Balandin AA, Ghosh S, Bao W, et al. Superior Thermal Conductivity of Single-Layer Graphene. *Nano Lett*. 2008;8(3):902-907. doi:10.1021/nl0731872

48. Seol JH, Jo I, Moore AL, et al. Two-Dimensional Phonon Transport in Supported Graphene. *Science (80-)*. 2010;328(5975):213-216. doi:10.1126/science.1184014

49. Piscanec S, Lazzeri M, Mauri F, Ferrari AC, Robertson J. Kohn Anomalies and Electron-Phonon Interactions in Graphite. *Phys Rev Lett*. 2004;93(18):185503. doi:10.1103/PhysRevLett.93.185503

50. Stoller MD, Park S, Zhu Y, An J, Ruoff RS. Graphene-Based Ultracapacitors. *Nano Lett*. 2008;8(10):3498-3502. doi:10.1021/nl802558y

51. Pei H, Li J, Lv M, et al. A Graphene-Based Sensor Array for High-Precision and Adaptive Target Identification with Ensemble Aptamers. *J Am Chem Soc*. 2012;134(33):13843-13849. doi:10.1021/ja305814u

52. Liu Y, Dong X, Chen P. Biological and chemical sensors based on graphene materials. *Chem Soc Rev*. 2012;41(6):2283-2307. doi:10.1039/C1CS15270J

53. Machado BF, Serp P. Graphene-based materials for catalysis. *Catal Sci Technol*. 2012;2(1):54-75. doi:10.1039/C1CY00361E

54. Raccichini R, Varzi A, Passerini S, Scrosati B. The role of graphene for electrochemical energy storage. *Nat Mater*. 2015;14(3):271-279. doi:10.1038/nmat4170

55. Olabi AG, Abdelkareem MA, Wilberforce T, Sayed ET. Application of graphene in energy storage device – A review. *Renew Sustain Energy Rev*. 2021;135:110026. doi:10.1016/j.rser.2020.110026

56. Bonaccorso F, Colombo L, Yu G, et al. Graphene, related two-dimensional crystals, and hybrid systems for energy conversion and storage. *Science (80-)*. 2015;347(6217):1246501. doi:10.1126/science.1246501

57. Lee C, Wei X, Kysar JW, Hone J. Measurement of the Elastic Properties and Intrinsic Strength of Monolayer Graphene. *Science (80-)*. 2008;321(5887):385-388. doi:10.1126/science.1157996

58. Frank IW, Tanenbaum DM, van der Zande AM, McEuen PL. Mechanical properties of suspended graphene sheets. *J Vac Sci Technol B Microelectron Nanom Struct Process Meas Phenom*. 2007;25(6):2558-2561. doi:10.1116/1.2789446

59. Nair RR, Blake P, Grigorenko AN, et al. Fine Structure Constant Defines Visual Transparency of Graphene. *Science (80-)*. 2008;320(5881):1308-1308. doi:10.1126/science.1156965

60. Liu Z, Lau SP, Yan F. Functionalized graphene and other two-dimensional materials for photovoltaic devices: device design and processing. *Chem Soc Rev*. 2015;44(15):5638-5679. doi:10.1039/C4CS00455H

61. Shahil KMF, Balandin AA. Thermal properties of graphene and multilayer graphene: Applications in thermal interface materials. *Solid State Commun*. 2012;152(15):1331-1340. doi:https://doi.org/10.1016/j.ssc.2012.04.034

62. Huang X, Qi X, Boey F, Zhang H. Graphene-based composites. *Chem Soc Rev*. 2012;41(2):666-686. doi:10.1039/C1CS15078B

63. Xia F, Mueller T, Lin Y, Valdes-Garcia A, Avouris P. Ultrafast graphene photodetector. *Nat Nanotechnol*. 2009;4(12):839-843. doi:10.1038/nnano.2009.292

64. Wu Z-S, Feng X, Cheng H-M. Recent advances in graphene-based planar micro-supercapacitors for on-chip energy storage. *Natl Sci Rev*. 2014;1(2):277-292. doi:10.1093/nsr/nwt003

65. Zhai Y, Dou Y, Zhao D, Fulvio PF, Mayes RT, Dai S. Carbon Materials for Chemical Capacitive Energy Storage. *Adv Mater*. 2011;23(42):4828-4850. doi:https://doi.org/10.1002/adma.201100984

66. Greco E, Nava G, Fathi R, et al. Few-layer graphene improves silicon performance in Li-ion battery anodes. *J Mater Chem A*. 2017;5(36):19306-19315. doi:10.1039/C7TA05395A

67. Palumbo S, Silvestri L, Ansaldo A, Brescia R, Bonaccorso F, Pellegrini V. Silicon Few-Layer Graphene Nanocomposite as High-Capacity and High-Rate Anode in Lithium-Ion Batteries. *ACS Appl Energy Mater*. 2019;2(3):1793-1802. doi:10.1021/acsaem.8b01927

68. Maroni F, Raccichini R, Birrozzi A, et al. Graphene/silicon nanocomposite anode with enhanced electrochemical stability for lithium-ion battery applications. *J Power Sources*. 2014;269:873-882. doi:10.1016/j.jpowsour.2014.07.064

69. Abouali S, Garakani MA, Silvestri L, et al. From scaled-up production of silicon-graphene nanocomposite to the realization of an ultra-stable full-cell Li-ion battery. *2D Mater*. 2021;8(3):035014. doi:10.1088/2053-1583/abe106

70. Huang G, Han J, Lu Z, et al. Ultrastable Silicon Anode by Three-Dimensional Nanoarchitecture Design. *ACS Nano*. 2020;14(4):4374-4382. doi:10.1021/acsnano.9b09928

71. Zhang Y, Gao Z, Song N, He J, Li X. Graphene and its derivatives in lithium–sulfur batteries. *Mater Today Energy*. 2018;9:319-335. doi:10.1016/j.mtener.2018.06.001

72. Yang T, Xia J, Piao Z, et al. Graphene-Based Materials for Flexible Lithium–Sulfur Batteries. *ACS Nano*. 2021;15(9):13901-13923. doi:10.1021/acsnano.1c03183

73. Venezia E, Carbone L, Bonaccorso F, Pellegrini V. Tuning the morphology of sulfur–few layer graphene composites via liquid phase evaporation for battery application. *Nanoscale Adv*. 2022;4(4):1136-1144. doi:10.1039/D1NA00733E

74. Carbone L, Del Rio Castillo AE, Kumar Panda J, et al. High-Sulfur-Content Graphene-Based Composite through Ethanol Evaporation for High-Energy Lithium-Sulfur Battery. *ChemSusChem*. 2020;13(6):1593-1602. doi:10.1002/cssc.201902305

75. Hod O. Graphite and Hexagonal Boron-Nitride have the Same Interlayer Distance. Why? *J Chem Theory Comput*. 2012;8(4):1360-1369. doi:10.1021/ct200880m

76. Zhang K, Feng Y, Wang F, Yang Z, Wang J. Two dimensional hexagonal boron nitride (2D-hBN): synthesis, properties and applications. *J Mater Chem C*. 2017;5(46):11992-12022. doi:10.1039/C7TC04300G

77. Ooi N, Rajan V, Gottlieb J, Catherine Y, Adams JB. Structural properties of hexagonal boron nitride. *Model Simul Mater Sci Eng*. 2006;14(3):515-535. doi:10.1088/0965-0393/14/3/012

78. Wentorf RH. Synthesis of the Cubic Form of Boron Nitride. *J Chem Phys*. 1961;34(3):809-812. doi:10.1063/1.1731679

79. Nagakubo A, Ogi H, Sumiya H, Kusakabe K, Hirao M. Elastic constants of cubic and wurtzite boron nitrides. *Appl Phys Lett*. 2013;102(24):241909. doi:10.1063/1.4811789

80. Zedlitz R, Heintze M, Schubert MB. Properties of amorphous boron nitride thin films. *J Non Cryst Solids*. 1996;198-200:403-406. doi:10.1016/0022-3093(95)00748-2

81. Marom N, Bernstein J, Garel J, et al. Stacking and Registry Effects in Layered Materials: The Case of Hexagonal Boron Nitride. *Phys Rev Lett*. 2010;105(4):046801. doi:10.1103/PhysRevLett.105.046801

82. Jiang P, Qian X, Yang R, Lindsay L. Anisotropic thermal transport in bulk hexagonal boron nitride. *Phys Rev Mater*. 2018;2(6):064005. doi:10.1103/PhysRevMaterials.2.064005

83. Kostoglou N, Polychronopoulou K, Rebholz C. Thermal and chemical stability of hexagonal boron nitride (h-BN) nanoplatelets. *Vacuum*. 2015;112:42-45. doi:10.1016/j.vacuum.2014.11.009

84. Jo I, Pettes MT, Kim J, et al. Thermal Conductivity and Phonon Transport in Suspended Few-Layer Hexagonal Boron Nitride. *Nano Lett*. 2013;13(2):550-554. doi:10.1021/nl304060g

85. Shi Y, Hamsen C, Jia X, et al. Synthesis of Few-Layer Hexagonal Boron Nitride Thin Film by Chemical Vapor Deposition. *Nano Lett*. 2010;10(10):4134-4139. doi:10.1021/nl1023707

86. Molaei MJ, Younas M, Rezakazemi M. A Comprehensive Review on Recent Advances in Two-Dimensional (2D) Hexagonal Boron Nitride. *ACS Appl Electron Mater*. 2021;3(12):5165-5187. doi:10.1021/acsaelm.1c00720

87. Roy S, Zhang X, Puthirath AB, et al. Structure, Properties and Applications of Two-Dimensional Hexagonal Boron Nitride. *Adv Mater*. 2021;33(44):2101589. doi:10.1002/adma.202101589

88. Partoens B, Peeters FM. From graphene to graphite: Electronic structure around the K point. *Phys Rev B*. 2006;74(7):075404. doi:10.1103/PhysRevB.74.075404

89. Alem N, Erni R, Kisielowski C, Rossell MD, Gannett W, Zettl A. Atomically thin hexagonal boron nitride probed by ultrahigh-resolution transmission electron microscopy. *Phys Rev B*. 2009;80(15):155425. doi:10.1103/PhysRevB.80.155425

90. Bhimanapati GR, Glavin NR, Robinson JA. 2D Boron Nitride: Synthesis and Applications. In: Iacopi F, Boeckl JJ, Jagadish CBT-S and S, eds. *2D Materials*. Vol 95. Elsevier; 2016:101-147. doi:10.1016/bs.semsem.2016.04.004

91. Lindsay L, Broido DA. Enhanced thermal conductivity and isotope effect in single-layer hexagonal boron nitride. *Phys Rev B*. 2011;84(15):155421. doi:10.1103/PhysRevB.84.155421

92. Lindsay L, Broido DA. Theory of thermal transport in multilayer hexagonal boron nitride and nanotubes. *Phys Rev B*. 2012;85(3):035436. doi:10.1103/PhysRevB.85.035436

93. Cai W, Moore AL, Zhu Y, et al. Thermal Transport in Suspended and Supported Monolayer Graphene Grown by Chemical Vapor Deposition. *Nano Lett*. 2010;10(5):1645-1651. doi:10.1021/nl9041966

94. Lindsay L, Broido DA, Mingo N. Flexural phonons and thermal transport in graphene. *Phys Rev B*. 2010;82(11):115427. doi:10.1103/PhysRevB.82.115427

95. Alam MT, Bresnehan MS, Robinson JA, Haque MA. Thermal conductivity of ultra-thin chemical vapor deposited hexagonal boron nitride films. *Appl Phys Lett*. 2014;104(1):13113. doi:10.1063/1.4861468

96. Wang C, Guo J, Dong L, Aiyiti A, Xu X, Li B. Superior thermal conductivity in suspended bilayer hexagonal boron nitride. *Sci Rep*. 2016;6(1):25334. doi:10.1038/srep25334

97. Zhou H, Zhu J, Liu Z, et al. High thermal conductivity of suspended few-layer hexagonal boron nitride sheets. *Nano Res*. 2014;7(8):1232-1240. doi:10.1007/s12274-014-0486-z

98. Kumar R, Rajasekaran G, Parashar A. Optimised cut-off function for Tersoff-like potentials for a BN nanosheet: a molecular dynamics study. *Nanotechnology*. 2016;27(8):085706. doi:10.1088/0957-4484/27/8/085706

99. Li C, Bando Y, Zhi C, Huang Y, Golberg D. Thickness-dependent bending modulus of hexagonal boron nitride nanosheets. *Nanotechnology*. 2009;20(38):385707. doi:10.1088/0957-4484/20/38/385707

100. Boldrin L, Scarpa F, Chowdhury R, Adhikari S. Effective mechanical properties of hexagonal boron nitride nanosheets. *Nanotechnology*. 2011;22(50):505702. doi:10.1088/0957-4484/22/50/505702

101. Kim SM, Hsu A, Park MH, et al. Synthesis of large-area multilayer hexagonal boron nitride for high material performance. *Nat Commun*. 2015;6(1):8662. doi:10.1038/ncomms9662

102. Mahvash F, Eissa S, Bordjiba T, Tavares AC, Szkopek T, Siaj M. Corrosion resistance of monolayer hexagonal boron nitride on copper. *Sci Rep*. 2017;7(1):42139. doi:10.1038/srep42139

103. Li LH, Xing T, Chen Y, Jones R. Boron Nitride Nanosheets for Metal Protection. *Adv Mater Interfaces*. 2014;1(8):1300132. doi:https://doi.org/10.1002/admi.201300132

104. Chilkoor G, Karanam SP, Star S, et al. Hexagonal Boron Nitride: The Thinnest Insulating Barrier to Microbial Corrosion. *ACS Nano*. 2018;12(3):2242-2252. doi:10.1021/acsnano.7b06211

105. Parra C, Montero-Silva F, Henríquez R, et al. Suppressing Bacterial Interaction with Copper Surfaces through Graphene and Hexagonal-Boron Nitride Coatings. *ACS Appl Mater Interfaces*. 2015;7(12):6430-6437. doi:10.1021/acsami.5b01248

106. Harrison C, Weaver S, Bertelsen C, Burgett E, Hertel N, Grulke E. Polyethylene/boron nitride composites for space radiation

shielding. *J Appl Polym Sci*. 2008;109:2529-2538. doi:10.1002/app.27949

107. Chilkoor G, Jawaharraj K, Vemuri B, et al. Hexagonal Boron Nitride for Sulfur Corrosion Inhibition. *ACS Nano*. 2020;14(11):14809-14819. doi:10.1021/acsnano.0c03625

108. Li LH, Cervenka J, Watanabe K, Taniguchi T, Chen Y. Strong Oxidation Resistance of Atomically Thin Boron Nitride Nanosheets. *ACS Nano*. 2014;8(2):1457-1462. doi:10.1021/nn500059s

109. Liu Z, Gong Y, Zhou W, et al. Ultrathin high-temperature oxidation-resistant coatings of hexagonal boron nitride. *Nat Commun*. 2013;4:2541. doi:10.1038/ncomms3541

110. Zihlmann S, Makk P, Vaz CAF, Schönenberger C. Role of hexagonal boron nitride in protecting ferromagnetic nanostructures from oxidation. *2D Mater*. 2016;3(1):011008. doi:10.1088/2053-1583/3/1/011008

111. Prasad MK, Taverne MPC, Huang C-C, Mar JD, Ho Y-LD. Hexagonal Boron Nitride Based Photonic Quantum Technologies. *Materials (Basel)*. 2024;17(16):4122. doi:10.3390/ma17164122

112. Topsakal M, Aktürk E, Ciraci S. First-principles study of two- and one-dimensional honeycomb structures of boron nitride. *Phys Rev B*. 2009;79(11):115442. doi:10.1103/PhysRevB.79.115442

113. Wickramaratne D, Weston L, Van de Walle CG. Monolayer to Bulk Properties of Hexagonal Boron Nitride. *J Phys Chem C*. 2018;122(44):25524-25529. doi:10.1021/acs.jpcc.8b09087

114. Elias C, Valvin P, Pelini T, et al. Direct band-gap crossover in epitaxial monolayer boron nitride. *Nat Commun*. 2019;10(1):2639. doi:10.1038/s41467-019-10610-5

115. Mak KF, Lee C, Hone J, Shan J, Heinz TF. Atomically Thin MoS2: A New Direct-Gap Semiconductor. *Phys Rev Lett*. 2010;105(13):136805. doi:10.1103/PhysRevLett.105.136805

116. Watanabe K, Taniguchi T, Kanda H. Direct-bandgap properties and evidence for ultraviolet lasing of hexagonal boron nitride single crystal. *Nat Mater*. 2004;3(6):404-409. doi:10.1038/nmat1134

117. Cassabois G, Valvin P, Gil B. Hexagonal boron nitride is an indirect bandgap semiconductor. *Nat Photonics*. 2016;10(4):262-266. doi:10.1038/nphoton.2015.277

118. Lee G-H, Yu Y-J, Lee C, et al. Electron tunneling through atomically flat and ultrathin hexagonal boron nitride. *Appl Phys Lett*. 2011;99(24):243114. doi:10.1063/1.3662043

119. Shaik ABD, Palla P. Optical quantum technologies with hexagonal boron nitride single photon sources. *Sci Rep*. 2021;11(1):12285. doi:10.1038/s41598-021-90804-4

120. Rah Y, Jin Y, Kim S, Yu K. Optical analysis of the refractive index and birefringence of hexagonal boron nitride from the visible to near-infrared. *Opt Lett*. 2019;44(15):3797-3800. doi:10.1364/OL.44.003797

121. Watanabe K, Taniguchi T. Hexagonal Boron Nitride as a New Ultraviolet Luminescent Material and Its Application. *Int J Appl Ceram Technol*. 2011;8(5):977-989. doi:https://doi.org/10.1111/j.1744-7402.2011.02626.x

122. Liu H, Meng J, Zhang X, et al. High-performance deep ultraviolet photodetectors based on few-layer hexagonal boron nitride. *Nanoscale*. 2018;10(12):5559-5565. doi:10.1039/C7NR09438H

123. Kumbhakar P, Kole AK, Tiwary CS, et al. Nonlinear Optical Properties and Temperature-Dependent UV–Vis Absorption and Photoluminescence Emission in 2D Hexagonal Boron Nitride Nanosheets. *Adv Opt Mater*. 2015;3(6):828-835. doi:https://doi.org/10.1002/adom.201400445

124. Backes C, Abdelkader AM, Alonso C, et al. Production and processing of graphene and related materials. *2D Mater*. 2020;7(2):022001. doi:10.1088/2053-1583/ab1e0a

125. Hao Y, Wang L, Liu Y, et al. Oxygen-activated growth and bandgap tunability of large single-crystal bilayer graphene. *Nat Nanotechnol*. 2016;11(5):426-431. doi:10.1038/nnano.2015.322

126. Hao Y, Bharathi MS, Wang L, et al. The Role of Surface Oxygen in the Growth of Large Single-Crystal Graphene on Copper. *Science (80-)*. 2013;342(6159):720-723. doi:10.1126/science.1243879

127. Yi M, Shen Z. A review on mechanical exfoliation for the scalable production of graphene. *J Mater Chem A*. 2015;3(22):11700-11715. doi:10.1039/C5TA00252D

128. Mikhailov S. *Physics and Applications of Graphene - Experiments*. (Mikhailov S, ed.). InTech; 2011. doi:10.5772/590

129. Huang L, Chang QH, Guo GL, et al. Synthesis of high-quality graphene films on nickel foils by rapid thermal chemical vapor deposition. *Carbon N Y*. 2012;50(2):551-556. doi:https://doi.org/10.1016/j.carbon.2011.09.012

130. Miseikis V, Convertino D, Mishra N, et al. Rapid CVD growth of millimetre-sized single crystal graphene using a cold-wall reactor. *2D Mater*. 2015;2(1):014006. doi:10.1088/2053-1583/2/1/014006

131. Kim Y, Song W, Lee SY, et al. Low-temperature synthesis of graphene on nickel foil by microwave plasma chemical vapor deposition. *Appl Phys Lett*. 2011;98(26):263106. doi:10.1063/1.3605560

132. Reina A, Jia X, Ho J, et al. Large Area, Few-Layer Graphene Films on Arbitrary Substrates by Chemical Vapor Deposition. *Nano Lett*. 2009;9(1):30-35. doi:10.1021/nl801827v

133. Ramón ME, Gupta A, Corbet C, et al. CMOS-compatible synthesis of large-area, high-mobility graphene by chemical vapor deposition of acetylene on cobalt thin films. *ACS Nano*. 2011;5(9):7198-7204. doi:10.1021/nn202012m

134. Petrone N, Dean CR, Meric I, et al. Chemical vapor deposition-derived graphene with electrical performance of exfoliated graphene. *Nano Lett*. 2012;12(6):2751-2756. doi:10.1021/nl204481s

135. Coraux J, T N'Diaye A, Engler M, et al. Growth of graphene on Ir(111). *New J Phys*. 2009;11(2):23006. doi:10.1088/1367-2630/11/2/023006

136. Jiménez-Villacorta F, Álvarez-Fraga L, Bartolomé J, et al. Nanocrystalline cubic ruthenium carbide formation in the synthesis of graphene on ruthenium ultrathin films. *J Mater Chem C*. 2017;5(39):10260-10269. doi:10.1039/C7TC02855E

137. Sun J(孙捷), Cole MT, Lindvall N, Teo KBK(张谋瑾), Yurgens A. Noncatalytic chemical vapor deposition of graphene on high-temperature substrates for transparent electrodes. *Appl Phys Lett*. 2012;100(2):22102. doi:10.1063/1.3675632

138. Scott A, Dianat A, Börrnert F, et al. The catalytic potential of high-κ dielectrics for graphene formation. *Appl Phys Lett*. 2011;98(7):73110. doi:10.1063/1.3556639

139. Rümmeli MH, Bachmatiuk A, Scott A, et al. Direct Low-Temperature Nanographene CVD Synthesis over a Dielectric Insulator. *ACS Nano*. 2010;4(7):4206-4210. doi:10.1021/nn100971s

140. Strupinski W, Grodecki K, Wysmolek A, et al. Graphene Epitaxy by Chemical Vapor Deposition on SiC. *Nano Lett*. 2011;11(4):1786-1791. doi:10.1021/nl200390e

141. Aras FG, Yilmaz A, Tasdelen HG, et al. A review on recent advances of chemical vapor deposition technique for monolayer transition metal dichalcogenides (MX2: Mo, W; S, Se, Te). *Mater Sci Semicond Process*. 2022;148:106829. doi:https://doi.org/10.1016/j.mssp.2022.106829

142. Kang T, Tang TW, Pan B, Liu H, Zhang K, Luo Z. Strategies for Controlled Growth of Transition Metal Dichalcogenides by Chemical Vapor Deposition for Integrated Electronics. *ACS Mater Au*. 2022;2(6):665-685. doi:10.1021/acsmaterialsau.2c00029

143. Zhang Y, Yao Y, Sendeku MG, et al. Recent Progress in CVD Growth of 2D Transition Metal Dichalcogenides and Related Heterostructures. *Adv Mater*. 2019;31(41):1901694. doi:https://doi.org/10.1002/adma.201901694

144. Fernandes J, Queirós T, Rodrigues J, et al. Room-temperature emitters in wafer-scale few-layer hBN by atmospheric pressure CVD. *FlatChem*. 2022;33:100366. doi:https://doi.org/10.1016/j.flatc.2022.100366

145. Liu H, You CY, Li J, et al. Synthesis of hexagonal boron nitrides by chemical vapor deposition and their use as single photon emitters. *Nano Mater Sci*. 2021;3(3):291-312. doi:https://doi.org/10.1016/j.nanoms.2021.03.002

146. Ma KY, Kim M, Shin HS. Large-Area Hexagonal Boron Nitride Layers by Chemical Vapor Deposition: Growth and Applications for Substrates, Encapsulation, and Membranes. *Accounts Mater Res*. 2022;3(7):748-760. doi:10.1021/accountsmr.2c00061

147. Wang D, Zhou C, Filatov AS, et al. Direct synthesis and chemical vapor deposition of 2D carbide and nitride MXenes. *Science (80-)*. 2023;379(6638):1242-1247. doi:10.1126/science.add9204

148. Li X. Customizing MXenes. *Matter*. 2023;6(8):2519-2522. doi:https://doi.org/10.1016/j.matt.2023.05.033

149. Kern W, Schnable GL. Low-pressure chemical vapor deposition for very large-scale integration processing—A review. *IEEE Trans Electron Devices*. 1979;26(4):647-657. doi:10.1109/T-ED.1979.19473

150. Liu B, Fathi M, Chen L, Abbas A, Ma Y, Zhou C. Chemical Vapor Deposition Growth of Monolayer WSe2 with Tunable Device Characteristics and Growth Mechanism Study. *ACS Nano*. 2015;9(6):6119-6127. doi:10.1021/acsnano.5b01301

151. Gupta B, Notarianni M, Mishra N, Shafiei M, Iacopi F, Motta N. Evolution of epitaxial graphene layers on 3C SiC/Si (111) as a function of annealing temperature in UHV. *Carbon N Y*. 2014;68:563-572. doi:https://doi.org/10.1016/j.carbon.2013.11.035

152. Cai Z, Liu B, Zou X, Cheng H-M. Chemical Vapor Deposition Growth and Applications of Two-Dimensional Materials and Their Heterostructures. *Chem Rev*. 2018;118(13):6091-6133. doi:10.1021/acs.chemrev.7b00536

153. Khan K, Tareen AK, Aslam M, et al. Recent developments in emerging two-dimensional materials and their applications. *J Mater Chem C*. 2020;8(2):387-440. doi:10.1039/C9TC04187G

154. Rhyee J-S, Kwon J, Dak P, et al. High-Mobility Transistors Based on Large-Area and Highly Crystalline CVD-Grown MoSe2 Films on Insulating Substrates. *Adv Mater*. 2016;28(12):2316-2321. doi:https://doi.org/10.1002/adma.201504789

155. Wang M, Jang SK, Jang W-J, et al. A Platform for Large-Scale Graphene Electronics – CVD Growth of Single-Layer Graphene on CVD-Grown Hexagonal Boron Nitride. *Adv Mater*. 2013;25(19):2746-2752. doi:https://doi.org/10.1002/adma.201204904

156. Wang L, Chen L, Wong SL, et al. Electronic Devices and Circuits Based on Wafer-Scale Polycrystalline Monolayer MoS2 by Chemical Vapor Deposition. *Adv Electron Mater*. 2019;5(8):1900393. doi:https://doi.org/10.1002/aelm.201900393

157. Elbanna A, Jiang H, Fu Q, et al. 2D Material Infrared Photonics and Plasmonics. *ACS Nano*. 2023;17(5):4134-4179.

doi:10.1021/acsnano.2c10705

158. Shen F, Zhang Z, Zhou Y, et al. Transition metal dichalcogenide metaphotonic and self-coupled polaritonic platform grown by chemical vapor deposition. *Nat Commun*. 2022;13(1):5597. doi:10.1038/s41467-022-33088-0

159. Su G, Hadjiev VG, Loya PE, et al. Chemical Vapor Deposition of Thin Crystals of Layered Semiconductor SnS2 for Fast Photodetection Application. *Nano Lett*. 2015;15(1):506-513. doi:10.1021/nl503857r

160. Shi Z, Ci H, Yang X, Liu Z, Sun J. Direct-Chemical Vapor Deposition-Enabled Graphene for Emerging Energy Storage: Versatility, Essentiality, and Possibility. *ACS Nano*. 2022;16(8):11646-11675. doi:10.1021/acsnano.2c05745

161. Konar R, Nessim GD. A mini-review focusing on ambient-pressure chemical vapor deposition (AP-CVD) based synthesis of layered transition metal selenides for energy storage applications. *Mater Adv*. 2022;3(11):4471-4488. doi:10.1039/D2MA00091A

162. Li Y, Li Z, Lei L, et al. Chemical vapor deposition-grown carbon nanotubes/graphene hybrids for electrochemical energy storage and conversion. *FlatChem*. 2019;15:100091. doi:https://doi.org/10.1016/j.flatc.2019.100091

163. Cho AY, Arthur JR. Molecular beam epitaxy. *Prog Solid State Chem*. 1975;10:157-191. doi:10.1016/0079-6786(75)90005-9

164. Martínez-Galera AJ, Brihuega I, Gómez-Rodríguez JM. Ethylene Irradiation: A New Route to Grow Graphene on Low Reactivity Metals. *Nano Lett*. 2011;11(9):3576-3580. doi:10.1021/nl201281m

165. Jerng S-K, Seong Yu D, Hong Lee J, Kim C, Yoon S, Chun S-H. Graphitic carbon growth on crystalline and amorphous oxide substrates using molecular beam epitaxy. *Nanoscale Res Lett*. 2011;6(1):565. doi:10.1186/1556-276X-6-565

166. Garcia JM, He R, Jiang MP, et al. Multilayer graphene films grown by molecular beam deposition. *Solid State Commun*. 2010;150(17-18):809-811. doi:10.1016/j.ssc.2010.02.029

167. Ferrari AC, Bonaccorso F, Fal'ko V, et al. Science and technology roadmap for graphene-related two-dimensional crystals and hybrid systems. *Nanoscale*. 2015;7(11):4598-4810. doi:10.1039/C4NR01600A

168. Schultz RA, Jensen MC, Bradt RC. Single crystal cleavage of brittle materials. *Int J Fract*. 1994;65(4):291-312. doi:10.1007/BF00012370

169. Kakavelakis G, Del Rio Castillo AE, Pellegrini V, et al. Size-Tuning of WSe2 Flakes for High Efficiency Inverted Organic Solar Cells. *ACS Nano*. 2017;11(4):3517-3531. doi:10.1021/acsnano.7b00323

170. Parvez K, Casiraghi C. Biocompatible 2D Material Inks Enabled by Supramolecular Chemistry: From Synthesis to Applications. *Acc Chem Res*. 2025;58(2):189-198. doi:10.1021/acs.accounts.4c00596

171. Hernandez Y, Lotya M, Rickard D, Bergin SD, Coleman JN. Measurement of Multicomponent Solubility Parameters for Graphene Facilitates Solvent Discovery. *Langmuir*. 2010;26(5):3208-3213. doi:10.1021/la903188a

172. Solomon HM, Burgess BA, Kennedy GLJ, Staples RE. 1-Methyl-2-pyrrolidone (NMP): reproductive and developmental toxicity study by inhalation in the rat. *Drug Chem Toxicol*. 1995;18(4):271-293. doi:10.3109/01480549509014324

173. Yi M, Shen Z, Zhang X, Ma S. Achieving concentrated graphene dispersions in water/acetone mixtures by the strategy of tailoring Hansen solubility parameters. *J Phys D Appl Phys*. 2013;46(2):025301. doi:10.1088/0022-3727/46/2/025301

174. Ueberricke L, Coleman JN, Backes C. Robustness of Size Selection and Spectroscopic Size, Thickness and Monolayer Metrics of Liquid-Exfoliated WS 2. *Phys status solidi*. 2017;254(11):1700443. doi:10.1002/pssb.201700443

175. Backes C, Hanlon D, Szydlowska BM, et al. Preparation of Liquid-exfoliated Transition Metal Dichalcogenide Nanosheets with Controlled Size and Thickness: A State of the Art Protocol. *J Vis Exp*. 2016;(118). doi:10.3791/54806

176. Backes C, Smith RJ, McEvoy N, et al. Edge and confinement effects allow in situ measurement of size and thickness of liquid-exfoliated nanosheets. *Nat Commun*. 2014;5(1):4576. doi:10.1038/ncomms5576

177. Del Rio Castillo AE, Pellegrini V, Ansaldo A, et al. High-yield production of 2D crystals by wet-jet milling. *Mater Horizons*. 2018;5(5):890-904. doi:10.1039/C8MH00487K

178. Karagiannidis PG, Hodge SA, Lombardi L, et al. Microfluidization of Graphite and Formulation of Graphene-Based Conductive Inks. *ACS Nano*. 2017;11(3):2742-2755. doi:10.1021/acsnano.6b07735

179. Kong W, Kum H, Bae S-H, et al. Path towards graphene commercialization from lab to market. *Nat Nanotechnol*. 2019;14(10):927-938. doi:10.1038/s41565-019-0555-2

180. Mattevi C, Eda G, Agnoli S, et al. Evolution of Electrical, Chemical, and Structural Properties of Transparent and Conducting Chemically Derived Graphene Thin Films. *Adv Funct Mater*. 2009;19(16):2577-2583. doi:https://doi.org/10.1002/adfm.200900166

181. Najafi L, Bellani S, Oropesa-Nuñez R, et al. Engineered MoSe2-Based Heterostructures for Efficient Electrochemical Hydrogen Evolution Reaction. *Adv Energy Mater*. 2018;8(16):1703212. doi:10.1002/aenm.201703212

182. Eom SH, Park H, Mujawar SH, et al. High efficiency polymer solar cells via sequential inkjet-printing of PEDOT:PSS and P3HT:PCBM inks with additives. *Org Electron*. 2010;11(9):1516-1522. doi:https://doi.org/10.1016/j.orgel.2010.06.007

183. Akbari Garakani M, Bellani S, Pellegrini V, et al. Scalable spray-coated graphene-based electrodes for high-power

electrochemical double-layer capacitors operating over a wide range of temperature. *Energy Storage Mater*. 2021;34:1-11. doi:10.1016/j.ensm.2020.08.036

184. Hassan K, Nine MJ, Tung TT, et al. Functional inks and extrusion-based 3D printing of 2D materials: a review of current research and applications. *Nanoscale*. 2020;12(37):19007-19042. doi:10.1039/D0NR04933F

185. Moses OA, Gao L, Zhao H, et al. 2D materials inks toward smart flexible electronics. *Mater Today*. 2021;50:116-148. doi:https://doi.org/10.1016/j.mattod.2021.08.010

186. Bianca G, Zappia MI, Bellani S, et al. Liquid-Phase Exfoliated GeSe Nanoflakes for Photoelectrochemical-Type Photodetectors and Photoelectrochemical Water Splitting. *ACS Appl Mater Interfaces*. 2020;12(43):48598-48613. doi:10.1021/acsami.0c14201

187. Zappia M, Bianca G, Bellani S, et al. Solution-Processed GaSe Nanoflake-Based Films for Photoelectrochemical Water Splitting and Photoelectrochemical-Type Photodetectors. *Adv Funct Mater*. 2020;30:1909572. doi:10.1002/adfm.201909572

188. Bellani S, Bartolotta A, Agresti A, et al. Solution-processed two-dimensional materials for next-generation photovoltaics. *Chem Soc Rev*. 2021;50(21):11870-11965. doi:10.1039/D1CS00106J

189. Taheri B, Yaghoobi Nia N, Agresti A, et al. Graphene-engineered automated sprayed mesoscopic structure for perovskite device scaling-up. *2D Mater*. 2018;5(4):045034. doi:10.1088/2053-1583/aad983

190. Pescetelli S, Agresti A, Viskadouros G, et al. Integration of two-dimensional materials-based perovskite solar panels into a stand-alone solar farm. *Nat Energy*. 2022;7(7):597-607. doi:10.1038/s41560-022-01035-4

191. Agresti A, Pescetelli S, Palma AL, et al. Two-Dimensional Material Interface Engineering for Efficient Perovskite Large-Area Modules. *ACS Energy Lett*. 2019;4(8):1862-1871. doi:10.1021/acsenergylett.9b01151

192. Mariani P, Molina-García MÁ, Barichello J, et al. Low-temperature strain-free encapsulation for perovskite solar cells and modules passing multifaceted accelerated ageing tests. *Nat Commun*. 2024;15(1):4552. doi:10.1038/s41467-024-48877-y

193. Wang T, Quinn MDJ, Notley SM. Enhanced electrical, mechanical and thermal properties by exfoliating graphene platelets of larger lateral dimensions. *Carbon N Y*. 2018;129:191-198. doi:https://doi.org/10.1016/j.carbon.2017.12.034

194. Lotya M, King PJ, Khan U, De S, Coleman JN. High-Concentration, Surfactant-Stabilized Graphene Dispersions. *ACS Nano*. 2010;4(6):3155-3162. doi:10.1021/nn1005304

195. Kouroupis-Agalou K, Liscio A, Treossi E, et al. Fragmentation and exfoliation of 2-dimensional materials: a statistical approach. *Nanoscale*. 2014;6(11):5926-5933. doi:10.1039/C3NR06919B

196. Bracamonte M V, Lacconi GI, Urreta SE, Foa Torres LEF. On the Nature of Defects in Liquid-Phase Exfoliated Graphene. *J Phys Chem C*. 2014;118(28):15455-15459. doi:10.1021/jp501930a

197. Martín C, Kostarelos K, Prato M, Bianco A. Biocompatibility and biodegradability of 2D materials: graphene and beyond. *Chem Commun*. 2019;55(39):5540-5546. doi:10.1039/C9CC01205B

198. Pinto AM, Gonçalves IC, Magalhães FD. Graphene-based materials biocompatibility: A review. *Colloids Surfaces B Biointerfaces*. 2013;111:188-202. doi:10.1016/j.colsurfb.2013.05.022

199. Sasidharan A, Panchakarla LS, Sadanandan AR, et al. Hemocompatibility and Macrophage Response of Pristine and Functionalized Graphene. *Small*. 2012;8(8):1251-1263. doi:https://doi.org/10.1002/smll.201102393

200. Park J, Park S, Ryu S, et al. Graphene–Regulated Cardiomyogenic Differentiation Process of Mesenchymal Stem Cells by Enhancing the Expression of Extracellular Matrix Proteins and Cell Signaling Molecules. *Adv Healthc Mater*. 2014;3(2):176-181. doi:https://doi.org/10.1002/adhm.201300177

201. Pampaloni NP, Lottner M, Giugliano M, et al. Single-layer graphene modulates neuronal communication and augments membrane ion currents. *Nat Nanotechnol*. 2018;13(8):755-764. doi:https://doi.org/10.1038/s41565-018-0163-6

202. Jasim DA, Lozano N, Bussy C, et al. Graphene-based papers as substrates for cell growth: Characterisation and impact on mammalian cells. *FlatChem*. 2018;12:17-25. doi:https://doi.org/10.1016/j.flatc.2018.11.006

203. Gurunathan S, Kim J-H. Synthesis, toxicity, biocompatibility, and biomedical applications of graphene and graphene-related materials. *Int J Nanomedicine*. 2016;11:1927-1945. doi:10.2147/IJN.S105264

204. Fadeel B, Bussy C, Merino S, et al. Safety Assessment of Graphene-Based Materials: Focus on Human Health and the Environment. *ACS Nano*. 2018;12(11):10582-10620. doi:10.1021/acsnano.8b04758

205. Kostarelos K, Novoselov KS. Exploring the Interface of Graphene and Biology. *Science (80-)*. 2014;344(6181):261-263. doi:10.1126/science.1246736

206. Wick P, Louw-Gaume AE, Kucki M, et al. Classification Framework for Graphene-Based Materials. *Angew Chemie Int Ed*. 2014;53(30):7714-7718. doi:https://doi.org/10.1002/anie.201403335

207. Cheng C, Nie S, Li S, et al. Biopolymer functionalized reduced graphene oxide with enhanced biocompatibility via mussel inspired coatings/anchors. *J Mater Chem B*. 2013;1(3):265-275. doi:10.1039/C2TB00025C

208. Pinto AM, Moreira J-->Agostinho, Magalhães FD, Gonçalves IC. Polymer surface adsorption as a strategy to improve the

biocompatibility of graphene nanoplatelets. *Colloids Surfaces B Biointerfaces*. 2016;146:818-824. doi:10.1016/j.colsurfb.2016.07.031

209. Sasidharan A, Swaroop S, Koduri CK, et al. Comparative in vivo toxicity, organ biodistribution and immune response of pristine, carboxylated and PEGylated few-layer graphene sheets in Swiss albino mice: A three month study. *Carbon N Y*. 2015;95:511-524. doi:https://doi.org/10.1016/j.carbon.2015.08.074

210. Jasim DA, Murphy S, Newman L, et al. The Effects of Extensive Glomerular Filtration of Thin Graphene Oxide Sheets on Kidney Physiology. *ACS Nano*. 2016;10(12):10753-10767. doi:10.1021/acsnano.6b03358

211. Jasim DA, Boutin H, Fairclough M, et al. Thickness of functionalized graphene oxide sheets plays critical role in tissue accumulation and urinary excretion: A pilot PET/CT study. *Appl Mater Today*. 2016;4:24-30. doi:https://doi.org/10.1016/j.apmt.2016.04.003

212. Guiney LM, Wang X, Xia T, Nel AE, Hersam MC. Assessing and Mitigating the Hazard Potential of Two-Dimensional Materials. *ACS Nano*. 2018;12(7):6360-6377. doi:10.1021/acsnano.8b02491

213. Kenry, Lim CT. Biocompatibility and Nanotoxicity of Layered Two-Dimensional Nanomaterials. *ChemNanoMat*. 2017;3(1):5-16. doi:10.1002/cnma.201600290

214. Mateti S, Wong CS, Liu Z, et al. Biocompatibility of boron nitride nanosheets. *Nano Res*. 2018;11(1):334-342. doi:10.1007/s12274-017-1635-y

215. Siepi M, Morales-Narváez E, Domingo N, Monti DM, Notomista E, Merkoçi A. Production of biofunctionalized MoS 2 flakes with rationally modified lysozyme: a biocompatible 2D hybrid material. *2D Mater*. 2017;4(3):035007. doi:10.1088/2053-1583/aa7966

216. Teo WZ, Chng ELK, Sofer Z, Pumera M. Cytotoxicity of Exfoliated Transition-Metal Dichalcogenides (MoS2, WS2, and WSe2) is Lower Than That of Graphene and its Analogues. *Chem – A Eur J*. 2014;20(31):9627-9632. doi:https://doi.org/10.1002/chem.201402680

217. Latiff NM, Sofer Z, Fisher AC, Pumera M. Cytotoxicity of Exfoliated Layered Vanadium Dichalcogenides. *Chem – A Eur J*. 2017;23(3):684-690. doi:https://doi.org/10.1002/chem.201604430

218. Chia HL, Latiff NM, Sofer Z, Pumera M. Cytotoxicity of Group 5 Transition Metal Ditellurides (MTe2; M=V, Nb, Ta). *Chem – A Eur J*. 2018;24(1):206-211. doi:https://doi.org/10.1002/chem.201704316

219. Qu G, Liu W, Zhao Y, et al. Improved Biocompatibility of Black Phosphorus Nanosheets by Chemical Modification. *Angew Chemie Int Ed*. 2017;56(46):14488-14493. doi:https://doi.org/10.1002/anie.201706228

220. Liu T, Wang C, Gu X, et al. Drug Delivery with PEGylated MoS2 Nano-sheets for Combined Photothermal and Chemotherapy of Cancer. *Adv Mater*. 2014;26(21):3433-3440. doi:https://doi.org/10.1002/adma.201305256

221. Liu S, Shen Z, Wu B, et al. Cytotoxicity and Efflux Pump Inhibition Induced by Molybdenum Disulfide and Boron Nitride Nanomaterials with Sheetlike Structure. *Environ Sci Technol*. 2017;51(18):10834-10842. doi:10.1021/acs.est.7b02463

222. Latiff NM, Teo WZ, Sofer Z, Fisher AC, Pumera M. The Cytotoxicity of Layered Black Phosphorus. *Chem – A Eur J*. 2015;21(40):13991-13995. doi:https://doi.org/10.1002/chem.201502006

223. Mu X, Wang J-Y, Bai X, et al. Black Phosphorus Quantum Dot Induced Oxidative Stress and Toxicity in Living Cells and Mice. *ACS Appl Mater Interfaces*. 2017;9(24):20399-20409. doi:10.1021/acsami.7b02900

224. Liu T, Shi S, Liang C, et al. Iron Oxide Decorated MoS2 Nanosheets with Double PEGylation for Chelator-Free Radiolabeling and Multimodal Imaging Guided Photothermal Therapy. *ACS Nano*. 2015;9(1):950-960. doi:10.1021/nn506757x

225. Tao W, Zhu X, Yu X, et al. Black Phosphorus Nanosheets as a Robust Delivery Platform for Cancer Theranostics. *Adv Mater*. 2017;29(1):1603276. doi:https://doi.org/10.1002/adma.201603276

226. Gou S, Yang S, Cheng Y, et al. Applications of 2D Nanomaterials in Neural Interface. *Int J Mol Sci*. 2024;25(16):8615. doi:10.3390/ijms25168615

227. Smith AT, LaChance AM, Zeng S, Liu B, Sun L. Synthesis, properties, and applications of graphene oxide/reduced graphene oxide and their nanocomposites. *Nano Mater Sci*. 2019;1(1):31-47. doi:https://doi.org/10.1016/j.nanoms.2019.02.004

228. Nguyen D, Valet M, Dégardin J, et al. Novel Graphene Electrode for Retinal Implants: An in vivo Biocompatibility Study. *Front Neurosci*. 2021;15. doi:10.3389/fnins.2021.615256

229. Tupone MG, Panella G, D'Angelo M, et al. An Update on Graphene-Based Nanomaterials for Neural Growth and Central Nervous System Regeneration. *Int J Mol Sci*. 2021;22(23):13047. doi:10.3390/ijms222313047

230. Ryu S, Kim B-S. Culture of neural cells and stem cells on graphene. *Tissue Eng Regen Med*. 2013;10(2):39-46. doi:10.1007/s13770-013-0384-6

231. Bei HP, Yang Y, Zhang Q, et al. Graphene-Based Nanocomposites for Neural Tissue Engineering. *Molecules*. 2019;24(4):658. doi:10.3390/molecules24040658

232. Xiong Z, Huang W, Liang Q, et al. Harnessing the 2D Structure-Enabled Viscoelasticity of Graphene-Based Hydrogel Membranes for Chronic Neural Interfacing. *Small Methods*. 2022;6(5). doi:10.1002/smtd.202200022

233. Dong M, Chen P, Zhou K, et al. Flexible neural recording electrodes based on reduced graphene oxide interfaces. *Chem Eng J*. 2023;478:147067. doi:10.1016/j.cej.2023.147067

234. Lim J, Lee S, Kim J, et al. Hybrid graphene electrode for the diagnosis and treatment of epilepsy in free-moving animal models. *NPG Asia Mater*. 2023;15(1):7. doi:10.1038/s41427-023-00464-1

235. Zhou Q, Chen Q, Tong Y, Wang J. Light-Induced Ambient Degradation of Few-Layer Black Phosphorus: Mechanism and Protection. *Angew Chemie Int Ed*. 2016;55(38):11437-11441. doi:https://doi.org/10.1002/anie.201605168

236. Zhang Y, Li C, Guo A, et al. Black phosphorus boosts wet-tissue adhesion of composite patches by enhancing water absorption and mechanical properties. *Nat Commun*. 2024;15(1):1618. doi:10.1038/s41467-024-46003-6

237. Liu Y, Tan Y, Cheng G, et al. Customized Intranasal Hydrogel Delivering Methylene Blue Ameliorates Cognitive Dysfunction against Alzheimer's Disease. *Adv Mater*. 2024;36(19):2307081. doi:https://doi.org/10.1002/adma.202307081

238. Tan H, Cao K, Zhao Y, et al. Brain-Targeted Black Phosphorus-Based Nanotherapeutic Platform for Enhanced Hypericin Delivery in Depression. *Small*. 2024;20(31):2310608. doi:https://doi.org/10.1002/smll.202310608

239. Qian Y, Yuan W-E, Cheng Y, Yang Y, Qu X, Fan C. Concentrically Integrative Bioassembly of a Three-Dimensional Black Phosphorus Nanoscaffold for Restoring Neurogenesis, Angiogenesis, and Immune Homeostasis. *Nano Lett*. 2019;19(12):8990-9001. doi:10.1021/acs.nanolett.9b03980

240. Wang Y, Qian Y, Zhang L, et al. Conductive Metal–Organic Framework Microelectrodes Regulated by Conjugated Molecular Wires for Monitoring of Dopamine in the Mouse Brain. *J Am Chem Soc*. 2023;145(4):2118-2126. doi:10.1021/jacs.2c07053

241. Zhou L, Yang R, Li X, et al. COF-Coated Microelectrode for Space-Confined Electrochemical Sensing of Dopamine in Parkinson's Disease Model Mouse Brain. *J Am Chem Soc*. 2023;145(43):23727-23738. doi:10.1021/jacs.3c08256

242. Niu H, Bu H, Zhao J, Zhu Y. Metal–Organic Frameworks-Based Nanoplatforms for the Theranostic Applications of Neurological Diseases. *Small*. 2023;19(23):2206575. doi:https://doi.org/10.1002/smll.202206575

243. Stolz RM, Kolln AF, Rocha BC, et al. Epitaxial Self-Assembly of Interfaces of 2D Metal–Organic Frameworks for Electroanalytical Detection of Neurotransmitters. *ACS Nano*. 2022;16(9):13869-13883. doi:10.1021/acsnano.2c02529

244. Gürbüz B, Ciftci F. Bio-electric-electronics and tissue engineering applications of MXenes wearable materials: A review. *Chem Eng J*. 2024;489:151230. doi:10.1016/j.cej.2024.151230

245. Driscoll N, Richardson AG, Maleski K, et al. Two-Dimensional Ti3C2 MXene for High-Resolution Neural Interfaces. *ACS Nano*. 2018;12(10):10419-10429. doi:10.1021/acsnano.8b06014

246. Driscoll N, Erickson B, Murphy BB, et al. MXene-infused bioelectronic interfaces for multiscale electrophysiology and stimulation. *Sci Transl Med*. 2021;13(612). doi:10.1126/scitranslmed.abf8629

247. Sha B, Zhao S, Gu M, et al. Doping-induced assembly interface for noninvasive in vivo local and systemic immunomodulation. *Proc Natl Acad Sci*. 2023;120(49):e2306777120. doi:10.1073/pnas.2306777120

248. Sun H, Li D, Yue X, et al. A Review of Transition Metal Dichalcogenides-Based Biosensors. *Front Bioeng Biotechnol*. 2022;10. doi:10.3389/fbioe.2022.941135

249. Yang SM, Shim JH, Cho H-U, et al. Hetero-Integration of Silicon Nanomembranes with 2D Materials for Bioresorbable, Wireless Neurochemical System. *Adv Mater*. 2022;34(14):2108203. doi:https://doi.org/10.1002/adma.202108203

250. Kireev D, Okogbue E, Jayanth RT, Ko T-J, Jung Y, Akinwande D. Multipurpose and Reusable Ultrathin Electronic Tattoos Based on PtSe2 and PtTe2. *ACS Nano*. 2021;15(2):2800-2811. doi:10.1021/acsnano.0c08689

251. Yan Z, Xu D, Lin Z, et al. Highly stretchable van der Waals thin films for adaptable and breathable electronic membranes. *Science (80-)*. 2022;375(6583):852-859. doi:10.1126/science.abl8941

252. McManus D, Vranic S, Withers F, et al. Water-based and biocompatible 2D crystal inks for all-inkjet-printed heterostructures. *Nat Nanotechnol*. 2017;12(4):343-350. doi:10.1038/nnano.2016.281

253. Hossain RF, Deaguero IG, Boland T, Kaul AB. Biocompatible, large-format, inkjet printed heterostructure MoS2-graphene photodetectors on conformable substrates. *npj 2D Mater Appl*. 2017;1(1):28. doi:10.1038/s41699-017-0034-2

254. Martín C, Merino S, González-Domínguez JM, et al. Graphene Improves the Biocompatibility of Polyacrylamide Hydrogels: 3D Polymeric Scaffolds for Neuronal Growth. *Sci Rep*. 2017;7(1):10942. doi:10.1038/s41598-017-11359-x

255. Koyappayil A, Yagati AK, Lee M-H. Recent Trends in Metal Nanoparticles Decorated 2D Materials for Electrochemical Biomarker Detection. *Biosensors*. 2023;13(1):91. doi:10.3390/bios13010091

256. Lei Z-L, Guo B. 2D Material-Based Optical Biosensor: Status and Prospect. *Adv Sci*. 2022;9(4):2102924. doi:https://doi.org/10.1002/advs.202102924

257. Gao X, Gao Y, Qi R, Han L. One-pot synthesis of a recyclable ratiometric fluorescent probe based on MOFs for turn-on sensing of Mg 2+ ions and bioimaging in live cells. *New J Chem*. 2019;43(46):18377-18383. doi:10.1039/C9NJ04536H

258. Das G, Benyettou F, Sharama SK, et al. Covalent organic nanosheets for bioimaging. *Chem Sci*. 2018;9(44):8382-8387. doi:10.1039/C8SC02842G

259. Ma Y-H, Dou W-T, Pan Y-F, et al. Fluorogenic 2D Peptidosheet Unravels CD47 as a Potential Biomarker for Profiling Hepatocellular Carcinoma and Cholangiocarcinoma Tissues. *Adv Mater*. 2017;29(5):1604253. doi:https://doi.org/10.1002/adma.201604253

260. Zhang Y, Zhang H, Wang Y, et al. Hydrophilic graphene oxide/bismuth selenide nanocomposites for CT imaging, photoacoustic imaging, and photothermal therapy. *J Mater Chem B*. 2017;5(9):1846-1855. doi:10.1039/C6TB02137A

261. Yong Y, Zhou L, Gu Z, et al. WS2 nanosheet as a new photosensitizer carrier for combined photodynamic and photothermal therapy of cancer cells. *Nanoscale*. 2014;6(17):10394-10403. doi:10.1039/C4NR02453B

262. Lin H, Wang Y, Gao S, Chen Y, Shi J. Theranostic 2D Tantalum Carbide (MXene). *Adv Mater*. 2018;30(4):1703284. doi:https://doi.org/10.1002/adma.201703284

263. Cheng L, Liu J, Gu X, et al. PEGylated WS2 Nanosheets as a Multifunctional Theranostic Agent for in vivo Dual-Modal CT/Photoacoustic Imaging Guided Photothermal Therapy. *Adv Mater*. 2014;26(12):1886-1893. doi:https://doi.org/10.1002/adma.201304497

264. Patel MA, Yang H, Chiu PL, et al. Direct Production of Graphene Nanosheets for Near Infrared Photoacoustic Imaging. *ACS Nano*. 2013;7(9):8147-8157. doi:10.1021/nn403429v

265. Song G, Hao J, Liang C, et al. Degradable Molybdenum Oxide Nanosheets with Rapid Clearance and Efficient Tumor Homing Capabilities as a Therapeutic Nanoplatform. *Angew Chemie Int Ed*. 2016;55(6):2122-2126. doi:https://doi.org/10.1002/anie.201510597

266. Dai C, Lin H, Xu G, Liu Z, Wu R, Chen Y. Biocompatible 2D Titanium Carbide (MXenes) Composite Nanosheets for pH-Responsive MRI-Guided Tumor Hyperthermia. *Chem Mater*. 2017;29(20):8637-8652. doi:10.1021/acs.chemmater.7b02441

267. Park M, Lee N, Choi SH, et al. Large-Scale Synthesis of Ultrathin Manganese Oxide Nanoplates and Their Applications to T1 MRI Contrast Agents. *Chem Mater*. 2011;23(14):3318-3324. doi:10.1021/cm200414c

268. Chen Y, Ye D, Wu M, et al. Break-up of Two-Dimensional MnO2 Nanosheets Promotes Ultrasensitive pH-Triggered Theranostics of Cancer. *Adv Mater*. 2014;26(41):7019-7026. doi:https://doi.org/10.1002/adma.201402572

269. Zhang S, Yan Z, Li Y, Chen Z, Zeng H. Atomically Thin Arsenene and Antimonene: Semimetal–Semiconductor and Indirect–Direct Band-Gap Transitions. *Angew Chemie Int Ed*. 2015;54(10):3112-3115. doi:https://doi.org/10.1002/anie.201411246

270. Hong H, Zhang Y, Engle JW, et al. In vivo targeting and positron emission tomography imaging of tumor vasculature with 66Ga-labeled nano-graphene. *Biomaterials*. 2012;33(16):4147-4156. doi:https://doi.org/10.1016/j.biomaterials.2012.02.031

271. Huang H, Feng W, Chen Y. Two-dimensional biomaterials: material science, biological effect and biomedical engineering applications. *Chem Soc Rev*. 2021;50(20):11381-11485. doi:10.1039/D0CS01138J

272. Rana VK, Choi M-C, Kong J-Y, et al. Synthesis and Drug-Delivery Behavior of Chitosan-Functionalized Graphene Oxide Hybrid Nanosheets. *Macromol Mater Eng*. 2011;296(2):131-140. doi:10.1002/mame.201000307

273. Chauhan G, Chopra V, Tyagi A, Rath G, Sharma RK, Goyal AK. "Gold nanoparticles composite-folic acid conjugated graphene oxide nanohybrids" for targeted chemo-thermal cancer ablation: In vitro screening and in vivo studies. *Eur J Pharm Sci*. 2017;96:351-361. doi:https://doi.org/10.1016/j.ejps.2016.10.011

274. Zhu W, Gao X, Li Q, et al. Controlled Gas Exfoliation of Boron Nitride into Few-Layered Nanosheets. *Angew Chemie Int Ed*. 2016;55(36):10766-10770. doi:10.1002/anie.201605515

275. Robinson JT, Xie C, Pohlmeyer E, et al. Developing Next-Generation Brain Sensing Technologies—A Review. *IEEE Sens J*. 2019;19(22):10163-10175. doi:10.1109/JSEN.2019.2931159

276. Yang K, Wan J, Zhang S, Zhang Y, Lee S-T, Liu Z. In Vivo Pharmacokinetics, Long-Term Biodistribution, and Toxicology of PEGylated Graphene in Mice. *ACS Nano*. 2011;5(1):516-522. doi:10.1021/nn1024303

277. Zhu W, Yang Y, Jin Q, et al. Two-dimensional metal-organic-framework as a unique theranostic nano-platform for nuclear imaging and chemo-photodynamic cancer therapy. *Nano Res*. 2019;12(6):1307-1312. doi:10.1007/s12274-018-2242-2

278. Jiang ZW, Zou YC, Zhao TT, Zhen SJ, Li YF, Huang CZ. Controllable Synthesis of Porphyrin-Based 2D Lanthanide Metal–Organic Frameworks with Thickness- and Metal-Node-Dependent Photocatalytic Performance. *Angew Chemie Int Ed*. 2020;59(8):3300-3306. doi:https://doi.org/10.1002/anie.201913748

279. Melamed JR, Edelstein RS, Day ES. Elucidating the Fundamental Mechanisms of Cell Death Triggered by Photothermal Therapy. *ACS Nano*. 2015;9(1):6-11. doi:10.1021/acsnano.5b00021

280. Yang K, Zhang S, Zhang G, Sun X, Lee S-T, Liu Z. Graphene in Mice: Ultrahigh In Vivo Tumor Uptake and Efficient Photothermal Therapy. *Nano Lett*. 2010;10(9):3318-3323. doi:10.1021/nl100996u

281. Lafond M, Yoshizawa S, Umemura S. Sonodynamic Therapy: Advances and Challenges in Clinical Translation. *J Ultrasound Med*. 2019;38(3):567-580. doi:https://doi.org/10.1002/jum.14733

282. Choi V, Rajora MA, Zheng G. Activating Drugs with Sound: Mechanisms Behind Sonodynamic Therapy and the Role of Nanomedicine. *Bioconjug Chem*. 2020;31(4):967-989. doi:10.1021/acs.bioconjchem.0c00029

283. Ma A, Chen H, Cui Y, et al. Metalloporphyrin Complex-Based Nanosonosensitizers for Deep-Tissue Tumor Theranostics by

Noninvasive Sonodynamic Therapy. *Small*. 2019;15(5):1804028. doi:10.1002/smll.201804028

284. Dai C, Zhang S, Liu Z, Wu R, Chen Y. Two-Dimensional Graphene Augments Nanosonosensitized Sonocatalytic Tumor Eradication. *ACS Nano*. 2017;11(9):9467-9480. doi:10.1021/acsnano.7b05215

285. Sun D, Pang X, Cheng Y, et al. Ultrasound-Switchable Nanozyme Augments Sonodynamic Therapy against Multidrug-Resistant Bacterial Infection. *ACS Nano*. 2020;14(2):2063-2076. doi:10.1021/acsnano.9b08667

286. Liang R, Li Y, Huo M, Lin H, Chen Y. Triggering Sequential Catalytic Fenton Reaction on 2D MXenes for Hyperthermia-Augmented Synergistic Nanocatalytic Cancer Therapy. *ACS Appl Mater Interfaces*. 2019;11(46):42917-42931. doi:10.1021/acsami.9b13598

287. Gao S, Lu X, Zhu P, et al. Self-evolved hydrogen peroxide boosts photothermal-promoted tumor-specific nanocatalytic therapy. *J Mater Chem B*. 2019;7(22):3599-3609. doi:10.1039/C9TB00525K

288. Cheng L, Shen S, Shi S, et al. FeSe2-Decorated Bi2Se3 Nanosheets Fabricated via Cation Exchange for Chelator-Free 64Cu-Labeling and Multimodal Image-Guided Photothermal-Radiation Therapy. *Adv Funct Mater*. 2016;26(13):2185-2197. doi:https://doi.org/10.1002/adfm.201504810

289. Zhang X-D, Chen J, Min Y, et al. Metabolizable Bi2Se3 Nanoplates: Biodistribution, Toxicity, and Uses for Cancer Radiation Therapy and Imaging. *Adv Funct Mater*. 2014;24(12):1718-1729. doi:https://doi.org/10.1002/adfm.201302312

290. Xian L, Pérez Paz A, Bianco E, Ajayan PM, Rubio A. Square selenene and tellurene: novel group VI elemental 2D materials with nontrivial topological properties. *2D Mater*. 2017;4(4):041003. doi:10.1088/2053-1583/aa8418

291. He L, Nie T, Xia X, et al. Designing Bioinspired 2D MoSe2 Nanosheet for Efficient Photothermal-Triggered Cancer Immunotherapy with Reprogramming Tumor-Associated Macrophages. *Adv Funct Mater*. 2019;29(30):1901240. doi:https://doi.org/10.1002/adfm.201901240

292. Zhu W, Chen Q, Jin Q, et al. Sonodynamic therapy with immune modulatable two-dimensional coordination nanosheets for enhanced anti-tumor immunotherapy. *Nano Res*. 2021;14(1):212-221. doi:10.1007/s12274-020-3070-8

293. Li T, Liu ZL, Xiao M, et al. Impact of bone marrow mesenchymal stem cell immunomodulation on the osteogenic effects of laponite. *Stem Cell Res Ther*. 2018;9(1):100. doi:10.1186/s13287-018-0818-0

294. Zhang J, Chen H, Zhao M, Liu G, Wu J. 2D nanomaterials for tissue engineering application. *Nano Res*. 2020;13(8):2019-2034. doi:10.1007/s12274-020-2835-4

295. Banerjee AN. Graphene and its derivatives as biomedical materials: future prospects and challenges. *Interface Focus*. 2018;8(3):20170056. doi:10.1098/rsfs.2017.0056

296. Liu S, Zeng TH, Hofmann M, et al. Antibacterial Activity of Graphite, Graphite Oxide, Graphene Oxide, and Reduced Graphene Oxide: Membrane and Oxidative Stress. *ACS Nano*. 2011;5(9):6971-6980. doi:10.1021/nn202451x

297. Ran X, Du Y, Wang Z, et al. Hyaluronic Acid-Templated Ag Nanoparticles/Graphene Oxide Composites for Synergistic Therapy of Bacteria Infection. *ACS Appl Mater Interfaces*. 2017;9(23):19717-19724. doi:10.1021/acsami.7b05584

298. Raslan A, Saenz del Burgo L, Ciriza J, Pedraz JL. Graphene oxide and reduced graphene oxide-based scaffolds in regenerative medicine. *Int J Pharm*. 2020;580:119226. doi:10.1016/j.ijpharm.2020.119226

299. Ghazy E, Rahdar A, Barani M, Kyzas GZ. Nanomaterials for Parkinson disease: Recent progress. *J Mol Struct*. 2021;1231:129698. doi:10.1016/j.molstruc.2020.129698

300. Jiang L, Chen D, Wang Z, et al. Preparation of an Electrically Conductive Graphene Oxide/Chitosan Scaffold for Cardiac Tissue Engineering. *Appl Biochem Biotechnol*. 2019;188(4):952-964. doi:10.1007/s12010-019-02967-6

301. Ghasemi A, Imani R, Yousefzadeh M, Bonakdar S, Solouk A, Fakhrzadeh H. Studying the Potential Application of Electrospun Polyethylene Terephthalate/Graphene Oxide Nanofibers as Electroconductive Cardiac Patch. *Macromol Mater Eng*. 2019;304(8):1900187. doi:https://doi.org/10.1002/mame.201900187

302. Cheng L, Cai Z, Zhao J, et al. Black phosphorus-based 2D materials for bone therapy. *Bioact Mater*. 2020;5(4):1026-1043. doi:https://doi.org/10.1016/j.bioactmat.2020.06.007

303. Gaharwar AK, Cross LM, Peak CW, et al. 2D Nanoclay for Biomedical Applications: Regenerative Medicine, Therapeutic Delivery, and Additive Manufacturing. *Adv Mater*. 2019;31(23):1900332. doi:https://doi.org/10.1002/adma.201900332

304. Gao Y, Du H, Xie Z, et al. Self-adhesive photothermal hydrogel films for solar-light assisted wound healing. *J Mater Chem B*. 2019;7(23):3644-3651. doi:10.1039/C9TB00481E

305. Hu T, Mei X, Wang Y, Weng X, Liang R, Wei M. Two-dimensional nanomaterials: fascinating materials in biomedical field. *Sci Bull*. 2019;64(22):1707-1727. doi:https://doi.org/10.1016/j.scib.2019.09.021

306. Rohaizad N, Mayorga-Martinez CC, Fojtů M, Latiff NM, Pumera M. Two-dimensional materials in biomedical, biosensing and sensing applications. *Chem Soc Rev*. 2021;50(1):619-657. doi:10.1039/D0CS00150C

307. Lu T, Wang L, Jiang Y, Liu Q, Huang C. Hexagonal boron nitride nanoplates as emerging biological nanovectors and their potential applications in biomedicine. *J Mater Chem B*. 2016;4(36):6103-6110. doi:10.1039/c6tb01481j

308. Kıvanç M, Barutca B, Koparal AT, Göncü Y, Bostancı SH, Ay N. Effects of hexagonal boron nitride nanoparticles on antimicrobial and antibiofilm activities, cell viability. *Mater Sci Eng C*. 2018;91:115-124. doi:10.1016/j.msec.2018.05.028

309. Li X, Wang X, Zhang J, et al. Hollow boron nitride nanospheres as boron reservoir for prostate cancer treatment. *Nat Commun*. 2017;8(1):13936. doi:10.1038/ncomms13936

310. Nurunnabi M, Nafiujjaman M, Lee S-J, Park I-K, Huh KM, Lee Y. Preparation of ultra-thin hexagonal boron nitride nanoplates for cancer cell imaging and neurotransmitter sensing. *Chem Commun*. 2016;52(36):6146-6149. doi:10.1039/C5CC10650H

311. Liu K, Zhang G, Pu J, Ma F, Wu G, Lu Z. Impermeability of boron nitride defect-sensitive monolayer with atomic-oxygen-healing ability. *Ceram Int*. 2018;44(12):13888-13893. doi:10.1016/j.ceramint.2018.04.236

312. Prozorovska L, Kidambi PR. State-of-the-Art and Future Prospects for Atomically Thin Membranes from 2D Materials. *Adv Mater*. 2018;30(52):1801179. doi:https://doi.org/10.1002/adma.201801179

313. Li X, Gong B, Jin Y, Chen Z, Yang W. Intelligent water-borne coatings with self-reporting, self-healing, and robust barrier performance for the active corrosion protection of Q235 steels. *Prog Org Coatings*. 2024;189:108366. doi:https://doi.org/10.1016/j.porgcoat.2024.108366

314. Zhao H-R, Ding J-H, Yu H-B. Phosphorylated Boron Nitride Nanosheets as Highly Effective Barrier Property Enhancers. *Ind Eng Chem Res*. 2018;57(42):14096-14105. doi:10.1021/acs.iecr.8b03220

315. Goswami RN, Mourya P, Saini R, et al. Polyaniline-wrapped h-boron nitride nanosheets as anticorrosive filler in epoxy coatings for substantially enhanced protection of mild steel. *J Ind Eng Chem*. 2024;140:285-297. doi:https://doi.org/10.1016/j.jiec.2024.05.048

316. Wu Y, Yu J, Zhao W, Wang C, Wu B, Lu G. Investigating the anti-corrosion behaviors of the waterborne epoxy composite coatings with barrier and inhibition roles on mild steel. *Prog Org Coatings*. 2019;133:8-18. doi:https://doi.org/10.1016/j.porgcoat.2019.04.028

317. Wang S, Tang J, Xiang H, et al. Mechanism Insights in Anticorrosion Performance of Waterborne Epoxy Coatings Reinforced by PEI-Functionalized Boron Nitride Nanosheets. *Langmuir*. 2024;40(21):10980-10991. doi:10.1021/acs.langmuir.4c00346

318. Wu Y, He Y, Chen C, et al. Non-covalently functionalized boron nitride by graphene oxide for anticorrosive reinforcement of water-borne epoxy coating. *Colloids Surfaces A Physicochem Eng Asp*. 2020;587:124337. doi:https://doi.org/10.1016/j.colsurfa.2019.124337

319. Du Y, Zhang Y, Zhang R, Lin S. Synthesis of Ultrathin Functional Boron Nitride Nanosheets and Their Application in Anticorrosion. *ACS Appl Nano Mater*. 2021;4(10):11088-11096. doi:10.1021/acsanm.1c02565

320. Tanaka K, Ibe H, Kumazawa H. Sub-micrometer Size Emulsification Using a High Pressure Wet-type Jet Mill. *Kagaku Kogaku Ronbushu*. 2003;29(6):740-747. doi:10.1252/kakoronbunshu.29.740

321. Hamada S, Aoki N, Suzuki Y. Effects of Water Soaking on Bread-Making Quality of Brown Rice Flour. *Food Sci Technol Res*. 2012;18:25-30. doi:10.3136/fstr.18.25

322. Omura N, Hotta Y, Sato K, Kinemuchi Y, Kume S, Watari K. Wet jet milling of Al2O3 slurries. *J Eur Ceram Soc*. 2007;27(2-3):733-737. doi:10.1016/j.jeurceramsoc.2006.04.001

323. Tominaga Y, Sato K, Shimamoto D, Imai Y, Hotta Y. Wet-jet milling-assisted exfoliation of h-BN particles with lamination structure. *Ceram Int*. 2015;41(9):10512-10519. doi:10.1016/j.ceramint.2015.04.143

324. Omura N, Hotta Y, Sato K, Kinemuchi Y, Kume S, Watari K. Fabrication of Stable Al2O3 Slurries and Dense Green Bodies Using Wet Jet Milling. *J Am Ceram Soc*. 2006;89(9):2738-2743. doi:10.1111/j.1551-2916.2006.01142.x

325. Thakur S, Jadon AS, Imran K, et al. Nanoparticles and their application in biomedical science. *Int J Mod Pharm Res*. 2022;6(11):61-68.

326. Wu X, Yokoyama Y, Takahashi H, et al. Improved In Vivo Delivery of Small RNA Based on the Calcium Phosphate Method. *J Pers Med*. 2021;11(11):1160. doi:10.3390/jpm11111160

327. Liu W-Y, Hsieh Y-S, Ko H-H, Wu Y-T. Formulation Approaches to Crystalline Status Modification for Carotenoids: Impacts on Dissolution, Stability, Bioavailability, and Bioactivities. *Pharmaceutics*. 2023;15(2):485. doi:10.3390/pharmaceutics15020485

328. Omura N, Hotta Y, Sato K, Kinemuchi Y, Kume S, Watai K. Slip Casting of Al2O3 Slurries Prepared by Wet Jet Milling. *J Ceram Soc Japan*. 2005;113(1319):495-497. doi:10.2109/jcersj.113.495

329. Isobe T, Hotta Y, Watari K. Dispersion of nano- and submicron-sized Al2O3 particles by wet-jet milling method. *Mater Sci Eng B*. 2008;148(1-3):192-195. doi:10.1016/j.mseb.2007.09.072

330. Bellani S, Petroni E, Del Rio Castillo AE, et al. Scalable Production of Graphene Inks via Wet-Jet Milling Exfoliation for Screen-Printed Micro-Supercapacitors. *Adv Funct Mater*. 2019;29(14):1-14. doi:10.1002/adfm.201807659

331. Chaney LE, van Beek A, Downing JR, et al. Bayesian Optimization of Environmentally Sustainable Graphene Inks Produced by Wet Jet Milling. *Small*. 2024;20(33):1-11. doi:10.1002/smll.202309579

332. Hotta Y, Yilmaz H, Shirai T, Ohota K, Sato K, Watari K. State of the Dispersant and Particle Surface During Wet-Jet Milling

for Preparation of a Stable Slurry. *J Am Ceram Soc*. 2008;91(4):1095-1101. doi:10.1111/j.1551-2916.2008.02310.x

333. Seyhan AT, Göncü Y, Durukan O, Akay A, Ay N. Silanization of boron nitride nanosheets (BNNSs) through microfluidization and their use for producing thermally conductive and electrically insulating polymer nanocomposites. *J Solid State Chem*. 2017;249:98-107. doi:10.1016/j.jssc.2017.02.020

334. Buzaglo M, Shtein M, Regev O. Graphene Quantum Dots Produced by Microfluidization. *Chem Mater*. 2016;28(1):21-24. doi:10.1021/acs.chemmater.5b03301

335. Jiang H, Li J, Xie Y, et al. Rapid exfoliation and surface hydroxylation of high-quality boron nitride nanosheets enabling waterborne polyurethane with high thermal conductivity and flame retardancy. *Adv Compos Hybrid Mater*. 2024;7(1):8. doi:10.1007/s42114-023-00818-x

336. Marsh KL, Souliman M, Kaner RB. Co-solvent exfoliation and suspension of hexagonal boron nitride. *Chem Commun*. 2015;51(1):187-190. doi:10.1039/C4CC07324J

337. Paton KR, Varrla E, Backes C, et al. Scalable production of large quantities of defect-free few-layer graphene by shear exfoliation in liquids. *Nat Mater*. 2014;13(6):624-630. doi:10.1038/nmat3944

338. Saha SK, Waghmare U V, Krishnamurthy HR, Sood AK. Phonons in few-layer graphene and interplanar interaction: A first-principles study. *Phys Rev B*. 2008;78(16):165421. doi:10.1103/PhysRevB.78.165421

339. Lennard-Jones JE. Cohesion. *Proc Phys Soc*. 1931;43(5):461-482. doi:10.1088/0959-5309/43/5/301

340. Shibuta Y, Elliott JA. Interaction between two graphene sheets with a turbostratic orientational relationship. *Chem Phys Lett*. 2011;512(4-6):146-150. doi:10.1016/j.cplett.2011.07.013

341. Lui CH, Malard LM, Kim S, et al. Observation of Layer-Breathing Mode Vibrations in Few-Layer Graphene through Combination Raman Scattering. *Nano Lett*. 2012;12(11):5539-5544. doi:10.1021/nl302450s

342. Choi C-H, Kwak Y, Malhotra R, Chang C-H. Microfluidics for Two-Dimensional Nanosheets: A Mini Review. *Processes*. 2020;8(9):1067. doi:10.3390/pr8091067

343. Jacobsen H, Zwicker G, Lortz W, Stachowiak E, Brandes R. Characterisation of Oxide-CMP Slurries with Fumed-Silica Abrasive Particles Modified by Wet-Jet Milling. In: *CMP-MIC*. ; 2004.

344. Del Rio Catillo AE, Ansaldo A, Pellegrini V, Bonaccorso F. Exfoliation of layered materials by wet-jet milling techniques. Published online 2019.

345. White AM, Sankey BM. Thermal stabilization of N-methyl-2-pyrrolidone. Published online 1978.

346. JOKOH. JOKOH NANO GENESIS. Published 2025. https://jokoh.com/en/products/nano-genesis/

347. Muñoz López CA, Peeters K, Van Impe J. Data-Driven Modeling of the Spray Drying Process. Process Monitoring and Prediction of the Particle Size in Pharmaceutical Production. *ACS Omega*. 2024;9(24):25678-25693. doi:10.1021/acsomega.3c08032

348. Molina-Garcia MA, Bellani S, Del Rio Castillo AE, et al. Wet-jet milling exfoliated hexagonal boron nitride as industrial anticorrosive pigment for polymeric coatings. *J Phys Mater*. 2023;6(3):035006. doi:10.1088/2515-7639/acd0d8

349. Huang C, Chen C, Ye X, et al. Stable colloidal boron nitride nanosheet dispersion and its potential application in catalysis. *J Mater Chem A*. 2013;1(39):12192. doi:10.1039/c3ta12231j

350. Cai W, Hong N, Feng X, et al. A facile strategy to simultaneously exfoliate and functionalize boron nitride nanosheets via Lewis acid-base interaction. *Chem Eng J*. 2017;330:309-321. doi:10.1016/j.cej.2017.07.162

351. Kumar AM, Khan A, Hussein MA, et al. Hybrid nanocomposite coatings from PEDOT and BN-TiO2 nanosheets: Enhanced invitro corrosion resistance, wettability and biocompatibility for biomedical applications. *Prog Org Coatings*. 2022;170:106946. doi:https://doi.org/10.1016/j.porgcoat.2022.106946

352. Matović B, Luković J, Nikolić M, et al. Synthesis and characterization of nanocrystaline hexagonal boron nitride powders: XRD and luminescence properties. *Ceram Int*. 2016;42(15):16655-16658. doi:https://doi.org/10.1016/j.ceramint.2016.07.096

353. Bellani S, Gabatel L, Del Rio Catillo AE, et al. Coating system for protecting a substrate. Published online 2022.

354. Hou B, Li X, Ma X, et al. The cost of corrosion in China. *npj Mater Degrad*. 2017;1(1):4. doi:10.1038/s41529-017-0005-2

355. Cole IS, Marney D. The science of pipe corrosion: A review of the literature on the corrosion of ferrous metals in soils. *Corros Sci*. 2012;56:5-16. doi:https://doi.org/10.1016/j.corsci.2011.12.001

356. Koch G. Cost of corrosion. In: El-Sherik AM, ed. *Trends in Oil and Gas Corrosion Research and Technologies: Production and Transmission*. Woodhead Publishing Series in Energy. Woodhead Publishing; 2017:3-30. doi:10.1016/b978-0-08-101105-8.01001-9

357. Wen G, Bai P, Tian Y. A Review of Graphene-Based Materials for Marine Corrosion Protection. *J Bio- Tribo-Corrosion*. 2021;7(1):27. doi:10.1007/s40735-020-00456-6

358. AhadiParsa M, Dehghani A, Ramezanzadeh M, Ramezanzadeh B. Rising of MXenes: Novel 2D-functionalized nanomaterials as a new milestone in corrosion science - a critical review. *Adv Colloid Interface Sci*. 2022;307:102730.

doi:https://doi.org/10.1016/j.cis.2022.102730

359. Al-Moubaraki AH, Obot IB. Corrosion challenges in petroleum refinery operations: Sources, mechanisms, mitigation, and future outlook. *J Saudi Chem Soc*. 2021;25(12):101370. doi:https://doi.org/10.1016/j.jscs.2021.101370

360. Cui G, Bi Z, Zhang R, Liu J, Yu X, Li Z. A comprehensive review on graphene-based anti-corrosive coatings. *Chem Eng J*. 2019;373:104-121. doi:https://doi.org/10.1016/j.cej.2019.05.034

361. Böhm S. Graphene against corrosion. *Nat Nanotechnol*. 2014;9(10):741-742. doi:10.1038/nnano.2014.220

362. Chen S, Brown L, Levendorf M, et al. Oxidation Resistance of Graphene-Coated Cu and Cu/Ni Alloy. *ACS Nano*. 2011;5(2):1321-1327. doi:10.1021/nn103028d

363. Prasai D, Tuberquia JC, Harl RR, Jennings GK, Bolotin KI. Graphene: Corrosion-Inhibiting Coating. *ACS Nano*. 2012;6(2):1102-1108. doi:10.1021/nn203507y

364. Topsakal M, Şahin H, Ciraci S. Graphene coatings: An efficient protection from oxidation. *Phys Rev B*. 2012;85(15):155445. doi:10.1103/PhysRevB.85.155445

365. Kang D, Kwon JY, Cho H, et al. Oxidation Resistance of Iron and Copper Foils Coated with Reduced Graphene Oxide Multilayers. *ACS Nano*. 2012;6(9):7763-7769. doi:10.1021/nn3017316

366. Zhao Y, Xie Y, Hui YY, et al. Highly impermeable and transparent graphene as an ultra-thin protection barrier for Ag thin films. *J Mater Chem C*. 2013;1(32):4956. doi:10.1039/c3tc30743c

367. Wu Y, Zhu X, Zhao W, Wang Y, Wang C, Xue Q. Corrosion mechanism of graphene coating with different defect levels. *J Alloys Compd*. 2019;777:135-144. doi:https://doi.org/10.1016/j.jallcom.2018.10.260

368. Schriver M, Regan W, Gannett WJ, Zaniewski AM, Crommie MF, Zettl A. Graphene as a Long-Term Metal Oxidation Barrier: Worse Than Nothing. *ACS Nano*. 2013;7(7):5763-5768. doi:10.1021/nn4014356

369. Cui C, Lim ATO, Huang J. A cautionary note on graphene anti-corrosion coatings. *Nat Nanotechnol*. 2017;12(9):834-835. doi:10.1038/nnano.2017.187

370. Yu F, Camilli L, Wang T, et al. Complete long-term corrosion protection with chemical vapor deposited graphene. *Carbon N Y*. 2018;132:78-84. doi:https://doi.org/10.1016/j.carbon.2018.02.035

371. Camilli L, Yu F, Cassidy A, Hornekær L, Bøggild P. Challenges for continuous graphene as a corrosion barrier. *2D Mater*. 2019;6(2):022002. doi:10.1088/2053-1583/ab04d4

372. Sørensen PA, Kiil S, Dam-Johansen K, Weinell CE. Anticorrosive coatings: a review. *J Coatings Technol Res*. 2009;6(2):135-176. doi:10.1007/s11998-008-9144-2

373. Cui G, Bi Z, Wang S, et al. A comprehensive review on smart anti-corrosive coatings. *Prog Org Coatings*. 2020;148:105821. doi:10.1016/j.porgcoat.2020.105821

374. Verma C, Dubey S, Barsoum I, Alfantazi A, Ebenso E, Quraishi MA. Hexagonal Boron Nitride as a Cutting-Edge 2D Material for Additive Application in Anticorrosive Coatings: Recent Progress, Challenges and Opportunities. *Mater Today Commun*. 2023;35:106367. doi:10.1016/j.mtcomm.2023.106367

375. Pourhashem S, Saba F, Duan J, et al. Polymer/Inorganic nanocomposite coatings with superior corrosion protection performance: A review. *J Ind Eng Chem*. 2020;88:29-57. doi:https://doi.org/10.1016/j.jiec.2020.04.029

376. Yi M, Shen Z, Zhang W, et al. Hydrodynamics-assisted scalable production of boron nitride nanosheets and their application in improving oxygen-atom erosion resistance of polymeric composites. *Nanoscale*. 2013;5(21):10660-10667. doi:10.1039/C3NR03714B

377. Husain E, Narayanan TN, Taha-Tijerina JJ, Vinod S, Vajtai R, Ajayan PM. Marine Corrosion Protective Coatings of Hexagonal Boron Nitride Thin Films on Stainless Steel. *ACS Appl Mater Interfaces*. 2013;5(10):4129-4135. doi:10.1021/am400016y

378. Fan Y, Yang H, Fan H, et al. Corrosion Resistance of Modified Hexagonal Boron Nitride (h-BN) Nanosheets Doped Acrylic Acid Coating on Hot-Dip Galvanized Steel. *Materials (Basel)*. 2020;13(10):2340. doi:10.3390/ma13102340

379. Alabdullah, F.T.; Ali, C.; Mishra B. Evaluation of Corrosion Resistance Properties of Hexagonal Boron Nitride Based Polymer Composite Coatings for Carbon Steel in a Saline Environment. *Corros Sci Technol*. 2022;21(1):41-52.

380. Bai C, Wang F, Zhao Z, Zhang B, Yu Y, Zhang J. Mussel-inspired facile fabrication of dense hexagonal boron nitride nanosheet-based coatings for anticorrosion and antifriction applications. *Mater Today Nano*. 2021;15:100129. doi:https://doi.org/10.1016/j.mtnano.2021.100129

381. Zhang C, He Y, Li F, Di H, Zhang L, Zhan Y. h-BN decorated with Fe3O4 nanoparticles through mussel-inspired chemistry of dopamine for reinforcing anticorrosion performance of epoxy coatings. *J Alloys Compd*. 2016;685:743-751. doi:https://doi.org/10.1016/j.jallcom.2016.06.220

382. Sun J, Xiao X, Meng G, Gu L. Mussel-inspired hydrophobic modification of boron nitride nanosheets to enhance the dispersion and anticorrosive performance in polymeric coatings. *Prog Org Coatings*. 2022;170:106986. doi:https://doi.org/10.1016/j.porgcoat.2022.106986

383. Liu Z, Li J, Liu X. Novel Functionalized BN Nanosheets/Epoxy Composites with Advanced Thermal Conductivity and Mechanical Properties. *ACS Appl Mater Interfaces*. 2020;12(5):6503-6515. doi:10.1021/acsami.9b21467

384. Kuila C, Maji A, Phadikar U, Mallisetty PK, Murmu NC, Kuila T. Alkali-assisted functionalization of hexagonal boron nitride reinforced epoxy composite to improve the thermomechanical and anticorrosion performance for advanced thermal management. *Polym Compos*. 2024;45(6):5643-5655. doi:10.1002/pc.28154

385. Yan Y, Jiang X, Liao K, et al. Effects of OCF content and oxidation treatment on thermal conductivity and corrosion resistance of CF/BN/EPN coating. *Surf Coatings Technol*. 2024;481:130664. doi:https://doi.org/10.1016/j.surfcoat.2024.130664

386. Yan Y, Liao K, Hu J, et al. Effects of h-BN content and silane functionalization on thermal conductivity and corrosion resistance of h-BN/EPN coating. *Surf Coatings Technol*. 2024;476:130185. doi:https://doi.org/10.1016/j.surfcoat.2023.130185

387. Sun J, Tang Z, Meng G, Gu L. Silane functionalized plasma-treated boron nitride nanosheets for anticorrosive reinforcement of waterborne epoxy coatings. *Prog Org Coatings*. 2022;167:106831. doi:https://doi.org/10.1016/j.porgcoat.2022.106831

388. Xia Y, Zhang S, Tong L, Lin G, Bai Z, Liu X. Enhanced effect of phenyl silane-modified hexagonal boron nitride nanosheets on the corrosion protection behavior of poly(arylene ether nitrile) coating. *Colloids Surfaces A Physicochem Eng Asp*. 2022;652:129869. doi:10.1016/j.colsurfa.2022.129869

389. Wang L, Yuan M, Zhao Y, Guo Z, Lu X, Xin Z. Fabrication of superhydrophobic bio-based polybenzoxazine/hexagonal boron nitride composite coating for corrosion protection. *Prog Org Coatings*. 2022;167:106863. doi:https://doi.org/10.1016/j.porgcoat.2022.106863

390. Lu F, Liu C, Chen Z, et al. Polypyrrole-functionalized boron nitride nanosheets for high-performance anti-corrosion composite coating. *Surf Coatings Technol*. 2021;420:127273. doi:https://doi.org/10.1016/j.surfcoat.2021.127273

391. Cui M, Ren S, Chen J, et al. Anticorrosive performance of waterborne epoxy coatings containing water-dispersible hexagonal boron nitride (h-BN) nanosheets. *Appl Surf Sci*. 2017;397:77-86. doi:10.1016/j.apsusc.2016.11.141

392. Zhao H, Ding J, Yu H. The efficient exfoliation and dispersion of hBN nanoplatelets: advanced application to waterborne anticorrosion coatings. *New J Chem*. 2018;42(17):14433-14443. doi:10.1039/C8NJ03113D

393. Wang S, Zhang Q, Tang J, et al. Highly effective anti-corrosion composite coatings enhanced by non-covalent functionalized boron nitride nanosheets via a facile latex approach. *Compos Commun*. 2022;32:101153. doi:10.1016/j.coco.2022.101153

394. Tang G, Hou X, Wang Y, et al. Hexagonal Boron Nitride/Polyaniline Nanocomposites for Anticorrosive Waterborne Epoxy Coatings. *ACS Appl Nano Mater*. 2022;5(1):361-372. doi:10.1021/acsanm.1c03173

395. Li J, Huang X, Bi J. Enhancement of the Anticorrosion Properties of Epoxy Resin Composites through Incorporating Hydroxylated and Silanised Hexagonal Boron Nitride (h-BN). *Int J Electrochem Sci*. 2022;17(3):22032. doi:https://doi.org/10.20964/2022.03.16

396. Wan S, Chen H, Cai G, Liao B, Guo X. Functionalization of h-BN by the exfoliation and modification of carbon dots for enhancing corrosion resistance of waterborne epoxy coating. *Prog Org Coatings*. 2022;165:106757. doi:https://doi.org/10.1016/j.porgcoat.2022.106757

397. Emanet M, Sen Ö, Taşkin IÇ, Çulha M. Synthesis, Functionalization, and Bioapplications of Two-Dimensional Boron Nitride Nanomaterials. *Front Bioeng Biotechnol*. 2019;7(December). doi:10.3389/fbioe.2019.00363

398. Luo W, Wang Y, Hitz E, Lin Y, Yang B, Hu L. Solution Processed Boron Nitride Nanosheets: Synthesis, Assemblies and Emerging Applications. *Adv Funct Mater*. 2017;27(31):1701450. doi:https://doi.org/10.1002/adfm.201701450

399. Wu Y, He Y, Zhou T, et al. Synergistic functionalization of h-BN by mechanical exfoliation and PEI chemical modification for enhancing the corrosion resistance of waterborne epoxy coating. *Prog Org Coatings*. 2020;142:105541. doi:10.1016/j.porgcoat.2020.105541

400. Li A, Sun M, Ma Z, et al. Anticorrosion performance of polyvinyl butyral composite coatings improved by polyaniline-multiwalled carbon nanotubes/poly (methylhydrosiloxane). *Thin Solid Films*. 2020;712:138347. doi:https://doi.org/10.1016/j.tsf.2020.138347

401. Anandkumar B, Geetisubhra J, Pongachira GR, Philip J. Polydimethylsiloxane–graphene oxide nanocomposite coatings with improved anti-corrosion and anti-biofouling properties. *Environ Sci Pollut Res*. 2021;28(6):7404-7422. doi:https://doi.org/10.1007/s11356-020-11068-5

402. Cai J, Murugadoss V, Jiang J, et al. Waterborne polyurethane and its nanocomposites: a mini-review for anti-corrosion coating, flame retardancy, and biomedical applications. *Adv Compos Hybrid Mater*. 2022;5(2):641-650. doi:10.1007/s42114-022-00473-8

403. Wang H, Han M, Song Y, Zhang H. Design, manufacturing and applications of wearable triboelectric nanogenerators. *Nano Energy*. 2021;81:105627. doi:https://doi.org/10.1016/j.nanoen.2020.105627

404. Zadeh MK, Yeganeh M, Shoushtari MT, Esmaeilkhanian A. Corrosion performance of polypyrrole-coated metals: A review of perspectives and recent advances. *Synth Met*. 2021;274:116723. doi:https://doi.org/10.1016/j.synthmet.2021.116723

405. Bouabdallaoui M, Aouzal Z, El Guerraf A, et al. Influence of polythiophene overoxidation on its physicochemical properties

and corrosion protection performances. *Mater Today Proc*. 2020;31:S69-S74. doi:10.1016/j.matpr.2020.06.067

406. Liu H, Feng J, Nicoli E, et al. Predicting the reliability of polyisobutylene seal for photovoltaic application. In: Dhere NG, Wohlgemuth JH, eds. *Proc. SPIE 8472, Reliability of Photovoltaic Cells, Modules, Components, and Systems V*. Vol 8472. ; 2012:84720Y. doi:10.1117/12.931240

407. Christensen SF, Everland H, Hassager O, Almdal K. Observations of peeling of a polyisobutylene-based pressure-sensitive adhesive. *Int J Adhes Adhes*. 1998;18(2):131-137. doi:https://doi.org/10.1016/S0143-7496(97)00037-7

408. Kim Y, Kim H, Graham S, Dyer A, Reynolds JR. Durable polyisobutylene edge sealants for organic electronics and electrochemical devices. *Sol Energy Mater Sol Cells*. 2012;100:120-125. doi:https://doi.org/10.1016/j.solmat.2011.12.012

409. Groenewolt M, Brezesinski T, Schlaad H, Antonietti M, Groh PW, Iván B. Polyisobutylene-block-Poly(ethylene oxide) for Robust Templating of Highly Ordered Mesoporous Materials. *Adv Mater*. 2005;17(9):1158-1162. doi:https://doi.org/10.1002/adma.200401549

410. Haldar U, Bauri K, Li R, Faust R, De P. Polyisobutylene-Based pH-Responsive Self-Healing Polymeric Gels. *ACS Appl Mater Interfaces*. 2015;7(16):8779-8788. doi:10.1021/acsami.5b01272

411. Reid J, Barker J. Understanding Polyisobutylene Succinimides (PIBSI) and Internal Diesel Injector Deposits. In: *SAE Technical Paper 2013-01-2682*. ; 2013:12. doi:10.4271/2013-01-2682

412. Funke W. Problems and progress in organic coatings science and technology. *Prog Org Coatings*. 1997;31(1-2):5-9. doi:10.1016/S0300-9440(97)00013-1

413. Ramezanzadeh B, Attar MM. Studying the corrosion resistance and hydrolytic degradation of an epoxy coating containing ZnO nanoparticles. *Mater Chem Phys*. 2011;130(3):1208-1219. doi:https://doi.org/10.1016/j.matchemphys.2011.08.065

414. Mansfeld F. Tafel Slopes and Corrosion Rates from Polarization Resistance Measurements. *Corrosion*. 1973;29(10):397-402. doi:10.5006/0010-9312-29.10.397

415. Flitt HJ, Schweinsberg DP. Evaluation of corrosion rate from polarisation curves not exhibiting a Tafel region. *Corros Sci*. 2005;47(12):3034-3052. doi:https://doi.org/10.1016/j.corsci.2005.06.014

416. Mansfeld F. Fundamental aspects of the polarization resistance technique—the early days. *J Solid State Electrochem*. 2009;13(4):515-520. doi:10.1007/s10008-008-0652-x

417. Nautiyal A, Qiao M, Cook JE, Zhang X, Huang T-S. High performance polypyrrole coating for corrosion protection and biocidal applications. *Appl Surf Sci*. 2018;427:922-930. doi:https://doi.org/10.1016/j.apsusc.2017.08.093

418. Ashassi-Sorkhabi H, Kazempour A, Frouzat Z. Superior potentials of hydrazone Schiff bases for efficient corrosion protection of mild steel in 1.0 M HCl. *J Adhes Sci Technol*. 2021;35(2):164-184. doi:10.1080/01694243.2020.1794357

419. Bandeira RM, van Drunen J, Garcia AC, Tremiliosi-Filho G. Influence of the thickness and roughness of polyaniline coatings on corrosion protection of AA7075 aluminum alloy. *Electrochim Acta*. 2017;240:215-224. doi:https://doi.org/10.1016/j.electacta.2017.04.083

420. Zhang R, Wan W, Qiu L, Wang Y, Zhou Y. Preparation of hydrophobic polyvinyl alcohol aerogel via the surface modification of boron nitride for environmental remediation. *Appl Surf Sci*. 2017;419:342-347. doi:https://doi.org/10.1016/j.apsusc.2017.05.044

421. Gao X, Li R, Hu L, et al. Preparation of boron nitride nanofibers/PVA composite foam for environmental remediation. *Colloids Surfaces A Physicochem Eng Asp*. 2020;604:125287. doi:10.1016/j.colsurfa.2020.125287

422. Palla-Papavlu A, Dinca V, Dinescu M, et al. Matrix-assisted pulsed laser evaporation of chemoselective polymers. *Appl Phys A*. 2011;105(3):651-659. doi:10.1007/s00339-011-6624-5

423. Sulekha PB, Joseph R, George KE. Studies on polyisobutylene bound paraphenylene diamine antioxidant in natural rubber. *Polym Degrad Stab*. 1999;63(2):225-230. doi:https://doi.org/10.1016/S0141-3910(98)00096-2

424. Amiri S, Mokhtari S. Synthesis and characterization of modified polyisobutylene-based dispersants from polyisobutylene succinimides. *Polym Bull*. 2022;79(2):1069-1079. doi:https://doi.org/10.1007/s00289-021-03538-8

425. Li R, Lv X, Yu J, Wang X, Huang P. Dielectric, thermally conductive, and heat-resistant polyimide composite film filled with silver nanoparticle-modified hexagonal boron nitride. *High Perform Polym*. 2020;32(10):1181-1190. doi:10.1177/0954008320938846

426. Oh H, Kim J. Fabrication of polymethyl methacrylate composites with silanized boron nitride by in-situ polymerization for high thermal conductivity. *Compos Sci Technol*. 2019;172(October 2018):153-162. doi:10.1016/j.compscitech.2019.01.021

427. Yu J, Huang X, Wu C, Wu X, Wang G, Jiang P. Interfacial modification of boron nitride nanoplatelets for epoxy composites with improved thermal properties. *Polymer (Guildf)*. 2012;53(2):471-480. doi:10.1016/j.polymer.2011.12.040

428. Acharya L, Babu P, Behera A, Pattnaik SP, Parida K. Novel synthesis of boron nitride nanosheets from hexagonal boron nitride by modified aqueous phase bi-thermal exfoliation method. *Mater Today Proc*. 2021;35:239-242. doi:10.1016/j.matpr.2020.05.328

429. Hou J, Li G, Yang N, et al. Preparation and characterization of surface modified boron nitride epoxy composites with enhanced

thermal conductivity. *RSC Adv*. 2014;4(83):44282-44290. doi:10.1039/C4RA07394K

430. Mahdizadeh A, Farhadi S, Zabardasti A. Microwave-assisted rapid synthesis of graphene-analogue hexagonal boron nitride (h-BN) nanosheets and their application for the ultrafast and selective adsorption of cationic dyes from aqueous solutions. *RSC Adv*. 2017;7(85):53984-53995. doi:10.1039/C7RA11248C

431. Huang K, Archer LA, Fuller GG. Microstructural Dynamics of a Homopolymer Melt Investigated Using Two-Dimensional Raman Scattering. *Macromolecules*. 1996;29(3):966-972. doi:10.1021/ma9507352

432. De Luca AC, Rusciano G, Pesce G, Caserta S, Guido S, Sasso A. Diffusion in Polymer Blends by Raman Microscopy. *Macromolecules*. 2008;41(15):5512-5514. doi:10.1021/ma800866m

433. Cui M, Ren S, Qin S, Xue Q, Zhao H, Wang L. Non-covalent functionalized hexagonal boron nitride nanoplatelets to improve corrosion and wear resistance of epoxy coatings. *RSC Adv*. 2017;7(70):44043-44053. doi:10.1039/C7RA06835B

434. Qiu S, Li W, Zheng W, Zhao H, Wang L. Synergistic Effect of Polypyrrole-Intercalated Graphene for Enhanced Corrosion Protection of Aqueous Coating in 3.5% NaCl Solution. *ACS Appl Mater Interfaces*. 2017;9(39):34294-34304. doi:10.1021/acsami.7b08325

435. Mahjani MG, Moshrefi R, Sharifi-Viand A, et al. Surface investigation by electrochemical methods and application of chaos theory and fractal geometry. *Chaos, Solitons & Fractals*. 2016;91:598-603. doi:10.1016/j.chaos.2016.08.011

436. Liu J, Zhang J, Tang J, et al. Polydimethylsiloxane Resin Nanocomposite Coating with Alternating Multilayer Structure for Corrosion Protection Performance . *ES Mater Manuf* . 2020;10:29-38. doi:10.30919/esmm5f912

437. Wang S, Yang J, Cao J, Gao L, Yan C. A Mechanistic Study of Corrosion of Graphene and Low zinc- rich Epoxy Coatings on Carbon Steel in Salt Environment. *Int J Electrochem Sci*. 2019;14(10):9671-9681. doi:https://doi.org/10.20964/2019.07.17

438. Ding J, Zhao H, Ji D, et al. Achieving long-term anticorrosion via the inhibition of graphene's electrical activity. *J Mater Chem A*. 2019;7(6):2864-2874. doi:10.1039/C8TA10337B

439. Ding Y, Zhong J, Xie P, et al. Protection of Mild Steel by Waterborne Epoxy Coatings Incorporation of Polypyrrole Nanowires/Graphene Nanocomposites. *Polymers (Basel)*. 2019;11(12):1998. doi:10.3390/polym11121998

440. Ding J, Zhao H, Xu B, Zhao X, Su S, Yu H. Superanticorrosive Graphene Nanosheets through π Deposition of Boron Nitride Nanodots. *ACS Sustain Chem Eng*. 2019;7(12):10900-10911. doi:10.1021/acssuschemeng.9b01796

441. Chang K-C, Ji W-F, Lai M-C, et al. Synergistic effects of hydrophobicity and gas barrier properties on the anticorrosion property of PMMA nanocomposite coatings embedded with graphene nanosheets. *Polym Chem*. 2014;5(3):1049-1056. doi:10.1039/C3PY01178J

442. Zhu G, Cui X, Zhang Y, et al. Poly (vinyl butyral)/Graphene oxide/poly (methylhydrosiloxane) nanocomposite coating for improved aluminum alloy anticorrosion. *Polymer (Guildf)*. 2019;172:415-422. doi:10.1016/j.polymer.2019.03.056

443. Ma Z, Sun M, Li A, Zhu G, Zhang Y. Anticorrosion behavior of polyvinyl butyral (PVB) / polymethylhydrosiloxane (PMHS) / chitosan (Ch) environment-friendly assembled coatings. *Prog Org Coatings*. 2020;144:105662. doi:https://doi.org/10.1016/j.porgcoat.2020.105662

444. Parida B, Iniyan S, Goic R. A review of solar photovoltaic technologies. *Renew Sustain Energy Rev*. 2011;15(3):1625-1636. doi:https://doi.org/10.1016/j.rser.2010.11.032

445. Green MA. Photovoltaic principles. *Phys E Low-dimensional Syst Nanostructures*. 2002;14(1-2):11-17. doi:10.1016/S1386-9477(02)00354-5

446. Jäger K-D, Isabella O, Smets AHM, van Swaaij RACMM, Zeman M. *Solar Energy: Fundamentals, Technology and Systems*. NV-1 o. UIT Cambridge; 2016.

447. Jeong J, Kim M, Seo J, et al. Pseudo-halide anion engineering for α-FAPbI3 perovskite solar cells. *Nature*. 2021;592(7854):381-385. doi:10.1038/s41586-021-03406-5

448. Gao P, Grätzel M, Nazeeruddin MK. Organohalide lead perovskites for photovoltaic applications. *Energy Environ Sci*. 2014;7(8):2448-2463. doi:10.1039/C4EE00942H

449. Kim JY, Lee J-W, Jung HS, Shin H, Park N-G. High-Efficiency Perovskite Solar Cells. *Chem Rev*. 2020;120(15):7867-7918. doi:10.1021/acs.chemrev.0c00107

450. Borriello I, Cantele G, Ninno D. Ab initio investigation of hybrid organic-inorganic perovskites based on tin halides. *Phys Rev B*. 2008;77(23):235214. doi:10.1103/PhysRevB.77.235214

451. Bianca G. Development of novel two-dimensional materials for energy conversion applications. Published online 2022.

452. Huang J, Yuan Y, Shao Y, Yan Y. Understanding the physical properties of hybrid perovskites for photovoltaic applications. *Nat Rev Mater*. 2017;2(7):17042. doi:10.1038/natrevmats.2017.42

453. Xiao Z, Dong Q, Bi C, Shao Y, Yuan Y, Huang J. Solvent Annealing of Perovskite-Induced Crystal Growth for Photovoltaic-Device Efficiency Enhancement. *Adv Mater*. 2014;26(37):6503-6509. doi:https://doi.org/10.1002/adma.201401685

454. Marinova N, Valero S, Delgado JL. Organic and perovskite solar cells: Working principles, materials and interfaces. *J Colloid*

Interface Sci. 2017;488:373-389. doi:10.1016/j.jcis.2016.11.021

455. Dou L, Yang Y (Micheal), You J, et al. Solution-processed hybrid perovskite photodetectors with high detectivity. *Nat Commun*. 2014;5(1):5404. doi:10.1038/ncomms6404

456. Cao M, Tian J, Cai Z, Peng L, Yang L, Wei D. Perovskite heterojunction based on CH3NH3PbBr3 single crystal for high-sensitive self-powered photodetector. *Appl Phys Lett*. 2016;109(23):233303. doi:10.1063/1.4971772

457. Tan Z-K, Moghaddam RS, Lai ML, et al. Bright light-emitting diodes based on organometal halide perovskite. *Nat Nanotechnol*. 2014;9(9):687-692. doi:10.1038/nnano.2014.149

458. Xing G, Mathews N, Lim SS, et al. Low-temperature solution-processed wavelength-tunable perovskites for lasing. *Nat Mater*. 2014;13(5):476-480. doi:10.1038/nmat3911

459. Wang R, Mujahid M, Duan Y, Wang Z-K, Xue J, Yang Y. A Review of Perovskites Solar Cell Stability. *Adv Funct Mater*. 2019;29(47):1808843. doi:https://doi.org/10.1002/adfm.201808843

460. Schileo G, Grancini G. Halide perovskites: current issues and new strategies to push material and device stability. *J Phys Energy*. 2020;2(2):21005. doi:10.1088/2515-7655/ab6cc4

461. Bryant D, Aristidou N, Pont S, et al. Light and oxygen induced degradation limits the operational stability of methylammonium lead triiodide perovskite solar cells. *Energy Environ Sci*. 2016;9(5):1655-1660. doi:10.1039/C6EE00409A

462. Weerasinghe HC, Dkhissi Y, Scully AD, Caruso RA, Cheng Y-B. Encapsulation for improving the lifetime of flexible perovskite solar cells. *Nano Energy*. 2015;18:118-125. doi:https://doi.org/10.1016/j.nanoen.2015.10.006

463. Kim M, Jeong J, Lu H, et al. Conformal quantum dot–SnO2 layers as electron transporters for efficient perovskite solar cells. *Science (80-)*. 2022;375(6578):302-306. doi:10.1126/science.abh1885

464. Min H, Lee DY, Kim J, et al. Perovskite solar cells with atomically coherent interlayers on SnO2 electrodes. *Nature*. 2021;598(7881):444-450. doi:10.1038/s41586-021-03964-8

465. National Renewable Energy Laboratory. Best Research-Cell Efficiency Chart. Published 2024. Accessed March 13, 2025. https://www.nrel.gov/pv/cell-efficiency.html

466. Green MA, Dunlop ED, Yoshita M, et al. Solar cell efficiency tables (Version 63). *Prog Photovoltaics Res Appl*. 2024;32(1):3-13. doi:10.1002/pip.3750

467. Wang P, Wu Y, Cai B, Ma Q, Zheng X, Zhang W-H. Solution-Processable Perovskite Solar Cells toward Commercialization: Progress and Challenges. *Adv Funct Mater*. 2019;29(47):1807661. doi:10.1002/adfm.201807661

468. Holzhey P, Prettl M, Collavini S, Chang NL, Saliba M. Toward commercialization with lightweight, flexible perovskite solar cells for residential photovoltaics. *Joule*. 2023;7(2):257-271. doi:https://doi.org/10.1016/j.joule.2022.12.012

469. De Bastiani M, Larini V, Montecucco R, Grancini G. The levelized cost of electricity from perovskite photovoltaics. *Energy Environ Sci*. 2023;16(2):421-429. doi:10.1039/D2EE03136A

470. Faheem MB, Khan B, Hashmi JZ, et al. Insights from scalable fabrication to operational stability and industrial opportunities for perovskite solar cells and modules. *Cell Reports Phys Sci*. 2022;3(4):100827. doi:https://doi.org/10.1016/j.xcrp.2022.100827

471. Lan D, Green MA. Combatting temperature and reverse-bias challenges facing perovskite solar cells. *Joule*. 2022;6(8):1782-1797. doi:https://doi.org/10.1016/j.joule.2022.06.014

472. Ma S, Yuan G, Zhang Y, Yang N, Li Y, Chen Q. Development of encapsulation strategies towards the commercialization of perovskite solar cells. *Energy Environ Sci*. 2022;15(1):13-55. doi:10.1039/D1EE02882K

473. Zhang D, Li D, Hu Y, Mei A, Han H. Degradation pathways in perovskite solar cells and how to meet international standards. *Commun Mater*. 2022;3(1):58. doi:10.1038/s43246-022-00281-z

474. Brennan MC, Draguta S, Kamat P V, Kuno M. Light-Induced Anion Phase Segregation in Mixed Halide Perovskites. *ACS Energy Lett*. 2018;3(1):204-213. doi:10.1021/acsenergylett.7b01151

475. Slotcavage DJ, Karunadasa HI, McGehee MD. Light-Induced Phase Segregation in Halide-Perovskite Absorbers. *ACS Energy Lett*. 2016;1(6):1199-1205. doi:10.1021/acsenergylett.6b00495

476. Cheng Y, Ding L. Pushing commercialization of perovskite solar cells by improving their intrinsic stability. *Energy Environ Sci*. 2021;14(6):3233-3255. doi:10.1039/D1EE00493J

477. Yuan Y, Huang J. Ion Migration in Organometal Trihalide Perovskite and Its Impact on Photovoltaic Efficiency and Stability. *Acc Chem Res*. 2016;49(2):286-293. doi:10.1021/acs.accounts.5b00420

478. Conings B, Drijkoningen J, Gauquelin N, et al. Intrinsic Thermal Instability of Methylammonium Lead Trihalide Perovskite. *Adv Energy Mater*. 2015;5(15):1500477. doi:https://doi.org/10.1002/aenm.201500477

479. Yang S, Chen S, Mosconi E, et al. Stabilizing halide perovskite surfaces for solar cell operation with wide-bandgap lead oxysalts. *Science (80-)*. 2019;365(6452):473-478. doi:10.1126/science.aax3294

480. Zhao J, Deng Y, Wei H, et al. Strained hybrid perovskite thin films and their impact on the intrinsic stability of perovskite

solar cells. *Sci Adv*. 2017;3(11). doi:10.1126/sciadv.aao5616

481. Jeon NJ, Noh JH, Yang WS, et al. Compositional engineering of perovskite materials for high-performance solar cells. *Nature*. 2015;517(7535):476-480. doi:10.1038/nature14133

482. Shao M, Bie T, Yang L, et al. Over 21% Efficiency Stable 2D Perovskite Solar Cells. *Adv Mater*. 2022;34(1):2107211. doi:https://doi.org/10.1002/adma.202107211

483. Grancini G, Nazeeruddin MK. Dimensional tailoring of hybrid perovskites for photovoltaics. *Nat Rev Mater*. 2019;4(1):4-22. doi:10.1038/s41578-018-0065-0

484. Zheng X, Chen B, Dai J, et al. Defect passivation in hybrid perovskite solar cells using quaternary ammonium halide anions and cations. *Nat Energy*. 2017;2(7):17102. doi:10.1038/nenergy.2017.102

485. Gao F, Zhao Y, Zhang X, You J. Recent Progresses on Defect Passivation toward Efficient Perovskite Solar Cells. *Adv Energy Mater*. 2020;10(13):1902650. doi:https://doi.org/10.1002/aenm.201902650

486. Liu L, Huang S, Lu Y, et al. Grain-Boundary "Patches" by In Situ Conversion to Enhance Perovskite Solar Cells Stability. *Adv Mater*. 2018;30(29):1800544. doi:https://doi.org/10.1002/adma.201800544

487. Niu T, Lu J, Munir R, et al. Stable High-Performance Perovskite Solar Cells via Grain Boundary Passivation. *Adv Mater*. 2018;30(16):1706576. doi:https://doi.org/10.1002/adma.201706576

488. Isikgor FH, Zhumagali S, T. Merino L V, De Bastiani M, McCulloch I, De Wolf S. Molecular engineering of contact interfaces for high-performance perovskite solar cells. *Nat Rev Mater*. 2023;8(2):89-108. doi:10.1038/s41578-022-00503-3

489. Masi S, Gualdrón-Reyes AF, Mora-Seró I. Stabilization of Black Perovskite Phase in FAPbI3 and CsPbI3. *ACS Energy Lett*. 2020;5(6):1974-1985. doi:10.1021/acsenergylett.0c00801

490. Leguy AMA, Hu Y, Campoy-Quiles M, et al. Reversible Hydration of CH3 NH3 PbI3 in Films, Single Crystals, and Solar Cells. *Chem Mater*. 2015;27(9):3397-3407. doi:10.1021/acs.chemmater.5b00660

491. Aristidou N, Eames C, Sanchez-Molina I, et al. Fast oxygen diffusion and iodide defects mediate oxygen-induced degradation of perovskite solar cells. *Nat Commun*. 2017;8(1):15218. doi:10.1038/ncomms15218

492. Li G, Su Z, Canil L, et al. Highly efficient p-i-n perovskite solar cells that endure temperature variations. *Science (80-)*. 2023;379(6630):399-403. doi:10.1126/science.add7331

493. Ni Z, Jiao H, Fei C, et al. Evolution of defects during the degradation of metal halide perovskite solar cells under reverse bias and illumination. *Nat Energy*. 2022;7(1):65-73. doi:10.1038/s41560-021-00949-9

494. Wang Y, Ahmad I, Leung T, et al. Encapsulation and Stability Testing of Perovskite Solar Cells for Real Life Applications. *ACS Mater Au*. 2022;2(3):215-236. doi:10.1021/acsmaterialsau.1c00045

495. Wang T, Yang J, Cao Q, et al. Room temperature nondestructive encapsulation via self-crosslinked fluorosilicone polymer enables damp heat-stable sustainable perovskite solar cells. *Nat Commun*. 2023;14(1):1342. doi:10.1038/s41467-023-36918-x

496. Matteocci F, Cinà L, Lamanna E, et al. Encapsulation for long-term stability enhancement of perovskite solar cells. *Nano Energy*. 2016;30:162-172. doi:10.1016/j.nanoen.2016.09.041

497. Emery Q, Remec M, Paramasivam G, et al. Encapsulation and Outdoor Testing of Perovskite Solar Cells: Comparing Industrially Relevant Process with a Simplified Lab Procedure. *ACS Appl Mater Interfaces*. 2022;14(4):5159-5167. doi:10.1021/acsami.1c14720

498. Raman RK, Gurusamy Thangavelu SA, Venkataraj S, Krishnamoorthy A. Materials, methods and strategies for encapsulation of perovskite solar cells: From past to present. *Renew Sustain Energy Rev*. 2021;151:111608. doi:10.1016/j.rser.2021.111608

499. Sultan B-Å, Sörvik E. Thermal degradation of EVA and EBA—A comparison. II. Changes in unsaturation and side group structure. *J Appl Polym Sci*. 1991;43(9):1747-1759. doi:https://doi.org/10.1002/app.1991.070430918

500. Xiang L, Gao F, Cao Y, et al. Progress on the stability and encapsulation techniques of perovskite solar cells. *Org Electron*. 2022;106:106515. doi:https://doi.org/10.1016/j.orgel.2022.106515

501. Cros S, de Bettignies R, Berson S, et al. Definition of encapsulation barrier requirements: A method applied to organic solar cells. *Sol Energy Mater Sol Cells*. 2011;95:S65-S69. doi:https://doi.org/10.1016/j.solmat.2011.01.035

502. Shi L, Bucknall MP, Young TL, et al. Gas chromatography–mass spectrometry analyses of encapsulated stable perovskite solar cells. *Science (80-)*. 2020;368(6497):eaba2412. doi:10.1126/science.aba2412

503. Emami S, Martins J, Ivanou D, Mendes A. Advanced hermetic encapsulation of perovskite solar cells: the route to commercialization. *J Mater Chem A*. 2020;8(5):2654-2662. doi:10.1039/C9TA11907H

504. Martins J, Emami S, Madureira R, Mendes J, Ivanou D, Mendes A. Novel laser-assisted glass frit encapsulation for long-lifetime perovskite solar cells. *J Mater Chem A*. 2020;8(38):20037-20046. doi:10.1039/D0TA05583B

505. Boyd CC, Cheacharoen R, Bush KA, Prasanna R, Leijtens T, McGehee MD. Barrier Design to Prevent Metal-Induced Degradation and Improve Thermal Stability in Perovskite Solar Cells. *ACS Energy Lett*. 2018;3(7):1772-1778.

doi:10.1021/acsenergylett.8b00926

506. Cheacharoen R, Rolston N, Harwood D, Bush KA, Dauskardt RH, McGehee MD. Design and understanding of encapsulated perovskite solar cells to withstand temperature cycling. *Energy Environ Sci*. 2018;11(1):144-150. doi:10.1039/C7EE02564E

507. Cheacharoen R, Boyd CC, Burkhard GF, et al. Encapsulating perovskite solar cells to withstand damp heat and thermal cycling. *Sustain Energy Fuels*. 2018;2(11):2398-2406. doi:10.1039/C8SE00250A

508. Kim Y, Kim G, Jeon NJ, Lim C, Seo J, Kim BJ. Methoxy-Functionalized Triarylamine-Based Hole-Transporting Polymers for Highly Efficient and Stable Perovskite Solar Cells. *ACS Energy Lett*. 2020;5(10):3304-3313. doi:10.1021/acsenergylett.0c01901

509. Han F, Wu Y, He R, et al. Hyperstable Perovskite Solar Cells Without Ion Migration and Metal Diffusion Based on ZnS Segregated Cubic ZnTiO3 Electron Transport Layers. *Sol RRL*. 2021;5(3):2000654. doi:10.1002/solr.202000654

510. Peng J, Walter D, Ren Y, et al. Nanoscale localized contacts for high fill factors in polymer-passivated perovskite solar cells. *Science (80-)*. 2021;371(6527):390-395. doi:10.1126/science.abb8687

511. Bush KA, Palmstrom AF, Yu ZJ, et al. 23.6%-efficient monolithic perovskite/silicon tandem solar cells with improved stability. *Nat Energy*. 2017;2(4):17009. doi:10.1038/nenergy.2017.9

512. He J, Li T, Liu X, et al. Influence of phase transition on stability of perovskite solar cells under thermal cycling conditions. *Sol Energy*. 2019;188:312-317. doi:https://doi.org/10.1016/j.solener.2019.06.025

513. Siegler TD, Dawson A, Lobaccaro P, et al. The Path to Perovskite Commercialization: A Perspective from the United States Solar Energy Technologies Office. *ACS Energy Lett*. 2022;7(5):1728-1734. doi:10.1021/acsenergylett.2c00698

514. Shimpi TM, Moffett C, Sampath WS, Barth KL. Materials selection investigation for thin film photovoltaic module encapsulation. *Sol Energy*. 2019;187:226-232. doi:https://doi.org/10.1016/j.solener.2019.04.095

515. Zhang L, Xie Y, Tian Z, Liu Y, Geng C, Xu S. Thermal Conductive Encapsulation Enables Stable High-Power Perovskite-Converted Light-Emitting Diodes. *ACS Appl Mater Interfaces*. 2021;13(25):30076-30085. doi:10.1021/acsami.1c07194

516. Fabini D. Quantifying the Potential for Lead Pollution from Halide Perovskite Photovoltaics. *J Phys Chem Lett*. 2015;6(18):3546-3548. doi:10.1021/acs.jpclett.5b01747

517. Hailegnaw B, Kirmayer S, Edri E, Hodes G, Cahen D. Rain on Methylammonium Lead Iodide Based Perovskites: Possible Environmental Effects of Perovskite Solar Cells. *J Phys Chem Lett*. 2015;6(9):1543-1547. doi:10.1021/acs.jpclett.5b00504

518. Li J, Cao H-L, Jiao W-B, et al. Biological impact of lead from halide perovskites reveals the risk of introducing a safe threshold. *Nat Commun*. 2020;11(1):310. doi:10.1038/s41467-019-13910-y

519. Paetzold R, Winnacker A, Henseler D, Cesari V, Heuser K. Permeation rate measurements by electrical analysis of calcium corrosion. *Rev Sci Instrum*. 2003;74(12):5147-5150. doi:10.1063/1.1626015

520. Kempe MD, Nobles DL, Postak L, Calderon JA. Moisture ingress prediction in polyisobutylene-based edge seal with molecular sieve desiccant. *Prog Photovoltaics Res Appl*. 2018;26(2):93-101. doi:10.1002/pip.2947

521. Castriotta LA, Zendehdel M, Yaghoobi Nia N, et al. Reducing Losses in Perovskite Large Area Solar Technology: Laser Design Optimization for Highly Efficient Modules and Minipanels. *Adv Energy Mater*. 2022;12(12):2103420. doi:https://doi.org/10.1002/aenm.202103420

522. Palma AL, Matteocci F, Agresti A, et al. Laser-Patterning Engineering for Perovskite Solar Modules With 95% Aperture Ratio. *IEEE J Photovoltaics*. 2017;7(6):1674-1680. doi:10.1109/JPHOTOV.2017.2732223

523. Kunal K, Paluch M, Roland CM, Puskas JE, Chen Y, Sokolov AP. Polyisobutylene: A most unusual polymer. *J Polym Sci Part B Polym Phys*. 2008;46(13):1390-1399. doi:10.1002/polb.21473

524. Luo W, Khoo YS, Hacke P, et al. Potential-induced degradation in photovoltaic modules: a critical review. *Energy Environ Sci*. 2017;10(1):43-68. doi:10.1039/C6EE02271E

525. Weng Q, Wang X, Zhi C, Bando Y, Golberg D. Boron Nitride Porous Microbelts for Hydrogen Storage. *ACS Nano*. 2013;7(2):1558-1565. doi:10.1021/nn305320v

526. Pakdel A, Zhi C, Bando Y, Nakayama T, Golberg D. Boron Nitride Nanosheet Coatings with Controllable Water Repellency. *ACS Nano*. 2011;5(8):6507-6515. doi:10.1021/nn201838w

527. Yoon SI, Ma KY, Kim T-Y, Shin HS. Proton conductivity of a hexagonal boron nitride membrane and its energy applications. *J Mater Chem A*. 2020;8(6):2898-2912. doi:10.1039/C9TA12293A

528. Cai Q, Scullion D, Gan W, et al. High thermal conductivity of high-quality monolayer boron nitride and its thermal expansion. *Sci Adv*. 2019;5(6). doi:10.1126/sciadv.aav0129

529. Guerra V, Wan C, McNally T. Thermal conductivity of 2D nano-structured boron nitride (BN) and its composites with polymers. *Prog Mater Sci*. 2019;100:170-186. doi:https://doi.org/10.1016/j.pmatsci.2018.10.002

530. Castro-Hermosa S, Top M, Dagar J, Fahlteich J, Brown TM. Quantifying Performance of Permeation Barrier—Encapsulation Systems for Flexible and Glass-Based Electronics and Their Application to Perovskite Solar Cells. *Adv Electron Mater*.

2019;5(10):1800978. doi:https://doi.org/10.1002/aelm.201800978

531. Khenkin M V, Katz EA, Abate A, et al. Consensus statement for stability assessment and reporting for perovskite photovoltaics based on ISOS procedures. *Nat Energy*. 2020;5(1):35-49. doi:10.1038/s41560-019-0529-5

532. Rombach FM, Haque SA, Macdonald TJ. Lessons learned from spiro-OMeTAD and PTAA in perovskite solar cells. *Energy Environ Sci*. 2021;14(10):5161-5190. doi:10.1039/D1EE02095A

533. Lamanna E, Matteocci F, Calabrò E, et al. Mechanically Stacked, Two-Terminal Graphene-Based Perovskite/Silicon Tandem Solar Cell with Efficiency over 26%. *Joule*. 2020;4(4):865-881. doi:10.1016/j.joule.2020.01.015

534. Mariani P, Najafi L, Bianca G, et al. Low-Temperature Graphene-Based Paste for Large-Area Carbon Perovskite Solar Cells. *ACS Appl Mater Interfaces*. 2021;13(19):22368-22380. doi:10.1021/acsami.1c02626

535. Biccari F, Gabelloni F, Burzi E, et al. Graphene-Based Electron Transport Layers in Perovskite Solar Cells: A Step-Up for an Efficient Carrier Collection. *Adv Energy Mater*. 2017;7(22):1701349. doi:10.1002/aenm.201701349

536. Lucarelli G, De Rossi F, Taheri B, Brown TM, Brunetti F. Phenethylammonium Iodide Passivation Layers for Flexible Planar Perovskite Solar Cells. *Energy Technol*. 2022;10(11):2200314. doi:10.1002/ente.202200314

537. Vesce L, Stefanelli M, Castriotta LA, et al. Hysteresis-Free Planar Perovskite Solar Module with 19.1% Efficiency by Interfacial Defects Passivation. *Sol RRL*. 2022;6(7):2101095. doi:10.1002/solr.202101095

538. Szabó G, Park N-G, De Angelis F, Kamat P V. Are Perovskite Solar Cells Reaching the Efficiency and Voltage Limits? *ACS Energy Lett*. 2023;8(9):3829-3831. doi:10.1021/acsenergylett.3c01649

539. Jiang Q, Zhao Y, Zhang X, et al. Surface passivation of perovskite film for efficient solar cells. *Nat Photonics*. 2019;13(7):460-466. doi:10.1038/s41566-019-0398-2

540. Kasparavicius E, Franckevičius M, Malinauskiene V, Genevičius K, Getautis V, Malinauskas T. Oxidized Spiro-OMeTAD: Investigation of Stability in Contact with Various Perovskite Compositions. *ACS Appl Energy Mater*. 2021;4(12):13696-13705. doi:10.1021/acsaem.1c02375

541. Xu R, Pan F, Chen J, et al. Optimizing the Buried Interface in Flexible Perovskite Solar Cells to Achieve Over 24% Efficiency and Long-Term Stability. *Adv Mater*. 2024;36(7):2308039. doi:10.1002/adma.202308039

542. Dewi HA, Li J, Wang H, et al. Excellent Intrinsic Long-Term Thermal Stability of Co-Evaporated MAPbI3 Solar Cells at 85 °C. *Adv Funct Mater*. 2021;31(22):2100557. doi:10.1002/adfm.202100557

543. Zhang Z, Wang H, Jacobsson TJ, Luo J. Big data driven perovskite solar cell stability analysis. *Nat Commun*. 2022;13(1):7639. doi:10.1038/s41467-022-35400-4

544. Pescetelli S, Agresti A, Razza S, et al. Synergic use of two-dimensional materials to tailor interfaces in large area perovskite modules. *Nano Energy*. 2022;95:107019. doi:10.1016/j.nanoen.2022.107019

545. Gharibzadeh S, Fassl P, Hossain IM, et al. Two birds with one stone: dual grain-boundary and interface passivation enables >22% efficient inverted methylammonium-free perovskite solar cells. *Energy Environ Sci*. 2021;14(11):5875-5893. doi:10.1039/D1EE01508G

546. Vesce L, Stefanelli M, Herterich JP, et al. Ambient Air Blade-Coating Fabrication of Stable Triple-Cation Perovskite Solar Modules by Green Solvent Quenching. *Sol RRL*. 2021;5(8):2100073. doi:https://doi.org/10.1002/solr.202100073

547. Wang Y, Lv P, Pan J, et al. Grain Boundary Elimination via Recrystallization-Assisted Vapor Deposition for Efficient and Stable Perovskite Solar Cells and Modules. *Adv Mater*. 2023;35(44):2304625. doi:https://doi.org/10.1002/adma.202304625

548. Fujimori M, Kohno T, Tsuno Y, Morita K. Applicability of highly accelerated thermal cycling testing for multiple types of polycrystalline silicon photovoltaic modules. In: *The 33rd European Photovoltaic Solar Energy Conference and Exhibition*. ; 2017.

549. Schiller CH, Rendler LC, Eberlein D, Mülhöfer G, Kraft A, Neuhaus DH. Accelerated TC Test in Comparison With Standard TC Test for PV Modules. In: *36th European Photovoltaic Solar Energy Conference and Exhibiton*. ; 2019:9-13.

550. Kipke DR, Shain W, Buzsáki G, et al. Advanced Neurotechnologies for Chronic Neural Interfaces: New Horizons and Clinical Opportunities. *J Neurosci*. 2008;28(46):11830-11838. doi:10.1523/JNEUROSCI.3879-08.2008

551. Lebedev MA, Nicolelis MAL. Brain–machine interfaces: past, present and future. *Trends Neurosci*. 2006;29(9):536-546. doi:10.1016/j.tins.2006.07.004

552. Schwartz AB, Cui XT, Weber DJ, Moran DW. Brain-Controlled Interfaces: Movement Restoration with Neural Prosthetics. *Neuron*. 2006;52(1):205-220. doi:10.1016/j.neuron.2006.09.019

553. Humayun MS. Intraocular retinal prosthesis. *Trans Am Ophthalmol Soc*. 2001;99:271-300.

554. Polikov VS, Tresco PA, Reichert WM. Response of brain tissue to chronically implanted neural electrodes. *J Neurosci Methods*. 2005;148(1):1-18. doi:10.1016/j.jneumeth.2005.08.015

555. Chen R, Canales A, Anikeeva P. Neural recording and modulation technologies. *Nat Rev Mater*. 2017;2(2):16093. doi:10.1038/natrevmats.2016.93

556. Jeong J-W, Shin G, Park S Il, Yu KJ, Xu L, Rogers JA. Soft Materials in Neuroengineering for Hard Problems in Neuroscience. *Neuron*. 2015;86(1):175-186. doi:10.1016/j.neuron.2014.12.035

557. Angotzi GN, Boi F, Lecomte A, et al. SiNAPS: An implantable active pixel sensor CMOS-probe for simultaneous large-scale neural recordings. *Biosens Bioelectron*. 2019;126(October 2018):355-364. doi:10.1016/j.bios.2018.10.032

558. Kandel ER, Schwartz JH, Jessell TM, Siegelbaum SA, Hudspeth AJ. *Principles of Neural Science*. 5th ed. (Sydor A, Lobowitz H, eds.). McGraw-Hill Education; 2014. http://accessbiomedicalscience.mhmedical.com/content.aspx?aid=1101675601

559. Stanslaski S, Herron J, Chouinard T, et al. A Chronically Implantable Neural Coprocessor for Investigating the Treatment of Neurological Disorders. *IEEE Trans Biomed Circuits Syst*. 2018;12(6):1230-1245. doi:10.1109/TBCAS.2018.2880148

560. Liu X, Zhang M, Xiong T, et al. A Fully Integrated Wireless Compressed Sensing Neural Signal Acquisition System for Chronic Recording and Brain Machine Interface. *IEEE Trans Biomed Circuits Syst*. 2016;10(4):874-883. doi:10.1109/TBCAS.2016.2574362

561. Berdondini L, van der Wal PD, Guenat O, et al. High-density electrode array for imaging in vitro electrophysiological activity. *Biosens Bioelectron*. 2005;21(1):167-174. doi:10.1016/j.bios.2004.08.011

562. Chiappalone M, Koudelka-hep M. Network Dynamics and Synchronous Activity in Cultured Cortical Neurons. *Int J Neural Syst*. 2007;17(2):87-103.

563. Berdondini L, Imfeld K, Maccione A, et al. Active pixel sensor array for high spatio-temporal resolution electrophysiological recordings from single cell to large scale neuronal networks. *Lab Chip*. 2009;9(18):2644. doi:10.1039/b907394a

564. Perna A, Angotzi GN, Berdondini L, Ribeiro JF. Advancing the interfacing performances of chronically implantable neural probes in the era of CMOS neuroelectronics. *Front Neurosci*. 2023;17. doi:10.3389/fnins.2023.1275908

565. Kozai TDY, Jaquins-Gerstl AS, Vazquez AL, Michael AC, Cui XT. Brain Tissue Responses to Neural Implants Impact Signal Sensitivity and Intervention Strategies. *ACS Chem Neurosci*. 2015;6(1):48-67. doi:10.1021/cn500256e

566. Sommakia S, Lee HC, Gaire J, Otto KJ. Materials approaches for modulating neural tissue responses to implanted microelectrodes through mechanical and biochemical means. *Curr Opin Solid State Mater Sci*. 2014;18(6):319-328. doi:10.1016/j.cossms.2014.07.005

567. Prodanov D, Delbeke J. Mechanical and Biological Interactions of Implants with the Brain and Their Impact on Implant Design. *Front Neurosci*. 2016;10(February). doi:10.3389/fnins.2016.00011

568. Kook G, Lee S, Lee H, Cho I, Lee H. Neural Probes for Chronic Applications. *Micromachines*. 2016;7(10):179. doi:10.3390/mi7100179

569. Jorfi M, Skousen JL, Weder C, Capadona JR. Progress towards biocompatible intracortical microelectrodes for neural interfacing applications. *J Neural Eng*. 2015;12(1):011001. doi:10.1088/1741-2560/12/1/011001

570. Kim C, Jeong J, Kim SJ. Recent Progress on Non-Conventional Microfabricated Probes for the Chronic Recording of Cortical Neural Activity. *Sensors*. 2019;19(5):1069. doi:10.3390/s19051069

571. Hsu J-M, Rieth L, Normann RA, Tathireddy P, Solzbacher F. Encapsulation of an Integrated Neural Interface Device With Parylene C. *IEEE Trans Biomed Eng*. 2009;56(1):23-29. doi:10.1109/TBME.2008.2002155

572. Mario J, Morales H. Evaluating biocompatible barrier films as encapsulants of medical micro devices. Published online 2016.

573. Nguyen CK, Srikanthan B, Bhandari R, Cogan SF, Negi S. Increasing the Lifetime of the Implantable Neural Devices. In: *2022 International Electron Devices Meeting (IEDM)*. Vol 2022-Decem. IEEE; 2022:29.7.1-29.7.4. doi:10.1109/IEDM45625.2022.10019503

574. Qin Y, Howlader MMR, Deen MJ, Haddara YM, Selvaganapathy PR. Polymer integration for packaging of implantable sensors. *Sensors Actuators, B Chem*. 2014;202:758-778. doi:10.1016/j.snb.2014.05.063

575. Bellmann C, Beshchasna N, Uhlemann J, Wolter KJ. Parylene C and silicone as biocompatible protection encapsulants for PCBs. In: *2009 32nd International Spring Seminar on Electronics Technology*. IEEE; 2009:1-6. doi:10.1109/ISSE.2009.5206975

576. Castagnola V, Descamps E, Lecestre A, et al. Parylene-based flexible neural probes with PEDOT coated surface for brain stimulation and recording. *Biosens Bioelectron*. 2015;67:450-457. doi:10.1016/j.bios.2014.09.004

577. Wang M-H, Ji B-W, Gu X-W, et al. Direct electrodeposition of Graphene enhanced conductive polymer on microelectrode for biosensing application. *Biosens Bioelectron*. 2018;99(May 2017):99-107. doi:10.1016/j.bios.2017.07.030

578. Yao J, Qiang W, Wei H, et al. Ultrathin and Robust Micro–Nano Composite Coating for Implantable Pressure Sensor Encapsulation. *ACS Omega*. 2020;5(36):23129-23139. doi:10.1021/acsomega.0c02897

579. Prodromakis T, Michelakis K, Zoumpoulidis T, Dekker R, Toumazou C. Biocompatible encapsulation of CMOS based chemical sensors. In: *2009 IEEE Sensors*. IEEE; 2009:791-794. doi:10.1109/ICSENS.2009.5398537

580. Seymour JP, Kipke DR. Neural probe design for reduced tissue encapsulation in CNS. *Biomaterials*. 2007;28(25):3594-3607. doi:10.1016/j.biomaterials.2007.03.024

581. Onuki Y, Bhardwaj U, Papadimitrakopoulos F, Burgess DJ. A Review of the Biocompatibility of Implantable Devices: Current Challenges to Overcome Foreign Body Response. *J Diabetes Sci Technol*. 2008;2(6):1003-1015. doi:10.1177/193229680800200610

582. Shin S, Kim J-H, Jeong J, Gwon TM, Lee S-H, Kim SJ. Novel four-sided neural probe fabricated by a thermal lamination process of polymer films. *J Neurosci Methods*. 2017;278:25-35. doi:10.1016/j.jneumeth.2016.12.017

583. Wang Y, Papadimitrakopoulos F, Burgess DJ. Polymeric "smart" coatings to prevent foreign body response to implantable biosensors. *J Control Release*. 2013;169(3):341-347. doi:10.1016/j.jconrel.2012.12.028

584. Puskas JE, Kaszas G. *Encyclopedia of Polymer Science and Technology*. 4th ed. Wiley; 2002. doi:10.1002/0471440264

585. Olabisi O, Adewale K. *Handbook of Thermoplastics*. 2nd ed. (Olabisi O, Adewale K, eds.). CRC Press; 2016. doi:10.13140/RG.2.1.2068.4881

586. Hay J, Herbert E. Measuring the Complex Modulus of Polymers by Instrumented Indentation Testing. *Exp Tech*. 2013;37(3):55-61. doi:10.1111/j.1747-1567.2011.00732.x

587. Herbert EG, Oliver WC, Pharr GM. Nanoindentation and the dynamic characterization of viscoelastic solids. *J Phys D Appl Phys*. 2008;41(7):074021. doi:10.1088/0022-3727/41/7/074021

588. Herbert EG, Oliver WC, Lumsdaine A, Pharr GM. Measuring the constitutive behavior of viscoelastic solids in the time and frequency domain using flat punch nanoindentation. *J Mater Res*. 2009;24(3):626-637. doi:10.1557/jmr.2009.0089

589. Herbert EG, Sudharshan Phani P, Johanns KE. Nanoindentation of viscoelastic solids: A critical assessment of experimental methods. *Curr Opin Solid State Mater Sci*. 2015;19(6):334-339. doi:10.1016/j.cossms.2014.12.006

590. Wright WJ, Nix WD. Storage and loss stiffnesses and moduli as determined by dynamic nanoindentation. *J Mater Res*. 2009;24(3):863-871. doi:10.1557/jmr.2009.0112

591. Lu H, Huang G, Wang F. Measurements of viscoelastic properties of polymers using flat punch indenter. In: *Proceedings of the SEM Annual Conference and Exposition on Experimental and Applied Mechanics*. Vol 2. ; 2007:697-704.

592. Moudam O, Lakbita O. Potential End-Use of a Europium Binary Photoluminescent Ink for Anti-Counterfeiting Security Documents. *ACS Omega*. 2021;6(44):29659-29663. doi:10.1021/acsomega.1c03949

593. Bellamy LJ. *The Infra-Red Spectra of Complex Molecules*. 3rd ed. Springer Netherlands; 1975. doi:10.1007/978-94-011-6017-9

594. LibreTexts. Infrared Spectroscopy Absorption Table. Accessed April 17, 2025. https://chem.libretexts.org/Ancillary_Materials/Reference/Reference_Tables/Spectroscopic_Reference_Tables/Infrared_Spectroscopy_Absorption_Table

595. Kumar P, Khan N, Kumar D. Polyvinyl butyral (PVB), versetile template for designing nanocomposite/composite materials: A review. *Green Chem Technol Lett*. 2016;2(4):185-194. doi:10.18510/gctl.2016.244

596. Dorn RW, Ryan MJ, Kim T-H, et al. Identifying the Molecular Edge Termination of Exfoliated Hexagonal Boron Nitride Nanosheets with Solid-State NMR Spectroscopy and Plane-Wave DFT Calculations. *Chem Mater*. 2020;32(7):3109-3121. doi:10.1021/acs.chemmater.0c00104

597. Qiao Y, Duan L. Curcumin-loaded polyvinyl butyral film with antibacterial activity. *e-Polymers*. 2020;20(1):673-681. doi:10.1515/epoly-2020-0042

598. DIVERSIFIED Enterprises. Critical Surface Tension and Contact Angle with Water for Various Polymers. Accessed April 16, 2025. https://www.accudynetest.com/polytable_03.html?sortby=contact_angle

599. Bremner T, Hill DJT, O'Donnell JH, Senake Perera MC, Pomery PJ. Mechanism of radiation degradation of polyisobutylene. *J Polym Sci Part A Polym Chem*. 1996;34(6):971-984. doi:10.1002/(SICI)1099-0518(19960430)34:6<971::AID-POLA6>3.0.CO;2-L

600. Kolawole EG. Natural weathering, photo- and thermal oxidation of the two-phase system polyisobutylene and poly(methyl methacrylate). *Eur Polym J*. 1984;20(6):629-633. doi:10.1016/0014-3057(84)90107-1

601. Pavoni S, Jarray R, Nassor F, et al. Small-molecule induction of Aβ-42 peptide production in human cerebral organoids to model Alzheimer's disease associated phenotypes. Ginsberg SD, ed. *PLoS One*. 2018;13(12):e0209150. doi:10.1371/journal.pone.0209150

602. Gonon L, Troquet M, Fanton E, Gardette J-L. Thermo and photo-oxidation of polyisobutylene—II. Influence of the temperature. *Polym Degrad Stab*. 1998;62(3):541-549. doi:10.1016/S0141-3910(98)00040-8

603. Feller RL, Curran M, Colaluca V, Bogaard J, Bailie C. Photochemical deterioration of poly(vinylbutyral) in the range of wavelengths from middle ultraviolet to the visible. *Polym Degrad Stab*. 2007;92(5):920-931. doi:10.1016/j.polymdegradstab.2005.11.015

604. Cei N, Canesi I, Nejrotti S, et al. A UV-Protective Textile Coating Based on Recycled Poly(vinyl butyral) (PVB): A New Life for a Waste Polymer. *Polymers (Basel)*. 2024;16(23):3439. doi:10.3390/polym16233439

605. Kuru D, Borazan AA, Ay N. Physical, Optical and Mechanical Properties of Boron Nitride Nanosheets/Polyvinyl Butyral

Coatings Under UV Irradiation. *Emerg Mater Res*. 2020;9(2):1-8. doi:10.1680/jemmr.20.00040

606. Behúnová A, Knapčíková L, Behún M, Mandičák T, Mésároš P. Intelligent Designing and Increasing the Variability of Healthy Residential Buildings by Customizing Recycled Polyvinyl Butyral. *Sustainability*. 2021;13(16):9073. doi:10.3390/su13169073

607. Andreozzi L, Briccoli Bati S, Fagone M, Ranocchiai G, Zulli F. Weathering action on thermo-viscoelastic properties of polymer interlayers for laminated glass. *Constr Build Mater*. 2015;98:757-766. doi:10.1016/j.conbuildmat.2015.08.010

608. Ruediger T, Berg A, Guellmar A, et al. Cytocompatibility of polymer-based periodontal bone substitutes in gingival fibroblast and MC3T3 osteoblast cell cultures. *Dent Mater*. 2012;28(10):e239-e249. doi:https://doi.org/10.1016/j.dental.2012.05.008

609. Pinchuk L. The use of polyisobutylene-based polymers in ophthalmology. *Bioact Mater*. 2022;10:185-194. doi:https://doi.org/10.1016/j.bioactmat.2021.09.005

610. Whitlow HJ, Nagy G. Proton beam induced degradation of Pioloform® (polyvinyl butyral (PVB)) support films used for analysis of biomedical tissue sections. *Nucl Instruments Methods Phys Res Sect B Beam Interact with Mater Atoms*. 2023;539:136-140. doi:10.1016/j.nimb.2023.03.028

611. Barczikai D, Domokos J, Szabó D, et al. Polyisobutylene—New Opportunities for Medical Applications. *Molecules*. 2021;26(17):5207. doi:10.3390/molecules26175207

612. Vieyra H, Juárez E, Figueroa-López U, et al. Cytotoxicity and biocompatibility of a material based in recycled polyvinyl butyral PVB and high-density polyethylene HDPE determined in human peripheral leukocytes. *Mater Res Express*. 2024;11(10):105402. doi:10.1088/2053-1591/ad82ad

613. Azemi E, Lagenaur CF, Cui XT. The surface immobilization of the neural adhesion molecule L1 on neural probes and its effect on neuronal density and gliosis at the probe/tissue interface. *Biomaterials*. 2011;32(3):681-692. doi:10.1016/j.biomaterials.2010.09.033

614. Salatino JW, Ludwig KA, Kozai TDY, Purcell EK. Glial responses to implanted electrodes in the brain. *Nat Biomed Eng*. 2017;1(11):862-877. doi:10.1038/s41551-017-0154-1